JUSTUS-LIEBIG-
UNIVERSITÄT
GIESSEN

Establishment of improved genetically encoded fluorescence-based biosensors to monitor redox and energy dynamics in the malaria parasite *Plasmodium falciparum*

INAUGURALDISSERTATION

zur Erlangung des Grades
Doktor der Naturwissenschaften
– Dr. rer. nat. –

des Fachbereichs Biologie und Chemie, FB 08
der Justus-Liebig-Universität Gießen

vorgelegt von
Kim Christin Heimsch

Gießen, Januar 2022

Die vorliegende Arbeit wurde im interdisziplinären Forschungszentrum der Justus-Liebig-Universität Gießen an der Professur für Biochemie und Molekularbiologie angefertigt. Leitung der Professur bis Ende 2019 hatte Prof. Dr. Katja Becker. Ab 2020 unterlag die Professur der Leitung von PD Dr. Jude Przyborski. Teile der experimentellen Arbeiten wurden an der Westfälischen Wilhelms-Universität Münster am Institut für Biologie und Biotechnologie der Pflanzen unter Leitung von Prof. Dr. Markus Schwarzländer durchgeführt.

Erstgutachterin: **Prof. Dr. med. Katja Becker**
Professur für Biochemie und Molekularbiologie
Institut für Ernährungswissenschaften
Justus-Liebig-Universität Gießen
Interdisziplinäres Forschungszentrum
Heinrich-Buff-Ring 26-32, 35392 Gießen

Zweitgutachter: **Prof. Dr. Albrecht Bindereif**
Institut für Biochemie
Justus-Liebig-Universität Gießen
Heinrich-Buff-Ring 17, 35392 Gießen

Weitere Mitglieder der Prüfungskommission:
Prof. Dr. Lienhard Schmitz
PD Dr. Jude Przyborski

DANKSAGUNG

In erster Linie möchte ich mich bei **Prof. Dr. Katja Becker** für die Betreuung meiner Doktorarbeit bedanken. Hierdurch hat sie mir nicht nur das spannende Feld der Malariaforschung eröffnet, sondern auch aufgezeigt welche Verantwortung und welches Potential wir als Gesellschaft bei der Bekämpfung vernachlässigter Tropenerkrankungen haben. Durch die Promotionszeit konnte ich mich fachlich, vor allem aber auch persönlich weiterentwickeln, wofür ich sehr dankbar bin.

Herrn **Prof. Dr. Albrecht Bindereif** danke ich für die Übernahme der Zweitbetreuung und sein Interesse an dieser Arbeit. Auch den weiteren Mitgliedern des Prüfungskomitees gilt mein Dank: **PD Dr. Jude Przyborski,** danke ich auch für seine Ratschläge während meiner Promotionszeit und das entgegengebrachte Vertrauen, welches es mir ermöglichte meine Ideen zu verfolgen und Experimente frei zu gestalten. **Prof. Dr. Lienhard Schmitz** danke ich außerdem für die Unterstützung in der humanen Zellkultur, die ich in seinem Labor erlernen und durchführen durfte.

Weiterhin möchte ich mich bei **Prof. Dr. Markus Schwarzländer** und **Dr. Thomas Nietzel** (Westfälische Wilhelms-Universität Münster) bedanken, für ihr Interesse und ihre Unterstützung während des „sfroGFP2 Projektes“ sowie die geduldige Beantwortung all meiner Fragen. **Prof. Dr. David Fidock** (Columbia University, NY, USA), **Prof. Dr. Elisabeth Davioud-Charvet** (Université de Strasbourg), **Prof. Dr. Holger Gohlke** und **Dr. Christoph Gertzen** (Heinrich-Heine-Universität Düsseldorf) danke ich für die erfolgreichen Kooperationen während meiner Promotionszeit.

Ein besonderer Dank gilt **Dr. Katharina Schuh, Norma Schulz, Melanie Moser** und **Eric Springer** für ihre Unterstützung und Hilfe während der gesamten Promotionszeit.

Bei allen (ehemaligen) Mitgliedern der AG Becker/ AG Przyborski möchte ich mich bedanken, insbesondere bei: **Dr. Karin Fritz-Wolf** und **Michaela Stumpf** für ihre Hilfe und ihr Mitwirken bei kristallographischen Arbeiten. Bei **Siegrid Franke** für ihre Unterstützung in der Malaria Zellkultur. Mein Dank gilt außerdem **Dr. Christina Brandstädter** und **Dr. Stefan Rahlfs** für ihre Hilfestellungen sowie **Timothy D. Bostick** für das Korrekturlesen von Papern und meiner Doktorarbeit. Weiterhin danke ich meinen Masterstudentinnen **Diana Krickeberg** und **Jana Niermann** für ihr großes Engagement im Labor.

Ganz besonders danken möchte ich meiner Familie und meinen Freunden für ihre immerwährende Unterstützung und die Freude, die sie in mein Leben bringen.

LIST OF PUBLICATIONS

Heimsch KC, Springer E, Krickeberg D, Przyborski J, Becker K. Dynamic measurements of OxD, pH, NADPH, and NADH:NAD$^+$ in the malaria parasite *Plasmodium falciparum*.
In preparation

Heimsch KC, Gertzen C, Schuh AK, Nietzel T, Rahlfs S, Przyborski JM, Gohlke H, Schwarzländer M, Becker K, Fritz-Wolf K. (**2022**) Structure and function of redox-sensitive superfolder green fluorescent protein variant. **Antioxid redox signal**.
Online ahead of print

Berneburg I, Peddibhotla S, **Heimsch KC**, Preuss J, Maloney P, Gosalia P, Haeussler K, Rahbari M, Skorokhod O, Valente E, Ulliers D, Simula LF, Buchholz K, Hedrick MP, Hershberger P, Chung TDY, Jackson MR, Schwarzer E, Rahlfs S, Bode L, Becker K, Pinkerton AB. (**2022**) An optimized dihydrodibenzothiazepine lead compound (SBI-0797750) as a potent and selective inhibitor of *Plasmodium falciparum* and *vivax* glucose 6-phosphate dehydrogenase 6-phosphogluconolactonase. **Antimicrob Agents Chemother.** e0210921.

Siddiqui G*, Giannangelo C*, De Paoli A, Schuh AK, **Heimsch KC**, Anderson D, Brown TG, MacRaild CA, Wu J, Wang X, DongY, Vennerstrom JL, Becker K, Creek DJ. (**2022**) Peroxide antimalarial drugs impact redox homeostasis in *Plasmodium falciparum* infected red blood cells. **ACS Infect. Dis.** 8(1):210-226.

Cichocki BA*, Donzel M*, **Heimsch KC***, Lesanavičius M*, Feng L, Montagut EJ, Becker K, Aliverti A, Elhabiri M, Čėnas N, Davioud-Charvet E. (**2021**) *Plasmodium falciparum* Ferredoxin-NADP$^+$ Reductase-Catalyzed Redox Cycling of Plasmodione Generates Both Predicted Key Drug Metabolites: Implication for Antimalarial Drug Development. **ACS Infect. Dis**. 7(7):1996-2012.
*shared first-authorship

Gnädig NF, Stokes BH, Edwards RL, Kalantarov GF, **Heimsch KC**, Kuderjavy M, Crane A, Lee MCS, Straimer J, Becker K, Odom John AR, Trakht IN, Mok S, Fidock DA. (**2020**) Insights into the intracellular localization, protein associations and artemisinin resistance properties of *Plasmodium falciparum* K13. **PLoSPathog** 16(4):e1008482.

Schuh AK, Rahbari M, **Heimsch KC**, Mohring F, Gabryszewski SJ, Weder S, Buchholz K, Rahlfs S, Fidock DA, Becker K. (**2018**) Stable integration and comparison of hGrx1-roGFP2 and sfroGFP2 redox probes in the malaria parasite *Plasmodium falciparum*. **ACS Infect. Dis.** 4(11):1601-1612.

CONTRIBUTIONS TO CONFERENCES

Final Symposium of the SPP1710 Dynamics of thiol-based redox switches in cellular physiology, online conference, March 29th - 31st 2021, *poster*.

1st digital Conference of the International Giessen Graduate School for the Life Sciences, Giessen, September 29th – 30th 2020, *short talk*.

Molecular approaches to malaria 2020, Lorne, Victoria, Australia, February 23rd – 27th 2020, *poster*.

SPP1710 Conference on thiol-based switches and redox regulation - from microbes to men, Sant Feliu de Guixols, Spain, September 15th – 20th 2019, *poster*.

12th Annual Conference of the International Giessen Graduate School for the Life Sciences, Giessen, September 4th – 5th 2019, *poster*.

15th Annual BioMalPar conference on the “Biology and Pathology of the Malaria Parasite” Heidelberg, Germany, May 28th – 30th 2019, *poster*.

11th Annual Conference of the International Giessen Graduate School for the Life Sciences, Giessen, September 19th – 20th 2018, *poster*.

11th Summer school for Young Parasitologists, Bernhard Nocht Institute for Tropical Medicine Hamburg, July/August 30th – 3rd 2018, *talk*.

SUMMARY

The development of genetically encoded fluorescence-based biosensors has started a new era in redox biology research, allowing non-invasive monitoring of specialized redox couples such as glutathione, NADP(H), and NAD(H). Former obstacles, for example, the introduction of artifacts, impossibility of dynamic measurements, low selectivity, and non-reversibility, could be overcome with this technology. Redox research and studying the associated ROS have attracted more and more attention in recent years. The dual role of ROS, which on the one hand are essential in signal transduction but on the other hand can also lead to severe diseases resulting from an imbalance between ROS and the antioxidant capacity of the cell, is the focus of attention [Kostyuk et al. 2020]. ROS also play a central role in one of the most life-threatening diseases–malaria. During its complex life cycle, the malaria parasite *Plasmodium* is exposed to substantial redox challenges [Jortzik and Becker 2012; Allen et al. 2015]. The oxidative burden on the parasite can be increased to such an extent via inhibition of central metabolic processes, such as the polymerization of hemozoin that the parasites' antioxidative system can no longer sufficiently counteract the development of ROS, which ultimately leads to the death of the parasite. This circumstance has been exploited in the development of numerous antimalarial drugs currently used. However, the development of resistance mechanisms "against established and frequently used drugs is a growing global health problem" [Blum et al. 2021]. Research into new control strategies continues to be essential as the risk of vector-borne diseases, especially malaria, has increased due to the global warming that human activities have induced. Changes in the ecosystem and climate, political instability, health policies, and the resulting increased refugee migration from endemic countries make the fight against malaria a global issue [Rossati et al. 2016]. The development of new, effective drugs and understanding the emergence of resistance mechanisms are therefore indispensable. Genetically encoded sensors can play an important role in answering the questions of which metabolic pathways an agent targets, which specific redox couples are affected, and whether this differs between drug-sensitive and -resistant parasite lines.

In the context of this work, important findings for sensor development could be obtained. The repertoire of biosensors stably integrated into *Plasmodium* parasites could be extended, and an improved measuring method could be established, thereby allowing the drug-induced effects on various redox couples to be monitored to a broader extent.

To identify the molecular basis of the improved FI of the redox-biosensor sfroGFP2, comparative *in vitro* and *in cellulo* studies were performed. This biosensor comprised the full set of superfolder mutations (S30R, Y39N, N105T, Y145F, I171V, and A206V) [Pédelacq et al. 2006], the cycle-3 mutations (F99S, M153T, and V163A) [Crameri et al. 1996], and the F223R substitution from roTurbo [Dooley et al. 2012]. *In cellulo*, this biosensor showed an improved FI, which was, however, not detectable *in vitro*. By generating different mutants and through comparative crystallographic investigations, an improved structural stability of sfroGFP2 over commonly used redox-sensors

could be identified. The basis of this improved stability was the formation of a complex ion network, which resulted from the sf substitution S30R and the related new structural interactions.

In addition to the improved proximity-based biosensor hGrx1-sfroGFP2, additional genetically encoded biosensors (mSc.-I-SoNar, mSc.-I-iNap2, and sfpHluorin) stably integrated into the parasitic genome were used in this work to study drug-induced effects via a medium throughput flow cytometry-based assay. In particular, within this work, the mode of action of the selective PfGluPho inhibitor SBI-750 could be confirmed. This compound destroyed redox homeostasis after short-term incubations. Inhibition of the pentose phosphate pathway resulted in a significant decrease in NADPH levels. Furthermore, a significant oxidation of the cytosolic glutathione pool was detectable. Treatment with SBI-750 did not seem to have any effect on the NAD(H) couple for the tested conditions. These investigations could be carried out for the first time in living parasites, using the sensors and methods established in this work. Since many drug-induced reactions are presumable mainly mediated in certain subcellular compartments, in addition to the circumstance that the parasites’ cytosol is highly reducing, it would be of great interest to target the biosensors to those compartments in order to be able to monitor drug-induced effects within the entire complex network of the cell even more efficiently.

ZUSAMMENFASSUNG

Die Entwicklung genetisch kodierter fluoreszenzbasierter Biosensoren hat eine neue Ära in der Redoxbiologie-Forschung eröffnet. Diese Methode ermöglicht die nicht-invasive Überwachung spezieller Redoxpaare wie Glutathion, NADP(H) und NAD(H). Hindernisse, wie die Entstehung von Artefakten, die Unmöglichkeit dynamischer Messungen, die geringe Selektivität und die fehlende Reversibilität konnten durch diese Technologie überwunden werden. Die Redox-Forschung und die Untersuchung der damit verbundenen ROS haben in den letzten Jahren immer mehr Aufmerksamkeit auf sich gezogen. Die duale Rolle von ROS, die einerseits für die Signaltransduktion unerlässlich sind, andererseits aber auch zu schweren Krankheiten führen können, was auf ein Ungleichgewicht zwischen ROS und der antioxidativen Kapazität der Zelle zurückzuführen ist, steht im Mittelpunkt der Aufmerksamkeit [Kostyuk et al. 2020]. ROS spielen auch eine zentrale Rolle bei einer der lebensbedrohlichsten Krankheiten–der Malaria. Während seines komplexen Lebenszyklus ist der Malariaparasit *Plasmodium* erheblichem Redox-Stress ausgesetzt [Jortzik and Becker 2012; Allen et al. 2015]. Die oxidative Belastung des Parasiten kann durch Hemmung zentraler Stoffwechselprozesse, wie der Polymerisation von Hämozoin, so stark erhöht werden, dass die antioxidativen Systeme des Parasiten der Entstehung von ROS nicht mehr ausreichend entgegenwirken können, was letztlich zum Tod des Parasiten führt. Dieser Umstand wurde bei der Entwicklung zahlreicher bisher eingesetzter Malariamittel genutzt. Die Entwicklung von Resistenzmechanismen gegen etablierte und häufig verwendete Medikamente stellt jedoch ein wachsendes globales Gesundheitsproblem dar [Blum et al. 2021]. Die Erforschung neuer Bekämpfungsstrategien ist nach wie vor von entscheidender Bedeutung, da das Risiko von durch Vektoren übertragenen Krankheiten, insbesondere von Malaria, aufgrund der durch menschliche Aktivitäten verursachten globalen Erwärmung gestiegen ist. Veränderungen des Ökosystems und des Klimas, politische Instabilität und Gesundheitspolitik, aber auch die daraus resultierende verstärkte Flüchtlingsmigration aus endemischen Ländern machen die Malariabekämpfung zu einer globalen Angelegenheit [Rossati et al. 2016]. Die Entwicklung neuer wirksamer Medikamente sowie das Verständnis für die Entstehung von Resistenzmechanismen sind daher unerlässlich. Genetisch kodierte Sensoren können eine wichtige Rolle bei der Beantwortung der Fragen spielen, auf welche Stoffwechselwege ein Wirkstoff abzielt, welche spezifischen Redoxpaare betroffen sind und ob sich dies bei medikamenten-sensitiven und -resistenten Parasitenlinien unterscheidet.

Im Rahmen dieser Arbeit konnten nicht nur wichtige Erkenntnisse für die Sondenentwicklung gewonnen werden, darüber hinaus konnte das Repertoire der in *Plasmodium* stabil integrierten Biosensoren erweitert und eine verbesserte Messmethode etabliert werden, welche es erlaubt, medikamenten-induzierte Effekte auf verschiedene Redoxpaare in einem breiteren Umfang zu überwachen.

Um die molekulare Basis der verbesserten FI des Redox-Biosensors sfroGFP2 zu identifizieren, wurden vergleichende *in vitro* und *in cellulo* Experimente durchgeführt. Dieser Biosensor beinhaltet alle superfolder Mutationen (S30R, Y39N, N105T, Y145F, I171V und A206V) [Pédelacq et al.

2006], die cycle-3 Mutationen (F99S, M153T, V163A) [Crameri et al. 1996] sowie die F223R Substitution von roTurbo [Dooley et al. 2012]. *In cellulo* zeigt dieser Biosensor eine verbesserte FI, die jedoch *in vitro* nicht nachweisbar ist. Durch die Erzeugung verschiedener Mutanten und vergleichende kristallographische Untersuchungen konnte eine verbesserte strukturelle Stabilität von sfroGFP2 gegenüber gängigen Redox-Sensoren identifiziert werden. Grundlage dieser verbesserten Stabilität ist die Bildung eines komplexen Ionennetzwerkes, das aus der sf Substitution S30R und den damit verbundenen neuen strukturellen Wechselwirkungen resultiert.

Neben dem verbesserten Biosensor hGrx1-sfroGFP2 wurden in dieser Arbeit weitere genetisch kodierte Biosensoren (mSc.-I-SoNar, mSc.-I-iNap2 und sfpHluorin), die stabil in das Genom von *Plasmodium* Parasiten integriert wurden, verwendet, um medikamenteninduzierte Wirkungen mittels eines auf Durchflusszytometrie basierenden Assays mit mittlerem Durchsatz zu untersuchen. Im Rahmen dieser Arbeit konnte insbesondere die Wirkungsweise des selektiven PfGluPho-Inhibitors SBI-750 bestätigt werden. Dieser Compound zerstört die Redox-Homöostase bereits nach kurzen Inkubationszeiten. Die Hemmung des Pentosephosphatweges führt zu einer signifikanten Abnahme der NADPH-Spiegel. Weiterhin ist durch die Behandlung eine signifikante Oxidation des zytosolischen Glutathion-Pools nachweisbar. Die Behandlung mit SBI-750 scheint unter den getesteten Bedingungen keine Auswirkungen auf das NAD(H)-Paar zu haben. Diese Untersuchungen konnten erstmals, mittels den in der vorliegenden Arbeit etablierten Sensoren und Methoden, an lebenden Parasiten durchgeführt werden. Da viele Reaktionen, induziert durch antimalaria Medikamente hauptsächlich in bestimmten subzellulären Kompartimenten vermittelt werden und noch dazu das Zytosol der Parasiten stark reduzierend ist, ist es von großem Interesse, die Biosensoren an diese Kompartimente zu *targeten*, um die Wirkungen von Medikamenten im gesamten und komplexen Netzwerk der Zelle noch effizienter überwachen zu können.

TABLE OF CONTENTS

LIST OF FIGURES

LIST OF TABLES

LIST OF ABBREVIATIONS

ε	Extinction coefficient
$\lambda_{Em.}$	Emission wavelength
$\lambda_{Exc.}$	Excitation wavelength
λ_{iso}	Isosbestic point
6PGD	6-phosphogluconate dehydrogenase
6PGL	6-phosphogluconolactolase
6xHis-tag	Hexahistidyl-tag
A	Absorption
ACTs	Artemisinin-based combination therapies
ART	Artemisinin
ATeam	Adenosine 5'-Triphosphate indicator based on Epsilon subunit for Analytical Measurements
ATM	Artemether
ATQ	Atovaquone
ATS	Artesunate
av	*Aequorea victoria*
bp	Base pairs
BSA	Bovine serum albumin
BSD	Blasticidin S Desaminase
BSO	Buthionine sulphoximine
CDC	Centers for Disease Control and Prevention
CHX	Cycloheximide
CLSM	Confocal laser scanning microscopy
Cn, Cn^{R}	Carbenicilin, Carbenicilin resistance
cpYFP	Circular permuted yellow fluorescent protein
CQ	Chloroquine
CV	Column volume
DAPI	4',6-Diamidin-2-phenylindol
DIA	Diamide/diazenedicarboxamide
DMSO	Dimethylsulfoxide
DNA	Deoxyribonucleic acid
dNTP	Desoxynucleotide triphosphate
DOXY	Doxycycline
DPS	4,4´-Dipydidyl disulfide
DTT	1,4-dithiothreitol
DV	Digestive vacuole

EC_{50}	Half maximal effective concentration
EDTA	Ethylenediaminetetraacetic acid
E_{GSH}	Glutathione redox potential
FAD	Flavinadenindinucleotide
FPLC	Fast protein liquid chromatography
FPPIX	Ferriprotoporphyrine IX
FSC	Forward scatter
G418	Genticin
G6PD	Glucose-6-phosphate dehydrogenase
GFP	Green fluorescent protein
GLP	Glutaredoxin-like protein
GluPho	Glucose-6-phosphate dehydrogenase– 6-phosphogluconolactonase
GR	Glutathione reductase
Grx	Glutaredoxin
GS	Glutathione synthetase
GSH	Reduced glutathione
GSSG	Glutathione disulfide
GST	Glutathione S-transferase
H_2O_{dd}	Double-distilled water
hDHFR	Human dihydrofolate reductase
hGrx	Human glutaredoxin
His	Histidine
hpi	Hours post infection
IFA	Immunofluorescence assay
iNap	Indicators for NADPH
IPTG	Isopropyl-β-D-thiogalactopyranoside
iRBC	Infected red blood cell
Kan, Kan^R	Kanamycin, Kanamycin resistance
kb	Kilo base
kDa	Kilo Dalton
LB	Lysogeny Broth-Medium
MoA	Mode of action
MQ	Mefloquine
Na	Nicotinic acid
NaAD	Nicotinate adenine dinucleotide
NAD(H)	Nicotinamide adenine dinucleotide (oxidized/reduced)
NADP(H)	Nicotinamide adenine dinucleotide phosphate (oxidized/reduced)
Nam	Nicotinamide

NaMN	Nicotinate mononucleotide
NEM	N-ethylmaleimide
neo^R	Neomycin resistance
OD_{600}	Optical density at 600 nm
P. falciparum	*Plasmodium falciparum*
PBS	Phosphate buffered saline
PCR	Polymerase chain reaction
PEG	Polyethylenglycol
PfHSP70	*P. falciparum* heat-shock protein 70
Plrx	Plasmoredoxin
PPP	Pentose phosphate pathway
Prx	Peroxiredoxin
QY	Quantum Yield
RBC	Red blood cell
RFU	Relative fluorescence units
RNA	Ribonucleic acid
RNS	Reactive nitrogen species
roGFP	Reduction-oxidation-sensitive green fluorescent protein
ROI	Region of interest
ROS	Reactive oxygen species
rpm	Rounds per minute
RT	Room temperature
SD	Standard deviation
SDS	Sodium dodecyl sulfate
SDS-PAGE	Sodium dodecyl sulfate – polyacrylamide gel electrophoresis
sf	Superfolder, superfolding
SoNar	Sensor of NAD(H) redox
SSC	Sideward scatter
TB	Terrific Broth-Medium
TKT	Transketolase
Tris	Tris(hydroxymethyl)-aminomethan
Trx	Thioredoxin
TrxR	Thioredoxinreductase
WHO	World Health Organization
wt	Wild type

ABBREVIATION OF NUCELOTIDES

Nucleotide	Abbreviation
Adenine	A
Thymine	T
Cytosine	C
Guanine	G
Uracil	U

ABBREVIATIONS OF AMINO ACIDS

Amino Acid	3 letter code	1 letter code
Alanine	Ala	A
Arginine	Arg	R
Asparagine	Asn	N
Aspartic acid	Asp	D
Cysteine	Cys	C
Glutamic acid	Glu	E
Glutamine	Gln	Q
Glycine	Gly	G
Histidine	His	H
Isoleucine	Ile	I
Leucine	Leu	L
Lysine	Lys	K
Methionine	Met	M
Phenylalanine	Phe	F
Proline	Pro	P
Serine	Ser	S
Threonine	Thr	T
Thyrosine	Tyr	Y
Tryptophane	Trp	W
Valine	Val	V

1. INTRODUCTION

1.1 Malaria

Malaria, from the Italian ‘mal’aria’, which means ‘bad air’ [Knobloch 2003], caused by protozoans of the genus *Plasmodium* [Trampuz et al. 2003], is a nonspecific, complex multiorganic disease [Clark and Cowden 2003]. Malaria is one of the deadliest infectious diseases [Lucius et al. 2018] and probably one of the oldest as it is believed that malaria has been with humans for a million years. According to Indian, Chinese, and Egyptian texts, periodic malaria fevers have been known since 2700 BC [Knobloch 2003].

In 1880, Alphonse Laveran described *Plasmodia* for the first time and suggested classifying them as parasites. In 1907 he received the Nobel Prize for his discovery [Knobloch 2003]. Almost 20 years after the first description, in 1897, Ronald Ross detected the importance of mosquitos in transmitting malaria [Lucius et al. 2018] and was also honored with the Nobel Prize in 1902 [Knobloch 2003]. During that time, Giovanni Battista Grassi identified female *Anopheles* mosquitos as vectors for malaria [Knobloch 2003]. However, it took almost another 50 years before Short and Garnham described the exoerythrocytic phase of *Plasmodium* in 1948 [Lucius et al. 2018].

Over the past five thousand years, malaria has been the leading cause of early mortality in many parts of the world. It is therefore not surprising that it is the strongest force for selective pressure on the human genome described so far [Kariuki and Williams 2020]. In this context, many genetic alterations have been described that have a protective effect against malaria; the most important, however, affect the function or structure of red blood cells (RBC) [Kariuki and Williams 2020]. Genetic illnesses such as sickle cell disease, glucose-6-phosphate dehydrogenase (G6PD) deficiency, and thalassemia supposedly have a survival advantage in the presence of malaria and show geographic distributions that are roughly similar to that of malaria [White et al. 2014]. Characterizing how these genetic disorders mediate their protective effect, may provide new therapeutic approaches to combat malaria [Kariuki and Williams 2020].

1.1.1 Malaria infection

Five *Plasmodium spp*. cause human disease, namely *Plasmodium falciparum (P. falciparum), P. vivax, P. ovale, P. malariae, and P. knowlesi* [Milner 2018], with *P. falciparum* being the most lethal and responsible for almost 90% of all infections [Ashley and Phyo 2018]. *P. vivax*–the most geographically widespread species [Rossati et al. 2016]–and *P. ovale* generate dormant liver-stages required for relapsing malaria [Ashley and Phyo 2018]. How hypnozoite relapse is triggered is still unknown. However, elimination and control of these relapsing species are more difficult than *falciparum* malaria [Rossati et al. 2016]. Interestingly, in Africa, it has been reported that *P. malariae* exhibits opposite seasonal fluctuations with *P. falciparum,* with a prevalence of *P. malaria* in the dry season [Rossati et al. 2016]. A characteristic of *P. knowlesi* is a predominantly zoonotic infection, with macaques being the natural host [Ashley and Phyo 2018]. Furthermore, there are reports of human infections with *Plasmodium spp*. that infect monkeys, for example *P. cynomolgi*, however, they are not epidemiologically important [Rossati et al. 2016].

Usually, the infection period is 12-14 days from the infecting bite. At first, nonspecific symptoms occur, including headache, fatigue, muscle aches, and abdominal discomfort. These symptoms are followed by fever, nausea, and vomiting. An infection with *falciparum* malaria can lead to generalized seizures and might be followed by a coma (cerebral malaria) [White et al. 2014].

In 2019, about 229 million cases of malaria occurred worldwide, with most cases in sub-Saharan Africa (215 million cases or 94%). Globally, there were approximately 409,000 deaths in 2019, with children under the age of five being the most affected [WHO 2019b; CDC 2020a; WHO 2021b]. The malaria mortality rate, representing “deaths per 100,000 population at risk” [WHO 2021b], has dwindled steadily over the last 20 years, with a rate of 25 in 2000 to a rate of 12 in 2015 and a rate of 10 in 2019.

With 736,000 deaths in 2000 to 409,000 deaths in 2019, malaria deaths have dwindled continuously over time. Looking at the most vulnerable group, the percentage of total malaria deaths among children aged five decreased by 17% from 2000 to 2019 (from 84% to 67%) (**Figure 1**). However, it is questionable whether this trend will continue since the severe acute respiratory syndrome coronavirus 2, leading to COVID-19, spread to all malaria-endemic areas by April 2020, causing significant limitations in malaria services [WHO 2021b].

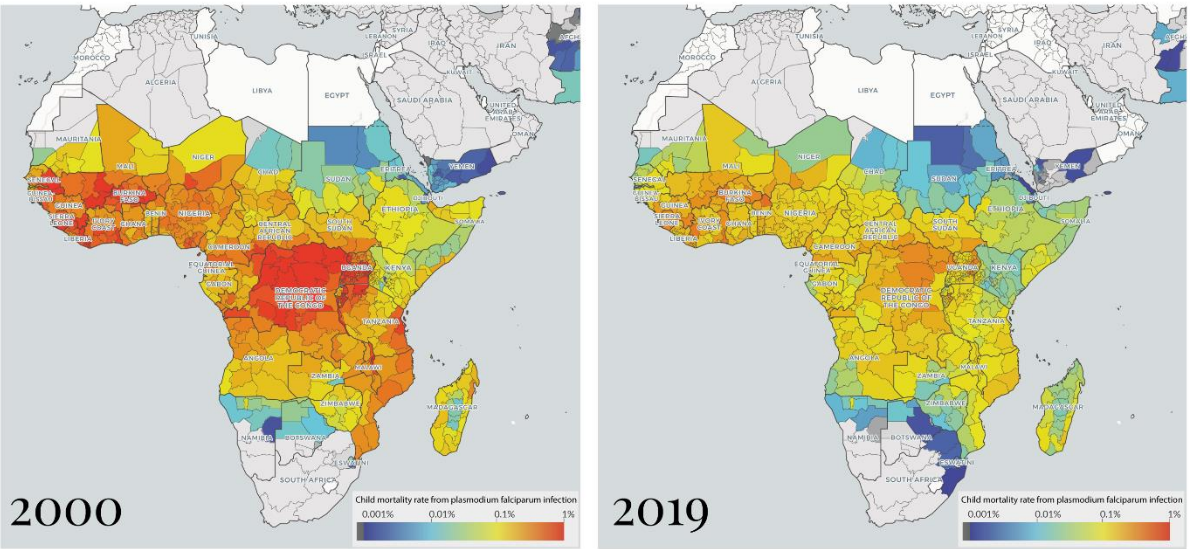

Figure 1. Malaria mortality rate of children in 2000 and 2019. The mortality rate of children under five due to *falciparum* malaria is shown, (modified from OurWorldinData.org, IHME Malaria Atlas Project (2020) ihmeuw.org/5dhp).

1.1.2 *Plasmodium* parasites

Malaria parasites are obligate intraerythrocytic protozoa of the genus *Plasmodium* [Trampuz et al. 2003], belonging to the phylum *Apicomplexa* [Seeber and Steinfelder 2016]. A characteristic feature of *Apicomplexa* is their apical complex (**Figure 2A**), which is located at the front of the cell within the invasive parasite-stages. This apical complex contains several organelles that enable the merozoite-stage of the malaria parasite to penetrate erythrocytes or other host cells [Lucius et al. 2018].

Sequencing the *P. falciparum* strain 3D7–a parasite line cloned from NF54, which itself is a *P. falciparum* line of African origin [Molina-Cruz et al. 2012]–revealed a 23.3 Mb AT-rich genome (GC content of under 20%) that is organized into 14 chromosomes. Moreover, it contains the extrachromosomal DNA of the mitochondria (6 kb) and the apicoplast (35 kb). The genome consists of 5,383 genes, with about 54% of them containing introns [UniProt; Lucius et al. 2018].

In the trophozoite-stage (~30 hours post infection (hpi)) the parasite contains one mitochondrion and the apicoplast, a plastid organelle that evolved via secondary endosymbiosis, explaining the presence of its four membranes [Lim and McFadden 2010; Lucius et al. 2018] (**Figure 2C**) The apicoplast is a unique and essential plastid without photosynthetic ability in which many essential biochemical pathways take place, such as synthesis of isoprenoid and certain fatty acids, as well as heme synthesis [Arisue and Hashimoto 2015; Lucius et al. 2018]. As most of the pathways of this subcellular organelle are of bacterial origin and therefore differ from the metabolism of the host, they are possible targets for the development of new antimalarial agents [Lucius et al. 2018]. The parasite also possesses a food vacuole (digestive vacuole, DV, or pigment vacuole), a specialized proteolytic organelle, where nutrients are absorbed and processed [Lucius et al. 2018]. During asexual erythrocytic development, the parasite consumes the erythrocytes' content, ingesting

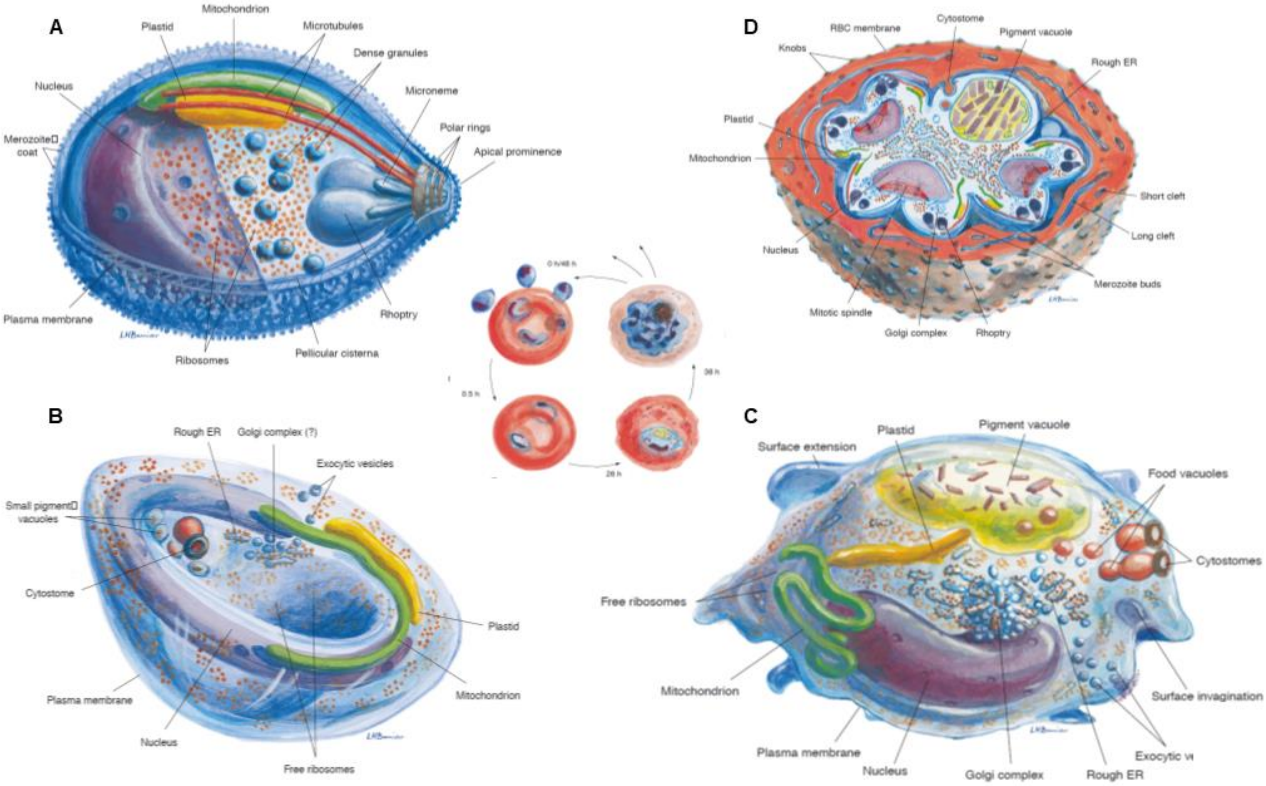

Figure 2. *Plasmodium* stages of the asexual erythrocytic cycle. Three-dimensional organization of *Plasmodium falciparum* (A) merozoite, (B) early ring-stage, (C) mid-trophozoite-stage, and (D) schizont. Moreover, the parasites' development inside the red blood cell is shown, adapted from [Bannister et al. 2000].

25-75% of host hemoglobin and degrades it in the DV [White et al. 2014]. Catabolism of hemoglobin provides amino acids for growth and maturation, which is essential for the parasite, as *de novo* synthesis or exogenous uptake of amino acids is limited [Goldberg 2005]. During the breakdown of hemoglobin, free heme is released, which has to be detoxified via polymerization. Together with lipids and proteins, heme is converted into the nontoxic, insoluble, and crystalline malaria pigment, hemozoin [Goldberg 2005; Lucius et al. 2018].

During intraerythrocytic development, the parasite modifies the surface of the infected erythrocyte, leading to an adhesive phenotype. Thus, the parasite is removed from circulation for nearly half of the asexual cycle. The infected RBCs (iRBCs) can adhere to vessel walls and bind to each other or to uninfected erythrocytes, which is called *rosetting*, and if they enter organs–especially the brain–they can cause severe malaria [White et al. 2014; Milner 2018].

1.1.3 The life cycle of *Plasmodium*

Plasmodium has a complex two-host life cycle [Matthews et al. 2018], which is characterized by an exogenous sexual phase (sporogony)–here, the parasites multiply in numerous species of *Anopheles* mosquitos–and an endogenous asexual phase (schizogony), that takes place in the vertebrate host [Rossati et al. 2016]. This life cycle starts when a mammal is bitten during a blood meal by an infected female *Anopheles* mosquito, inoculating parasites in the form of sporozoites into the human host dermis [Mawson 2013; CDC 2020a] (**Figure 3.1**). After 1-3 h, the sporozoites reach and penetrate a blood vessel, entering the bloodstream. The parasites enter the liver via the bloodstream, where they start invasion upon interaction with hepatocytes. During the next 2-10 days sporozoites transform to the liver-stage or exo-erythrocytic form, multiplying asexually without causing any symptoms [Mawson 2013; Cowman et al. 2016]. At the end of this developmental process, ~40,000 merozoite-stage parasites are released into the bloodstream [Bannister et al. 2000] (**Figure 3.2**). Within 2 min, the merozoites invade erythrocytes in a fast, dynamic, and multi-step process [Mawson 2013; Cowman et al. 2016]. After invasion, the approximately 1.6 µm long and 1 µm wide merozoites flatten into the ring form of the trophozoite-stage [Bannister et al. 2000] (**Figure 2B**). The ring-stage changes shape to a more rounded trophozoite, which finally undergoes repetitive nuclear division [Bannister et al. 2000] (**Figure 2C**). Once the trophozoite starts dividing, it is called a schizont [Trampuz et al. 2003]. After a cell cycle of 24-72 h, depending on the *Plasmodium spp.*, schizogony results in 16-32 merozoites [Marks et al. 2014]. A new cycle of schizogony starts once the infected erythrocyte ruptures and the merozoites invade new erythrocytes [Trampuz et al. 2003] (**Figure 3.3**). Malaria symptoms are caused by these asexual stages [Marks et al. 2014]. Due to the rupture of schizonts, not only parasites but also host cellular material is released into the blood, activating monocytes and macrophages and inducing the release of proinflammatory cytokines, which cause fever and other pathological effects [White et al. 2014]. This stage of the parasites is immunologically important as it is briefly exposed to the host’s immune system and is vulnerable to antibodies between leaving one erythrocyte and entering the next [Bannister et al. 2000; Kats et al. 2008].

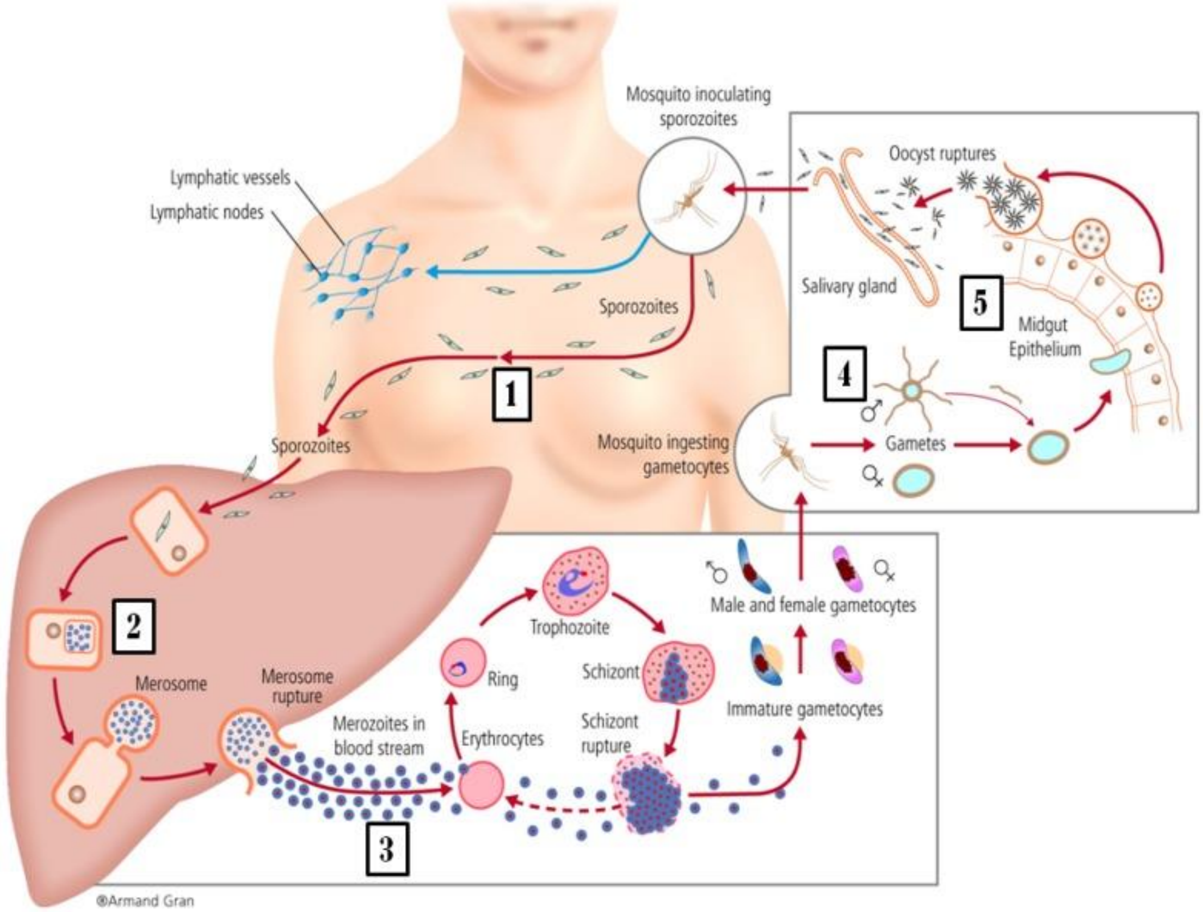

Figure 3. Life cycle of *Plasmodium falciparum*. (**1**) Malaria infection starts with the bite of a female *Anopheles* mosquito containing sporozoites. (**2**) Sporozoites invade hepatocytes, initiating liver stage development. (**3**) Merozoites are released into the bloodstream, rapidly invading erythrocytes–asexual blood-stage development begins. In order to transmit, parasites develop into gametocytes, which are ingested by mosquitoes. (**4**) In the mosquito midgut, gametocytes form gametes, which further develop into ookinetes. (**5**) The ookinetes develop into oocyst, which mature and release sporozoites into the salivary gland. The life cycle is completed with the bite of an infectious mosquito, inoculating sporozoites into the circulatory system [García-Basteiro et al. 2012].

During rounds of schizogony, some of the parasites differentiate into sexual erythrocytic stages–male (microgametocytes) and female (macrogametocytes) gametocytes [Cowman et al. 2016; CDC 2018]. About 11 days after commitment has started, a male gametocyte is infectious for a mosquito [Cowman et al. 2016]. During this time the gametocytes are absent from blood circulation to avoid clearance from the spleen before they finally emerge in the peripheral circulation. Here, they circulate until being taken up by a feeding mosquito [Joice et al. 2014; Cowman et al. 2016]. All of these multiplication steps within the human host take place via mitosis. Meiosis and therefore genetic recombination takes place only in the mosquito [White et al. 2014]. In its midgut lumen, formation of gametes (major sex cells) is activated [Aly et al. 2009]. During the sporogonic cycle–the multiplication within the mosquito–the microgametes penetrate the macrogametes, generating zygotes, which become motile and elongate, developing into ookinetes (**Figure 3.4**). After invading the midgut wall of the mosquito, ookinetes develop into oocysts [Mawson 2013; CDC 2020b]. The development ends with the production of thousands of active sporozoites [Mawson 2013]. Once the oocyst bursts, sporozoites are released and enter the salivary glands of the mosquito (Figure 3.5). Depending on the *Plasmodium spp*. the time required for the sporogonic cycle is 7-30 days [Rossati et al. 2016]. Transmission of sporozoites through the bite of an infectious mosquito completes the *Plasmodium* life cycle [Mawson 2013].

1.1.4 Malaria control

Over the last 15 years, malaria case numbers and deaths have more than halved, however, resistance to drug therapy has increased steadily [Ashley and Phyo 2018]. Still, “every 2 minutes, a child dies of malaria” [WHO 2019a], showing the urgent need to control malaria globally. There are different strategies to reach this goal, including preventive measures, such as vector control and chemoprevention in pregnant women and young children but also early diagnosis and malaria treatment, for example with artemisinin-based combination therapies (ACTs) [Ashley and Phyo 2018].

Vector control as an essential component in malaria prevention includes not only the presence of mosquito nets but also their treatment with insecticides [White et al. 2014]. Mosquito nets treated with the insecticide pyrethroid reduced mortality in children under five years of age by about 20%, preventing roughly one in four infant deaths [Phillips-Howard et al. 2003]. This number continues to rise–today long-lasting, insecticidal bed nets protect roughly 53% of the population in sub-Saharan Africa, representing an increase of 51% in the last 21 years [Nothing but nets 2021]. While mosquito nets are effective during the night, there are some main mosquito vectors biting outside in the evening or morning, where the efficacy of mosquito nets fails. Therefore, indoor residual spraying with insecticides such as dichlorodiphenyltrichloroethane that kill the mosquito vector is an important component of malaria control [White et al. 2014]. However, complete eradication of mosquitos is impossible [Skwarczynski et al. 2020]. Therefore, the treatment of malaria with several chemical and herbal compounds is still essential. The currently used antimalarials can be assigned to seven different drug classes: 4-aminoquinolines (e.g. chloroquine (CQ) and amodiaquine), arylaminoalcohols (e.g. quinine, mefloquine (MQ), halofantrine, and lumefantrine), 8-aminoquinolines (primaquine), artemisinins (e.g. artemether (ATM), artesunate (ATS)), antifolates (sulfadoxine/pyrimethamine, dapsone/chloroguanil), inhibitors of the respiratory chain (atovaquone (ATQ), proguanil), and antibiotics (doxycycline (DOXY), clindamycin) [Schlitzer 2008]. Some of the common antimalarials used today will be discussed shortly in the following paragraphs.

<u>4-aminoquinolines:</u>

Normally, ferriprotoporphyrine IX (FPPIX), which is formed due to the degradation of hemoglobin, is polymerized into non-toxic hemozoin to prevent the parasites’ death. 4-aminoquinolines bind to FPPIX, thereby preventing its polymerization, which leads to the accumulation of the oxidative toxic FPPIX. As a result, the production of reactive oxygen species (ROS) increases, killing the parasite [Schlitzer 2008; Kavishe et al. 2017]. CQ was used in the 1940s to treat all forms of malaria with few side effects but during the 1950s resistance developed. The reason for this is a mutation (K76T) in the gene of the chloroquine resistance transporter [Schlitzer 2008]. Nonetheless, CQ is still used to treat uncomplicated malaria caused by *P. vivax*, *P. ovale*, and *P. malariae* but in some areas such as Indonesia and Papua New Guinea, where failure rates are high, CQ treatment was replaced by ACTs [White et al. 2014; Ashley and Phyo 2018].

Arylaminoalcohols:

The exact mechanism of action is not yet known but this drug class seems to inhibit the same metabolism as 4-aminoquinolines [Sato 2021]. They are thought to bind to heme either in the DV and/or in the cytosol of the parasite thus, preventing the detoxification of FPPIX. Furthermore, it could be demonstrated that MQ can bind to cysteine proteases, inducing ROS production *in vitro* [Kavishe et al. 2017]. Resistance to some antimalarials of this class has already occurred and could be linked to a mutation in the multi-drug resistance 1 transport protein, which enables uptake of arylaminoalcohols into the DV [Schlitzer 2008].

8-aminoquinolines:

The only 8-aminoquinoline currently used is primaquine, which differs from other antimalarials due to its efficacy against the liver and the sexual blood-stages of different *Plasmodium spp.* [Schlitzer 2008]. Primaquine is metabolized into 5-hydroxyprimaquine, which leads to cytoskeletal and membrane lipid peroxidation and hemolysis through the formation of ROS in erythrocytes. The high ROS production can lead to a rapid depletion of reduced glutathione (GSH) in RBCs, therefore, this antimalarial agent is contraindicated in persons with G6PD deficiency. Before applying primaquine, patients should therefore be tested for G6PD deficiency since daily use of primaquine in these patients could potentially lead to life-threatening hemolysis [White et al. 2014; Kavishe et al. 2017].

Artemisinins:

Artemisinins are the most active and rapidly acting antimalarials known today, with the capacity to reduce the parasites' biomass by 10,000-fold in a single asexual cycle [Schlitzer 2008]. They act against both late ring-stages and small ring-stages, which occur just a few hours after infection by acting on multiple cellular processes that involve ROS in *Plasmodium* cells [Schlitzer 2008; Sato 2021]. Membrane damage and potential parasite death can be induced by the production of artemisinin–FPPIX adducts and ROS, which are formed due to the accumulation of artemisinin derivatives in the DV [Kavishe et al. 2017].

Artemisinin (ART) has been used in China for thousands of years as an antimalarial known as qinghaosu, representing an active ingredient from the sweet wormwood (*Artemisia annua*) [Knobloch 2003; Schlitzer 2008]. ART was further developed into the semi-synthetic derivatives ATM, arteether, and ATS [Knobloch 2003]. These prodrugs are transformed into the active metabolite dihydroartemisinin (DHA) [Tse et al. 2019], which has a fairly short elimination half-life of 40-60 min [Schlitzer 2008], thus representing one reason for the use of ACTs, where artemisinins are combined with an antimalarial with a longer half-life. Nowadays, ACTs make up the majority of modern antimalarial treatments [Ashley and Phyo 2018]. The currently most used combinations are ATM-lumefantrine, DHA-piperaquine, ATS-amodiaquine, ATS-MQ, and ATS-sulfadoxine-pyrimethamine, as well as pyronaridine-ATS, ART-naphthoquine, and arterolane-piperaquine, with arterolane being a newer synthetic peroxide, that resembles the ART derivative, which was developed in India [Ashley and Phyo 2018]. In 2008, the first resistance against ART in western Cambodia was reported, which is clinically manifested as delayed parasite clearance [Tse et al. 2019]. Furthermore, ACTs failed in Vietnam and Thailand. In 2014 mutations in the Kelch gene on chromosome 13 of the parasite were described as the molecular marker for ART resistance [Ariey et al. 2014]. Moreover, in several areas resistance to amodiaquine, sulfodoxine-pyrimethamine, and MQ also occurred, limiting the deployment of ACTs that contain these drugs [White et al. 2014].

Antifolate:

Antifolate drugs impair folate metabolism with dihydrofolate reductase (DHFR) and dihydropteroate synthase being the main targets of these antimalarial agents. Due to the inhibition of DHFR and dihydropteroate synthase, the level of fully reduced tetrahydrofolate, an important cofactor in purine, pyrimidine, and amino acid biosynthetic pathways, decreases [Gregson and Plowe 2005].

Inhibitors of the respiratory chain:

ATQ, a hydroxynaphthoquinone, binds to the ubiquinone binding site of the cytochrome complex, thereby blocking the movement of an iron-sulfur cluster. Due to this binding, the mitochondrial electron transport chain is inhibited, resulting in a breakdown of the mitochondrial membrane potential [Schlitzer 2008].

Antibiotics:

Antibiotics, e.g. DOXY, mediate antimalarial efficacy through interaction with the prokaryote-like protein biosynthesis machinery of the parasites apicoplast and/or mitochondrion [Schlitzer 2008].

An important addition to these currently used malaria control strategies is the development of a malaria vaccine. The first malaria vaccine that underwent phase 3 evaluation in Africa is the circumsporozoite protein-based particle vaccine RTS,S/AS01. This vaccine induces an immune response to the circumsporozoite protein that is present on the surface of pre-erythrocytic *P. falciparum* stages (sporozoites and liver-stage schizonts) [RTS 2014]. The overall effectiveness of RTS,S/AS01 ranged from 5-45% [Metzger et al. 2020]. In 2015, the vaccine received a positive vote from the European Medicines Agency and is now being marketed by GlaxoSmithKline under the name Mosquirix^{TM} [Metzger et al. 2020]. Recently–on the 6th of October 2021–WHO recommended the widespread use of the RTS,S malaria vaccine, although this leading malaria vaccine candidate could not achieve the WHO goal of 75% efficacy [WHO 2021a]. A promising novel pre-erythrocytic malaria vaccine candidate is called R21. This vaccine immunogen is similar to RTS,S; however, there are specific differences, e.g. a higher density of circumsporozoite protein epitopes on the particle surface. After phase 2b R21/MM (MM, adjuvant Matrix-M^{TM}) showed high efficacy of up to 77%. The vaccine candidate appears to be safe and very immunogenic. This phase 2 trial will continue for a second malaria season to prove whether this high efficacy can be maintained [Datoo et al. 2021].

1.2 ‘Oxidative stress’ and malaria

For organisms living under aerobic conditions, exposure to ROS is unavoidable [Martindale and Holbrook 2002]. ROS are mediators of redox regulation in cells, forming a complex network of interactions together with pyridine nucleotides (NADPH:NADP$^+$ and NADH:NAD$^+$) and thiols [Zhao et al. 2018]. However, at high levels, ROS can lead to ‘oxidative stress’, defined as an imbalance between antioxidants and oxidants, in favor of the latter [Sies 1997]. Both endogenous production, resulting from normal cell functions, and exogenous sources such as direct uptake from the extracellular milieu are sources of ROS, potentially resulting in severe damage of DNA, lipids, and proteins. For proteins, the cysteine and methionine residues are especially prone to oxidation [Martindale and Holbrook 2002]. Redox regulation of proteins occurs via oxidation of specific cysteinyl thiols (Cys-SH), leading to the formation of sulfenic acids (Cys-SOH), which are highly reactive (**Figure 4**). Further oxidation results in the formation of sulfinic acids (Cys-SO_2H). Both of those oxidative steps are reversible; however, further reaction of sulfinic acids with ROS cause the generation of sulfonic acids (Cys-SO_3H), which is an irreversible reaction and may limit protein function [Ghezzi 2005; Reddie and Carroll 2008]. In addition to ROS, redox biology can be affected by other reactive species, like reactive nitrogen species (RNS), reactive sulfur species, reactive carbonyl species, and reactive selenium species [Sies et al. 2017]. Therefore, further redox modifications of cysteines are possible, such as *S*-glutathionylation (Cys-SSG), *S*-nitrosation (Cys-SNO), and *S*-sulfhydration (Cys-SSH) [Yang et al. 2016]. **Figure 4** presents an overview of different oxidation states of cysteine residues, varying from regulatory effects up to irreversible oxidation, which results from ‘oxidative stress’.

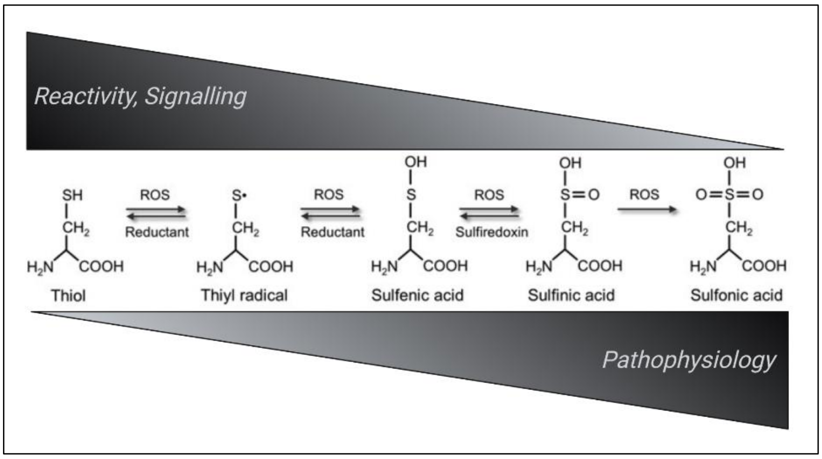

Figure 4. Oxidation states of cysteine residues. Reversible oxidation of thiol groups can regulate proteins. However, oxidation to sulfonic acid can not be reduced anymore and is therefore an irreversible process, modified from [Jortzik et al. 2012], created with BioRender.com.

Plasmodium parasites live in erythrocytes in a pro-oxidant environment. The parasites’ rapid growth and multiplication result in a high metabolic rate, leading to the generation of large amounts of toxic, redox-active byproducts [Becker et al. 2004]. The degradation of hemoglobin by the parasite, thereby obtaining necessary amino acids, represents a major endogenous source of ‘oxidative stress'. After taking up hemoglobin from the host's RBC, it is digested in the acidic food vacuole [Becker et al. 2004]. The majority of the resulting heme is converted into hemozoin but due to degradation, iron is released, which can react with hydrogen peroxide in the Fenton reaction, thereby generating highly toxic hydroxyl radicals ($HO^{\bullet}$) [Jaeger and Flohé 2006] (**Figure 5**). The ROS and free radicals generated from the degradation of hemoglobin can lead to lipid peroxidation, oxidative DNA damage, and inhibition of parasitic enzymes but also to redox damage of the host's proteins and membranes [Becker et al. 2004; Jortzik and Becker 2012].

The oxidative burden on the parasite is further increased by the host's immune response. Due to infection with malaria parasites, immune cells such as macrophages and neutrophils generate high amounts of ROS and RNS [Percário et al. 2012; Rahbari et al. 2015].

In general, a disturbance of redox equilibrium can cause impaired redox regulation and finally lead to oxidative damage and parasite death. The ability of oxidative stress to promote parasite death could be shown *in vitro* by incubating *P. yoelli* (a rodent *Plasmodium spp.*) with glucose and glucose oxidase, leading to the formation of H_2O_2, which was able to kill the parasites [Percário et al. 2012].

To maintain redox balance, the malaria parasite possesses two antioxidative systems, namely the glutathione and thioredoxin redox system–working in an NADPH-dependent manner [Jortzik and Becker 2012; Müller 2015]. The central role of these two antioxidative systems is even more important due to the absence of crucial redox enzymes such as catalase and glutathione peroxidase [Becker et al. 2003]. The glutathione system comprises a glutathione reductase (GR) and glutathione. Thioredoxin reductase (TrxR) and three thioredoxins (Trx) are part of the thioredoxin system. Furthermore, different redox-active proteins depend on these systems, including four glutaredoxins (Grx), three glutaredoxin-like proteins, one glutathione S-transferase (GST), two thioredoxin-like proteins, plasmoredoxin (Plrx), and five different peroxiredoxins (Prx) [Rahlfs et al. 2003; Jortzik and Becker 2012; Tiwari et al. 2021].

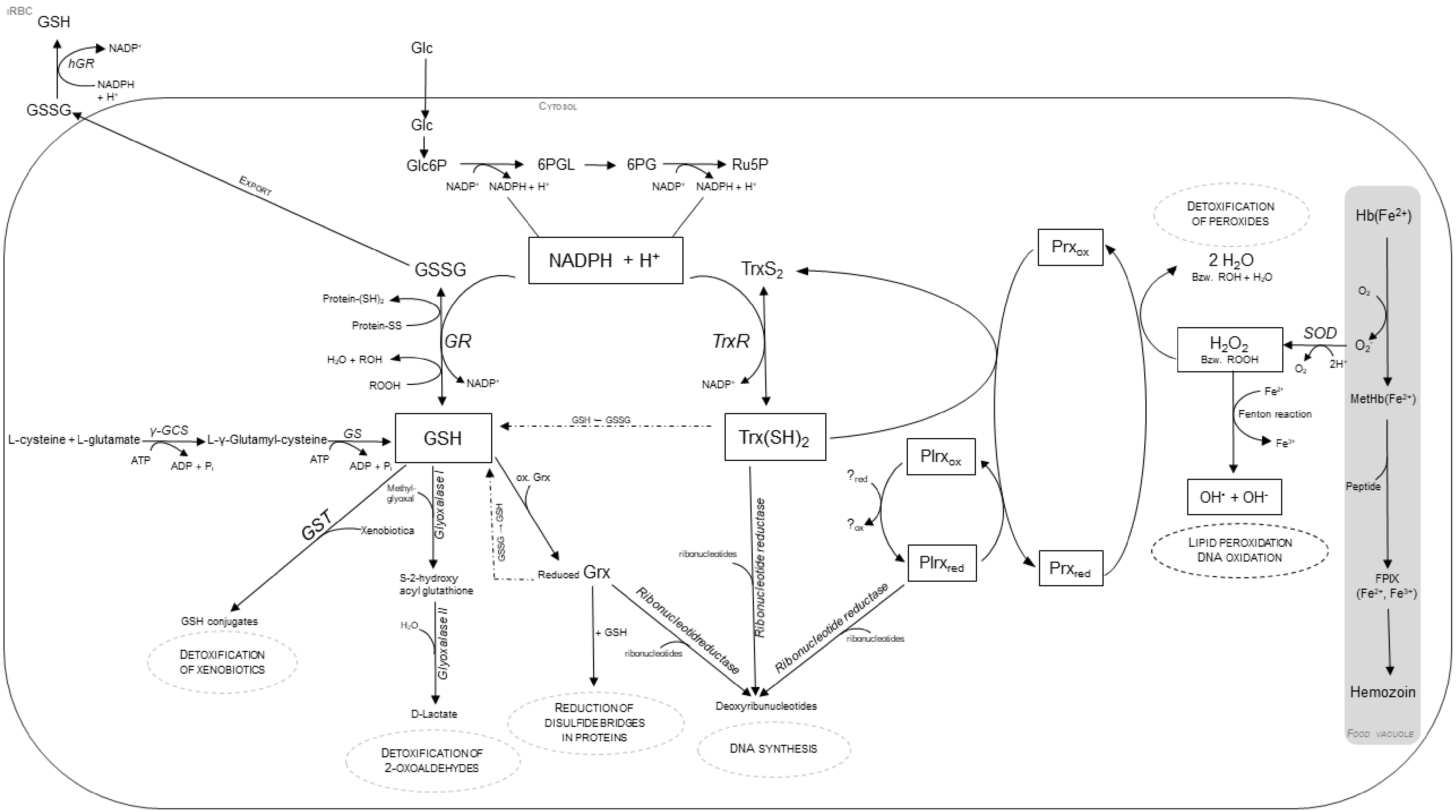

Figure 5. Sources of ‘oxidative stress’ in *P. falciparum* and its antioxidative defense. GSH = reduced glutathione, GSSG = oxidized glutathione, GR = glutathione reductase, TrxR = thioredoxin reductase, Trx = thioredoxin, Prx = peroxiredoxin, Plrx = plasmoredoxin, Grx = glutaredoxin, GST = glutathione-S-transferase. Adapted from [Jortzik and Becker 2012].

1.2.1 The glutathione redox system

With a concentration of around 2 mM in the cytosol of trophozoite-stage parasites–and thereby in a notably higher concentration than [NADPH] (< 100 µM) and [thioredoxin] ($Trx(SH)_2$ < 50 µM)–reduced GSH is highly responsible for the redox state of malaria parasites, representing the predominant low-molecular weight thiol in most cells [Becker et al. 2003; Jortzik and Becker 2012]. It is synthesized *de novo* via two ATP-dependent reactions, whereby first L-cysteine and L-glutamate are ligated. γ-glutamylcysteine synthetase catalyzes this rate-limiting step [Lüersen et al. 2000]. Subsequently, glutathione synthetase adds glycin [Meierjohann et al. 2002] (**Figure 5**). Buthionine sulfoximine (BSO) can inhibit γ-glutamylcysteine synthetase, causing rapid depletion of glutathione and inhibition of intraerythrocytic parasite development. GSH can abolish this effect, showing that an adequate glutathione status is essential for the parasites' survival [Becker et al. 2003]. The main function of GSH is protection from 'oxidative stress' by trapping ROS that would otherwise react with other potential targets [Ghezzi 2005]. Furthermore, GSH plays an important role in redox-regulation by modulating enzyme activity via glutathionylation [Rahbari et al. 2015]. Thereby GSH has oxidized itself, leading to the formation of oxidized glutathione (glutathione disulfide, GSSG), which is toxic for the cell above concentrations of 100 µM (normally present at 10 µM or less) [Becker et al. 2003]. GSH is re-generated via GR with the following reaction:

$$GSSG + NADPH + H^+ \rightleftarrows 2\ GSH + NADP^+$$

Here, the ubiquitous homodimeric (2 x 55 kDa) flavoenzyme uses NADPH as a source of reducing equivalents [Sarma et al. 2003]. Due to this mechanism, the majority of the intracellular glutathione pool is maintained in a reduced state [Jortzik and Becker 2012] with a GSH:GSSG ratio of 285 (20 to 1000, depending on metabolic conditions) [Bohme et al. 2000; Becker et al. 2003]. Each GR subunit contains two cysteine residues that communicate with the prosthetic FAD. Depending on the redox state, the enzyme changes between oxidized and reduced forms. In the latter, a more prevalent two-electron form and a four-electron reduced form are distinguished [Jortzik and Becker 2012]. Within the parasites' genome, GR is a single copy gene, but supposedly due to alternative translation, two isoforms of the enzyme exist, located in the cytosol and the apicoplast of the parasite [Kehr et al. 2010].

GSSG can also be reduced by other processes like reduction by reduced Trx, whereby Trx acts as an electron shuttle between GSSG and TrxR. This reaction takes place in the presence of NADPH and represents an alternative pathway of GSSG reduction if GR activity is insufficient [Becker et al. 2003]. This seems to play an important role especially in the merozoite-stage since they contain GSH, but no detectable GR activity [Krauth-Siegel et al. 1996; Jaeger and Flohé 2006]. Furthermore, GSSG can be reduced in a reversible process by Plrx [Rahlfs et al. 2003] and in an NADPH-independent way by the combined action of Grx and dihydolipoamide [Becker et al. 2003], demonstrating several backup systems to reduce GSSG [Jortzik and Becker 2012]. GSSG is also exported into the erythrocytes' cytosol to maintain low intracellular GSSG concentrations [Jakob and Reichmann 2013].

The *P. falciparum* Grx (PfGrx1), a small heat-stable dithiol–disulfide oxidoreductase, possesses the active site motif CPYC [Becker et al. 2003; Rahlfs et al. 2003] and is located in the parasites' cytosol [Kehr et al. 2010]. Its major functions are the reduction of disulfide bridges in proteins and the reduction of intermolecular disulfides by transferring electrons from one or two GSHs [Becker et al. 2003; Deponte et al. 2005; Jortzik and Becker 2012]. Additionally, PfGrx1 modulates *S*-glutathionylation of proteins by catalyzing deglutathionylation, thereby affecting protein functions. A non-enzymatically reaction reduces oxidized Grx via GSH [Jortzik and Becker 2012]. Besides this classic Grx, *P. falciparum* has three 1-Cys Grxs named glutaredoxin-like proteins (PfGLP1-3) possessing only one conserved cysteine residue at the active site [Rahlfs et al. 2003; Deponte et al. 2005]. PfGLP1 and PfGLP2 are located in the cytosol whereas PfGLP3 is located in the mitochondria of the parasite [Kehr et al. 2010]. A possible function of these GLP is deglutathionylation as only the first cysteine of the active site motive is required for this [Jortzik and Becker 2012].

Another member of the glutathione system is GST, an enzyme that catalyzes the nucleophilic attack of GSH's sulfur atom on electrophilic substrates in the other substrate [Becker et al. 2003; Hiller et al. 2006]. In this way, it is involved in the detoxification of xenobiotics.

The glyoxalase system, consisting of glyoxalase I and glyoxalase II, also uses glutathione [Sousa Silva et al. 2012]. To detoxify 2-oxoaldehydes, they are converted into their corresponding non-toxic 2-hydroxycarboxylic acids. In the second step of this pathway, GSH is reproduced. An example therefore is the detoxification of methylglyoxal by converting it into D-lactate [Becker et al. 2003] (**Figure 5**).

1.2.2 The thioredoxin redox system

Trx, a 12 kDa multifunctional protein, plays a central role in the antioxidative defense system of *P. falciparum*. It has two active site cysteines that form a disulfide bridge ($TrxS_2$) in the oxidized state of the protein [Kanzok et al. 2002; Rahlfs et al. 2002]. Due to reduction catalyzed by the homodimeric flavoenzyme TrxR (61 kDa per subunit), the disulfide bridge is converted into a dithiol ($Trx(SH)_2$) in an NADPH-dependent manner:

$TrxS_2 + NADPH + H^+ \rightleftarrows Trx(SH)_2 + NADP^+$

PfTrxR is located in the cytosol and mitochondria [Kehr et al. 2010] and contains two catalytic units, whereby in each unit, electron transfer from NADPH via FAD to the first cysteine pair of one subunit is followed by electron transfer to the C-terminal cysteine pair of the other subunit and subsequently to thioredoxin disulfide [Kanzok et al. 2002].

In the malaria parasite three classic Trxs are distinguished (PfTrx1-3), which are localized in the cytosol (Trx1), the mitochondria (Trx2), and the endoplasmic reticulum (Trx3) [Kehr et al. 2010; Jortzik and Becker 2012]. Trx acts as a backup system for the glutathione system as it can directly reduce GSSG [Jortzik and Becker 2012]. Furthermore, it can directly detoxify H_2O_2, tert-butylhydroperoxide, and *S*-nitrosoglutathione [Rahlfs et al. 2003] and donate reducing equivalents to ribonucleotide reductase [Kanzok et al. 2000]. Additionally, Trxs maintain the antioxidative capacity of ascorbate, lipoic acid, and lipoamide. Moreover, Trx is an efficient electron donor to thioredoxin peroxidase 1 (PfTPx-1), an enzyme consisting of two 21.8 kDa subunits, that belongs to the enzyme family of peroxiredoxins.

Besides these classic Trxs, *P. falciparum* possesses two thioredoxin-like proteins (PfTlp1-2), which TrxR cannot reduce [Jortzik and Becker 2012].

In total, *P. falciparum* possesses five Prxs, whereas two of them are 2-Cys peroxiredoxins (PfTPx1 = PfPrx1a, PfTPX2 = PfPrx1m) located in the cytosol and mitochondria [Kanzok et al. 2002]. PfPrx5 (antioxidant protein, AOP), which is located in the apicoplast, PfPrx6, and PfPrxQ (located in the nuclei) are 1-Cys Prxs [Kehr et al. 2010; Jortzik and Becker 2012]. Prxs represent the first-line defense against peroxynitrite ($ONOO^-$) and ROS. In more detail, they reduce hydroxyl-peroxides by converting them into the corresponding alcohols and water (reduction of H_2O_2 results in two molecules of H_2O) corresponding to the following reaction:

$ROOH \rightarrow ROH + H_2O$

Furthermore, they are possibly involved in cellular signaling [Gretes et al. 2012]. The electron donor for the reaction of 2-cys peroxidases is Trx and in the case of PfTPx1 also Plrx, a member of the Trx superfamily only found in *Plasmodium spp*. [Rahlfs and Becker 2001; Jortzik and Becker 2012]. With only about 30% identity to PfTrx and PfGrx, it is clustered in a separate group [Jortzik and Becker 2012]. Beside its role as an electron donor for peroxiredoxins, it is also able to reduce GSSG and provides electrons for ribonucleotide reductase [Rahlfs et al. 2003]. The function, regulation, and interaction between ROS/RNS generation and antioxidative defense via the glutathione and thioredoxin system are shown in **Figure 5**.

1.2.3 The pentose phosphate pathway of *Plasmodium falciparum*

The pentose phosphate pathway (PPP), present in the cytosol of all cells, is the main source of NADPH, which is used as a reducing agent, and ribulose 5-phosphate, which is required for the synthesis of nucleotide and nucleic acid [Wamelink et al. 2008; Haeussler et al. 2019, 2019]. The reactions within the PPP can be subdivided into two biochemical branches, the oxidative and the non-oxidative PPP [Stincone et al. 2015]. In the oxidative branch, three irreversible reactions take place, leading to the production of NADPH and pentose phosphate. In more detail, G6PD catalyzes the dehydrogenation of glucose-6-phosphate into 6-phosphoglucono-δ-lactone, where simultaneously NADPH is produced. After hydrolyzation to 6-phosphogluconate, catalyzed by 6-phosphogluconolactolase (6PGL), the 6-phosphogluconate dehydrogenase (6PGD) catalyzes the oxidative decyarboxylation of 6-phosphogluconate, resulting in the production of ribulose-5-phosphate, CO_2, and NADPH [Wamelink et al. 2008] (**Figure 6**). Within the non-oxidative branch, pentose phosphates are reconverted into glucose-6-phosphate. First, ribulose-5-phosphate, which was produced by the oxidative branch can either be epimerized to xylulose-5-phosphate or isomerized to ribose-5-phosphate, which can be used for nucleotide and nucleic acid synthesis. However, since many biosynthetic processes require NADPH, transketolase most often converts ribose-5-phosphate and xylulose-5-phsophate into glyceraldehyde-3-phosphate and sedoheptulose-7-phosphate. Subsequently, transaldolase further metabolizes them to erythrose-4-phosphate and fructose-6-phosphate. Additionally, the conversation of erythrose-4-phosphate and xylulose-5-phosphate to glyceraldehyde-3-phosphate and fructose-6-phosphate also takes place via transketolase [Wamelink et al. 2008] (**Figure 6**). All reactions of the non-oxidative branch are reversible [Stincone et al. 2015].

In *Plasmodium*, the first two enzymes of the PPP (G6PD and 6PGL) are combined in a unique bifunctional enzyme, called GluPho (glucose-6-phosphate dehydrogenase 6-phosphoglucono-lactonase). Here, the C-terminus is homologous with other G6PDs; however, an interruption with an insertion of 62 amino acids is present. The N-terminus of GluPho is highly similar to other 6PGLs [Jortzik et al. 2011]. Therefore, PfGluPho differs structurally from its human counterparts. Furthermore, using double crossover disruption of the PfGluPho gene, the enzyme could be identified as essential for the growth of blood-stage parasites, making it and the associated PPP a potential drug target [Allen et al. 2015].

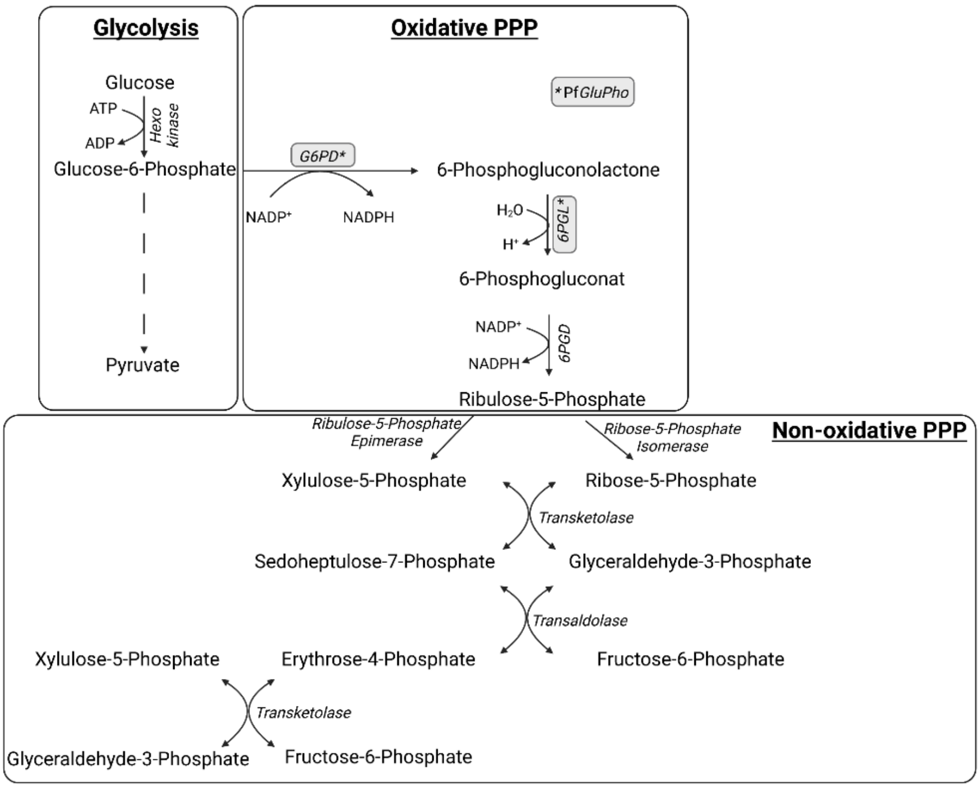

Figure 6. Schematic representation of the pentose phosphate pathway. The connection between glycolysis and the oxidative branch of the PPP is shown. In *Plasmodium*, the first both enzymes of the PPP are combined in a bifunctional enzyme named GluPho. Connected to the oxidative branch, the non-oxidative branch of the PPP takes place. G6PD = glucose-6-phosphate-dehydrogenase, 6PGL = 6-phosphogluconolactolase, 6PGD = 6-phosphogluconate dehydrogenase. Adapted from [Wamelink et al. 2008], created with BioRender.com.

1.3 The energy metabolism of *Plasmodium falciparum*

The intraerythrocytic asexual and sexual *Plasmodium* stages are thought to be primarily dependent on glycolysis for ATP synthesis and survival [MacRae et al. 2013; O'Hara et al. 2014; Oyelade et al. 2016]. Anaerobic glycolysis, with pyruvate being converted into lactate, plays an especially central role in the parasites' energy production [Oyelade et al. 2016]. Therefore, sugars, notably glucose, are essential for the growth and reproduction of the parasites since the aforementioned parasite-stages do not store glycogen or other reverse polysaccharides. This is furthermore confirmed by the fact that glucose utilization of iRBCs is about 75 times higher than in uninfected RBC [Sherman 1979]. In addition to this increase in glucose use, the activity of nearly all glycolytic enzymes is increased in iRBCs [Roth, JR et al. 1988; Zerez et al. 1990]. This primary reliance on anaerobic respiration and the associated increased lactate production is consistent with clinical symptoms associated with malaria, such as lactic acidosis and hypoglycemia [MacRae et al. 2013; O'Hara et al. 2014].

In glycolysis, nicotinamide adenine dinucleotide (NAD^+) plays a key role as a cofactor. In uninfected RBCs, NAD^+ is synthesized exclusively via the Preiss–Handler pathway. First, nicotinic acid (Na) is converted via nicotinic acid phosphoribosyl transferase to nicotinate mononucleotide (NaMN). Then, NaMN is adenylylated to nicotinate adenine dinucleotide (NaAD). The enzyme nicotinamide mononucleotide adenylyl transferase catalyzes this reaction. Finally, NaAD is amidated to NAD^+ through NAD^+ synthetase (**Figure 7**). In uninfected RBCs, Na is the only educt for the synthesis of NAD^+. However, in other human or vertebrates tissues, nicotinamide (Nam) can also be used for NAD^+ synthesis [Zerez et al. 1990; O'Hara et al. 2014]. Interestingly, in human RBCs infected with *P. falciparum*, the NAD^+ content is increased tenfold [Zerez et al. 1990].

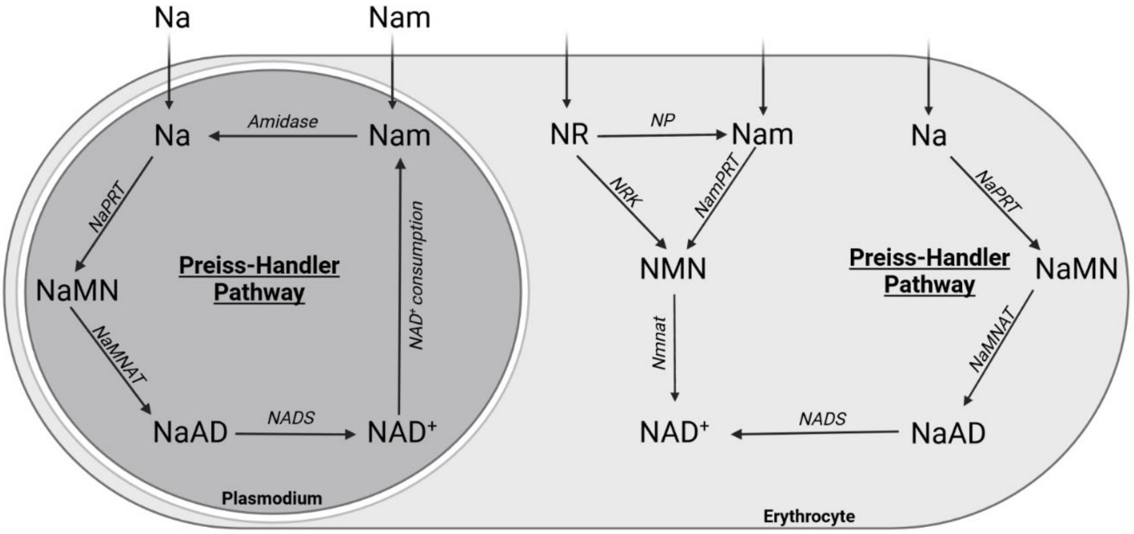

Figure 7. *Plasmodium falciparum* NAD^+ metabolism. Overview of the parasitic and host cell NAD^+ metabolism. NA = nicotinic acid, Nam = nicotinamide, NaMN = nicotinate mononucleotide, NaAD = nicotinate adenine dinucleotide, NaPRT = nicotinic acid phosphoryltransferase, NaMNAT = nicotinamide mononucleotide adenylyltransferase. Adapted from [Bathke 2014; O'Hara et al. 2014], created with BioRender.com.

De novo synthesis of NAD^+ depends on the utilization of aspartate in prokaryotes. In eukaryotes, however, *de novo* synthesis of NAD^+ relies on intermediates generated from the breakdown of tryptophan. Although, in *P. falciparum*, there are no enzymes for *de novo* synthesis from either aspartate or tryptophan. Therefore, NAD^+ synthesis takes place via the Preiss–Handler pathway, showing one difference to the host's pathway; due to the presence of a nicotinamidase in *Plasmodium*, conversion from Nam to Na is possible [O'Hara et al. 2014].

1.4 Genetically encoded fluorescence-based biosensors

1.4.1 GFP

Green fluorescent proteins (GFPs) are a class of proteins, responsible for the green bioluminescence of marine invertebrates of the phylum *Coelenterata. In vivo* GFPs are activated by an energy transfer process via Ca^{2+}-activated photoproteins or a luciferase [Prasher et al. 1992; Tsien 1998].

GFP was discovered as a companion protein to aequorin and was first isolated in 1962 [Shimomura et al. 1962; Tsien 1998]. In the jellyfish *Aequorea victoria* (*av*)*,* the photoprotein aequorin emits blue light, resulting from an intramolecular reaction after adding Ca^{2+}, which leads to the formation of a blue fluorescent protein. After energy transfer to GFP green light is emitted [Morise et al. 1974]. The GFP sequence was determined twenty years later and revealed the consistence of 238 amino acids [Prasher et al. 1992] and a molecular weight of 27 kDa [Shimomura 1979]. The structure of GFP is organized into an 11-stranded β-barrel, where each strand consists of 9 to 13 residues. This barrel forms a nearly perfect cylinder, which is 42 Å long and 24 Å in width (**Figure 8A**). The barrel is wrapped around a single central α-helix containing the covalently bound chromophore 4-(p-hydroxybenzylidene)imidazolidine-5-one [Ormö et al. 1996]. Looking at the structure in more detail

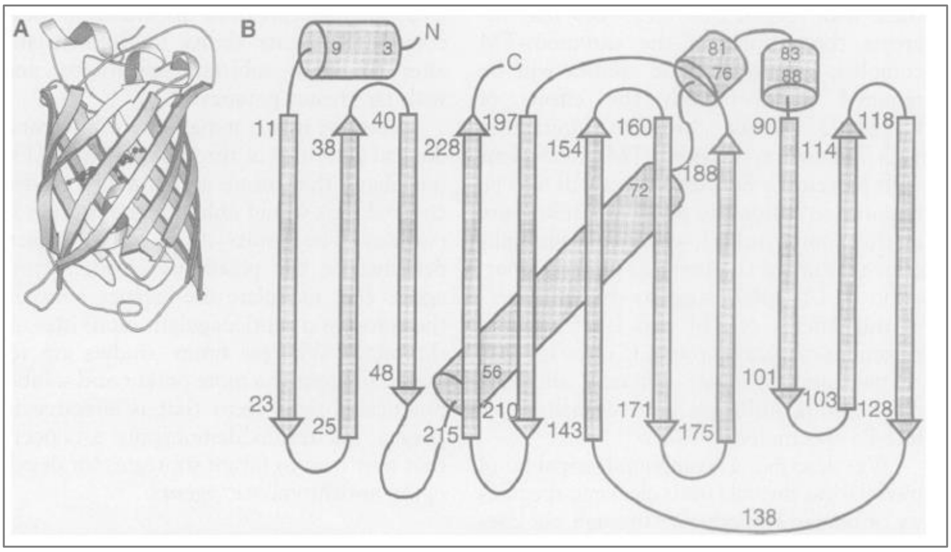

Figure 8. Structure of wild type *av*GFP. (**A**) Schematic structure of the wt *av*GFP. (**B**) Schematic drawing of the GFP fold. Residue numbers mark the beginning and end of the structure elements [Ormö et al. 1996].

reveals three antiparallel strands, located at the N-terminus of the protein, followed by the central helix and another three antiparallel strands. The second half of the barrel is formed by a Greek key motif consisting of five strands (**Figure 8B**) [Ormö et al. 1996].

The chromophore, which is formed by the three amino acids Gly, Ser, and Tyr is highly protected from the surrounding solvent due to the β-barrel and is responsible for the green fluorescence of the protein (**Figure 8A**). The formation of the fluorophore starts with cyclization, induced by a nucleophile attack of the amide nitrogen of Gly67 onto the carbonyl carbon of Ser65, resulting in the formation of a five-membered ring. After the elimination of H_2O, an imidazolin-5-one intermediate is formed. Chromophore building is fulfilled after atmospheric oxygen oxidizes the hydroxybenzyl side chain of Tyr66, thereby producing H_2O_2 [Cubitt et al. 1995; Wachter 2007] (**Figure 9A**). The chromophore achieves fluorescence and absorbance only at this stage. Furthermore, the amino acids placed around the chromophore (Q69, Q94, R96, H148, T203, S205, and E222) are necessary for fluorescence [Benčina 2013]. In all known GFP mutants, Gly67 is conserved due to its minimal steric hindrance; therefore, it is the best nucleophile in such cyclizations [Tsien 1998]. The formation of two rings linked by a double bond is the basis for all naturally occurring fluorescent protein chromophores. Furthermore, in all known examples, these two rings are derived from the dipeptide tyrosine-glycine [Remington 2011].

The GFP chromophore has two coincident absorbance and excitation bands, which can be explained due to the existence of an anionic or neutral form of the chromophore [Remington 2011]. The neutral protonated form (A band) of the wild type (wt) *av*GFP chromophore absorbs at about 395 nm, while the anionic form (B band) absorbs at about 475 nm (**Figure 9B**) [Remington 2011]. This second excitation peak is about three times lower in amplitude [Tsien 1998]. Both bands are at equilibrium in an A:B intensity ratio of about 6:1 in wt *av*GFP. This ratio is insensitive to environmental salt concentrations and pH values [Remington 2011]. The mechanism of A band emission can be explained by excited state proton transfer (**Figure 9C**) [Remington 2011]. Due to excitation of the A band, the chromophore deprotonates. Subsequently, a proton transport occurs, which is assumed to proceed via a hydrogen-bonded network involving an internal water molecule (W25), a serine residue (S205), and an ionized glutamate (E222), acting as a terminal proton

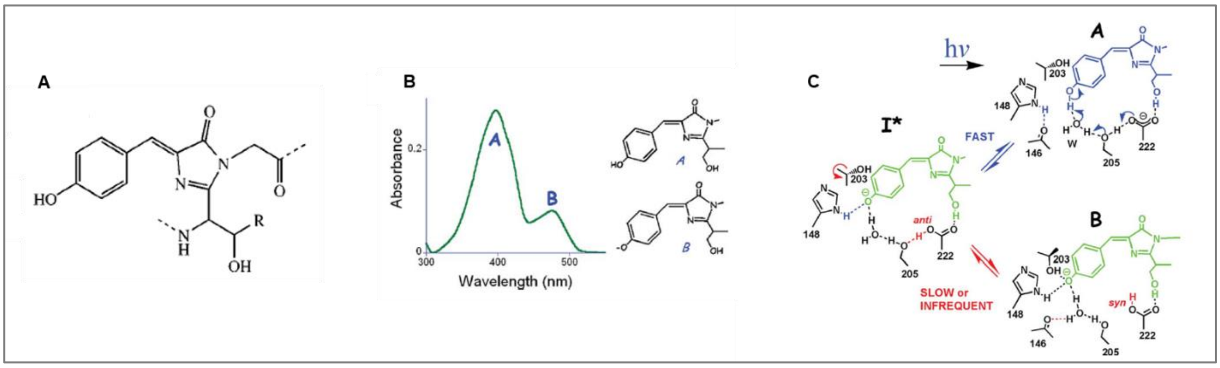

Figure 9. Chromophore behavior of wild type *av*GFP. (**A**) Chromophore structure. (**B**) Absorbance spectra of wt *av*GFP. Chromophore forms responsible for the two peaks are represented. (**C**) Proposed reaction scheme for excited state proton transfer in wt *av*GFP. Adapted from [Tsien 1998; Remington 2011].

acceptor. From this, an intermediate state (I*) results (**Figure 9C**), consisting of a deprotonated anionic chromophore and a protonated neutral glutamate, representing the emitting state of GFP [Kennis et al. 2004]. In contrast to this proton transfer, converting the A band in the excited state into the I* form, a conformational change converts the I* form into the B band [Palm et al. 1997]. Emission from the anionic chromophore (B band) can be described as a "transition from the first singlet excited state to ground" [Remington 2011].

The extinction coefficient of wt *av*GFP at a wavelength of 395 nm (A band) is $\varepsilon = 21{,}000\ M^{-1}cm^{-1}$ [Heim et al. 1995] and describes the 'capacity' of the fluorophore as it is "a measure of the ability of a material to absorb radiation of a certain wavelength" [Kahana and Silver 2001]. The 'efficiency' of a fluorophore can be declared as quantum yield (QY), reflecting the ratio of photons emitted (longer wavelength) to photons absorbed (shorter wavelength) [Kahana and Silver 2001]. For wt *av*GFP the QY is ~0.77, meaning per 100 photons absorbed, 77 photons are emitted. The product of ε and QY can be described as fluorescence 'intensity' [Heim et al. 1995; Kahana and Silver 2001].

GFP has become a unique tool in molecular biology because of different protein properties. It becomes brightly fluorescent in different organisms, showing that its function is independent of cofactors, and no additional gene products from *A. victoria* are required for its fluorescence [Chalfie et al. 1994; Heim et al. 1995; Palm et al. 1997]. Furthermore, GFP can be detected easily and thereby used to monitor protein localization or gene expression in living organisms [Chalfie et al. 1994]. As isolated GFP is extremely stable, the protein's fluorescence is unchanged under most physiological conditions. For example, the fluorescence of native GFP can be detected over a range of pH 7.0 to pH 12.2, as well as at temperatures over 65 °C. Furthermore, its fluorescence characteristics are retained when incubated with 8 M urea or 1% sodium dodecyl sulfate (SDS) [Kahana and Silver 2001].

To generate GFP variants that have high brightness and simple excitation and emission spectra– for example, more intense fluorescence, when excited at 488 nm, thereby using frequently utilized laser settings–mutations were inserted, resulting in GFPs that belong to classification class 2, representing GFPs with phenolate anions in the chromophore [Cormack et al. 1996; Tsien 1998].

All mutations made so far can be assigned into three categories: either they lead to no changes in phenotype, they change the folding efficiency, or they change the spectral properties. Mutations changing folding efficiency are mostly localized on the central α-helix [Palm et al. 1997]. A most often used mutation, causing ionization of the phenol of the chromophore, is S65T. Ser65 was mutated to different amino acids (Ala, Leu, Cys, or Thr) to test the hypothesis that it undergoes additional dehydration to form a vinyl side chain. Due to the neutral phenol, the wt *av*GFP excitation peak at 395 nm is decreased, whereas the 475 nm peak is enhanced and shifted to 470-490 nm. The mutation S65T showed the longest excitation and emission wavelengths (490 nm and 510 nm). For these reasons, it was selected for further characterization. In comparison to wt *av*GFP, post-translational oxidation, which is required for fluorophore forming, occurs in the S65T mutant about four times as fast [Heim et al. 1995]. Furthermore, in this mutant some conformational changes occurred, leading to a rotation of the carboxylate of E222. Therefore, the hydrogen bond to Ser205 is disrupted [Palm et al. 1997] allowing the chromophore to become ionized [Remington 2011]. Additional mutations were inserted to generate GFP variants with greater brightness at warmer temperatures such as 37 °C. It is reported that only mutants with the mutation F64L "could be expressed well at 37 °C and were examined further" [Palm et al. 1997]. Combination of the mutation S65T with F64L results in a 30-fold increase in fluorescence intensity (FI) over wt *av*GFP, suggesting that F64L is critical for maximal fluorescence [Cormack et al. 1996]. Due to DNA shuffling, the so-called cycle 3 mutations (F99S, M153T, and V163A) were generated, which are involved in the replacement of hydrophobic residues with more hydrophilic ones. *In vivo*, a hydrophobic contact area is involved in the binding between GFP and aequorin. This hydrophobic surface site could cause aggregation in the absence of aequorin and prevent autocatalytic activation of the chromophore. The cycle-3 mutations could counteract the hydrophobic site, thereby reducing aggregations and increasing chromophore activation [Crameri et al. 1996]. The mutation V163A results in a GFP variant that is more soluble in bacteria and forms its chromophore up to 25% faster than wt *av*GFP. A mutant, combining S65T and V163A showed the characteristic spectral shift of S65T and had a significantly more detectable signal than wt *av*GFP [Kahana and Silver 2001]. Furthermore, the mutations F64L and V163A are responsible for greater yield of soluble fluorescent protein [Palm et al. 1997]. Taken together, these mutations do not enhance the brightness of the properly folded molecule but rather improve the folding efficiency [Tsien 1998]. An innocuous mutation, occurring in most cDNA constructs derived from wt *av*GFP is Q80R. This mutation supposedly resulted from a PCR error [Tsien 1998]. However, since this mutation does not show any adverse effects, it is included in most versions of GFP. When expressed in *E. coli* cells, circularly permuted variants of GFP and GFP biosensors (fused receptor domains and GFPs) tend to aggregate or misfold. To receive a more robust folded GFP version that is unaffected by potentially misfolded fusion partners, the working group of Waldo generated superfolder GFP (sfGFP). Besides the already explained enhanced GFP mutations (S65T, F64L) and the cycle-3 mutations, this GFP variant contains six new mutations, namely S30R, Y39N, N105T, Y145F, I171V, and A206V, which were generated in four rounds of DNA shuffling [Pédelacq et al. 2006]. *E. coli* cells expressing sfGFP showed about twofold increased fluorescence compared to a GFP version with the cycle-3 mutations, the enhanced GFP mutations, and Q80R [Waldo et al. 1999; Pédelacq et al. 2006]. Excitation and emission spectra did not alter due to the mutations. The extinction coefficient of sfGFP is 83,300 $M^{-1}cm^{-1}$, and its QY is 0.65 [Pédelacq et al. 2006].

1.4.2 Redox-sensitive biosensors

The advantage of the charge state equilibrium of the GFPs chromophore led to the creation of ratiometric biosensors [Remington 2011]. Using plasmid DNA, these sensors can be incorporated into cells or organisms, leading to the expression of a functional sensor due to the transcriptional and translational machinery of the cell, and enabling the examination of biochemical processes within the complex cellular context [Palmer et al. 2011]. These genetically encoded biosensors have major advantages over conventional fluorescent dyes since no loading of dye is necessary, meaning noninvasive imaging is possible [Benčina 2013]. The operating principle of genetically encoded sensors is the use of one or more fluorescent or luminescent proteins. Due to a molecular event, a change in fluorescence or luminescence is triggered. Thereby a signal is generated that is detectable above the cellular autofluorescence. With this, a molecular event is converted into an optical signal that can be detected [Palmer et al. 2011]. Genetically encoded fluorescence biosensors allow monitoring of enzyme activity, conformational changes of channels, monitoring of molecules, ions, and second messengers, redox potentials, and ROS in living cells [Palmer et al. 2011; Benčina 2013]. Due to using specific target sequences, the sensors can be precisely targeted to almost any subcellular compartment [Benčina 2013].

The first GFP-based redox-sensitive biosensors were engineered by the working groups of Tsien and Remington [Hanson et al. 2004]. To generate reduction–oxidation–sensitive GFPs (roGFPs), surface-exposed residues in appropriate positions on adjacent β-strands close to the GFPs chromophore were substituted with cysteines that are able to form disulfide bonds. To prevent undesired cross-link formation, both naturally existing cysteines in wt *av*GFP at positions 48 and 70 were replaced with serine and alanine, respectively. However, the substitution of C70 impeded the generation of soluble, fluorescent protein. Therefore, the C48S construct was used as a template for further engineering. Insertion positions for cysteines were selected by visually verifying the atomic GFP model. To generate roGFP1 and roGFP2, S147 and Q204 were substituted with cysteines. The C48S/Q80R backbone was used for roGFP1 and the C48S/Q80R/S65T backbone for roGFP2 [Hanson et al. 2004]. In both roGFP variants, the excitation peaks at around 400 nm (A-band) and 475-490 nm (B-band) remained unchanged. For roGFP1, band A is the main excitation peak, whereas, for roGFP2, band B dominates. The isosbestic point was identified at ~425 nm [Meyer and Dick 2010]. The biosensors are still ratiometric by excitation, reducing or eliminating measuring errors that may result from changes in concentration, photobleaching, or cell thickness [Hanson et al. 2004].

The formation of a disulfide between both cysteines promotes the protonation of the chromophore. As a result, the excitation peak near 400 nm increases; in return, the peak near 490 nm decreases. The ratio of fluorescence after excitation at both wavelengths displays the extent of oxidation and thereby the redox potential. The change in ratio is large for roGFPs, with up to sixfold *in vitro* and up to threefold in mammalian cells [Dooley et al. 2004]. The protonation state of all roGFPs is not influenced by pH changes in the physiological range [Schwarzländer et al. 2016]. The midpoint potentials of roGFP1 and roGFP2 were -288 mV and -272 mV, respectively [Hanson et al. 2004]. However, Dooley and colleagues determined slightly more negative midpoint potentials, with - 294 mV for roGFP1 and -287 mV for roGFP2 [Dooley et al. 2004]. These differences can be attributed to different measurement methods. Depending on whether titration was carried out with DTT, lipoic acid, or bis(2-mercaptothyl)sulfone, the results differed slightly [Meyer and Dick 2010]. Therefore, a consensus midpoint potential of -291 mV for roGFP1 and -280 mV for roGFP2 was suggested [Dooley et al. 2004].

Undefined specificity limits conventional roGFPs [Gutscher et al. 2008]. However, they are capable of equilibrating with the glutathione couple through mediation with endogenous Grxs, although this equilibration is in many situations too slow and unselective to allow the detection of oxidative changes. It was hoped that the proximity of a covalently attached redox catalyst would allow rapid and complete equilibration with a defined cellular redox couple. Since several other redox-active compounds, such as NADPH or Trxs did not affect the redox state of roGFP *in vitro*, fusion of an appropriate Grx to roGFP seemed to be a reasonable strategy to ensure constant kinetic coupling and specificity of the biosensor [Meyer and Dick 2010]. Gutscher and colleagues fused roGFP2 to human Grx1, allowing the imaging of intracellular glutathione redox potential since specific real-time equilibration between hGrx1-roGFP2 and the glutathione couple is facilitated. This biosensor is capable of detecting nanomolar changes in GSSG against a backdrop of millimolar GSH [Gutscher et al. 2008; Rahbari 2017a]. GSSG-dependent oxidation of the fusion sensor is completely reversible. First, GSSG reacts with Grx1, leading to *S*-glutathionylation of Grx1. Then, roGFP2 deglutathionylates Grx1. The now *S*-glutathionylated roGFP2 forms a disulfide bond, thereby releasing GSH (**Figure 10**). Based on this mechanism, using a monothiol Grx is sufficient [Schwarzländer et al. 2016].

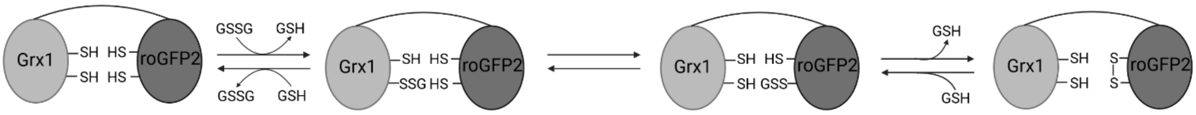

Figure 10. Redox equilibration mechanism of Grx1-roGFP2. Equilibration between the glutathione pool and roGFP2 catalyzed by Grx1. Adapted from [Schwarzländer et al. 2016], created with BioRender.com.

Numerous roGFP variants are now available. A much brighter redox-sensor that oxidizes more readily than roGFP2 is roTurbo. This sensor was developed by including the mutations F223R, A206K, and six of the sf mutations from sfGFP [Dooley et al. 2012]. The sf mutations were also used to generate roClover, which differs from roTurbo by substituting S65 (S65T in roTurbo and S65G in roClover) and additionally substituting T203H. Following these improvements, in previous work, sfroGFP2 containing the sf mutations (S30R, Y39N, N105T, Y145F, I171V, and A206V), the cycle-3 substitutions (F99S, M153T, and V163A), the F223R mutation, and the roGFP2 substitutions (L68V, A72S, Q80R, F64L, S65T, S147C, and Q204C) was engineered. Furthermore, sfroGFP2 was fused to hGrx1 to generate a proximity-based redox-biosensor with bright fluorescence [Schuh et al. 2018].

1.4.3 NADH:NAD$^+$ and NADPH biosensors

In 2011 the working groups of Yellen and Yang independently developed genetically encoded NADH biosensors called Frex and Peredox [Hung et al. 2011; Zhao et al. 2011]. The dynamic range of Frex sensors is much better than Peredox; however, their fluorescence is more pH-sensitive [Zhao et al. 2015]. Peredox only partially reflects the physiologically relevant NAD$^+$:NADH ratio, as its fluorescence response depends on the total NAD$^+$:NADH pool, making it more difficult to compare NAD$^+$:NADH ratios of different cells as one has to calibrate against the cytosolic pool of NADH and NAD$^+$ [Zhao et al. 2016]. Neither Frex nor Peredox show evident fluorescence response to NAD$^+$ [Zhao et al. 2015; Zhao et al. 2018]. Since Peredox is an intensity-based sensor with only one excitation and one emission peak, this sensor was fused with mCherry to achieve a ratiometric readout [Zhao et al. 2018]. A few years later Yang's group published a genetically encoded biosensor to monitor NAD$^+$ and NADH redox states. This second-generation genetically encoded sensor called SoNar (sensor of NAD(H) redox) was described to be highly fluorescent, showing a rapid response, having a wide dynamic range, and being pH resistant [Zhao et al. 2015]. Furthermore, its coding sequence is much shorter (1.2 kb) than first-generation biosensors [Zhao et al. 2016]. SoNar was engineered by inserting cpYFP between two truncated subunits of the NADH binding domain of the Rex protein from the gram-positive bacteria *Thermus aquaticus* (T-Rex). Rex represents a homodimer with a C-terminal NADH binding domain and an N-terminal DNA-binding domain. The conformation of Rex changes upon NADH binding from an open to a closed conformation [Zhao et al. 2016]. To generate SoNar the DNA binding domain of T-Rex was abolished [Zhao et al. 2015]. In cpYFP the N- and C-terminus of the original YFP are connected via a polypeptide linker, resulting in new termini in close proximity to the chromophore. The NADH binding protein Rex was then fused to the new termini of cpYFP therefore, changes in cpYFP's fluorescence are highly sensitive to changes in NAD$^+$:NADH [Zhao et al. 2016]. In SoNar, cpYFP was inserted after the amino acid F189 of Rex [Zhao et al. 2015] (**Figure 11**). The binding of NAD$^+$ or NADH induces conformational changes in the protein, affecting the sensor's fluorescent properties [Zhao et al. 2016]. SoNar's fluorescence is much more intense compared to the first-generation NADH biosensors as SoNar has one fluorescent protein chromophore per NAD$^+$:NADH binding site instead of 0.5 chromophores per binding site. Zhao and colleagues could show that this sensor reports the NAD$^+$:NADH ratio independently of the absolute concentrations of both nucleotides, demonstrating that under physiological conditions SoNar would be staffed by either NADH or NAD$^+$ and that SoNar's fluorescence would exactly report the NAD$^+$:NADH ratio, independent of the total NAD(H) pool [Zhao et al. 2015; Zhao et al. 2016]. Furthermore, SoNar is highly selective as no change in fluorescence could be observed in the presence of NADPH, NADP$^+$, ATP, or ADP [Zhao et al. 2015]. In this publication, a 15-fold dynamic range for SoNar was described. As the fluorescence of this biosensor responded immediately to the addition of NAD$^+$ and NADH, the authors suggest its utility in real-time measurements. However, even if this biosensor has a lot of advantages, some limitations are present. Using SoNar, it is not possible to directly quantify NAD$^+$ or NADH levels separately as this biosensor will report the NAD$^+$:NADH ratio instead of the absolute concentrations of both [Zhao et al. 2016]. One further disadvantage of SoNar is its pH sensitivity when excited at 485 nm, whereas the fluorescence excited at 420 nm is pH-insensitive [Zhao et al. 2015]. pH sensitivity is described as a major drawback of first-generation circularly permuted fluorescent proteins [Lukyanov and Belousov 2014]. In SoNar, the chromophore is protonated when excited at 420 nm and insensitive to pH, whereas the chromophore state that emits fluorescence when excited at 485 nm is deprotonated and highly sensitive towards pH. There are different possibilities to overcome this limitation, such as measuring with 420 nm excitation only, which is associated with a reduction in dynamic range and loss of ratiometric measurement, using cpYFP or another pH biosensor to monitor pH fluctuations, correcting SoNar's ratios, or fusing SoNar to a red fluorescent protein such as mCherry [Zhao et al. 2016; Tao et al. 2017] or mScarlet.

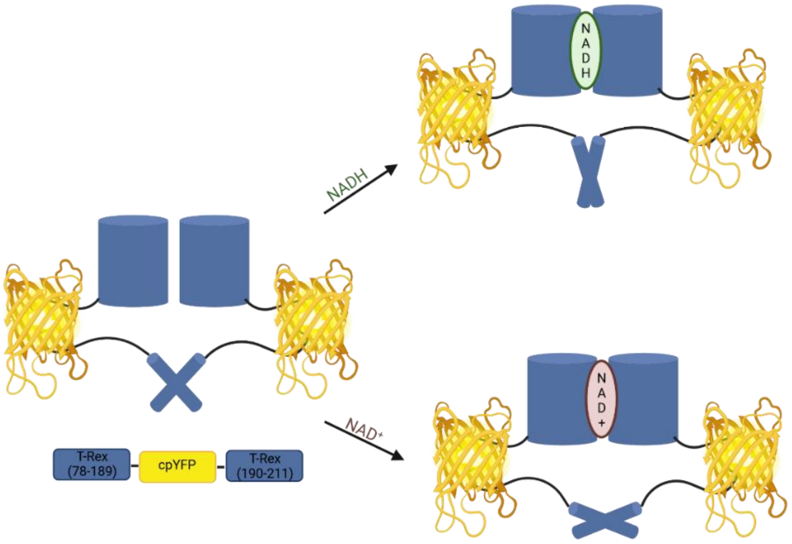

Figure 11. Design of SoNar. Fusion of the NADH binding protein Rex from *T. aquaticus* with cpYFP. Modified from [Zhao et al. 2015], created with BioRender.com.

A few years later Yang's working group evolved SoNar to generate an NADPH biosensor. Therefore, mutations were designed that switch the charges of the residues in the binding pocket of T-Rex [Tao et al. 2017]. Comparing NAD(H) and NADP(H) binding proteins reveal contrastingly charged residues close to the binding pocket. Those residues are negatively charged in NAD(H) binding proteins and positively charged for NADP(H) binding proteins. By doing so, various genetically encoded fluorescent indicators for NADPH (iNap sensors) were generated. iNap1 to iNap4 are highly selective to NADPH since they only respond to the NADPH concentration and not the NADPH:NADP$^+$ ratio and show different affinities (**Figure 12**). They have a dual excitation behavior, with excitation maxima at around 420 nm and 500 nm and one single emission peak near 515 nm. Since those biosensors are based on cpYFP, a pH dependency when excited at 485 nm is present [Tao et al. 2017; Zou et al. 2018]. However, fusion to a red fluorescent protein allows a ratiometric and pH-independent measurement [Tao et al. 2017].

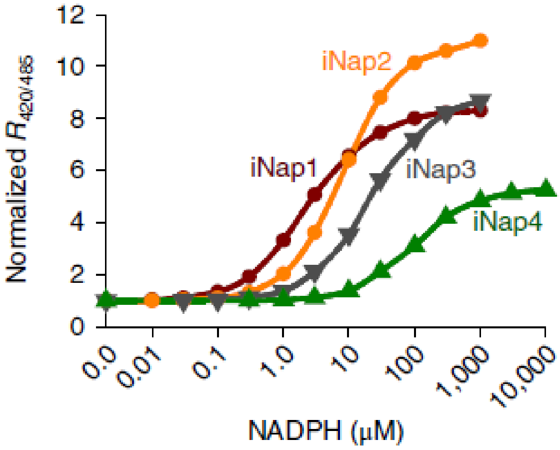

Figure 12. Specificity of different iNap variants. Normalized NADPH titration of iNap1-iNap4 [Zou et al. 2018].

In this work, SoNar and iNap2 were used as fusion biosensors, linked to the red fluorescent protein mScarlet-I. Plasmids of the fusion biosensors were kindly provided by Prof. Bruce Morgan (Saarland University).

1.4.4 pH biosensors

pH homeostasis can be understood with the development of genetically encoded fluorescent pH-sensitive sensors. With these, spatial and temporal imaging of pH dynamics is possible [Benčina 2013]. Since GFP is a pH-insensitive protein, the substitution of specific amino acids was required to generate a pH biosensor. A ratiometric pH-sensitive fluorescent protein called pHluorin was generated using the following mutations: E132D, S147E, N149L, N164I, K166Q, I167V, R168H, S202H, and L220F. This protein displays a reversible excitation ratio change between pH 5.5 and pH 7.5 [Miesenböck et al. 1998]. This pH biosensor was further optimized by integrating mammalized codons and the F64L mutation, resulting in pHluorin2 showing enhanced fluorescence. The desired pH-sensitivity was not affected [Mahon 2011]. However, probably due to misfolding of the protein, pHluorin is not suitable for pH measurements in certain subcellular compartments. To overcome this problem, a superfolder version was generated. Therefore, the sequence of pHluorin was compared to the sequence of sfGFP [Pédelacq et al. 2006]; then, the following mutations were introduced in sfGFP: T65S, S147E, N149L, I161T, N164I, K166Q, I167V, R168H, and S202H. The pH biosensor variant sfpHluorin allows reliable and straightforward pH determination, even in subcellular compartments such as the ER [Reifenrath and Boles 2018], and was used in this work.

1.5 Objectives of the study

Malaria is still one of the most life-threatening diseases in the world [WHO 2021b]. Although several antimalarial drugs are available, further research in this area is essential as the spread of resistance negates current treatment strategies. In particular, the increasing resistance to artemisinin, one of the leading antimalarials used as a standard treatment for malaria in the form of ACTs, demonstrates the urgent need for new effective drugs [Kozlov 2021]. To develop new compounds, it is beneficial to understand the mode of action (MoA) of previously used drugs and the parasitic strategies for resistance development. Since many antimalarial drugs mediate their effect, at least in part, through the perturbation of redox homeostasis [Kavishe et al. 2017], a detailed study of redox metabolism is helpful in clarifying unanswered questions regarding the MoA of various antimalarials and new compounds. Powerful tools to monitor redox and energy dynamics in real-time within living cells are so-called genetically encoded fluorescence-based biosensors (reviewed in [Kostyuk et al. 2020]). However, regarding the unicellular *Plasmodium* parasites, performing biosensor-based measurements encounters obstacles since the very small size of the parasites and their intraerythrocytic development complicate precise measurements due to the limited fluorescence intensity of commonly used biosensors. In previous work, the improved redox-biosensor sfroGFP2 and its enhanced FI *in cellulo* were described [Schuh et al. 2018].

In this work, the molecular basis of the improved *in cellulo* performance of sfroGFP2 over commonly used roGFP2 biosensor variants should be identified using functional and structural examinations. Therefore, the following steps were taken:

- Reversion of specific superfolding mutations and thus generation of sfroGFP2^{R30S}, sfroGFP2^{N39Y}, and sfroGFP2^{R223F} to study the impact of specific amino acids on the functional and structural sensor properties
- Recombinant production and purification of sfroGFP2, sfroGFP2^{R30S}, sfroGFP2^{N39Y}, sfroGFP2^{R223F}, hGrx1-sfroGFP2, roGFP2, and hGrx1-roGFP2
- Functional characterization of sfroGFP2, sfroGFP2^{R30S}, sfroGFP2^{N39Y}, sfroGFP2^{R223F}, and hGrx1-sfroGFP2 in comparison to roGFP2 and hGrx1-roGFP2
- Crystallization of sfroGFP2^{R30S}, sfroGFP2^{N39Y}, sfroGFP2^{R223F}, and hGrx1-sfroGFP2 to solve their three-dimensional structures.

In addition to using the improved redox-biosensor hGrx1-sfroGFP2, additional genetically encoded biosensors should be established in *Plasmodium*, namely the NADPH-level biosensor mScarlet-I-iNap2, the NADH:NAD^{+} ratio biosensor mScarlet-I-SoNar, and the pH biosensor sfpHluorin, in order to be able to investigate not only the glutathione-dependent redox potential but also other components of the redox and energy metabolism and thus, enable detailed investigation of the effects of new compounds on a broader basis. These biosensors were used to monitor changes in

(i) the GSSG:GSH ratio, (ii) NADPH levels, (iii) NADH:NAD$^+$ ratio, and (iv) pH values of drug-sensitive *P. falciparum* parasite lines. To reach this goal, the following steps were taken:

- Recombinant production, purification, and functional characterization of sfpHluorin
- Functional characterization of recombinant mScarlet-I-SoNar and mScarlet-I-iNap2
- Stable integration of mScarlet-I-SoNar and mScarlet-I-iNap2 in NF54*attB P. falciparum* blood-stage parasites
- Establishment of a medium throughput, flow cytometry-based assay to monitor redox and energy dynamics in whole *P. falciparum* culture
- Monitoring redox and energy dynamics of drug-sensitive *P. falciparum* parasite lines under pharmacological stress conditions.

2. MATERIALS

2.1 Equipment, consumables, software, and kits

2.1.1 Equipment

Equipment	Source
µCuvette® G1.0	Eppendorf, Hamburg
Accu-jet® pro	Brand, Wertheim
ÄKTA/ Unicorn-FPLC system - FPLC column HiLoad 16/60 Superdex 200 - Fraction collector Frac-900	GE Healthcare, Freiburg
Autoclave VX-95	Systec, Wettenberg
Beckman SW41-Ti ultracentrifuge	Beckman Coulter, Krefeld
Centifuge MiniSpin®	Eppendorf, Hamburg
Centrifuge Megafuge 1.0 R - Swing-out rotor 2704 - Centrifuge beaker 7570G - Adapter Type E 7576 + 7577	Heraeus Instruments, Hanau
Centrifuge Sorvall RC 6+ (Rotor SS-34, Rotor SLA-300, Rotor F9S-4x1000y)	Thermo Fisher Scientific, Dreieich
Clariostar plate reader	BMG Labtech, Ortenberg
Confocal microscope TCS SP5	Leica, Wetzlar
Crystallization robot Honeybee 961 - Peristaltic pump Masterflex® US® - Vacuum pump 6035A080-02	Digilab, Marlborough, MA, USA
CytoFLEX S	Beckman Coulter, Krefeld
Electrophoresis chamber Mini-PROTEAN 3 Cell	Bio-Rad, Munich
Electrophoresis chamber B1, B1A, B2	Owl Separation System Inc., Portsmouth, NH, USA
Electrophoresis Power Supply-EPS 200	Pharmacia Biotec, Dübendorf, Switzerland
Electroporator Gene pulser Xcell	Bio-Rad, Munich
Flake ice maker F80C	Icematic, Deutschland, Meerbusch
Freezing container, Nalgene® Mr. Frosty	Sigma-Aldrich, Steinheim
Gel chamber	Bio-Rad, Munich
Gel documentation system FAS Digi	Nippon Genetics Europe, Düren
Gene Pulser Xcell - PC Module	Bio-Rad, Munich

- CE Module	
Hamilton	Bonaduz, Switzerland
Heating block DRY BLOCK HEATER 2	IKA®, Staufen
Heating block neoBlock II	neoLab, Heidelberg
Heating block Thermomixer comfort	Eppendorf, Hamburg
Improved Neubauer counting chamber, Hemocytometer	Brand GmbH, Wertheim
HIDEX Sense Microplate Reader	Hidex Oy, Turku, Finland
Incubation shaker, single componants: - Heating unit: Mytron - Shaking unit: Orbital shaker	Thermo Fisher Scientific, Dreieich
Incubation shaker, single components: - Heating unit: certomat®H - Shaking unit: certomat®R	B. Braun, Melsungen
Incubator shaker KS500	Junke & Kundel, IKA-Werke, Staufen
Incubator shaker SM25	Edmund Bühler GmbH, Tübingen
Intas ECL ChemoStar	Onzas Science Imaging Instruments GmbH, Göttingen
Light microscope axiostar	Zeiss, Jena
Magnetic stirrer color squid	IKA®, Staufen
Magnetic stirrer HI-300N	Hanna Instruments, Leighton Buzzard
Magnetic stirrer IKA-RO 5 power	PCE, Meschede
Magnetic stirrer M15	CAT, Ballrechten-Dottingen
Magnetic stirrer RCT basic	IKA®, Staufen
Microprocessor pH meter 766 calimatic	Knick, Berlin
Mini-PROTEAN® Tetra system	Bio-Rad, Munich
Mini-spin table centrifuge	Eppendorf, Hamburg
Nalgene™ Oak ridge tube	Thermo Fisher Scientific, Dreieich
Nanodrop BioSpectrometer® basic	Eppendorf, Hamburg
Optima™ TLX Ultracentrifuge (120,000 rpm)	Beckman Coulter, Krefeld
Overhead shaker Trayster digital	IKA®, Staufen
PCR Cycler Fast Gene	Nippon Genetics, Düren
pH-Elektrode Sen Tix 20	Xylem Analytics (WTW), Weilheim
Pipettes Eppendorf Research Plus (10, 20, 100, 200, and 1000 µl)	Eppendorf, Hamburg
Pipettes Gilson Pipetman P10, P20, P100, P200, and P1000)	Gilson, Middleton
Power Pac 300 and 1,000	Bio-Rad, Munich
Precision scale ABT 120-5 DM	Kern, Balingen-Frommern

Quadro MACS™ separator system	Miltenyi Biotec, Bergisch Gladbach
Shaker HS 500	IKA®, Staufen
Shaker Innova®44	Eppendorf (New Brunswick™), Hamburg
Shaker Unimax 2010	Heidolph, Schwabach
Sorval RC 6+ and rotor SS-34	Thermo Fisher Scientific, Dreieich
Spectrophotometer U-2001	Hitachi, Schwäbisch Gmünd
Speed vac Savant	Thermo Fisher Scientific, Dreieich
Stereomicroscope system (M165 C, KL 1500 LED, camera EC 3)	Leica, Wetzlar
Thermo Scientific™ adapter for Nalgene™ Oak ridge tube	Thermo Fisher Scientific, Dreieich
Trans-Blot® Turbo™ transfer system	Bio-Rad, Munich
Ultrasonic wand Sonoplus HD 2070	Bandelin, Berlin
Ultrasound water bath Sonorex RK100	Bandelin electronic, Berlin
Vacuum gas pump	VWR, Darmstadt
Vortex MS2 Minishaker	IKA®, Staufen
Water system Astacus	membraPure, Hennigsdorf, Berlin
Zeiss Axio Observe Z1	Zeiss, Jena

2.1.2 Consumables

Consumables	Source
BD PLASTIKPAK™ tip, 1 ml	MEDI-KS, Berlin
Cell culture plate, 96-well, sterile, flat bottom	Eppendorf, Hamburg
Clear tape HDClear	ShurTec Brands, Avon, OH, USA
Cover slips 24x50 mm	Menzel, Brunswick
Cover slips, round 21 mm Ø	Menzel, Brunswick
Cryo.S™	Greiner Bio-One, Frickenhausen
Crystallization plate 24 well, Cryschem™ M plate	Hampton Research, Aliso Viejo, CA, USA
Crystallization plate 24 well, VDX plate	Hampton Research, Aliso Viejo, CA, USA
Crystallization plate 96 well, MRC 2 well	Jena Bioscience, Jena
Cuvettes	Sarstedt, Nümbrecht
Discofix®	B. Braun, Melsungen
EpT.I.P.S Standard	Eppendorf, Hamburg
Falcon tubes cellstar tubes 15 ml, 50 ml	Greiner Bio-One, Frickenhausen
GenePulser® cuvettes	Bio-Rad, Munich

Glass fiber filters EasyTab™-C self-aligning filters, RG	Perkin-Elmer, Rodgau-Jügesheim
Ibidi 6 channel µ-slide poly-L-lysine-coated	Ibidi, Martinsried
Kimtech Science precision wipes	Kimberly-Clark professional, Koblenz-Rheinhafen
Low binding reaction vessels 1.5 ml	Sartstedt, Nümbrecht
MACS Columns D	Miltenyi Biotec, Bergisch Gladbach
Membrane Filters NC20 Whatman™	GE Healthcare, Freiburg
Microplate, 384-well, F-bottom, small volume, black	Greiner Bio-One, Frickenhausen
Microplate, 96-well, V-bottom. natural	Greiner Bio-One, Frickenhausen
Microplates 96-well, F-bottom, clear, sterile	Greiner Bio-One, Frickenhausen
Microplates 96-well-plates half area black	Greiner Bio-One, Frickenhausen
Microscope lens paper	Glaswarenfabrik Karl Hecht, Sondheim
Microscope slides Menzel SuperFrost®	Thermo Fisher Scientific, Dreieich
Microtube 2 ml grad AMBER	VWR, Darmstadt
Millex®-GP 0.22 µm	Merck, Darmstadt
Nalgene™ Superspeed centrifugation flasks 500 ml	ThermoFisher Scientific, Osterode
Nitrocellulose blotting membrane, 0.45 µm	GE Healthcare, Freiburg
Nunc™ Inoculating loops 1 µl and 10 µl	ThermoFisher Scientific, Osterode
Parafilm M PM-996	Bemis, Neenah, USA
Pasteur pipets	Hirschmann®, Eberstadt
Petri dishes, 60 mm, 100 mm, and 150 mm	Greiner Bio-One, Frickenhausen
Petri dishes, 60 mm, 100 mm, and 150 mm	Sarstedt, Nümbrecht
Pipette tips	Greiner Bio-One, Frickenhausen
Pipette tips blue	Ratiolab, Dreieich
Pipette tips colorless	Sarstedt, Nümbrecht
safeSeal reaction vessels 0.5 ml, 1.5 ml, 2 ml	Sarstedt, Nümbrecht
Serological pipettes, 1 ml, 5 ml, 10 ml, 25 ml, and 50 ml	Sarstedt, Nümbrecht
Serological pipettes, 1 ml, 5 ml, 10 ml, 25 ml, and 50 ml	Greiner Bio-One, Frickenhausen
STERICAN disposable hypodermic needle gr. 17	B. Braun, Melsungen
STERICAN disposable hypodermic needle gr. 21, blunt	B. Braun, Melsungen
Thermo Scientific centrifugation flasks 85 ml	Thermo Fisher Scientfic, Osterode

Tubes 0.5, 1.5, and 2 ml	Eppendorf, Hamburg
UV-STAR® Microplate 96-well, F-bottom, µClear®, transparent	Greiner Bio-One,Frickenhausen
Vivaspin 10,000 MWCO and 30,000 MWCO	Sartorius Stedim Biotech, Göttingen
Western blotting filter paper	Thermo Fisher Scientific, Dreieich
Whatman FP3010.2 CA-S, filter 0.2 µM	Siegma-Aldrich, Steinheim
Zeba™ Spin desalting columns	Thermo Fisher Scientific, Dreieich

2.1.3 Software

Software	Source
BioRender	BioRender Computer-Software, Toronto, ON, Canada
ChemoStar TS software	Intas Science Imaging Instruments GmbH, Göttingen
CytExpert	Beckman Coulter, Krefeld
Fiji	National Institute of Health, Bethesda (MD), USA; [Schindelin et al. 2012]
GraphPadPrism 8	GraphPad Software, Inc., La Jolla, CA, USA
LAS AF	Leica Microsystems GmbH, Wetzlar
LAS AF Lite	Leica Microsystems GmbH, Wetzlar
Mars	BMG Labtech, Ortenberg
SnapGene	GSL Biotech LLC, San Diego, CA, USA
UCSF Chimera	Resource for Biocomputing, Visualization, and Informatics (RBVI), University of California, San Francisco, USA
Unicorn 4.11 and 7.1	GE Healthcare, Freiburg
Zeiss ZEN	Zeiss, Jena

2.1.4 Kits

Kit	Source
Kappa Blood PCR-Mastermix B kit	Peqlab, Erlangen
PureYield™ plasmid miniprep system	Promega, Mannheim
QIA quick PCR purification kit	Qiagen, Hilden
QIAamp® DNA blood midi kit	Qiagen, Hilden
QIAGEN® plasmid maxi kit	Qiagen, Hilden
QIAGEN® plasmid mini kit	Qiagen, Hilden

2.2 Chemicals

Chemical	Source
Acetic acid	Roth, Karlsruhe
Acrylamide 30%	Roth, Karlsruhe
Agar-agar	Roth, Karlsruhe
Agarose	PeqLab, Erlangen
Albumax	Gibco, Karlsruhe
Aldrithiol-4 (4,4´-Dipydidyl disulfide, DPS)	Sigma-Aldrich, Steinheim
Ammonium persulfate (APS)	Sigma-Aldrich, Steinheim
Bio-Gel P-6 Gel	Bio-Rad, Munich
Bovine serum albumin (BSA)	Roth, Karlsruhe
Bradford reagent	Bio-Rad, Munich
Buffer solution pH 4	Roth, Karlsruhe
Buffer solution pH 7	Roth, Karlsruhe
Buffer solution pH 9.21	Hamilton, Schwerte
Calcium chloride	Applichem, Darmstadt
cOmplete^{TM} protease inhibitor cocktail	Roche, Mannheim
CONTRAD 70	Beckman Coulter, Krefeld
Coomassie brilliant blue R250	Sigma-Aldrich, Steinheim
Coumarin acid	Sigma-Aldrich, Steinheim
CytoFLEX Daily QC Fluorospheres	Beckman Coulter, Krefeld
CytoFLEX Sheath Fluid	Beckman Coulter, Krefeld
Diamide (DIA)	Sigma-Aldrich, Steinheim
Dimethysulfoxid (DMSO)	Roth, Karlsruhe
Dipotassium hydrogen phosphate	Roth, Karlsruhe
Dipotassium hydrogen phosphate	Roth, Karlsruhe
Dithian	Sigma-Aldrich, Steinheim
Dithiothreitol (DTT)	Roth, Karlsruhe
DNA Dye NonTox	AppliChem, Darmstadt
Ethanol Rotipuran > 99.8%	Roth, Karlsruhe
Ethylenediaminetetraacetic acid (EDTA)	Roth, Karlsruhe
FlowClean cleaning agent	Beckman Coulter, Krefeld
GeneRuler 1 kb	Thermo Fisher Scientific, Dreieich
Gene Ruler 1 kb plus	Thermo Fisher Scientific, Dreieich
Giemsa	Merck, Darmstadt
Glucose	Roth, Karlsruhe
Glutathione (GSH)	Roth, Karlsruhe

Glutathione disulfide (GSSG)	Roth, Karlsruhe
Glycerol	Sigma-Aldrich, Steinheim
HEPES	Roth, Karlsruhe
Hydrogenperoxide	Roth, Karlsruhe
Hypoxanthine	Sigma-Aldrich, Steinheim
Imidazole	Roth, Karlsruhe
Isopropanol	Roth, Karlsruhe
Luminol	Sigma-Aldrich, Steinheim
Lysozyme	Sigma-Aldrich, Steinheim
Magnesium chloride	Sigma-Aldrich, Steinheim
Marker PageRuler^{TM} prestained protein ladder 10 to 180 kDa	Thermo Fisher Scientific, Dreieich
MES	Roth, Karlsruhe
Methanol	Roth, Karlsruhe
Milk powder	Roth, Karlsruhe
M-PER^{TM} mammalian protein extraction reagent	Thermo Fisher Scientific, Dreieich
N,N,N',N'-tetramethylethylenediamine (TEMED)	Roth, Karlsruhe
Na_2-EDTA	Roth, Karlsruhe
N-ethylmaleimide	Siegma-Aldrich, Steinheim
Ni-NTA agarose	Invitrogen, Karlsruhe
Oxoid^{TM} yeast extract	Thermo Fisher Scientific, Dreieich
Percoll®	GE Healthcare, Freiburg
Phosphate buffered saline (PBS)	Sigma-Aldrich, Steinheim
Pierce^{TM} unstained protein MW marker	Thermo Fisher Scientific, Dreieich
Ponceau S	Sigma-Aldrich, Steinheim
Potassium chloride	Roth, Karlsruhe
Potassium hydrogen phosphate	Roth, Karlsruhe
Potassium hydrogen phosphate	Roth, Karlsruhe
Potassium phosphate	Roth, Karlsruhe
PureCube Ni-NTA agarose	Biozyme, Oldendorf
Restore^{TM} western blot stripping buffer	Thermo Fisher Scientific, Dreieich
ROTI® cell 10x PBS, sterile	Roth, Karlsruhe
RPMI 1640 medium	Gibco, Thermo Fisher Scientific, Dreieich
Saponin	Roth, Karlsruhe
Silicone oil 550	Merck, Darmstadt
Sodium chloride	Roth, Karlsruhe

Sodium dodecyl sulfate	Roth, Karlsruhe
Sodium oxamate	Cayman chemical company, Ann Arbor, MI, USA
Sodium pyruvate	Gibco, Thermo Fisher Scientific, Dreieich
Sorbitol	Roth, Karlsruhe
Triethylene glycol diamine tetraacetic acid (EGTA)	Fluka, Siegma-Aldrich, Steinheim
Tris-HCl	Roth, Karlsruhe
Triton X®100	Roth, Karlsruhe
Tryptone/peptone	Roth, Karlsruhe
Tween 20	Roth, Karlsruhe

2.3 Antibiotics and antimalarials

2.3.1 Antibiotics

Antibiotic	**Stock concentration, storage temperature**	**Working concentration**	**Source**
Carbenicillin (Cn)	50 mg/ml in 50% ethanol, -20 °C	100 µg/ml	Roth, Karlsruhe
Doxycyclin	10 mM in H_2O_{dd}, -20 °C	5 µM	Sigma-Aldrich, Steinheim
Gentamycin	400 mg/ml, 4 °C	22 µg/ml	Invitrogen, Karlsruhe
Kanamycin (Kan)	25 mg/ml in H_2O_{dd}, -20 °C	50 µg/ml	Roth, Karlsruhe

2.3.2 Antimalarials

Substance	**Stock solution**	**Source**
Atovaquone	10 mM in DMSO	Sigma-Aldrich, Steinheim
Buthionine sulphoximine	10 mM in DMSO	Sigma-Aldrich, Steinheim
Chloroquine	10 mM in H_2O_{dd}	Sigma-Aldrich, Steinheim
Compound 1o	10 mM in DMSO	Prof. Reimar Krieg, Jena
Cycloheximide (CHX)	10 mM in H_2O_{dd}	Sigma-Aldrich, Steinheim
Dehydroartemisinin	10 mM in DMSO	TCI, Merseyside, UK
Mefloquine	10 mM in DMSO	Sigma-Aldrich, Steinheim
Methylene blue (MB)	10 mM in H_2O_{dd}	Roth, Karlsruhe
Plasmodione (PD)	10 mM in DMSO	Prof. Elisabeth Davioud-Charvet
Quinine (QN)	10 mM in DMSO	ACROS Organics, Geel, Belgium
SBI-750	10 mM in DMSO	Anthony Pinkerton, La Jolla, CA, USA

2.4 Inductors, protease inhibitors, and selection drugs

2.4.1 Inductors

Inductor	Stock concentration, storage temperature	Working concentration	Source
IPTG	1 M in H_2O_{dd}, -20 °C	1 mM	Roth, Karlsruhe

2.4.2 Protease inhibitors

Protease inhibitor	Stock concentration, storage temperature	Working concentration	Source
Cystatin	40 µM in H_2O_{dd}, -20 °C	0.04 µM	Sigma-Aldrich, Steinheim
Pepstatin	0.3 mM in DMSO, -20 °C	0.15 µM	Sigma-Aldrich, Steinheim
Phenylmethanesulfonyl fluoride (PMSF)	100 mM in ethanol, -20 °C	0.1 mM	Sigma-Aldrich, Steinheim

2.4.3 Selection drugs

Substance	Final concentration	Source
Blasticidin S HCl	2.5 µg/µl	AppliChem, Darmstadt
Genticin (G418)	125 µg/µl	Roth, Karlsruhe

2.5 Enzymes, antibodies, and fluorescent dyes

2.5.1 Enzymes and enzyme buffers

Enzymes	Source
10x Accu Prime polymerase buffer*	Thermo Fisher Scientific, Dreieich
10x Buffer R	Thermo Fisher Scientific, Dreieich
5x ALLin^{TM} buffer*	HighQu, Kraichtal
Accu Prime	Thermo Fisher Scientific, Dreieich
ALLin^{TM} HiFI DNA polymerase	HighQu, Kraichtal
BamHI	Thermo Fisher Scientific, Dreieich
DNaseI	Sigma-Aldrich, Steinheim
DpnI	Promega, Wisconsin, USA
HindIII	Thermo Fisher Scientific, Dreieich

*Polymerase buffers contain Mg^{2+} and dNTPs.

2.5.2 Antibodies

Antibody	Source
IgG His Epitope-Tag unconjugated	Jackson ImmunoResearch Laboratories, Inc., West Grove
α-mouse IgG-HRP conjugated	Jackson ImmunoResearch Laboratories, Inc., West Grove
α–rabbit IgG-HRP conjugated	Dianoca, Hamburg
α-Aldolase, rabbit IgG	Thermo Fisher Scientific, Dreieich
α-GFP, mouse IgG	Roche, Basel
α-PfHSP70, mouse monoclonal IgG	Santa Cruz Biotechnologies, Dallas, TX, USA

2.5.3 Fluorescenct dyes

Fluorescent dyes	Source
4’,6-Diamidino-2-phenylindole (DAPI)	Life Technologies^{TM}, Thermo Fisher Scientific, Dreieich
SYBR^{TM} Green-I	Life Technologies^{TM}, Thermo Fisher Scientific, Dreieich

2.6 Buffer and medium

2.6.1 Medium for *E. coli* culture

Medium	Composition
2YT medium	16 g/l tryptone, 10 g/l yeast extract, 5 g/l NaCl
Lysogeny broth medium (LB)	5 g/l tryptone, 10 g/l yeast extract, 5 g/l NaCl
Terrific broth medium (TB)	12 g/l tryptone, 24 g/l yeast extract, 9.4 g/l potassium dihydrogen phosphate, 2.2 g/l dipotassium hydrogen phosphate, 4 ml/l glycerol

Constituents of medium were dissolved in H_2O_{dd} and autoclaved for 30 min at 121 °C.

2.6.2 DNA agarose gel electrophoresis buffer

Buffer	Composition
50x TAE	2 M Tris, 1 M acetic acid, 50 mM EDTA pH 8.0 adjusted with acetic acid

2.6.3 SDS-polyacrylamide gel electrophoresis buffers and solutions

Buffer	Composition
Coomassie staining solution (H_2O system)	160 mg brilliant blue R250. *add* 1 l H_2O_{dd}, 3 ml HCl, fuming, 37%
Electrophoresis buffer (4x)	25 mM tris, 192 mM glycerol, 0.1% (w/v) SDS, pH 8.3 adjusted with HCl
Sample gel buffer	0.5 M tris, pH 6.8
SDS-sample buffer with DTT (1x)	62.5 mM tris-HCl, pH 6.8, 2% (w/v) SDS, 25% (v/v) glycerol, 0.01% (w/v) bromphenol blue, 50 mM DTT
SDS-sample buffer with DTT (4x)	250 mM tris-HCl, pH 6.8, 8% (w/v) SDS, 40% (v/v) glycerol, 0.03% (w/v) bromphenol blue, 200 mM DTT
Separating gel buffer	1.5 M tris, pH 8.8

2.6.4 Gels

Gel	Composition
Agarose gel 0.7%	0.7% (w/v) agarose in TAE buffer
Agarose gel 1%	1% (w/v) agarose in TAE buffer
SDS-PAGE sample gel (4%)	3.05 ml H_2O_{dd}, 1.25 ml sample gel buffer, 0.65 ml acrylamide/bisacrylamide (30%), 0.05 ml SDS (10%), 25 µl APS (10%), 5 µl TEMED
SDS-PAGE separating gel (12%)	5.1 ml H_2O_{dd}, 3.75 ml separating gel buffer, 6 ml acrylamide/bisacrylamide (30%), 0.15 ml SDS (10%), 75 µl APS (10%), 7.5 µl TEMED

2.6.5 Western blot buffers and solutions

Buffer/solution	Composition
1x transfer buffer	25 mM tris, 192 mM glycin, 10% (v/v) EtOH, pH 8.3
Blocking buffer	5% (w/v) milk powder in TBST buffer
Chemiluminescence solution	1 ml luminol, 10 µl coumaric acid
Coumaric acid	0.11% coumaric acid in DMSO
Luminol	1.25 mM luminol, 0.0093% H_2O_2, 0.1 M tris-HCl, pH 8.6 (10 mg/40 ml, in 0.1 M tris HCl, pH 8.6, 12.4 µl of 30% H_2O_2, stored in the dark at 4 °C)
Ponceau destaining solution	1% acetic acid
Ponceau staining solution	1% Ponceau S, 1% acetic acid
TBS buffer	10 mM tris, 155 mM NaCl, pH 8.0 adjusted with HCl

TBST buffer	0.05% Tween 20 (500 µl in 1 l TBS buffer)

2.6.6 Assay buffer

Buffer/solution	Composition
HEPES assay buffer	100 mM HEPES, 100 mM NaCl, 0.5 mM Na_2-EDTA, pH 7.0
HEPES buffer	50 mM HEPES, 300 mM NaCl, pH 7.5
pH buffer pH 5.0 – 6.5	10 mM MES-KOH, 100 mM NaCl, 5 mM EDTA
pH buffer pH 7.0 – 8.0	100 mM HEPES-KOH, 100 mM NaCl, 5 mM EDTA
pH buffer pH 8.5 – 9.5	100 mM tris-HCl, 100 mM NaCl, 5 mM EDTA
Potassium phosphate buffer	100 mM potassium phosphate, 100 mM NaCl, 0.5 mM Na_2-EDTA, pH 7.0

2.6.7 *Plasmodium falciparum* cell culture buffers and medium

Medium	Composition
1x PBS	ROTI® cell 10x PBS sterile, in H_2O_{dd} autoclaved
Cytomix	120 mM KCl, 0.15 mM $CaCl_2$, 2 mM EGTA, 5 mM $MgCl_2$, 10 mM K_2HPO_4/KH_2PO_4, 25 mM HEPES, pH 7.6
DNA buffer	10 mM Tris, 1 mM EDTA, pH 7.5
Freezing solution	3% (w/v) sorbitol, 0.65% (w/v) NaCl, 28% (v/v) glycerol, *ad* 50 ml H_2O_{dd}
Modified RPMI medium	RPMI 1640 containing 0.5 % (w/v) AlbuMAX, 9 mM glucose, 0.2 mM hypoxanthine, 2.1 mM L-glutamine, 25 mM HEPES and 22 µg/ml gentamycin
Ringer's solution	122.5 mM NaCl, 5.4 mM KCl, 1.2 mM $CaCl_2$, 0.8 mM $MgCl_2$, 11 mM D-glucose, 25 mM HEPES,1 mM NaH_2PO_4 pH 7.4
Saponin lysis buffer	7 mM K_2HPO_4, 1 mM NaH_2PO_4, 11 mM $NaHCO_3$, 58 mM KCl, 1 mM $MgCl_2$, 14 mM glucose, 0.02% saponin, pH 7.4 adjusted with HCl
5% sorbitol	5% (w/v) sorbitol *ad* 50 ml H_2O_{dd}
SYBR Green-I buffer	20 mM tris-HCl, 5 mM EDTA, 0.16% (w/v) saponin and 1.6% (v/v) Triton X-100

The red cell concentrates (blood group A^+) for the *P. falciparum* cell culture were obtained from the blood bank of the University Hospital Giessen.

2.7 Primer and plasmids

2.7.1 Primer

2.7.1.1 Mutagenesis primer

Primer	Nucleotide sequence	Amplification of
C147Sas	5'-ATGTATACATTGTGAGAGTTAAAGTTGTAT-3'	hGrx1-sfroGFP2^{C147S}
C147Ss	5'-ATACAACTTTAACTCTCACAATGTATACAT-3'	hGrx1-sfroGFP2^{C147S}
C204Sas	5'-TTCGAAAGTACAGAAGATGTGGACAGGTAAT-3'	hGrx1-sfroGFP2^{C204S}
C204Ss	5'-ATTACCTGTCCACATCTTCTGTACTTTCGAA-3'	hGrx1-sfroGFP2^{C204S}
C26Sas	5'-TCTTGGGCCCTCCTGCTGTACGGGCAGGTGGG-3'	hGrx1-sfroGFP2^{C26S}
C26Ss	5'-CCCACCTGCCCGTACAGCAGGAGGGCCCAAGA-3'	hGrx1-sfroGFP2^{C26S}
sfroGFPN39Yas	5’-AAGGGTAAGTTTTCCATATGTTGCATCACCTTCA-3’	sfroGFP2^{N39Y}
sfroGFPN39Ys	5’-TGAAGGTGATGCAACATATGGAAAACTTACCCTT-3’	sfroGFP2^{N39Y}
sfroGFPR223Fas	5’-CCCAGCAGCTGTTACAAACTCAAGAAGGACCATGT-3’	sfroGFP2^{R223F}
sfroGFPR223Fs	5’-ACATGGTCCTTCTTGAGTTTGTAACAGCTGCTGGG-3’	sfroGFP2^{R223F}
sfroGFPR30Sas	5’-ACCTTCACCCTCTCCGCTGACAGAAAATTTGTG-3’	sfroGFP2^{R30S}
sfroGFPR30Ss	5’-CACAAATTTTCTGTCAGCGGAGAGGGTGAAGGT-3’	sfroGFP2^{R30S}

The underlined sequence represents the area to be mutated.

2.7.1.2 Primer to verify stable integration in the *P. falciparum* NF54*attB* genome

Primer	Nucleotide sequence
BSD R	5‘-ACGAATTCTTAGCTAATTCGCTTGTAAGA-3’
Cg6 5’F	5‘-GAAAATATTATTACAAAGGGTGAGG-3’

2.7.2 Plasmids

Plasmid	Antibiotic-resistance	Source
pQE60-[hGrx1-roGFP2]	Cn^R	Denis Kasozi/ AG Becker
pQE30-[roGFP2]	Cn^R	Marie Sorg/ AG Becker
pQE30-[sfroGFP2]	Cn^R	Katharina Schuh/ AG Becker
pQE30-[sfroGFP2^{R30S}]	Cn^R	Generated within this work
pQE30-[sfroGFP2^{N39Y}]	Cn^R	Generated within this work
pQE30-[sfroGFP2^{R223F}]	Cn^R	Generated within this work
pET28a(+)-[hGrx1-sfroGFP2]	Kan^R	Gene synthetically ordered
pET28a(+)-[hGrx1-sfroGFP2$^{C26S\text{-}C204S}$]	Kan^R	Generated within this work
pET28a(+)-[hGrx1-sfroGFP2$^{C26S\text{-}C174S}$]	Kan^R	Generated within this work
pDC2-CAM-[hGrx1-sfroGFP2]	Cn^R, BSD	Katharina Schuh/ AG Becker
pET28a(+)-[mScarlet-I-SoNar]	Kan^R	Diana Krickeberg/ AG Przyborski
pET28a(+)-[mScarlet-I-iNap2]	Kan^R	Diana Krickeberg/ AG Przyborski
pDC2-CAM-[mScarlet-I-SoNar]-*attP*	Cn^R, BSD	Diana Krickeberg/ AG Przyborski
pDC2-CAM-[mScarlet-I-iNap2]-*attP*	Cn^R, BSD	Diana Krickeberg/ AG Przyborski
pQE30-[sfpHluorin]	Cn^R	Eric Springer/ AG Przyborski
pDC2-CAM-[sfpHluorin]-*attP*	Cn^R, BSD	Eric Springer/ AG Przyborski

Cn^R = carbenicillin resistance, Kan^R = kanamycin resistance, BSD = blasticidin-S-deaminase resistance gene, selection agent: blasticidin S HCl.

2.8 Organisms

2.8.1 *Escherichia coli* cells

E. coli strain	Genotype	Source
BL21 (DE3)	F⁻ ompT gal dcm lon hsdS$_B$(r$_B^-$ m$_B^-$) λ(DE3 [lacI lacUV5-T7 gene 1 ind1 sam7 nin5]	Qiagen, Hilden

DH5-α	F^{-} *endA1 glnV44 thi-1 recA1 relA1 gyrA96 deoR nupG purB20* φ80d*lacZ*ΔM15 Δ(*lacZYA-argF*)U169, hsdR17($r_K^- m_K^+$), λ^{-}	Agilent Technologies, Inc., Santa Clara, CA, USA
KRX	F´, traD36, ΔompP, proA+B+, lacIq , Δ(lacZ)M15] ΔompT, endA1, recA1, gyrA96 (Nalr), thi-1, hsdR17 (rK –, mK +), e14– (McrA–), relA1, supE44, Δ(lac-proAB), Δ(rhaBAD)::T7 RNA polymerase	Promega, Mannheim
M15	F-, φ80ΔlacM15, thi, lac-, mtl-, recA+, Kan^{R}	Qiagen, Hilden
XL1-blue	recA1, endA1, gyrA96, thi-1, hsd-r17,supE44, relA1, lac, [F' pro AB, lacIqZ M15, Tn10, (Tetr)]	Stratagene, Amsterdam

2.8.2 *Plasmodium falciparum* strain

***P. falciparum* strain**	**Source**
NF54*attB*	David Fidock, Columbia University, NY, USA

2.9 Crystallization screens

Screen	**Source**
Additive Screen HT	Hampton Research, Aliso Viejo, CA; USA
JBScreen Classic HTS I	Jena Bioscience, Jena
JBScreen Classic HTS I	Jena Bioscience, Jena
JBScreen Classic Wizard 1 & 2 HTS	Jena Bioscience, Jena
JBScreen Classic Wizard 1 & 2 HTS	Jena Bioscience, Jena
JCSG Core I Suite	Qiagen, Hilden
JCSG Core II Suite	Qiagen, Hilden
JCSG Core III Suite	Qiagen, Hilden
JCSG Core IV Suite	Qiagen, Hilden
PEG Screen I	AG Becker
PEG Screen II	AG Becker
XP Screen	Jena Bioscience, Jena

3. METHODS

All lab work using *Escherichia coli* (*E. coli*) bacteria was carried out under safety level S1 conditions. Lab work using *P. falciparum* parasites was carried out under safety level S2 conditions. Solutions containing *E. coli* or *P. falciparum* were autoclaved at 121 °C for 30 min. Material for sterile work was first autoclaved or purchased sterile.

3.1 Molecular biological methods

The following plasmids were generated, using site-directed mutagenesis (**3.1.1**), as part of this doctoral thesis for heterologous overexpression in *E. coli* cells:

- pQE30-[sfroGFP2$^{\text{R30S}}$], pQE30-[sfroGFP2$^{\text{N39Y}}$], pQE30-[sfroGFP2$^{\text{R223F}}$], pET28a(+)-[hGrx1-sfroGFP2$^{\text{C26S-C147S}}$], and pET28a(+)-[hGrx1-sfroGFP2$^{\text{C26S-C204S}}$]

The working group of Prof. Becker/ Prof. Przyborski generated additional plasmids used within this doctoral thesis. Marie Sorg generated pQE30-[roGFP2]. Diana Krickeberg generated the plasmids pET28a(+)-[mScarlet-I-SoNar], pET28a(+)-[mScarlet-I-iNap2], pDC2-[mScarlet-I-SoNar]-*attP*, and pDC2-[mScarlet-I-iNap2]-*attP*. Eric Springer molecularly cloned pQE30-[sfpHluorin] and pDC2-[sfpHluorin]-*attP*. pDC2-[hGrx1-sfroGFP2]-*attP* was molecularly cloned in cooperation with Dr. Katharina Schuh and is described within her doctoral thesis.

3.1.1 Site-directed mutagenesis

Site-directed mutagenesis using the polymerase chain reaction (PCR) was used to generate different sfroGFP2 mutants, namely sfroGFP2$^{\text{R30S}}$, sfroGFP2$^{\text{N39Y}}$, and sfroGFP2$^{\text{R223F}}$. Therefore, sfroGFP2 in pQE30 was used as a template. The nucleotide sequences of specific primer pairs containing the desired mutated codons used are listed in **2.7.1.1**. PCR conditions were as follows:

PCR mixture

Volume	Substance
1.0 µl	Template DNA (~100 ng/µl)
1.0 µl	Forward primer (100 µM)
1.0 µl	Reverse primer (100 µM)
5.0 µl	10x polymerase buffer
2.5 µl	DMSO
1.0 µl	AccuPrime polymerase (2 U/ml)
37.5 µl	H_2O_{dd} autoclaved
50 µl	

PCR program

Temperature/Time	Program
94 °C for 90 sec	Initial denaturation
94 °C for 30 sec	Denaturation
60 °C for 1 min	Annealing
68 °C for 5 min	Elongation
20x	Cycles
68 °C for 7 min	Final extension
4 °C	Hold

Furthermore, site-directed mutagenesis was used to generate two different hGrx1-sfroGFP2 mutants, namely hGrx1-sfroGFP2$^{C26S\text{-}C147S}$ and hGrx1-sfroGFP2$^{C26S\text{-}C204S}$. Here, the resolving cysteine of hGrx1 was mutated to serine (C26S). In addition, both redox-active cysteine residues of sfroGFP2 were mutated to serines (C147S and C204S) one at a time. For this purpose, hGrx1-sfroGFP2 in pET28a(+) was used as a template. First hGrx1-sfroGFP2^{C26S} was generated using specific primer pairs (**2.7.1.1**). Successful integration was verified via sequencing (LGC, Biosearch Technologies, Berlin). Subsequently, hGrx1-sfroGFP2^{C26S} in pET28a(+) was used as a template in order to generate hGrx1-sfroGFP2$^{C26S\text{-}C147S}$ and hGrx1-sfroGFP2$^{C26S\text{-}C204S}$ in pET28a(+), respectively. The nucleotide sequences of specific primer pairs, containing the desired mutations, are listed in **2.7.1.1**. PCR conditions were as follows:

PCR mixture

Volume	Substance
2.0 µl	Template (~55 ng/µl)
1.0 µl	Forward primer (100 µM)
1.0 µl	Reverse primer (100 µM)
5.0 µl	10x polymerase buffer
2.5 µl	DMSO
1.0 µl	AccuPrime polymerase (2 U/ml)
33.5 µl	H_2O_{dd} autoclaved
50 µl	

PCR program

Temperature/Time	Program
94 °C for 90 sec	Initial denaturation
94 °C for 30 sec	Denaturation
60 °C for 1 min	Annealing
68 °C for 7:30 min	Elongation
30x	Cycles
68 °C for 10 min	Final extension
4 °C	Hold

LGC, Biosearch Technologies, Berlin verified the correct insertions of all specific mutations via sequencing.

All PCR products were purified using the QIAquick PCR purification kit (Qiagen, Hilden). Purification was carried out following the manufacturer's instructions. Elution volume was 20 µl. To reduce false positive colonies methylated template DNA was digested using the restriction enzyme DpnI (Promega, Wisconsin, USA). DpnI-digestion (37 °C, 1 h) conditions were as follows:

DpnI digestion

Volume	Substance
20 µl	Plasmid
4 µl	10x tango buffer
2 µl	DpnI (10 U/µl)
14 µl	H_2O_{dd} autoclaved
40 µl	

After DpnI digestion, DNA was again purified using the QIAquick PCR purification kit (Qiagen, Hilden).

3.1.2 Preparation of plasmid DNA

The mini-prep method was used to purify small amounts of DNA. Therefore, 3 ml LB medium containing the appropriate antibiotic were inoculated with a transformed *E. coli* colony (**3.2.1**). The antibiotic Cn was used at a concentration of 100 µg/ml. Kan was used at a concentration of 50 µg/ml. The cells were allowed to grow overnight at 37 °C with constant shaking (180 rpm). Plasmid DNA was isolated using the PureYield^{TM} Plasmid Miniprep System (Promega, Mannheim), following the manufacturer's protocol. For this purpose 600 µl *E. coli* culture was used. Elution volume was 30 µl. The QIAGEN® plasmid mini kit (Qiagen, Hilden) was used in order to prepare higher amounts of plasmid DNA, which was isolated as described in the manufacturer's instructions. Therefore, 1-5 ml *E. coli* culture was used. Elution volume was 50 µl.

In order to obtain larger DNA amounts for transfection of *P. falciparum* parasites, the QIAGEN® plasmid maxi kit (Qiagen, Hilden) was used. 3 ml LB medium containing 100 µg/ml Cn was inoculated with a transformed *E. coli* colony (**3.2.1**). The cells could grow for 8 h at 37 °C with constant shaking (180 rpm). Subsequently, this pre-culture was transferred into 250 ml LB medium containing 100 µg/ml Cn. The cells were allowed to grow overnight at 37 °C with constant shaking (180 rpm). The plasmid DNA was prepared according to the manufacturer's instructions. The DNA was eluted with high salt buffer, desalted via isopropanol precipitation and washed with 70% ethanol. The DNA was allowed to dry under sterile conditions. Thereafter, the DNA was resuspended in 100 µl of DNA buffer (**2.6.7**).

3.1.3 Agarose gel electrophoresis

Agarose gel electrophoresis was used to separate and analyze DNA fragments. Therefore, DNA samples were mixed with DNA Dye NonTox (5:1) (AppliChem, Darmstadt) and loaded onto a 0.7% or 1% agarose gel (**2.6.4**). DNA fragments were separated using electrophoresis by applying 100 V for 30-45 min. 1x TAE buffer (**2.6.2**) was used as a running buffer. The 1 kb or 1 kb plus DNA ladder GeneRuler (Thermo Fisher Scientific, Dreieich) was used to compare DNA sizes. The DNA bands were visualized using UV light in the gel documentation system FAS Digi (Nippon Genetics, Düren).

3.1.4 DNA quantification

Spectrophotometric determination of the DNA concentration of a sample was performed by measuring absorbance at a wavelength of 260 nm. The ratio of absorbance at 260 nm over absorbance at 280 nm was used to assess the purity of a DNA sample. A sample was defined as pure with a ratio of $A_{260\ nm}/A_{280\ nm}$ = 1.8–2.0 [Carson et al. 2012].

3.2 Microbiological methods

3.2.1 Transformation of *E. coli* cells

Transformation describes the introduction of foreign DNA into bacteria cells. Various methods, for example using calcium chloride, can be used to make *E. coli* cells receptive for the uptake of foreign DNA. In this work, different *E. coli* cell types were used for transformation, depending on the intended use. *E. coli* XL1blue cells and *E. coli* DH5α cells were used to generate plasmid DNA. *E. coli* M15 cells and *E. coli* BL21 cells were used for homologous overexpression of recombinant protein. Depending on whether transformation was performed using plasmid DNA or a PCR product and on the respective concentration it had, the volume used varied. 20 µl of purified PCR product or up to 5 µl plasmid DNA was added to 100-125 µl *E. coli* cells and incubated for 30 min on ice, to allow the DNA to accumulate at the bacteria membrane. After heat shock at 42 °C for 90 sec, causing the uptake of foreign DNA, the cells were incubated on ice for 2 min. Subsequently, 300 µl LB medium was added to the cell DNA mixture. Transformed *E. coli* cells were incubated at 37 °C for 1 h under constant shaking (180 rpm). Thereafter, cells were plated onto an LB agar plate, containing the necessary antibiotics and incubated at 37 °C overnight. Plates were stored at 4 °C until use.

3.2.2 Heterologous overexpression in *E. coli* cells

Recombinant sfroGFP2 was heterologously expressed according to Schuh et al. 2018 [Schuh et al. 2018]. Recombinant hGrx1-roGFP2 was expressed as described in [Kasozi et al. 2013]. mScarlet-I-SoNar and mScarlet-I-iNap2 were expressed as established by Diana Krickeberg. Expression conditions are published within her master's thesis and are therefore not described in detail within this work [Krickeberg 2020].

Expression conditions for all other recombinant proteins used within this doctoral thesis are summarized in **Table 1**. Recombinant production of the proteins of interest were carried out as follows: A pre-culture of 3 ml LB-medium, containing the specific antibiotic, was inoculated with a single colony of *E. coli* cells containing the corresponding plasmid DNA and was incubated at 37 °C for 8 h with continuous shaking at 180 rpm. Subsequently, 50-100 ml LB-, TB-, or 2YT-medium, containing the specific antibiotics as described in **Table 1**, were inoculated with 3 ml of the pre-culture and incubated at 37 °C overnight with constant shaking at 180 rpm. 20–30 ml of overnight culture was added to 1 l LB-, TB-, or 2YT-medium, containing the specific antibiotic, to obtain an OD_{600} of about 0.1 at the beginning. The culture was incubated at 37 °C with constant shaking at 180 rpm until the OD_{600} reached a value of 0.6 to 0.8. By adding 1 mM IPTG (Roth, Karlsruhe), overexpression was induced. The culture was incubated at the ideal temperature and time duration for the protein in question (**Table 1**). Subsequently, cells were harvested via centrifugation for 15 min with 8,000 rpm at 4 °C. Dry pellets were stored at -20 °C.

Table 1. Conditions of heterologous expression for recombinant proteins.

Protein of interest	**Vector**	***E. coli* cell type**	**Medium**	**Antibiotic**	**Temp. [°C]**	**Duration [h]**
sfroGFP2^{R30S}	pQE30	M15	LB	Cn, Kan	22	4
sfroGFP2^{R223F}	pQE30	M15	LB	Cn, Kan	37	4
sfroGFP2^{N39Y}	pQE30	M15	TB	Cn, Kan	37	2
roGFP2	pQE30	M15	LB	Cn, Kan	37	4
hGrx1-sfroGFP2	pET28a(+)	BL21	LB	Kan	22	20
hGrx1-sfroGFP2$^{C26S-C147S}$	pET28a(+)	BL21	2YT	Kan	16	20
hGrx1-sfroGFP2$^{C26S-C204S}$	pET28a(+)	BL21	TB	Kan	22	20
sfpHluorin	pQE30	M15	LB	Cn, Kan	37	20

Cn was used in a concentration of 100 µg/ml. Kan was used in a concentration of 50 µl/ml.

3.3 Protein biochemical methods

3.3.1 Purification of recombinant proteins using affinity chromatography

Frozen *E. coli* cell pellets were thawed and resuspended in an appropriate volume of HEPES buffer (**2.6.6**) (**Table 2**). A mixture of protease inhibitors was added (150 nM pepstatin, 40 nM cystatin, and 100 µM PMSF; Sigma-Aldrich, Steinheim) as well as a small amount of DNaseI (Sigma-Aldrich, Steinheim) and 16 mg/l lysozyme (Sigma-Aldrich, Steinheim). Subsequently, the mixture was stirred on ice for a defined time (**Table 2**). After incubation, the cells were manually sonicated three times for 30 sec each at 60% maximum power. Afterwards, the cell debris was centrifuged at 18,000 rpm, for 30 min (4 °C). After centrifugation, the clear supernatant was applied to a Ni-NTA column (Ni-NTA agarose, Invitrogen, Karlsruhe or PureCube Ni-NTA Agarose, Biozyme, Oldendorf), which had been equilibrated with 10 column volumes (CVs) of HEPES buffer. The supernatant could run slowly through the column material. Meanwhile, recombinant proteins bound to the column via their 6xHis-tag. Column material was washed with 10 CVs of HEPES buffer to remove nonspecifically bound proteins. Recombinant proteins were eluted stepwise using increasing imidazole concentrations (10 mM to 500 mM imidazol). Thereafter, samples from pellet, supernatant, flow through, washing step, and elution fractions were analyzed using SDS-PAGE (**3.3.3**).

sfroGFP2, hGrx1-roGFP2, mSc.-I-SoNar, and mSc.-I-iNap2 were purified as described elsewhere [Kasozi et al. 2013; Schuh et al. 2018; Krickeberg 2020].

Table 2. Purification conditions of recombinant proteins.

Protein of interest	Buffer volume [ml per l *E. coli* culture]	Lysis additives	Duration of lysis [h]	Ni-NTA volume [ml]
sfroGFP2^{R30S}	40	-	1	1
sfroGFP2^{R223F}	40	-	1	2
sfroGFP2^{N39Y}	40	-	1	1
roGFP2	40	-	1	1
hGrx1-sfroGFP2	30	10% glycerol	0:30	1
hGrx1-sfroGFP2$^{C26S-C147S}$	40	-	1	1
hGrx1-sfroGFP2$^{C26S-C204S}$	80	-	1	1.5
sfpHluorin	60	-	1	4

3.3.2 Size exclusion chromatography

Size exclusion chromatography was used to increase the purity of sfroGFP2^{R30S}, sfroGFP2^{N39Y}, sfroGFP2^{R223F}, and hGrx1-sfroGFP2. With this technique, proteins can be separated according on the molecular weight of their native form. The smaller the proteins, the better they can infiltrate the porous column material. This also means, larger proteins pass through the column material more quickly and thus elute earlier. The HiLoad 16/600 Superdex 200 prep grade column connected to an ÄKTA/Unicorn FPLC system (GE Healthcare, Freiburg) was equilibrated with HEPES buffer (**2.6.6**). Protein solutions were centrifuged for 15 min at 13,400 rpm (4 °C) to remove potential solid particles. The protein samples were applied to the column and eluted with a flow rate of 1 ml*min^{-1}. Elution of proteins was detected spectrophotometrically at 280 nm. Fractions of 2 ml were collected, and both peak areas and kAV values were evaluated using Unicorn 4.11 and 7.1 software. Individual fractions were analyzed using SDS-PAGE (**3.3.3**). Selected elution fractions were pooled and concentrated using Vivaspin tubes (10,000 MWCO and 30,000 MWCO, Sartorius Stedim Biotech, Göttingen).

3.3.3 Gel electrophoresis

Using sodium dodecyl sulfate-polyacrylamide gel electrophoresis (SDS-PAGE), proteins can be separated according to their molecular weight [Laemmli 1970]. Therefore, protein samples were mixed with 1x or 4x SDS sample buffer containing dithiothreitol (DTT) (**2.6.3**) and boiled at 95 °C for 5 min. DTT is used as an agent that reduces disulfide bridges. Due to the SDS contained in the sample buffer, the proteins are negatively charged, whereby charge correlates with protein mass [Laemmli 1970]. The denatured samples were applied to a 12% polyacrylamide gel (**2.6.4**), which was clamped into a running chamber filled with electrophoresis buffer (**2.6.3**). A voltage of 200 V was used to separate the samples since proteins migrate towards the positively charged anode in the electric field according to their size. For visualization of protein bands, gels were stained using Coomassie brilliant blue (**2.6.3**). Therefore, the gel was washed twice with water, following incubation with Coomassie brilliant blue staining solution for 10 min. The gel was heated in a microwave for 40 sec at 700 W, to enhance the efficiency of washing and staining. After staining, excess Coomassie was removed by washing the gel with water. If the gel was further used for immunoblotting (**3.3.5**), staining with Coomassie was waived.

3.3.4 Protein quantification with Bradford assay

The Bradford method was used to determine the concentration of the proteins of interest. This method is based on binding Coomassie brilliant blue G-250 to basic and aromatic amino acids, which shifts the absorption of the dye from 465 nm to 595 nm [Bradford 1976]. Furthermore, a color change from red to blue is visible. This assay can be used to determine protein concentration as the absorbance is proportional to the amount of protein. This assay is very stable since only large amounts of detergents, which were not used in this work, could potentially interact with the dye [Bradford 1976]. As a reference, a standard curve with 1, 2.5, 5, 7.5, 10, 15, and 20 µg/ml BSA solved in H_2O_{dd} was used. 500 µl of the standard or diluted protein sample was mixed with 125 µl of Bradford reagent (Bio-Rad, Munich), incubated for 15 min at RT and then measured photometrically at 595 nm.

3.3.5 Protein immunoblotting

Western blot analysis was used to specifically detect individual proteins. Here, specific antibodies are used to immunologically detect the protein of interest. Protein samples were first separated using SDS-PAGE (**3.3.3**). Subsequently, the proteins were transferred to a nitrocellulose membrane (GE Healthcare, Freiburg). In this work, a semidry procedure was used. 12 filter papers (Thermo Fisher Scientific, Dreieich), the nitrocellulose membrane, and the SDS gel were equilibrated in transfer buffer (**2.6.5**). After a few minutes of incubation, the filter papers, gel, and membrane were stacked onto a cathode graphite plate. Air bubbles were carefully removed from the sandwich. The proteins were transferred (blotted) at 13 V for 30 min with a Trans-Blot® Turbo™ transfer system (Bio-Rad, Munich). Transfer of proteins from the SDS gel to the membrane was verified using Ponceau S staining and 1% acetic acid (**2.6.5**). Due to the trichloroacetic acid contained in the dye solution, treatment with Ponceau S staining solution also has a fixing effect on the proteins on the blot. In order to remove the color, the membrane was washed three times with TBST (**2.6.5**). Non-specific binding sites of the membrane were blocked by incubating the membrane in blocking buffer (**2.6.5**) for 1 h at RT or overnight at 4 °C. The membrane was washed three times with TBST buffer for 5 min and then incubated for 1 h in a solution containing the first antibody (AB). After incubation, the membrane was washed three times for 5 min with TBST and then incubated for 1 h in a solution containing the secondary antibody. The specific antibodies and solution media used are listed in **Table 3**. Thereafter, the membrane was washed again three times with TBST buffer for 5 min.

Subsequently, the membrane was incubated for 1 min with the luminol-containing chemiluminescence mixture (**2.6.5**). Chemiluminescence was detected using the Intas ECL ChemoStar (Onzas Science Imaging Instruments GmbH, Göttingen).

To verify the different biosensors in *Plasmodium* parasites, the membrane was stripped using the Restore^{TM} western blot stripping buffer (Thermo Fisher Scientific, Dreieich). After an incubation time of 7 min at RT, the membrane was washed three times with TBST for 5-10 min. The membrane was incubated overnight in blocking buffer at 4 °C. After washing three times for 5 min with TBST, primary and secondary antibodies were bound again as described above. An anti-PfHSP70 AB or an anti-PfAldolase AB was used as a loading control (**Table 3**). Chemiluminescence was detected as described above.

Table 3. Antibodies used for Western blot analysis.

Identification of…	Primary antibody	Secondary antibody
6xHis-tag of recombinant proteins	IgG His epitope-tag unconj, 1:1,000 in BSA.	α-mouse IgG-HRP; 1:10,000 in 5% non-fat milk in TBST
Biosensors expressed in *P. falciparum*	α-GFP, 1:1,000 in 5% non-fat milk in TBST	α-mouse IgG-HRP, 1:10,000 in 5% non-fat milk in TBST
PfAldolase	α-PfAldolase, 1:5,000 in 5% non-fat milk in TBST	α–rabbit IgG-HRP, 1:5,000 In 5% non-fat milk in TBST
PfHSP70	α-PfHSP70, 1:500 in 5% non-fat milk in TBST	α–rabbit IgG-HRP, 1:2,000 In 5% non-fat milk in TBST

In order to examine the expression levels of various biosensors in *P. falciparum*, images from western blot analysis were analyzed using Fiji [Schindelin et al. 2012]. Therefore, background subtraction was performed using the rolling ball algorithm. Contrast was enhanced by 0.1%. Band intensities were measures using Fiji. The associated loading control normalized the GFP signal. The fold change of band intensity and the percentage change of the expression level were calculated.

3.3.6 Protein *S*-glutathionylation

Purified hGrx1-sfroGFP2$^{C26S\text{-}C147S}$ and hGrx1-sfroGFP2$^{C26S\text{-}C204S}$ were reduced with an equimolar concentration of DTT (2 mM) for 30–45 min on ice. Subsequently, DTT was removed using the Zeba^{TM} Spin Desalting Columns (Thermo Fisher Scientific, Dreieich) according to the manufacturer's instructions. Protein concentration was determined using the Bradford assay (**3.3.4**). Proteins were incubated at a ratio of 1:11 with GSSG for 30–45 min, followed by desalting as previously described. Subsequently, protein concentration was adjusted to 30 mg/ml. *S*-glutathionylated hGrx1-sfroGFP2$^{C26S\text{-}C147S}$ and hGrx1-sfroGFP2$^{C26S\text{-}C204S}$ were used for protein crystallization approaches (**3.4.1**). In this work, Norma Schulz conducted *S*-glutathionylation.

3.4 Structural biological methods

The function of a protein is determined primarily by its three-dimensional structure. Therefore, in order to understand proteins and biological systems at their molecular level, protein crystallography can play a major role [Chayen and Saridakis 2008]. However, before the 3D structure of a protein can be determined, generating a single protein crystal is the decisive obstacle [Benvenuti and Mangani 2007]. Therefore, several steps are necessary. First, the protein of interest must be expressed, which may require a pre-cloning step. Ideal expression conditions must be identified to enable sufficiently high protein yields. Secondly, the protein of interest has to be purified. Only when a pure and concentrated protein solution, typically 5-15 mg/ml, has been generated will the actual crystallization process begin. This process contains crystallization screening and optimization. Once a single crystal of a suitable size, longer than 10 μm^3, can be generated, x-ray analysis can start. Data can then be collected and the structure can be determined [Benvenuti and Mangani 2007; Chayen and Saridakis 2008].

3.4.1 Protein crystallization

Crystallization of a protein depends on the generation of a highly saturated solution, which, however, does not affect the natural state of the protein. The solution can be supersaturated by using precipitating agents, such as salts and polymers. Thereafter, different parameters, such as temperature, pH, or ionic strength can be changed [McPherson and Gavira 2014]. Testing a suitable protein concentration is also advisable. Various techniques such as microbatch crystallization and dialysis can be used to reach the supersaturation state. In this work, the vapor diffusion technique, a method based on the gradual change in concentration of a protein solution, was used. The slow increase in protein concentration is intended to initiate the formation of a protein crystal. This change in concentration is achieved by diffusing of a solvent vapor between the protein solution and a so-called reservoir solution. Therefore, the presence of a concentration gradient between the two solutions is necessary. The concentration gradient is balanced out via diffusion until a dynamic equilibrium prevails. Two variants of this vapor diffusion technique are distinguished: the sitting drop and hanging drop procedure. The differences in both approaches are shown in **Figure 13**. In the sitting drop approach, the drop sits in a well in the middle of or next to the reservoir solution, in the hanging drop approach it hangs above the reservoir solution. This is made possible by mounting the drop on a cover slide.

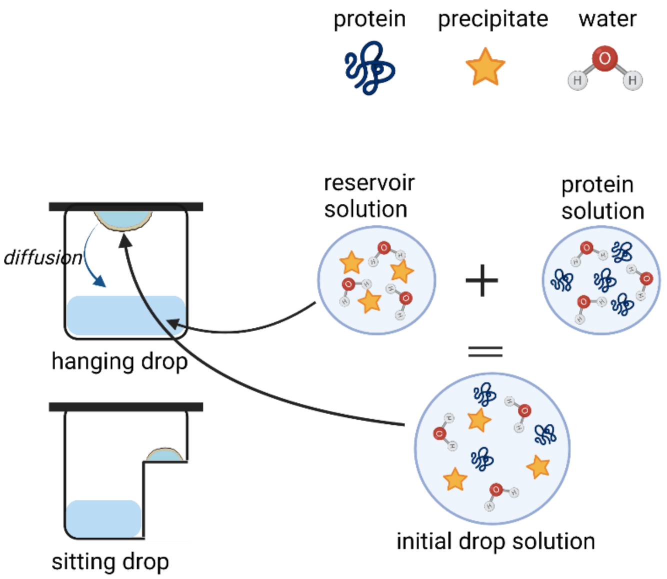

Figure 13. Protein crystallization using vapor diffusion technique. Created with BioRender.com.

3.4.2 Screening the crystallization conditions

Protein crystal growth is an empirical process [McPherson and Gavira 2014]. Commercially available crystallization screens (2.9) can be used to obtain ideal crystallization conditions. In this work, additional crystallization screens developed by the working group of Prof. Becker were used (2.9). The screenings were performed using the Honeybee crystallization robot 961 in 96-well two-drop trays, which Michaela Stumpf operated. 200 nl reservoir solution and 200 nl protein solution were comprised by the robot and pipetted into the wells next to the reservoir containing 100 µl reservoir solution. A control drop comprising of 200 nl reservoir solution and 200 nl buffer was placed into the control well so as to differentiate between salt and protein crystals. In some approaches, another protein drop with different conditions was tested instead of the control drop, for example to test different protein concentrations within one crystal approach. Thus, 192 different conditions could be tested at once. The wells were subsequently sealed airtight with clear adhesive tape (Clear tape HDClear, ShurTec Brands, Avon, OH, USA), and the plates were stored at RT. For some tests, the plates were stored at 4 °C. Crystals or crystal-like precipitation was checked on a regular basis using a stereomicroscope system (M165 C, KL 1500 LED, camera EC 3, Leica, Wetzlar).

3.4.3 Optimizing crystallization conditions

In order to optimize the crystallization conditions and generate sufficiently large protein crystals, manual preparations were partially carried out using the vapor diffusion technique in 24-well crystallization plates (crystallization plate 96-well, MRC 2-well, Jena Bioscience, Jena; crystallization plate 24-well, Cryschem^{TM} M plate, Hampton Research, Aliso Viejo, CA, USA) with sitting drop and hanging drop approaches. For the hanging drop approach, the reservoir wells were filled with 800 µl of reservoir solution. The clefts around the wells were covered with silicone oil (silicone oil 550, Merck, Darmstadt). This allows the wells to be hermetically sealed later on. In the center of a microscope cover slip (Ø 21 mm Menzel, Brunswick), 2 µl of protein solution was mixed with 2 µl of reservoir solution. The slip was put facedown onto the reservoir well. Also, for the sitting drop approach, 800 µl of reservoir solution was added to the reservoir well. 2 µl of protein solution and 2 µl of reservoir solution were mixed into the middle of a sitting drop crystallization plate (Crystallization plate 24 well, Cryschem^{TM} M plate, Hampton Research, Aliso Viejo, CA, USA). The plates were sealed with a clear adhesive tape (Clear tape HDClear, ShurTec Brands, Avon, OH, USA). The plates were then stored at RT or 4 °C and checked for crystals on a regular basis using a stereomicroscope system (M165 C, KL 1500 LED, camera EC 3, Leica, Wetzlar).

3.4.4 Data collection and processing

The protein crystals were further analyzed in Heidelberg at the Max-Planck Institute. Prior to data collection, the crystals were transferred to a cryo protection buffer containing the actual crystallization buffer and, additionally, glycerol or ethylene glycol. Then, the crystals were stored in liquid nitrogen. Dr. Karin Fritz-Wolf analyzed x-ray diffraction, which resulted in diffraction patterns. Those patterns were then used, to calculate the three-dimensional protein structure. Diffraction data was collected at X10SA (detector: Pilatus) of the Swiss Light Source, Villigen, Switzerland.

3.5 *In vitro* characterization of fluorescence-based biosensors

3.5.1 Spectral scans of recombinant fluorescence-based redox-biosensors

Recombinant redox-biosensor variants (roGFP2, hGrx1-roGFP2, sfroGFP2, sfroGFP2^{R30S}, sfroGFP2^{N39Y}, sfroGFP2^{R223F}, and hGrx1-sfroGFP2) were diluted to 10 µM in potassium phosphate buffer (2.6.6). Sensors were fully reduced using 10 mM DTT or fully oxidized using 1 mM 2,2-dithiopyridylsulfide (DPS). Spectral scans were performed using a Clariostar plate reader (BMG Labtech, Ortenberg, Germany). Excitation spectral scans were recorded for each redox-sensor. Recorded excitation ranged from 350 nm to 505 nm (with 1 nm resolution and 10 nm bandwidth), with emission in the range of 510 ± 10 nm. Moreover, emission spectral scans were recorded, with emission, ranging from 495 nm to 650 nm (with 1 nm resolution and 10 nm bandwidth) and with excitation at 405 ± 10 nm. Furthermore, emission from 510 nm to 650 nm (with 1 nm resolution and 10 nm bandwidth), with excitation at 485 ± 10 nm, was recorded. Reduced and oxidized potassium phosphate buffer was measured as an empty value. The measurements were carried out at different temperatures (~10 °C and 37 °C). For this purpose, both, cooled buffer and protein were used, or both the buffer and plate reader were heated to 37 °C. Measured values were corrected with the blank value. Four technical repeats each were measured. Relative fluorescence units (RFU) were plotted against wavelength using GraphPadPrism 8.

Furthermore, spectral scans were measured after incubation of recombinant redox-sensors in parasite cell extract (3.6.6). The different redox-biosensors roGFP2, hGrx1-roGFP2, sfroGFP2, and hGrx1-sfroGFP2 were either reduced using 10 mM DTT or oxidized using 1 mM DPS and incubated in parasite cell extract. Sensors were added to a final concentration of 10 µM. Redox-biosensors were excited sequentially at 400 ± 5 nm and 482 ± 8 nm in a Clariostar plate reader (BMG Labtech, Ortenberg, Germany). All measurements were performed using four technical repeats. Measured values were corrected with the blank value (reduced and oxidized parasite cell extract). RFU were plotted against wavelength using GraphPadPrism 8.

3.5.2 pH response of recombinant fluorescence-based biosensors

3.5.2.1 pH dependency of recombinant redox-biosensors

To determine the pH response, all redox biosensor variants (roGFP2, hGrx1-roGFP2, sfroGFP2, sfroGFP2^{R30S}, sfroGFP2^{N39Y}, sfroGFP2^{R223F}, and hGrx1-sfroGFP2) were equilibrated in buffers with pH values ranging from pH 5.0-9.5 (2.6.6). Redox-sensors were diluted to 10 µM, oxidized (1 mM DPS), and reduced (10 mM DTT). Excitation was performed sequentially at 400 ± 5 nm and 482 ± 8 nm using a Clariostar plate reader (BMG Labtech, Ortenberg, Germany). Four technical replicates each were measured. Blank values (corresponding buffer) were subtracted from the measuring values using Excel. The ratio was calculated by dividing the FI of emission at 510 nm after excitation at 405 nm by the FI of emission at 510 nm after excitation at 485 nm ($R=\frac{405\text{ nm}}{485\text{ nm}}$). This ratio was plotted against the different pH values using GraphPadPrism 8.

3.5.2.2 pH dependency of recombinant mScarlet-I-SoNar and mScarlet-I-iNap2

Diana Krickeberg carried out the pH response of recombinant mSc.-I-SoNar and mSc.-I-iNap2 in a pH ranging from 5.0–9.0 [Krickeberg 2020]. Within this work, pH response in a pH ranging from 6.5 to 8.5 was studied in more detail. Therefore, recombinant biosensors were diluted to a concentration of 1 µM in buffers, with pH ranging from 6.5–8.5. NAD^+, NADH, $NADP^+$, and NADPH stock solutions were diluted to a concentration of 10 µM in the different pH buffers. Concentrations of NADH and NADPH stock solutions were examined beforehand based on their absorption at 340 nm (Spectrophotometer U-2001, Hitachi, Schwäbisch Gmünd). Concentration was calculated as follows (equation 1):

$$c=\frac{A * V}{\varepsilon * vi} \qquad \text{Eq. 1}$$

Here, *A* is absorption at 340 nm, *V* is the total volume within the cuvette (1000 µl); *ε* is the extinction coefficient of NAD(P)H (6.22 $l*mmol^{-1}*cm^{-1}$); v_i represents the used volume of NAD(P)H stock solution (20 µl).

Spectral scans were recorded using a Clariostar plate reader (BMG Labtech, Ortenberg, Germany). Excitation scans were recorded in a range of 320 nm to 505 nm with a 10 nm bandwidth. Emission was measured at 530 ± 10 nm. Emission spectral scans were recorded in a range from 495 nm to 650 nm, from 510 nm to 650 nm, and from 594 nm to 740 nm after excitation at 420 nm, 485 nm, and 569 nm, respectively. Each bandwidth was 10 nm. Values were adjusted with the corresponding blank values (buffer control). Ratios were calculated using the FI at the respective emission maxima after excitation at the specific wavelength in each case. Ratios were plotted against pH using GraphPadPrism 8.

3.5.2.3 pH dependency of recombinant sfpHluorin

To examine pH-dependent spectral scans with purified recombinant sfpHluorin, buffers with various pH values ranging from pH 5.0 to pH 9.0 were prepared (**2.6.6**) and pre-heated to 37 °C. To examine spectral excitation and emission scans, a Clariostar plate reader (BMG Labtech, Ortenberg, Germany) was pre-heated to 37 °C. sfpHluorin was diluted in various buffers to a final concentration of 10 µM. Recorded excitation ranged from 340 nm to 490 nm (with 1 nm resolution and 10 nm bandwidth), with emission in the range of 530 ± 30 nm. Emission spectral scans were recorded ranging from 480 nm to 600 nm (with 1 nm resolution and 10 nm bandwidth) with excitation at 390 ± 16 nm. Emission spectral scans were additionally recorded ranging from 498 nm to 600 nm (with 1 nm resolution and 10 nm bandwidth) with excitation at 470 ± 16 nm. Three independent biological replications were performed. Fluorescence values were corrected using buffer controls. RFU were plotted against wavelength and ratio, which was calculated using the FI at 510 nm after excitation at 390 nm and 470 nm ($R=\frac{390\text{ nm}}{470\text{ nm}}$), against pH, using GraphPadPrism 8.

3.5.3 Determining the midpoint potential of recombinant fluorescence-based redox-biosensors

Redox titration was performed to determine the midpoint potentials of the different redox-biosensor variants (roGFP2, hGrx1-roGFP2 , sfroGFP2, sfroGFP2^{R30S}, sfroGFP2^{N39Y}, sfroGFP2^{R223F}, and hGrx1-sfroGFP2). Therefore, recombinant redox-biosensors were allowed to equilibrate for 1 h with DTT buffers (reduced form 1,4-dithiothreitol; oxidized form 1,3-dithiane). DTT_{red}/DTT_{ox} was used in a total concentration of 10 mM in degassed HEPES assay buffer (**2.6.6**). The relationship of DTT_{red} and DTT_{ox} to set a certain redox potential was calculated from the Nernst equation based on the standard reduction potential of DTT ($E^{0'}_{DTT}$) of -330 mV (equation 2).

$$E_{DTT} = E^{0'}_{DTT} - 2.303\,\frac{RT}{zF}\,\log\frac{DTT_{red}}{DTT_{ox}} \qquad \text{Eq. 2}$$

Here *R* is the gas constant (8.315 J K^{-1} mol^{-1}); *T* is the absolute temperature (310.45 K); *z* is the number of transferred electrons (2); *F* is the Faraday's constant (96,485 C mol^{-1}).

Redox potentials ranging from -220 mV to -360 mV were adjusted. Additionally, redox-biosensors were fully reduced (10 mM DTT) and fully oxidized (1 mM DPS). Redox-biosensors were excited sequentially at 400 ± 5 nm and 482 ± 8 nm in a Clariostar plate reader (BMG Labtech, Ortenberg, Germany). The degree of oxidation (OxD) was determined according to equation 3.

$$OxD = \frac{R-R_{red}}{\frac{I_{485ox}}{I_{485red}}(R_{ox}-R)+(R-R_{red})} \qquad \text{Eq. 3}$$

Here *R* represents the ratio of the FI measured at 510 nm after excitation at 405 nm and 485 nm ($R=\frac{405\text{ nm}}{485\text{ nm}}$); R_{red} and R_{ox} is the ratio of the FI of fully reduced or fully oxidized protein; I_{485ox} is the FI at 485 nm for fully oxidized protein; I_{485red} is the FI at 485 nm for fully reduced protein; both values are corrected by the blank.

To determine the midpoint potential $E^{0'}$ of the various redox-sensors, OxD was plotted against the calculated redox potential, which was adjusted with DTT_{red}/DTT_{ox}. Using GraphPadPrism 8, all data points were fitted to a sigmoidal dose response curve.

3.5.4 Dynamic change of ratio of recombinant fluorescence-based biosensors

3.5.4.1 Dynamic change of ratio of recombinant redox-biosensors

Purified recombinant redox-biosensors (roGFP2, hGrx1-roGFP2, sfroGFP2, and hGrx1-sfroGFP2) were pre-reduced using a final concentration of 10 mM DTT and incubated on ice for 45 min. Subsequently, redox biosensors were desalted using P-6 gel (Bio-Rad, Munich), and diluted in potassium phosphate buffer (2.6.6) to a concentration of 1.25 µM (final concentration per well = 1 µM). The desalination step again removed the previously added DTT. Prior to use, the buffer was pre-heated to 37 °C and degassed for at least 45 min using a sonication bath (ultrasound water bath Sonorex RK100, Bandelin electronic, Berlin). Emission at 530 ± 40 nm after excitation at 400 ± 10 nm and 482 ± 16 nm was measured over 80 sec using a Clariostar plate reader (BMG Labtech, Ortenberg, Germany), which was pre-heated to 37 °C. After 80 sec of basal measurement, DIA was added to a final concentration of 1 mM and emission was measured again over 80 sec. Subsequently, DTT was added to a final concentration of 10 mM and emission was measured over 80 sec. Three independent biological replications were performed. Ratio was calculated ($R = \frac{405\text{ nm}}{485\text{ nm}}$) and plotted against time, using GraphPadPrism 8.

3.5.4.2 Dynamic change of ratio of recombinant mScarlet-I-SoNar and mScarlet-I-iNap2

Purified recombinant mSc.-I-SoNar and mSc.-I-iNap2 were desalted using P-6 gel (Bio-Rad, Munich), and diluted in potassium phosphate buffer (2.6.6) to a concentration of 1.25 µM (final concentration in the well = 1 µM). Prior to use, the buffer was pre-heated to 37 °C and degassed for at least 45 min using a sonication bath (ultrasound water bath Sonorex RK100, Bandelin electronic, Berlin).

To determine dynamic changes of the ratio for mSc.-I-Sonar, after 80 sec of basal measurement, NADH was added to a final concentration of 1 µM, and emission was measured again over 80 sec. Subsequently, NAD^+ was added to a final concentration of 10 mM, and emission was measured over 80 sec.

To determine dynamic changes of the ratio for mSc.-I-iNap2, after 80 sec of basal measurement, NADPH was added to a final concentration of 20 µM, and emission was measured again over 80 sec. Subsequently, $NADP^+$ was added to a final concentration of 10 mM, and emission was measured over 80 sec. The concentrations of the NAD(P)H stock solutions were verified photometrically beforehand (3.5.2.2).

Three independent biological replications each were performed. Ratio was calculated and plotted against time using GraphPadPrism 8.
Moreover, measurements were performed with lower nucleotide concentrations (0.2 µM NADH and 2 mM NAD^+ as well as 20 µM NADPH and 2 mM $NADP^+$).

3.5.5 Direct interaction of recombinant fluorescence-based biosensors with compounds and antimalarials

Recombinant hGrx1-sfroGFP2 was pre-reduced using a final concentration of 10 mM DTT for 45 min on ice. DTT was removed prior to the experiment. Recombinant mSc.-I-SoNar, mSc.-I-iNap2, and sfpHluorin were used without any pre-treatment. All fluorescence-based biosensors were desalted using P-6 gel (Bio-Rad, Munich) and diluted in potassium phosphate buffer (**2.6.6**) to a final concentration of 1.25 µM. Prior to use, the buffer was pre-heated to 37 °C and degassed for at least 45 min using a sonication bath (ultrasound water bath Sonorex RK100, Bandelin electronic, Berlin). Various compounds and antimalarials (DHA, ATQ, CQ, QN, MB, compound 1o, SBI-750, pyruvate, oxamate, 2-DOG, H_2O_2, GSH, GSSG, DOXY, CHX) were solved in DMSO or H_2O_{dd}, depending on their solution behavior, and diluted to match the final concentrations. The compounds and antimalarials were mixed with the different biosensors in a 96-well plate (microplate, 96-well plate, half area, black, Greiner Bio-One, Frickenhausen). Various controls were measured in parallel. Therefore, biosensors were diluted in potassium phosphate buffer without any addition. Furthermore, the biosensors were treated with substances to increase or decrease their ratio. For hGrx1-sfroGFP2 a final concentration of 1 mM DIA was used to fully oxidize the sensor and a final concentration of 10 mM DTT was used to fully reduce the sensor. For mSc.-I-SoNar, NAD^+ and NADH were used as additional controls. mSc.-I-iNap2 was treated with $NADP^+$ and NADPH, additionally. For sfpHluorin, buffers with a pH value of 5 and 9 were used as further controls. The fluorescence-based biosensors were incubated with the substances for 5 min, 4 h, and 24 h. Ratios ($R = \frac{405\ \text{nm}}{485\ \text{nm}}$; $R = \frac{420\ \text{nm}}{569\ \text{nm}}$; or $R = \frac{390\ \text{nm}}{470\ \text{nm}}$) were calculated using the appropriate excitation- and emission wavelengths for the respective biosensor. Ratios were plotted using GraphPadPrism 8.

3.6 *Plasmodium falciparum* culture methods

3.6.1 *Plasmodium falciparum* maintenance

P. falciparum strains were cultivated in RPMI 1640 medium, containing 0.5% w/v albumax, 9 mM glucose, 0.2 mM hypoxanthine, 2.1 mM L-glutamine, 25 mM HEPES, and 22 µg/ml gentamycin, hereafter referred to as complete medium (**2.6.7**). A^+ erythrocytes were used to adjust a hematocrit of 3.3% (15 ml culture). Cultivation was performed at 37 °C in a gaseous mixture comprising 3% O_2, 3% CO_2, and 94% N_2. Giemsa-stained blood smears were used to count parasitemia according to equation 4.

$$\text{Parasitemia [\%]} = \frac{\text{Number of iRBCs}}{\text{Number of RBCs}} * 100 \qquad \text{Eq. 4}$$

3.6.2 Freezing stabilates

For parasite storage, blood stabilates were frozen in liquid nitrogen. For this purpose, a petri dish (100 mm, Greiner Bio-One, Frickenhausen or Sarstedt, Nümbrecht) containing a culture with predominantly ring-stage parasites was centrifuged at 2,100 rpm for 3 min (RT). The supernatant was discarded. The iRBCs were resuspended in 500 µl of freezing solution (**2.6.7**) and transferred to a 2 ml Cryo S^{TM} tube (Greiner Bio-One, Frickenhausen). The stabilates were slowly cooled down in a freezing container (Nalgene® Mr. Frosty, Sigma-Aldrich, Steinheim) at -80 °C. The freezing container, which contains isopropanol, causes the stabilates to cool by 1 °C per minute [manufactory's information]. Subsequently, the stabilates were stored in a tank with liquid nitrogen.

3.6.3 Sorbitol synchronization

Parasite strains were synchronized to the ring-stage using sorbitol (Roth, Karlsruhe) (**2.6.7**). Late-stage parasites (trophozoite-stages and schizonts) have developed specific ion channels through which sorbitol can be absorbed, causing osmotic lysis of the parasites. Since ring-stage parasites have not yet developed these channels, they survive treatment with sorbitol. For synchronization, 10 ml of parasite culture was transferred to a 15 ml falcon tube (Cellstar tubes, Greiner Bio-One, Frickenhausen). After centrifugation for 3 min at 2,100 rpm (RT), supernatant was discarded. The remaining iRBCs were resuspended in 5 ml sorbitol solution and incubated for 8 min at 37 °C. After subsequent centrifugation as described above, the supernatant was discarded and the iRBCs were washed once with complete medium (**2.6.7**). After renewed centrifugation, parasites were seeded to a new petri dish (100 mm, Greiner Bio-One, Frickenhausen or Sarstedt, Nümbrecht) and maintained as previously described (**3.6.1**).

3.6.4 Enrichment of trophozoite-stage parasites

In order to enrich trophozoite-stage parasites and remove non-infected RBCs and ring-stage parasites the magnetism of hemozoin was used [Paul et al. 1981]. MACS columns D (Miltenyi Biotec, Bergisch Gladbach) were connected to a STERICAN disposable hypodermic needle (Braun, Sempach) via a 3-way stopcock (Discofix®, B. Braun, Melsungen) and attached to the Quadro MACS^{TM} separating system (Miltenyi Biotec, Bergisch Gladbach). Columns were equilibrated with complete medium (**2.6.7**). *P. falciparum* cell suspension was added to the columns, and non-infected RBC and RBC containing ring-stage parasites were washed away with complete medium or 1x PBS (**2.6.7**). To elute the late-stage parasites, the columns were detached from the magnet. Cells were eluted with complete medium and allowed to rest for 2 h under normal culture conditions. The columns were washed with water (one column volume), 2 ml of 70%, and 1 ml of 100% ethanol and dried.

3.6.5 Preparation of parasite cell extract for anti-GFP Western blot analysis

Western blot analysis was performed with all NF54*attB* parasite lines expressing various biosensors. Therefore, the parasites were synchronized using sorbitol (**3.6.3**). Trophopzoite-stage parasites were used to generate Western blot samples. Therefore, 10 ml parasite culture, mainly containing trophozoite-stage parasites, was transferred to a falcon tube (Cellstar tubes, Greiner Bio-One, Frickenhausen) and centrifuged at 2,100 rpm for 3 min (RT). The supernatant was discarded, and the iRBCs were resuspended in 10 ml saponin lysis buffer (**2.6.7**). After an incubation time of 10 min at 37 °C, the mixture was centrifuged again. Depending on the effectiveness of the saponin lysis, this step was repeated one more time. After washing three times with 1x PBS, parasites were lysed using the M-PER^{TM} mammalian protein extraction reagent (Thermo Fisher Scientific, Dreieich). The samples were centrifuged at 13,400 rpm for 3 min at RT. Parasite supernatant was mixed with 4x sample buffer containing DTT (**2.6.3**) and boiled at 95 °C for 5 min. The amount of M-PER^{TM} buffer and sample buffer was calculated based on the parasitemia of the culture, which was counted beforehand. Samples were separated using SDS-PAGE (**3.3.3**), followed by Western blot analysis (**3.3.5**).

3.6.6 Preparation of parasite cell extract for spectral scans

For the generation of parasite cell extract, non-transfected NF54*attB* parasites were synchronized using sorbitol (**3.6.3**) and parasite pellets were generated. Therefore, the parasite culture, with predominantly trophozoite-stages, was transferred to a falcon tube (Cellstar tubes, Greiner Bio-One, Frickenhausen) and centrifuged at 2,100 rpm for 3 min (RT). The supernatant was discarded, and the iRBCs were resuspended in 10 ml saponin lysis buffer (**2.6.7**). After an incubation time of 10 min at 37 °C, the mixture was centrifuged again. This step was repeated twice before the iRBCs were washed with 1x PBS (**2.6.7**). At the end, the supernatant was removed again, and the pellet was stored at -80 °C. Parasite pellets were lysed by freezing and thawing multiple times in order to prepare parasite cell extracts. For this purpose, parasite pellets were diluted in 1x PBS (three times the volume). The reaction vessel containing the parasite pellet was alternately immersed in a lukewarm water bath and liquid nitrogen for 2 min, respectively. Parasites were disrupted with four cycles of freezing and thawing. The contents of the reaction vessel were mixed vigorously between the cycles. After centrifugation at 50,000 rpm for 30 min at 4 °C in an ultracentrifuge (Optima^{TM} TLX Ultracentrifuge, Beckman Coulter, Krefeld), the resulting supernatant was used to perform spectral scans with recombinant redox-biosensors (**3.5.1**).

3.6.7 Stable transfection of *Plasmodium falciparum*

Different biosensors were stably integrated into the genome of *P. falciparum* NF54*attB* parasites. Therefore, the *attB/attP* method as described by Nkrumah et al. 2006 was used (**Figure 14**).

In this method, the serine integrase of mycobacteriophage Bxb1 mediates the directed recombination between the *attP* site in the plasmid and the *attB* site in the parasitic genome

[Nkrumah et al. 2006]. Prof. David Fidock from the Columbia University, New York, USA provided NF54 parasites with the *attB* site and the pINT plasmid, as well as the pDC2-*attP* plasmid. The *attB* site was inserted into the locus of the non-essential *cg6* gene (**Figure 14**). The pINT plasmid (neo^R, neomycin resistance, mediates resistance to geneticin) is used to express the integrase. NF54*attB* parasites were co-transfected with the pDC2*attP* plasmid (BSD*,* blasticidin S deaminase selection marker, confers resistance to blasticidin S HCl), encoding the respective construct gene, e.g. mSc.-I-iNap2 along with the integrase-encoding plasmid pINT. Integrase-mediated *attB*x*attP*-based genomic recombination facilitates the insertion of DNA into the genomic *attB* locus. For the transfections, parasite culture (preferably ring-stage parasites 8-10 h, 5-8% parasitemia) was centrifuged at 2,100 rpm for 3 min and the supernatant was discarded. For each transfection, 50 µg of purified DNA with the target gene (pDC2-[X]-*attP*) and 50 µg of purified pINT DNA were mixed. The volume was filled up to 400 µl with cytomix (**2.6.7**). 200 µl of iRBCs were resuspended in the DNA/cytomix mixture. The transfection mixture was transferred to an electroporation cuvette (2 mm) and electroporated (310 V, 950 µF, capacitance ∞) with the Bio-Rad Gene Pulser. The time constant was between 10 and 15 ms. After electroporation the parasites were immediately resuspended with 1 ml complete medium (**2.6.7**) and transferred to an already prepared 5 ml conical containing 3.5 ml of complete medium and RBCs (4% hematocrit). An additional 1 ml of complete medium was added to the culture. The parasites were allowed to rest under normal culture conditions. After one hour, the medium was changed, which also removed lysed RBCs. After 24 h, selected drugs (2.5 µg/ml BSD and 125 µg/ml G418) were added for 6 days. The medium was changed every other day, and on day 6, an additional 50 µl of fresh RBCs were added. After 7 days, only BSD was used for selection. On days 10-13, the culture was split 1:2. This procedure was repeated weekly until the first parasites were seen using Giemsa-stained smears. Normally, NF54*attB* parasites could be recognized after four weeks.

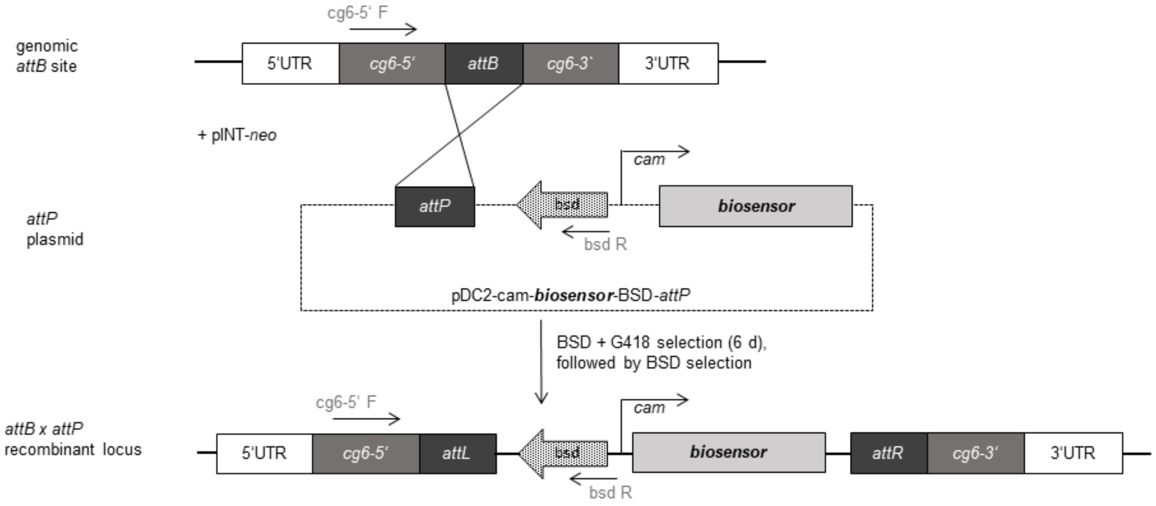

Figure 14. Site-specific integration in the *P. falciparum* chromosome mediated by mycobacteriophage Bxb1 integrase.

3.6.8 Integration PCR

Integration PCR using the KAPA Blood PCR Mastermix B Kit (Peqlab, Erlangen) and specific primer pairs (**2.7.1.2**) was performed to confirm successful stable integration of the biosensor into the parasites genome. The PCR was performed using the PCR Cycler Fast Gene (Nippon Genetics, Düren). The PCR mixture and PCR program were performed as follows:

PCR mixture

Volume	Substance
10 µl	KAPA Blood PCR Mix B
2 µl	Parasite culture
1 µl	Forward primer (5 µM)
1 µl	Reverse primer (5 µM)
6 µl	H_2O_{dd} autoclaved
20 µl	

PCR program

Temperature/Time	Program
95 °C for 10 min	Initial denaturation
95 °C for 30 sec	Denaturation
54 °C for 45 sec	Annealing
62 °C for 6 min	Elongation
35x	Cycles
4 °C	Hold

The samples were mixed with DNA-Dye NonTox (AppliChem, Darmstadt) and loaded onto an agarose gel (**3.1.3**). The GeneRuler 1 kb DNA ladder (Thermo Firscher Scientific, Dreieich) was used to compare DNA sizes.

3.6.9 Generation of clonal parasite lines

After confirmed stable integration of the biosensors, a clonal parasite line was generated in order to obtain a genomically homogeneous parasite population. Cloning plates were prepared using limited dilution. Therefore, a culture with predominantly ring-stage parasites (2-5% parasitemia) was diluted to 2.5 iRBCs/ml and 1.25 iRBCs/ml, respectively. 200 µl of this diluted culture was then seeded with the addition of RBCs in sterile 96-well microtiter plates (Greiner Bio-One, Frickenhausen). Assuming that 1 ml of packed RBCs corresponds to 10^{10} RBCs, the number of iRBC/ml was calculated using equation 5.

$$\text{iRBC/ml} = 1*10^{10}*\left(\frac{h}{100}\right)*\left(\frac{p}{100}\right) \qquad \text{Eq. 5}$$

Here, h is the hematocrit and p is the parasitemia of the culture.

The original culture was thoroughly resuspended and diluted to a hematocrit of 1.8%. 6 µl of this was transferred to a 15 ml falcon tube containing 12 ml of complete medium (**2.6.7**) with 1.8% RBCs. From this intermediate dilution, the required volume was calculated to achieve the final concentrations of 2.5 iRBC/ml and 1.25 iRBC/ml, respectively. On day 7 after seeding, 150 µl of medium was carefully removed without disturbing the cells and then replaced with 200 µl of fresh complete medium containing 0.4% fresh RBCs. To avoid cross-contamination, clean tips were used for each pipetting step. On days 14 and 17, the medium was changed again. Cloning plates were detected on day 20 using a SYBR Green assay. Therefore, 15 µl of a 3-fold SYBR Green-I solution (10,000 * stock solution) in SYBR Green-I buffer (**2.6.7**) was added to each well of a separate 96-

well plate (half area black, Greiner Bio-One, Frickenhausen), and mixed with 30 µl of culture from the cloning plate. After incubating for 30 min at 37 °C, fluorescence was measured using a Clariostar plate reader (BMG Labtech, Ortenberg, Germany) ($\lambda_{Exc.}$ 485 nm; $\lambda_{Em.}$ 535 nm). Since FI should correlate with parasitemia, wells containing parasites showed higher fluorescence signals than the background signal of non-parasitized wells. Wells with very high fluorescence signals were avoided as they were likely to contain more than one parasite per well at the beginning. Blood PCR was performed as described previously (**3.6.8**) to confirm stable integration. PCR and genomic integration of the constructs were verified via agarose gel electrophoresis (**3.1.3**). After verification, clones were transferred to a 2 ml culture (hematocrit 4%) on the same day and cultured as described above (**3.6.1**). Over time, parasites were propagated to 5 ml and finally to 15 ml culture. Stocks of the clonal parasite lines were frozen and stored in liquid nitrogen (**3.6.2**). Integration of the various biosensors was further verified microscopically (**3.6.10**) and via Western blot analysis (**3.3.5**).

3.6.10 Epifluorescence microscopy

In order to verify the fluorescence signal of clonal parasite lines, images were taken using an epifluorescence microscope (Zeiss Axio Observe Z1, Zeiss, Jena). Therefore, the culture was placed on a coverslip (microscope slides Menzel SuperFrost®, Thermo Fisher Scientific, Dreieich) and capped with a cover glass (Cover slips 24 x 50 mm, Menzel, Brunswick). DIC images and images from different channels were taken. DAPI (0.1 mg/ml in H_20_{dd}; 1:100 in culture) was used to stain the cell nucleus. Images were taken using Zeiss microscope software ZEN (Zeiss, Jena). Images were processed using Fiji [Schindelin et al. 2012]. The background was subtracted using the rolling ball algorithm and contrast was enhanced by 0.01%. To improve recognizability, signals from single channels are represented in grey. Merged images are represented in cyan (DAPI), yellow (GFP), and magenta (mScarlet).

3.7 *In cellulo* biosensor measurements

3.7.1 *In cellulo* spectral scans

3.7.1.1 *In cellulo* spectral scans of NF54*attB*$^{hGrx1\text{-}roGFP2}$, NF54*attB*^{sfroGFP2}, and NF54*attB*$^{hGrx1\text{-}sfroGFP2}$

Spectra were scanned using NF54*attB* parasites stably expressing hGrx1-roGFP2, sfroGFP2, or hGrx1-sfroGFP2, hereafter referred to as NF54*attB*$^{hGrx1\text{-}roGFP2}$, NF54*attB*^{sfroGFP2}, and NF54*attB*$^{hGrx1\text{-}sfroGFP2}$. Therefore, the parasites were synchronized using sorbitol (**3.6.3**). Trophozoite-stage parasites were magnetically enriched (**3.6.4**) and diluted in Ringer's solution (**2.6.7**). To ensure that the same amount of parasites was used for the measurements, cells were counted using an improved Neubauer counting chamber (hemocytometer, Brand GmbH, Wertheim). 2.0x 10^6 parasites were added to each well of a 348-well microplate (F-bottom, small volume, black, Greiner

Bio-One, Frickenhausen) and fully reduced using 10 mM DTT or fully oxidized using 1 mM DIA. Recorded excitation ranged from 350 nm to 505 nm (with 1 nm resolution and 10 nm bandwidth) with emission at 530 ± 10 nm (Clariostar plate reader, BMG Labtech, Ortenberg, Germany). RFU were plotted against wavelength using GraphPadPrism 8.

3.7.1.2 *In cellulo* spectral scans of NF54*attB*$^{\text{mScarlet-I-SoNar}}$ and NF54*attB*$^{\text{mScarlet-I-iNap2}}$

Spectra were scanned using NF54*attB* parasites stably expressing mSc.-I.-SoNar or mSc.-I-iNap2, hereafter referred to as NF54*attB*$^{\text{mSc.-I-SoNar}}$ and NF54*attB*$^{\text{mSc.-I-iNap2}}$. Therefore, the parasites were synchronized using sorbitol (**3.6.3**). Trophozoite-stage parasites were magnetically enriched (**3.6.4**) and diluted in Ringer's solution or 1x PBS (**2.6.7**). Cells were counted using an improved Neubauer counting chamber (hemocytometer, Brand GmbH, Wertheim). 2.0x 10^6 parasites were filled into each well of a 348-well microplate (F-bottom, small volume, black, Greiner Bio-One, Frickenhausen). Recorded excitation ranged from 320 nm to 505 nm (with 1 nm resolution and 10 nm bandwidth), with emission at 530 ± 10 nm (Clariostar plate reader, BMG Labtech, Ortenberg, Germany). RFU were plotted against wavelength using GraphPadPrism 8.

3.7.2 *In cellulo* dynamics of NF54*attB*$^{\text{mScarlet-I-SoNar}}$ and NF54*attB*$^{\text{mScarlet-I-iNap2}}$

NF54*attB*$^{\text{mSc.-I-SoNar}}$ and NF54*attB*$^{\text{mSc.-I-iNap2}}$ parasites were synchronized using sorbitol (**3.6.3**). Trophozoite-stage parasites were magnetically enriched (**3.6.4**) and diluted in Ringer's solution (**2.6.7**). Cells were counted using an improved Neubauer counting chamber (hemocytometer, Brand GmbH, Wertheim). 2.0x 10^6 parasites were filled into each well of a 348-well microplate (F-bottom, small volume, black, Greiner Bio-One, Frickenhausen). Using a Clariostar plate reader (BMG Labtech, Ortenberg, Germany) pre-heated to 37 °C, emission at 530 ± 40 nm after excitation at 420 ± 15 nm and emission at 606 ± 20 nm after excitation at 563 ± 15 nm were measured over 96 sec. Thereafter, 8 mM oxamate was added to the wells containing NF54*attB*$^{\text{mSc.-I-SoNar}}$ and 160 µM DIA was added to the wells containing NF54*attB*$^{\text{mSc.-I-iNap2}}$. The ratio was measured over 30 min and subsequently, plotted against time using GraphPadPrism 8.

3.7.3 Plate reader detection

For plate reader detection, NF54*attB*$^{\text{hGrx1-sfroGFP2}}$ parasites were magnetically enriched as described above (**3.6.4**). Parasites were allowed to rest for two hours under normal culture conditions before being washed in Ringer's solution (**2.6.3**) and resuspended. The cell count was determined using an improved Neubauer hemocytometer (Brand GmbH, Wertheim). 2.0x 10^6 cells were transferred into each well of a 384-well plate (black, flat bottom, Greiner Bio-One, Frickenhausen). FI were measured using a Clariostar plate reader (BMG labtech) with $\lambda_{\text{Exc.}}$ of 405 nm and 485 nm, emission was detected at 510 nm. Gain was adjusted to reach the full dynamic range of the biosensors. For redox-measurements, fully oxidized (1 mM DIA) and fully reduced parasites (10 mM DTT) were used in addition to mock-treated control cells. The focal height was adjusted for each measurement, and the ratio was calculated by dividing both FI ($R = \frac{405\text{ nm}}{485\text{ nm}}$) and plotted using GraphPadPrism 8.

3.7.4 Flow cytometry detection

Flow cytometry measurements were carried out using a cytoFLEX S (Beckman Coulter, Krefeld) equipped with four different lasers (violet, blue, yellow, and red). An internal quality control was performed prior to each measurement using the CytoFLEX daily CQ fluorophores (Beckman Coulter, Krefeld). The following channels were used for measurements with various biosensors: KO525 ($\lambda_{\text{Exc.}}$ 405 nm, violet laser, $\lambda_{\text{Em.}}$ 525/40 BP), FITC ($\lambda_{\text{Exc.}}$488 nm, blue laser, $\lambda_{\text{Em.}}$ 525/40 BP), and PE ($\lambda_{\text{Exc.}}$ 488 nm, blue laser, $\lambda_{\text{Em.}}$ 585/42 BP). Gains were set to best distinguish the fluorescence signals from the sensors from the intrinsic fluorescence of the parasites. Different combinations of forward scatter (FSC) area, width and height, and sideward scatter (SSC) area, width and height were used to exclude duplicates. Polygons were set manually to define the fluorescence range of the sensors. For pretests, magnetically enriched NF54*attB*$^{\text{hGrx1-sfroGFP2}}$ parasites were used. The amount of parasites measured was set using CytExpert software and the previously set sensor-positive polygons. Within a measurement series, the number of parasites measured remained unchanged. However, the number of measured cells varied between different measurement series from 1,000–100,000 cells per measurement. For the final measurements, whole cell-cultures with 10% HK in complete medium (2.6.3) were used. For short- and mid-term incubations, sorbitol-synchronized trophozoite-stage parasites were used. Long-term incubations (24 h) were started with sorbitol-synchronized ring-stage parasites. After 24 h, measurements were performed with trophozoite-stage parasites. Therefore, a suitable amount of culture was transferred to a 96-well plate (microplate, 96-well, V-bottom. natural, Greiner Bio-One, Frickenhausen) and treated with different antimalarials or compounds. The final DMSO concentration was 1%. Mock treated (DMSO or H_2O) cells were used as a control. The sensor-positive fluorescence regions were defined and separated from the fluorescence regions representing intrinsic fluorescence of the parasites or RBCs. To ensure that the settings do not change due to using different antimalarials or compounds, parasites without biosensor were treated with different substances to check whether the intrinsic fluorescence of the parasites changed due to the treatment. Using statistics settings of the CytExpert program, the median FI for all channels were output and used to calculate the ratios. A scatter plot with bars was plotted using GraphPadPrism 8, showing mean and error bars indicated as SD.

Moreover, the glutathione-dependent redox potential could be determined using equation 6.

$$E_{\text{roGFP2}} = E'^{\text{pH}}_{0(\text{roGFP2})} - \frac{2.303\,RT}{zF}\log_{10}\frac{(1-\text{OxD}_{\text{roGFP2}})}{\text{OxD}_{\text{roGFP2}}} \qquad \text{Eq. 6}$$

Here *R* is the gas constant (8.315 J K^{-1} mol^{-1}); *T* is the absolute temperature (310.45 K); *z* is the number of transferred electrons (2), and *F* represents the Faraday constant (96,485 C mol^{-1}).

4. RESULTS

4.1 sfroGFP2 as an improved redox-biosensor

The previously published redox-biosensor sfroGFP2–which differs from roGFP2 in the substitution of seven amino acids–showed improved spectral properties over commonly used roGFP2 variants when used *in cellulo* [Schuh et al. 2018]. Within this work, the molecular basis of these improved properties should be identified. To study the impact of selected superfolding mutations on the functional and structural properties of sfroGFP2, specific superfolding mutations were reversed, namely S30R, Y39N, and F223R. Successful mutations and thus generation of sfroGFP2^{R30S}, sfroGFP2^{N39Y}, and sfroGFP2^{R223F} were confirmed via sequencing. Further redox-biosensor variants (roGFP2, hGrx1-roGFP2, and hGrx1-sfroGFP2) were produced heterologously to perform comparative functional investigations.

4.1.1 Heterologous overexpression and purification of redox-biosensor variants

Recombinant hGrx1-roGFP2 was produced according to [Kasozi et al. 2013]. Recombinant sfroGFP2 and hGrx1-sfroGFP2 were produced as described in [Schuh et al. 2018].

To identify ideal expression conditions for all other redox-biosensor variants used within this work, test expressions were performed. For this purpose, different expression media, temperatures, and expression durations were tested. Numerous *E. coli* cells or expression vectors were not tested as sufficiently good expression conditions were quickly identified. Western blot analysis was used to compare the results of the test expressions and to select the best expression conditions. Since the redox-sensor variants are based on GFP, good expression conditions could already be detected optically due to a yellowish coloration of the *E. coli* pellets.

Recombinant roGFP2 was produced using *E. coli* M15 cells and the pQE30 expression vector, resulting in a 6xHis-tagged protein. Therefore, Ni-NTA could be used as column material for purification based on affinity chromatography. Additionally, size exclusion chromatography was used to improve the purity of the recombinant protein. A representative Coomassie gel of roGFP2 after affinity chromatography is shown in **Figure 15**. Imidazole concentrations of 100 mM and above were used for elution of the protein of interest. Small amounts of roGFP2 eluted even at lower imidazole concentrations. In these fractions, however, the level of impurities was too high. Therefore, these elution fractions were usually not used.

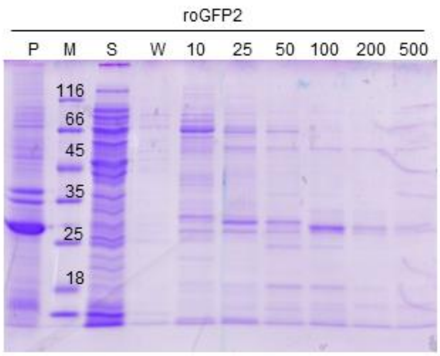

Figure 15. SDS-gel of a purification of roGFP2. Ni-NTA affinity chromatography was used to purify roGFP2. A 12% SDS-gel after Coomassie staining is shown. M = marker, size indicated in kDa; P = pellet; S = supernatant; W = wash fraction; the numbers above the gel indicate imidazole concentrations in mM. Molecular weight of roGFP2 = 27 kDa.

The best expression conditions to produce recombinant sfroGFP2^{R30S}, sfroGFP2^{N39Y}, and sfroGFP2^{R223F} could be achieved using *E. coli* M15 cells and the pQE30 expression vector, respectively. The recombinant proteins were purified using Ni-NTA affinity chromatography followed by size exclusion chromatography. A combination of both purification methods increased the purity of the proteins. Imidazole concentrations of 50 mM and above could be used to eluate sfroGFP2^{R30S}. Elution of sfroGFP2^{N39Y} already started at an imidazole concentration of 25 mM; however, in this fraction, the amount of impurities was quite high. Therefore, this elution fraction was usually not included. Imidazole concentrations of 75 mM and above were used to elute sfroGFP2^{R223F}. Representative Coomassie gels of sfroGFP2^{R30S}, sfroGFP2^{N39Y}, and sfroGFP2^{R223F} after affinity chromatography are shown in **Figure 16.**

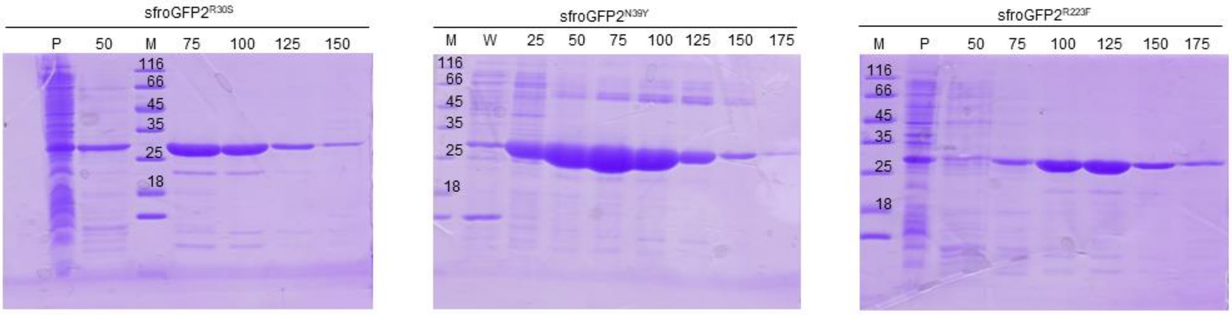

Figure 16. SDS-gel of sfroGFP2^{R30S}, sfroGFP2^{N39Y}, and sfroGFP2^{R223F} purified by Ni-NTA affinity chromatography. A 12% SDS-gel after Coomassie staining is shown. M = marker, size indicated in kDa; P = pellet; W = wash fraction; the numbers above the gel indicate imidazole concentrations in mM. Molecular weight of sfroGFP2^{R30S}, sfroGFP2^{N39Y}, and sfroGFP2^{R223F} = 27 kDa.

For subsequent structural studies of hGrx1-sfroGFP2, two mutants were generated in which the resolving cysteines of hGrx1 (C26) and sfroGFP2 (C147 or C204) were mutated to serine, thus abolishing the sensors operating principle. After successful generation of hGrx1-sfroGF2$^{C26S\text{-}C147S}$ and hGrx1-sfroGF2$^{C26S\text{-}C204S}$ in the pET28a(+) expression vector using site-directed mutagenesis, both proteins could be expressed heterologously using *E. coli* BL21 cells. The N-terminal 6xHis-tag was used for purification via affinity chromatography with Ni-NTA. Imidazole concentrations of 100 mM and above were used for elution of hGrx1-sfroGFP2$^{C26S\text{-}C147S}$. 50 mM imidazole could already be used to elute hGrx1-sfroGFP2$^{C26S\text{-}C204S}$. However, this elution fraction was usually not included as the level of impurities was too high. After affinity chromatography, size exclusion chromatography was used to increase the purity of both proteins. Representative gels of hGrx1-sfroGF2$^{C26S\text{-}C147S}$ and hGrx1-sfroGF2$^{C26S\text{-}C204S}$ after purification via affinity chromatography are shown in **Figure 17**.

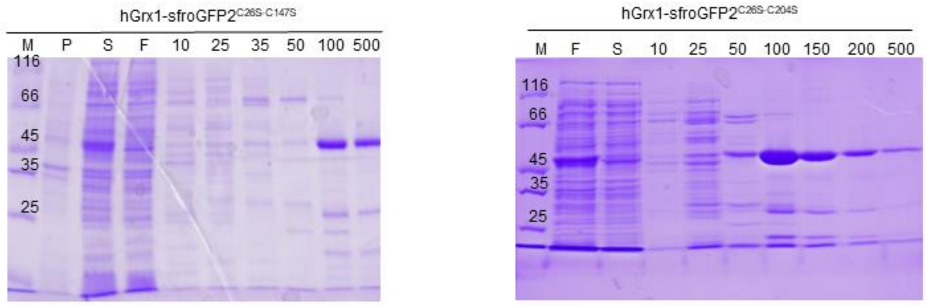

Figure 17. SDS-gel of hGrx1-sfroGFP2$^{C26S\text{-}C147S}$ and hGrx1-sfroGFP2$^{C26S\text{-}C204S}$ purified by Ni-NTA affinity chromatography. A 12% SDS-gel after Coomassie staining is shown. M = marker, size indicated in kDa; P = pellet; S = supernatant; F = flow through; the numbers above the gel indicate imidazole concentrations in mM. Molecular weight of hGrx1-sfroGFP2$^{C26S\text{-}C147S}$ and hGrx1-sfroGFP2$^{C26S\text{-}C204S}$ = 48 kDa.

All proteins used within this work were stored at 4 °C for up to two weeks. For long-term storage, the proteins were kept at -20 C°. Usage of additives to increase the stability of the proteins during storage was not necessary. Prior storage of the proteins was avoided if the proteins were used for crystallization approaches. Here, the proteins were used as soon as possible after the purification process.

4.1.2 *In vitro* characterization of recombinant redox-biosensor variants

To study sfroGFP2 properties, various redox-biosensor variants were functionally characterized *in vitro* in parallel. *In vitro* spectral scans were recorded to examine differences in the spectral behavior of the variants. Furthermore, the influence of different temperatures and the environment surrounding the sensors on spectral properties was investigated. For this purpose, spectral scans were recorded at around 10 °C and 37 °C. In addition to buffer, the recombinant sensors were further equilibrated in parasite cell extract. To ensure that the introduction of various superfolding mutations would not result in any adverse sensor characteristics, the pH response of the biosensors was investigated *in vitro* using buffers with various pH values. Additionally, redox titration was used to calculate the midpoint potential of the different biosensor variants.

4.1.2.1 Spectral scans of redox-biosensor variants

Spectral excitation and emission scans were recorded with recombinant biosensors equilibrated in buffer. The biosensor variants were fully oxidized (1 mM DPS) and fully reduced (10 mM DTT) prior to measurements. The spectral excitation scan for each sensor showed two major excitation peaks (**Figure 18**). With these, typical dual excitation behavior could be seen for all investigated redox-biosensor variants. For oxidized biosensors, a prominent peak was seen near 405 nm. A peak at around 485 nm was also visible. However, the height of the peak at 485 nm was increased for all reduced biosensors, which is typically for all redox-biosensors containing the S65T mutation (**Figure 18**). The emission spectral scans showed a single emission peak at around 510 nm after excitation at 405 nm (**Figure 19**) and after excitation at 485 nm (**Figure 20**) for all redox-biosensor variants. The excitation and emission patterns were comparable between the different sensors. However, slight differences could be seen in the isosbestic point (λ_{iso}). sfroGFP2 and sfroGFP2-based biosensors showed an isosbestic point at around 415 nm and thereby at a slightly lower wavelength than roGFP2 and roGFP2-based biosensors. Here, the isosbestic point was at about 422 nm (**Figure 18**). The FI at 405 nm for oxidized proteins and 485 nm for reduced proteins are summarized in **Table 4**. Comparing the FI between roGFP2 and sfroGFP2 showed a higher FI for roGFP2 than sfroGFP2 *in vitro*. Moreover, hGrx1-roGFP2 showed higher FI *in vitro* than hGrx1-sfroGFP2. Both biosensors, however, showed higher FI than the non-fused sensors roGFP2 and sfroGFP2. The sfroGFP2 mutants sfroGFP2^{R30S}, sfroGFP2^{N39Y}, and sfroGFP2^{R223F} showed FI similar to roGFP2. In comparison, the FI of sfroGFP2^{R30S} and sfroGFP2^{R223F} were even slightly higher (**Table 4, Figure 18**).

One difference between *in vitro* and *in cellulo* measurements is the temperature at which measurements are normally performed. To study the impact of a higher temperature on the spectral properties, spectral excitation and emission scans were recorded with recombinant redox-biosensors equilibrated in buffer preheated to 37 °C. Furthermore, the plate reader was heated to 37 °C, thus mimicking the conditions needed when performing measurements with *P. falciparum* parasites. At a higher temperature, the expected dual excitation behavior was visible (**Figure 18,** curves indicated with triangles). No changes in excitation and emission patterns, the position of peaks, and the isosbestic point were seen compared to measurements carried out at around 10 °C (**Figure 18, Figure 19, and Figure 20**). When comparing the FI between both measurements, a decrease in FI was detected for roGFP2 and hGrx1-roGFP2, for the measurement carried out at 37 °C (**Table 4**). Additionally, sfroGFP2 showed a slightly lower FI for the measurement at 37 °C. For this biosensor, the difference in FI between both measurements was, however, not as large. hGrx1-sfroGFP2 was the only sensor showing an increase in FI with rising measurement temperature for all measuring points considered (**Table 4**). Looking at the FI of the sfroGFP2 mutants, certain differences were recognizable. The FI of sfroGFP2^{R30S} at 405 nm for oxidized protein decreased slightly with higher temperature. However, for reduced protein at 485 nm, an increase in FI with higher temperature was visible. The FI of sfroGFP2^{N39Y} decreased slightly with higher temperature. The temperature-dependent decrease in FI of sfroGFP2^{R223F} was comparable to the decrease in FI for roGFP2 (**Table 4**).

Table 4. Fluorescence intensities of recombinant redox-biosensor variants equilibrated in buffer.

	***In vitro* (buffer)**			
Redox-biosensor	**Excitation ~10 °C**		**Excitation 37 °C**	
	$FI_{ox405nm}$	**$FI_{red485nm}$**	**$FI_{ox405nm}$**	**$FI_{red485nm}$**
roGFP2	24,947 ± 1,054	100,381 ± 2,899	22,366 ± 266	81,752 ± 609
hGrx1-roGFP2	55,045 ± 883	206,913 ± 3,459	47,590 ± 1,949	184,455 ± 5,934
sfroGFP2	15,646 ± 385	87,256 ± 6,528	14,925 ± 1,082	87,140 ± 5,089
hGrx1-sfroGFP2	31,398 ± 1,236	165,471 ± 1,913	41,981 ± 2,594	203,630 ± 2,127
sfroGFP2^{R30S}	34,719 ± 1,037	156,353 ± 6,884	34,548 ± 796	14,1394 ± 3,837
sfroGFP2^{N39Y}	19,852 ± 1,173	99,369 ± 5,847	18,250 ± 1,210	96,653 ± 7,312
sfroGFP2^{R223F}	29,190 ± 1,725	159,928 ± 9,153	22,797 ± 5,676	135,577 ± 4,084

$FI_{405ox.}$ = fluorescence intensity of oxidized sensors at 405 nm; $FI_{485red.}$ = fluorescence intensity of reduced sensors at 485 nm; FI are indicated in relative fluorescence units (RFU). Means ± SD are shown.

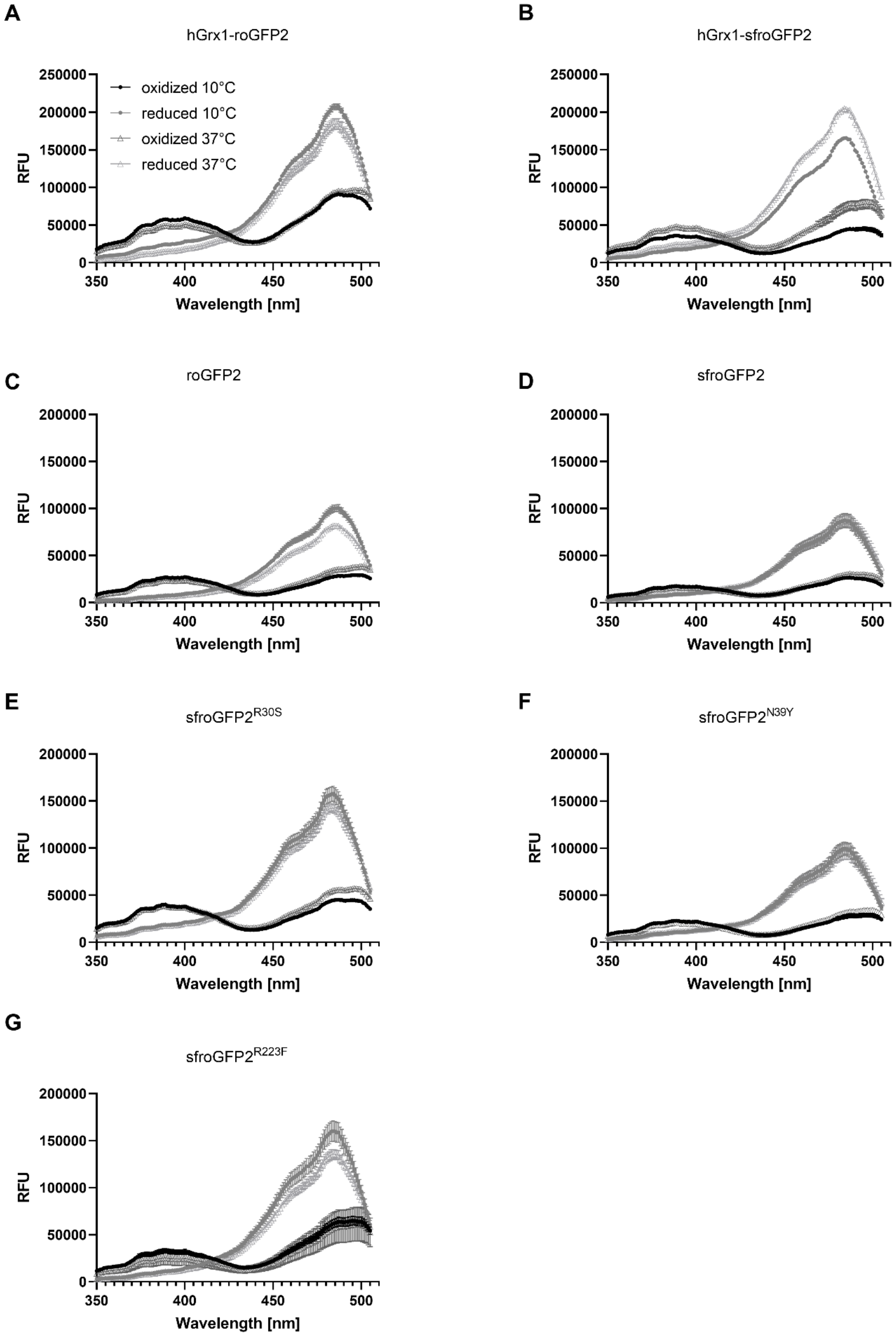

Figure 18. *In vitro* spectral excitation scans of various redox-biosensor variants. Spectral excitation scans were recorded at around 10 °C (circles) and 37 °C (triangles) for oxidized (1 mM DPS) (black/ dark grey) and reduced (10 mM DTT) (light grey) hGrx1-roGFP2 (**A**), hGrx1-sfroGFP2 (**B**), roGFP2 (**C**), sfroGFP2 (**D**),sfroGFP2^{R30S} (**E**), sfroGFP2^{N39Y} (**F**), and sfroGFP2^{R223F} (**G**), respectively. All biosensor variants showed typical dual excitation behavior. Means ± SD are shown. RFU = relative fluorescence units.

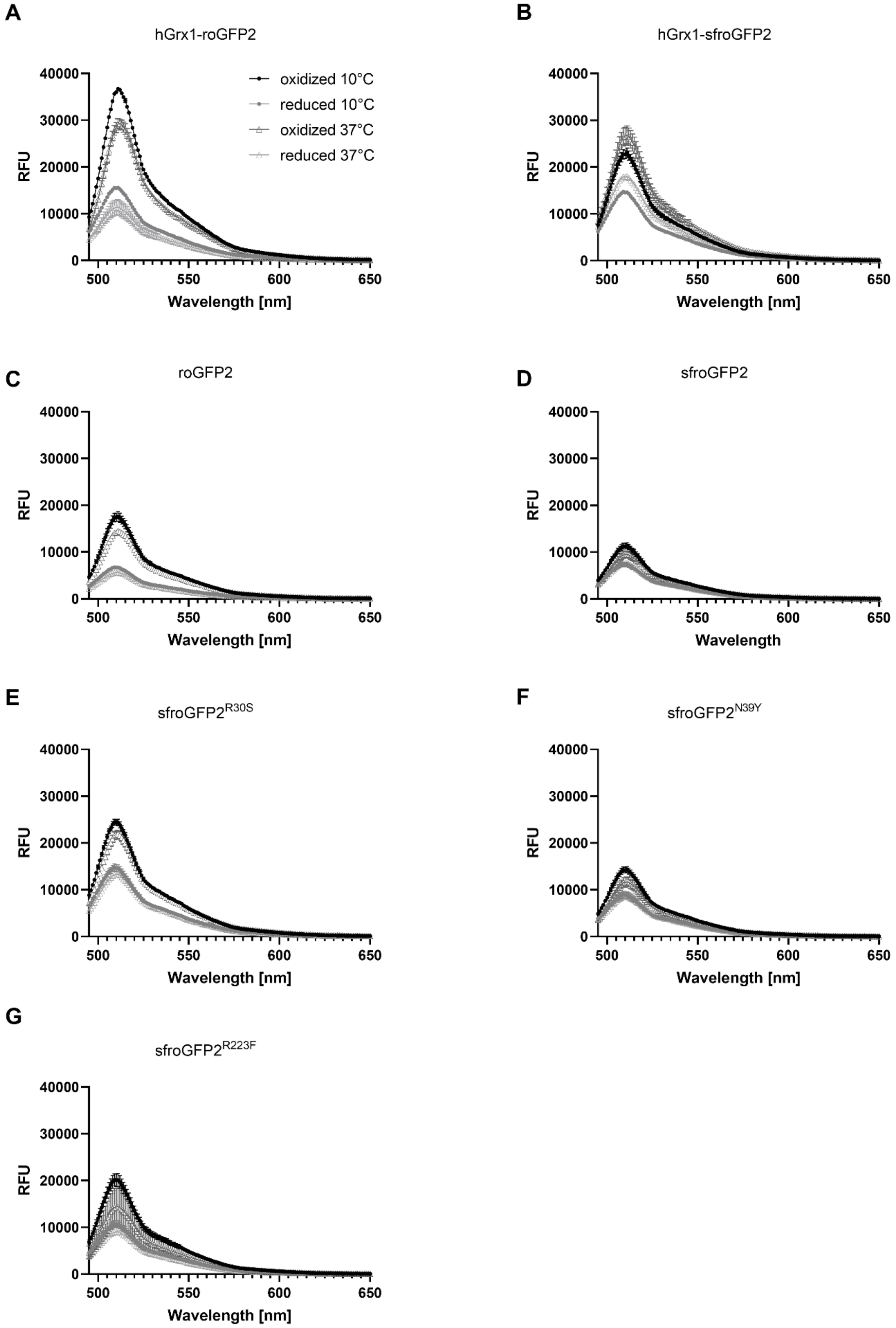

Figure 19. *In vitro* spectral emission scans after excitation at 405 nm of various redox-biosensor variants. Spectral emission scans after excitation at 405 nm were recorded at around 10 °C (circles) and 37 °C (triangles) for oxidized (1 mM DPS) (black/ dark grey) and reduced (10 mM DTT) (light grey) hGrx1-roGFP2 (**A**), hGrx1-sfroGFP2 (**B**), roGFP2 (**C**), sfroGFP2 (**D**), sfroGFP2^{R30S} (**E**), sfroGFP2^{N39Y} (**F**), and sfroGFP2^{R223F} (**G**), respectively. The expected single emission peak at 510 nm was visible for all biosensors investigated. Means ± SD are shown. RFU = relative fluorescence units.

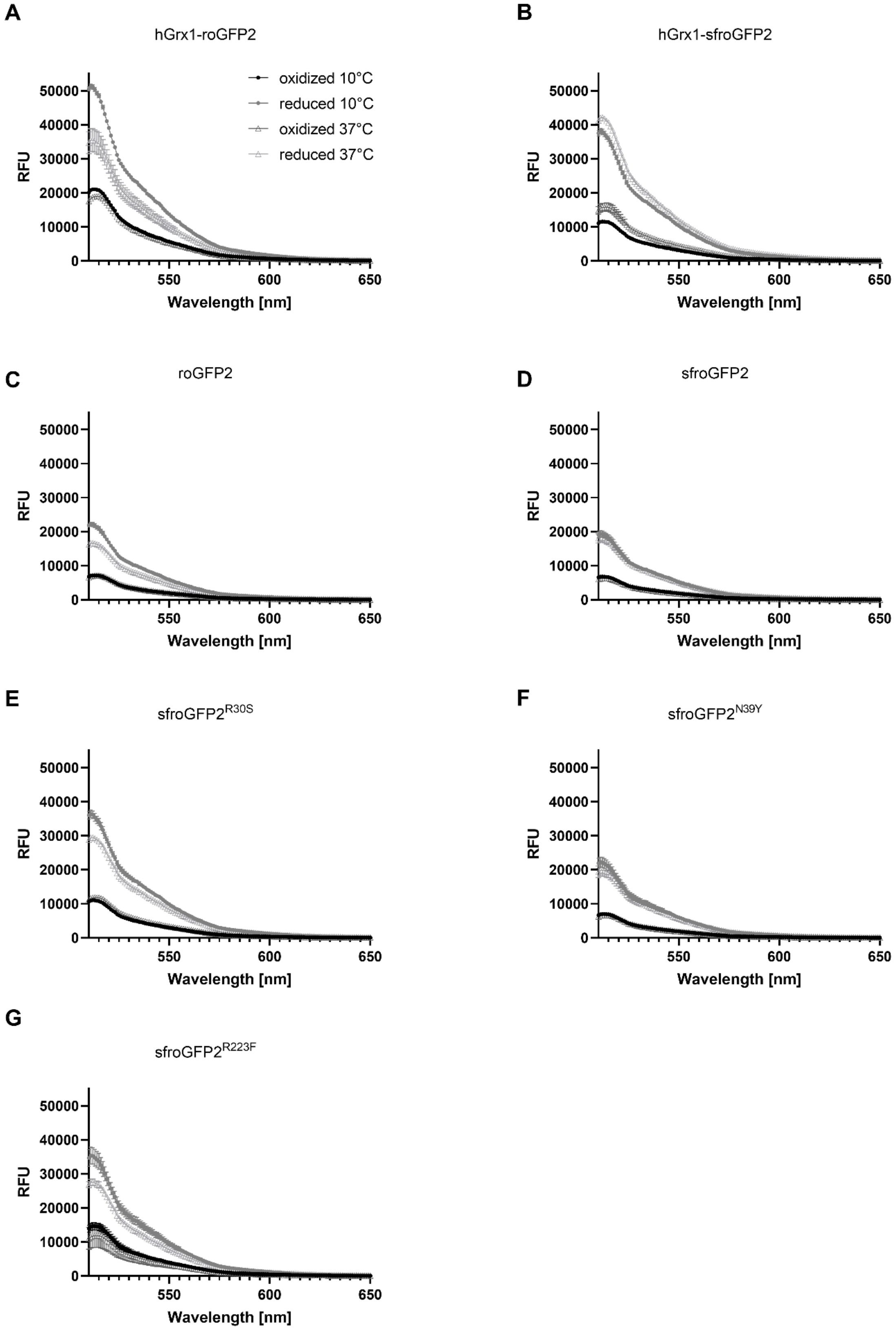

Figure 20. *In vitro* spectral emission scan after excitation at 485 nm of various redox-biosensor variants. Spectral emission scans after excitation at 485 nm were recorded at around 10 °C (circles) and 37 °C (triangles) for oxidized (1 mM DPS) (black/ dark grey) and reduced (10 mM DTT) (light grey) hGrx1-roGFP2 (**A**), hGrx1-sfroGFP2 (**B**), roGFP2 (**C**), sfroGFP2 (**D**), sfroGFP2^{R30S} (**E**), sfroGFP2^{N39Y} (**F**), and sfroGFP2^{R223F} (**G**), respectively. Due to technical measurement conditions, a better representation of the emission peak at 510 nm was not possible. Means ± SD are shown. RFU = relative fluorescence units.

To determine, whether potential protein-protein interactions occurring within the parasites could affect the FI of the redox-biosensors, spectral excitation scans were recorded with recombinant redox-biosensors equilibrated in parasite cell extract using non-transfected NF54*attB* parasites. The biosensors were fully oxidized (1 mM DPS) and fully reduced (10 mM DTT). The excitation pattern, position of peaks, and the position of the isosbestic point remained unchanged (**Figure 21**).

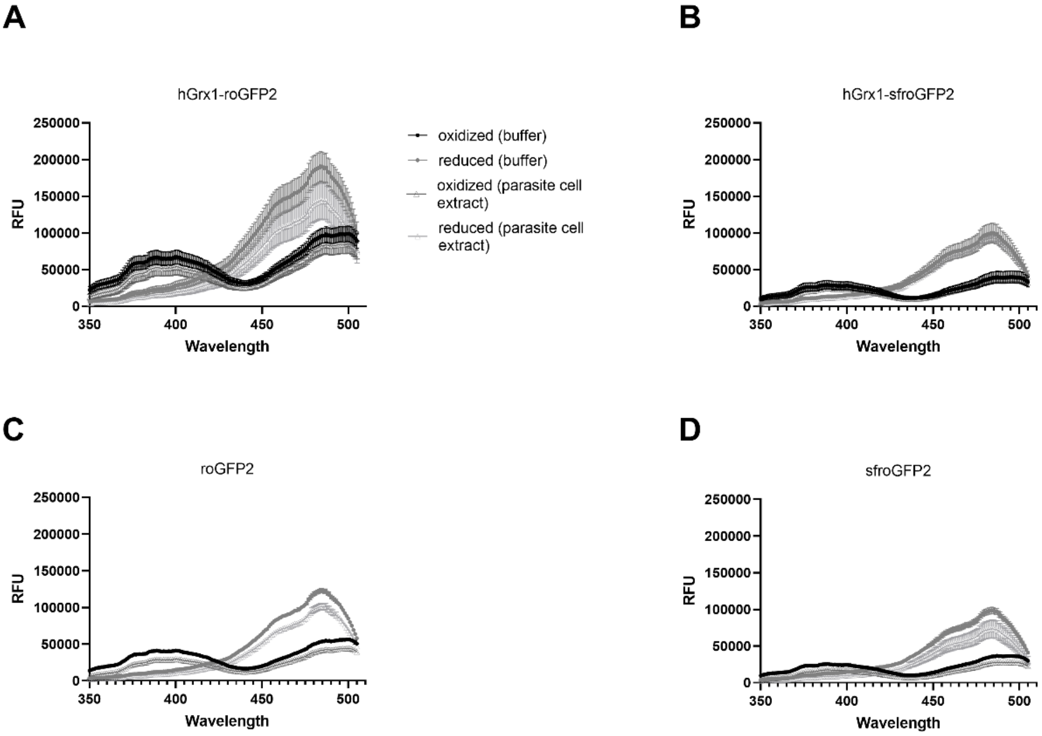

Figure 21. Spectral excitation scans of recombinant redox-biosensor variants equilibrated in parasite cell extract. Recombinant hGrx1-roGFP2 (**A**), hGrx1-sfroGFP2 (**B**), roGFP2 (**C**), and sfroGFP2 (**D**) were equilibrated in parasite cell extract (triangles). In comparison, excitation scans were recorded with recombinant protein equilibrated in buffer (circles). Means ± SD are shown. RFU = relative fluorescence units.

Table 5. Fluorescence intensities of recombinant redox-biosensors equilibrated in parasite cell extract.

	***In vitro* (parasite cell extract)**	
Redox-biosensor	**Excitation ~10 °C**	
	$FI_{ox405nm}$	$FI_{red485nm}$
roGFP2	27,697 ± 589	101,193 ± 4,227
hGrx1-roGFP2	50,992 ± 10,264	143,908 ± 25,027
sfroGFP2	15,740 ± 198	73,256 ± 12,122
hGrx1-sfroGFP2	22,054 ± 718	92,522 ± 4,195

$FI_{405ox.}$ = fluorescence intensity of oxidized sensors at 405 nm; $FI_{485red.}$ = fluorescence intensity of reduced sensors at 485 nm; FI are indicated in relative fluorescence units (RFU). Means ± SD are shown.

However, the FI rather tended to decrease for all redox-biosensors equilibrated in parasite cell extract (**Table 5**) compared to the measurements performed using buffer (**Table 4**). An improvement in FI of sfroGFP2 due to protein-protein interactions can therefore be excluded.

4.1.2.2 pH response of redox-biosensor variants

To test whether the superfolding mutations changed the pH response of the redox-biosensors, ratios ($R = \frac{405\ \text{nm}}{485\ \text{nm}}$) were calculated after equilibration of the biosensor variants in buffers with pH values varying between pH 5.0 and 9.0. This was performed for fully oxidized (1 mM DPS) and fully reduced (10 mM DTT) biosensors. In a range from 6.0 to 8.0, the pH did not affect the ratios of all biosensors (**Figure 22**). At acidic pH values below pH 6.0, only a minor effect started to become apparent. This, therefore, confirmed that pH insensitivity was retained in the different redox-biosensor variants.

4.1.2.3 Determination of the redox-biosensor variants' midpoint potential

Redox titration was performed with all redox-biosensor variants to determine the midpoint potential of each sensor. Therefore, the DTT/dithiane system was used. Based on the Nernst equation (**eq. 2**), the relationship between DTT and dithiane was calculated, which is needed to adjust specific redox potentials. Subsequently, the different redox-biosensor variants were allowed to equilibrate in buffers with various redox potentials. Moreover, all sensor variants were fully oxidized (1 mM DPS) and fully reduced (10 mM DTT). The OxD was calculated for each measuring point, and the midpoint potential was determined based on a sigmoidal dose-response curve. In this work, the midpoint potential of roGFP2 could be determined to be -280.03 mV and is thus in accordance with different publications [Dooley et al. 2004; Hanson et al. 2004; Meyer and Dick 2010]. The different superfolding mutations did not change the midpoint potential of the sensor to any major extent (**Figure 23**). The midpoint potential of sfroGFP2 was -283.6 ± 0.5 mV and is therefore only slightly more negative than the midpoint potential of roGFP2. The midpoint potentials of hGrx1 fusion and the other sensor variants are only slightly more negative, with -287.1 ± 0.4 mV for hGrx1-roGFP2, -285.8 ± 0.4 mV for hGrx1-sfroGFP2, -283.9 ± 0.2 mV for sfroGFP2^{R30S}, -286.8 ± 0.7 mV for sfroGFP2^{N39Y}, and -284.8 ± 0.4 mV for sfroGFP2^{R223F}.

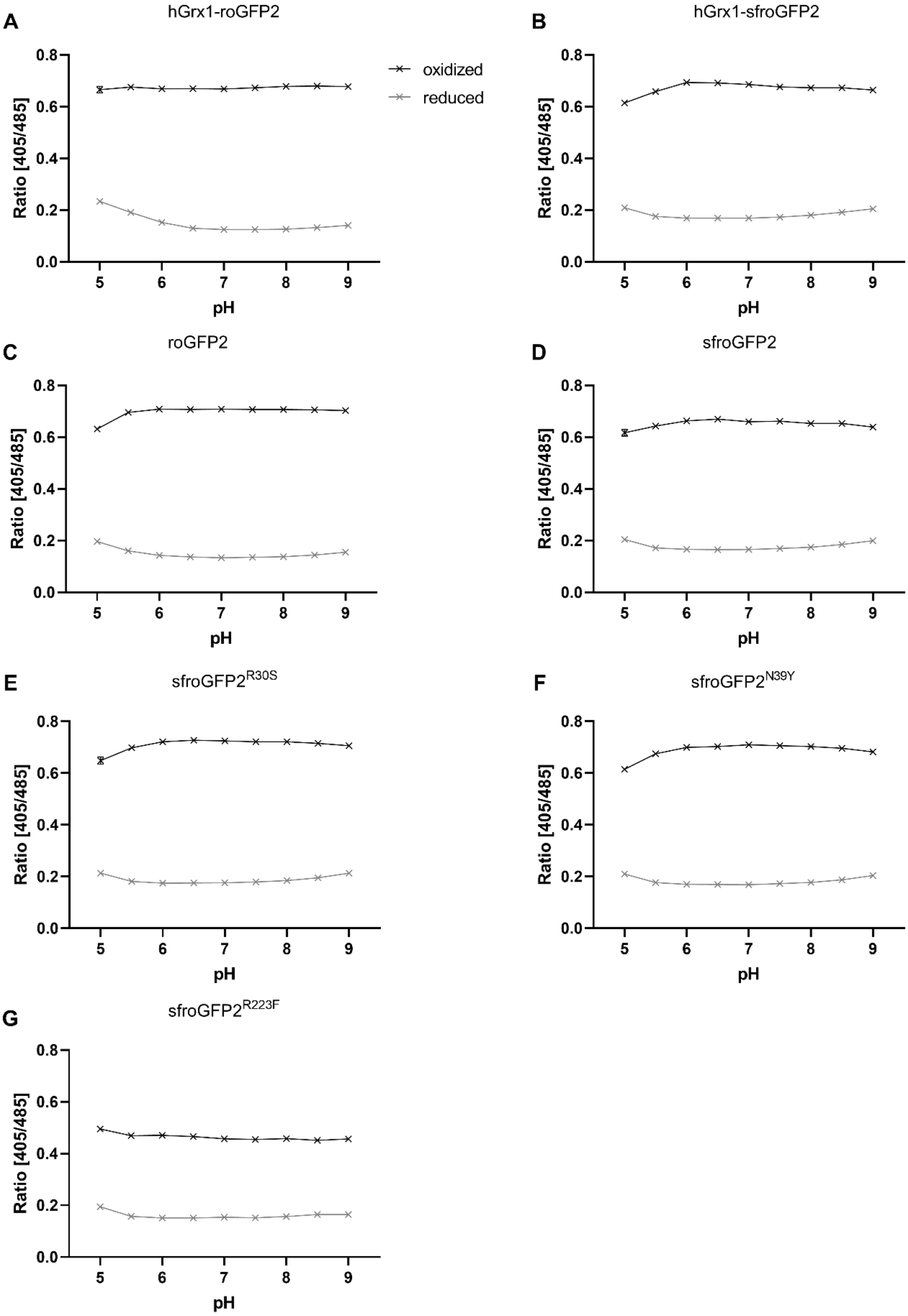

Figure 22. pH response of various redox-biosensor variants. pH dependencies of hGrx1-roGFP2 (**A**), hGrx1-sfroGFP2 (**B**), roGFP2 (**C**), sfroGFP2 (**D**), sfroGFP2^{R30S} (**E**), sfroGFP2^{N39Y} (**F**), and sfroGFP2^{R223F} (**G**) were determined using buffers with pH values ranging from 5.0 to 9.0. The ratio (R = $\frac{405\ \text{nm}}{485\ \text{nm}}$) was measured for fully oxidized biosensors (1 mM DPS) (black) and fully reduced biosensors (10 mM DTT) (grey). Means ± SD are shown.

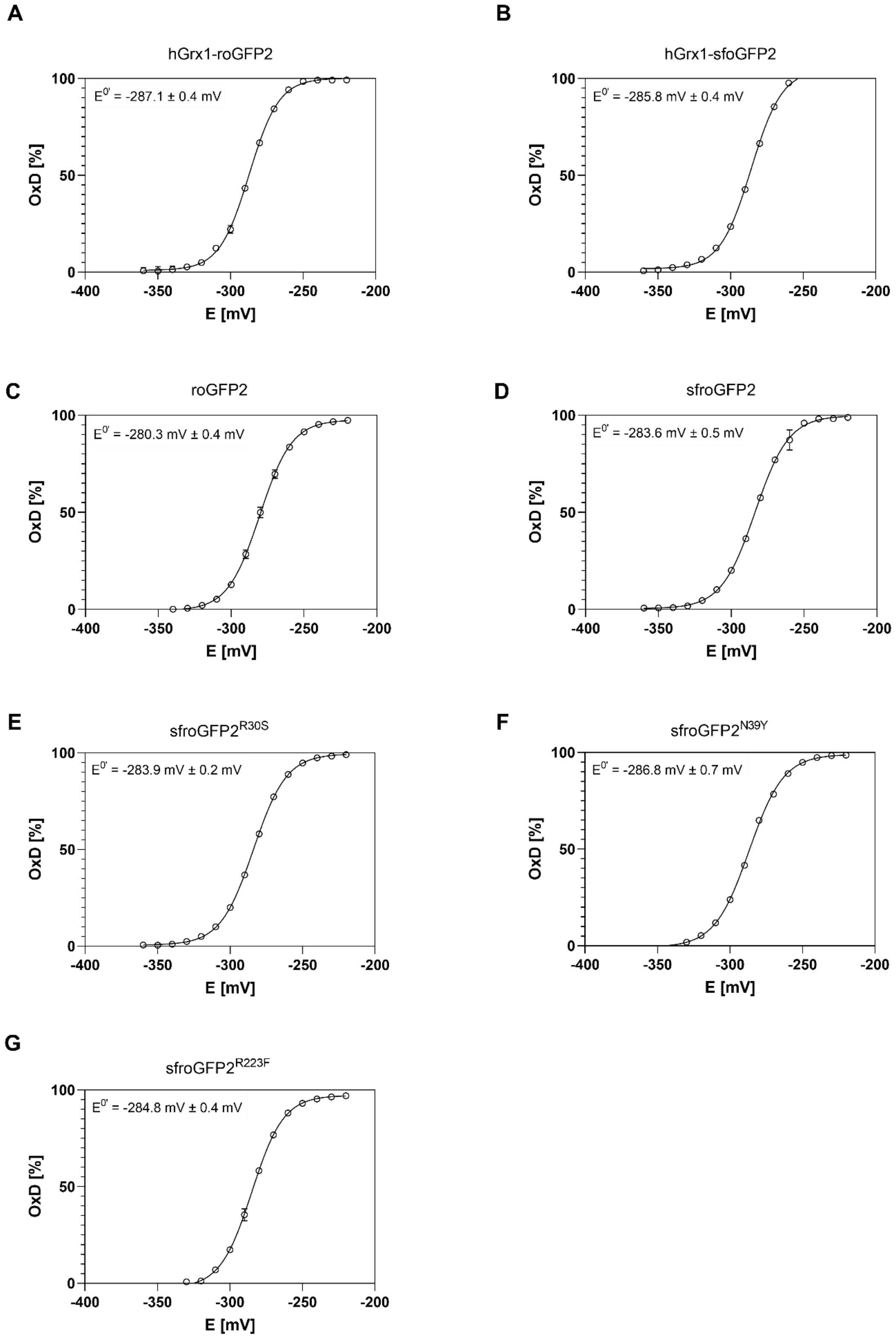

Figure 23. Redox titration of various redox-biosensor variants. Various redox potentials were adjusted using the DTT/dithiane system. Redox-biosensor variants were equilibrated in buffers with various redox potentials and in addition, fully oxidized (1 mM DPS) and fully reduced (10 mM DTT). OxD was calculated according to equation 2 and plotted against redox-potential using GraphPadPrism 8. (**A**) The midpoint potential of hGrx1-roGFP2 was - 287.1 ± 0.4 mV. (**B**) The midpoint potential of hGrx1-sfroGFP2 was -285.8 ± 0.4 mV. (**C**) The midpoint potential of roGFP2 was -280.03 ±0.4 mV. (**D**) The midpoint potential of sfroGFP2 was -283.6 mV ± 0.5 mV. (**E**) The midpoint potential of sfroGFP2^{R30S} was -283.9 mV ± 0.2 mV. (**F**) The midpoint potential of sfroGFP2^{N39Y} was -286.8 ± 0.7 mV (**G**) The midpoint potential of sfroGFP2^{R223F} was -284.8 ± 0.4 mV. Means ± SD are shown.

4.1.2.4 Dynamic change in ratio of recombinant redox-biosensor variants

The dynamic change in the ratio after oxidation and reduction was examined with recombinant roGFP2, hGrx1-roGFP2, sfroGFP2, and hGrx1-sfroGFP2. The ratio was first measured basally over time. Then, DIA was added to oxidize the sensors, and the ratio was again measured over time. Subsequently, DTT was added to reduce the biosensors. The ratio was again measured over time. The initial ratios of all investigated sensors were comparable. After adding DIA, the ratio increased for all redox-biosensor variants. This increase in ratio was in a comparable range, with roGFP2 showing the strongest increase and hGrx1-roGFP2 showing the slightest increase. Adding DTT led to a reduction in the ratio of all redox-biosensor variants. The initial ratio could almost be reached again (**Figure 24**).

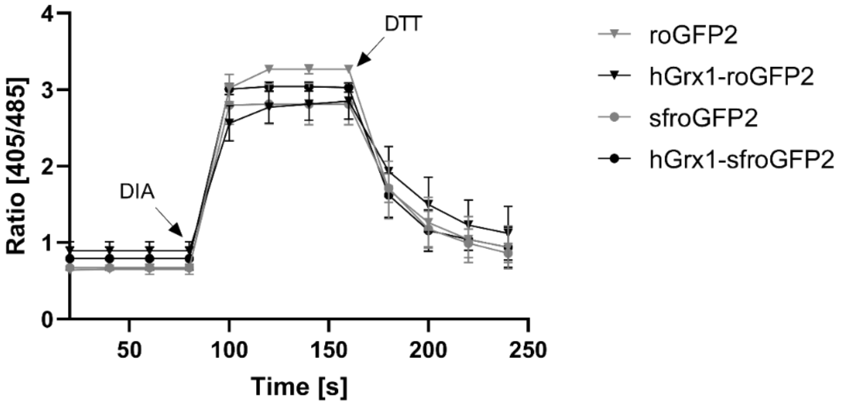

Figure 24. Dynamic change in ratio of different redox-biosensor variants. The ratios of roGFP2, hGrx1-roGFP2, sfroGFP2, and hGrx1-sfroGFP2 were monitored basally for 80 sec. 1 mM DIA was added to fully oxidize the sensors. Immediately after adding DIA, the ratio increased. After adding 10 mM DTT, the ratio decreased and almost assumed the initial value. Means ± SD are shown.

4.1.2.5 Direct interaction of recombinant hGrx1-sfroGFP2 with compounds and antimalarial drugs

The redox-biosensor hGrx1-sfroGFP2 was used for *in cellulo* studies with *P. falciparum* parasites. To differentiate between pharmacological effects of antimalarial drugs on the parasites' glutathione-dependent redox potential and direct interactions of drugs with the redox-biosensor, *in vitro* interaction studies with recombinant hGrx1-sfroGFP2 and certain antimalarial drugs and compounds were performed. Therefore, different antimalarials and compounds were diluted and equilibrated with the recombinant redox-biosensor, which was pre-reduced using DTT. DTT was removed prior to measurements. In addition to the antimalarial drugs, the biosensor was equilibrated with DIA, DTT, and DMSO. Biosensor equilibrated just in buffer without any additions was used as a control. The biosensors redox ratio ($R = \frac{405\text{ nm}}{485\text{ nm}}$) was measured after 5 min, 4 h, and 24 h incubation. The plate was incubated at 37 °C to mimic temperature conditions needed for *in cellulo* measurements. After 5 min incubation, an increase in ratio can be seen for hGrx1-sfroGFP2 incubated with 1 mM DIA, 10% DMSO, 1 mM MB, as well as different concentrations of GSH and

GSSG (**Figure 25A**). After 4 h (**Figure 25B**) and 24 h incubation (**Figure 25C**), the highest concentration of most of the tested antimalarial drugs and compounds led to an increase in ratio. The strongest effects were seen here for CQ, MB, PD, BSO, H_2O_2, and DOXY. Lower and therefore more physiologically relevant concentrations did not change the redox ratio compared to the control.

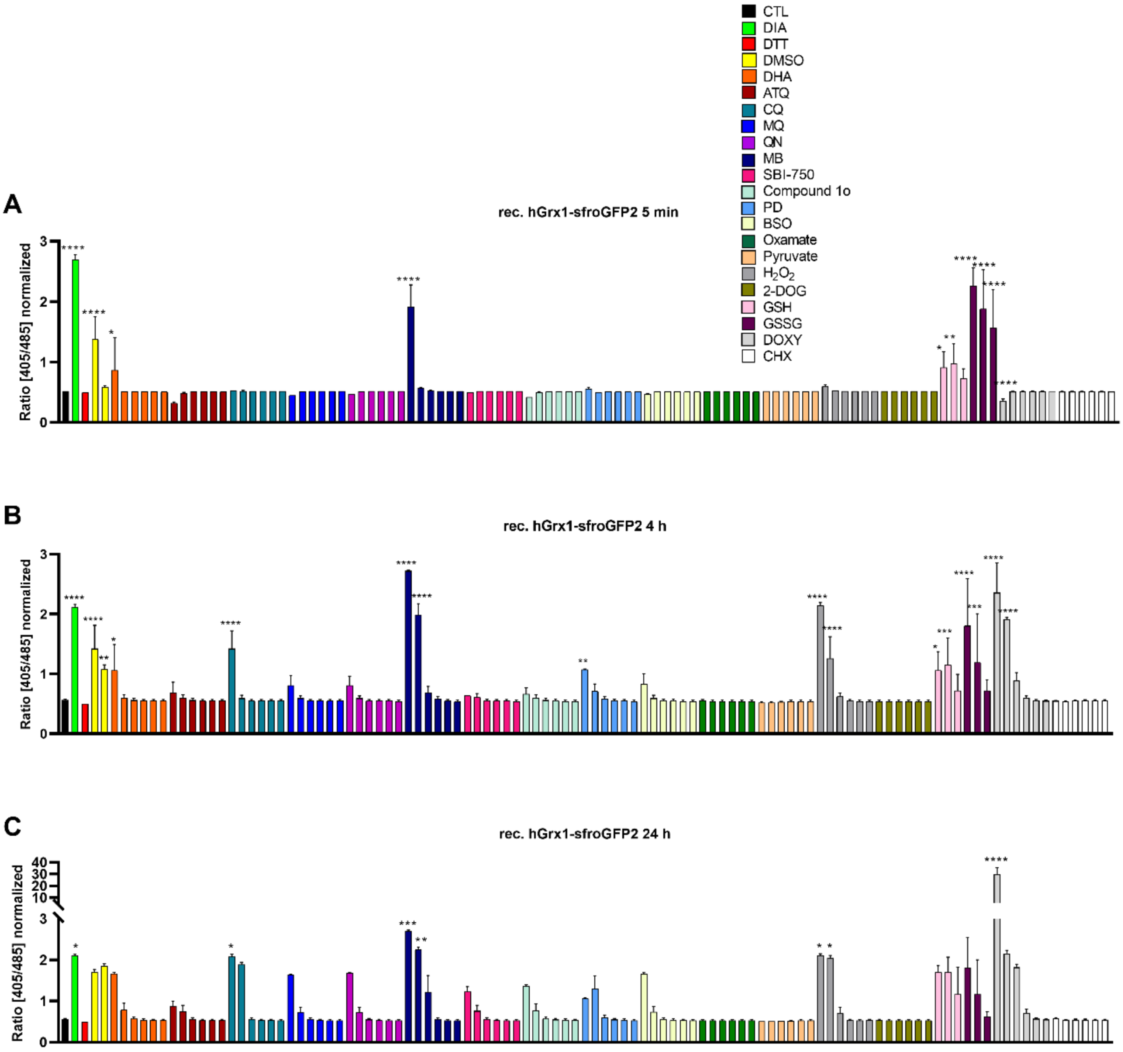

Figure 25. Direct interaction of antimalarial drugs and compounds with recombinant hGrx1-sfroGFP2. Recombinant hGrx1-sfroGFP2 was pre-reduced using 10 mM DTT for 45 min. Prior to measurements, DTT was removed again. The redox ratio was measured after 5 min incubation of hGrx1-sfroGFP2 with different antimalarial agents and compounds (**A**), after 4 h incubation (**B**), and after 24 h incubation (**C**). The measured concentrations are shown in decreasing order of magnitude (1 mM, 100 µM, 10 µM, 1 µM, 100 nM, and 10 nM). Oxamate, pyruvate, and 2-DOG were tested in the following concentrations: 10 mM, 1 mM, 100 µM, 10 µM, 1 µM, 100 nM). DMSO was tested in a concentration of 10% and 5%. Means ± SD are shown for three independent experiments. A one-way ANOVA test with 95% confidence intervals with the Dunnett's multiple comparison test was applied for statistical analysis of significance (*, $p < 0.05$; **, $p < 0.01$; ***, $p < 0.001$; ****, $p < 0.0001$). CTL = control, DIA = diamide, DTT = dithiothreitol, DHA = dihydroartemisinin. ATQ = atovaquone, CQ = chloroquine, MQ = mefloquine, QN = quinine, MB = methylenblue, PD = plasmodione, BSO = buthionine sulphoximine, 2-DOG = 2-dioxygluocose, GSH = reduced glutathione, GSSG = oxidized glutathione, DOXY = doxycycline, CHX = cycloheximinde.

4.1.3 *In cellulo* characterization of redox-biosensor variants

4.1.3.1 Comparison of in cellulo spectral scans of NF54*attB*$^{hGrx1\text{-}roGFP2}$, NF54*attB*^{sfroGFP2}, and NF54*attB*$^{hGrx1\text{-}sfroGFP2}$

Spectral excitation scans were recorded with NF54*attB P. falciparum* parasites stably expressing one of the following redox-biosensor variants: hGrx1-roGFP2, sfroGFP2, or hGrx1-sfroGFP2. For this purpose, trophozoite-stage NF54*attB*$^{hGrx1\text{-}roGFP2}$, NF54*attB*^{sfroGFP2}, and NF54*attB*$^{hGrx1\text{-}sfroGFP2}$ parasites were magnetically enriched. Redox-biosensors were fully reduced by treating the parasites with 10 mM DTT and were fully oxidized by treating the parasites with 1 mM DIA. Subsequently, spectral excitation scans were recorded. All parasite lines showed the expected dual excitation behavior with excitation maxima at around 405 nm for fully oxidized parasites and 485 nm for fully reduced parasites (**Figure 26**). Comparison of the FI showed higher FI for NF54*attB*^{sfroGFP2} and NF54*attB*$^{hGrx1\text{-}sfroGFP2}$ than NF54*attB*$^{hGrx1\text{-}roGFP2}$ (**Table 6**). The FI of NF54*attB*^{sfroGFP2} and NF54*attB*$^{hGrx1\text{-}sfroGFP2}$ were more than double than of NF54*attB*$^{hGrx1\text{-}roGFP2}$. This data confirms previously published results [Schuh et al. 2018]; however, it contrasts *in vitro* examinations (**4.1.2.1**).

Table 6. Fluorescence intensities of NF54*attB*$^{hGrx1\text{-}roGFP2}$, NF54*attB*^{sfroGFP2}, and NF54*attB*$^{hGrx1\text{-}sfroGFP2}$.

	In cellulo	
	Excitation 37 °C	
Redox-biosensor	**$FI_{ox405nm}$**	**$FI_{red485nm}$**
hGrx1-roGFP2	541 ± 110	3,072 ± 405
sfroGFP2	1,209 ± 410	11,549 ± 3,693
hGrx1-sfroGFP2	954 ± 184	9,599 ± 1,085

$FI_{405ox.}$ = fluorescence intensity of oxidized sensors at 405 nm; $FI_{485red.}$ = fluorescence intensity of reduced sensors at 485 nm; FI are indicated in relative fluorescence units (RFU). Means ± SD are shown.

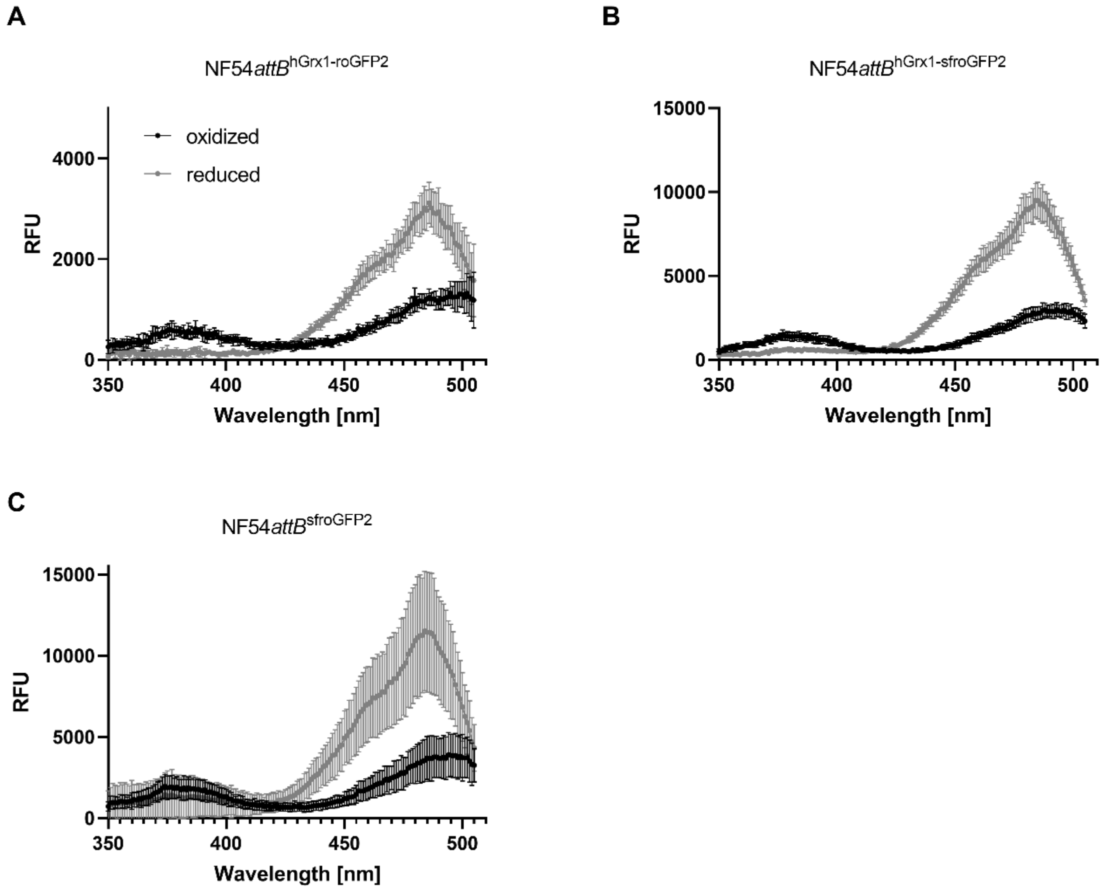

Figure 26. ***In cellulo*** **spectral excitation scans of NF54*attB*$^{\text{hGrx1-roGFP2}}$, NF54*attB*$^{\text{hGrx1-sfroGFP2}}$, and NF54*attB*$^{\text{sfroGFP2}}$.** Spectral excitation scans were recorded using magnetically enriched trophozoite-stage NF54*attB*$^{\text{hGrx1-roGFP2}}$ parasites (**A**), NF54*attB*$^{\text{hGrx1-sfroGFP2}}$ parasites (**B**), and NF54*attB*$^{\text{sfroGFP2}}$ parasites (**C**). The biosensors were fully oxidized by treating the parasites with 1 mM DIA and fully reduced by treating them with 10 mM DTT. Means ± SD are shown. RFU = relative fluorescence units.

4.1.3.2 *In cellulo* expression levels of NF54*attB*$^{\text{hGrx1-roGFP2}}$, NF54*attB*$^{\text{sfroGFP2}}$, and NF54*attB*$^{\text{hGrx1-sfroGFP2}}$

Western blot analysis was performed to examine the expression levels of the different redox-biosensors to exclude increased expression levels to be responsible for higher FI of sfroGFP2 and hGrx1-sfroGFP2, than hGrx1-roGFP2 *in cellulo*. Expression of redox-biosensor variants was verified using an anti-GFP AB. Bands with the expected size were visible in each case (Figure 27). Moreover, anti-PfHSP70 AB was used as a loading control. Bands with the expected size are detectable for every sample. Band intensities after anti-GFP Western blot analysis were normalized to the loading control and compared using Fiji [Schindelin et al. 2012]. The band intensity of the determined redox-biosensor variants differed between the NF54*attB*$^{\text{hGrx1-roGFP2}}$ and NF54*attB*$^{\text{sfroGFP2}}$ samples by -2.3% ± 11.2%. The difference in band intensity between the samples NF54*attB*$^{\text{hGrx1-roGFP2}}$ and NF54*attB*$^{\text{hGrx1-sfroGFP2}}$ was -28.7% ± 20.8%. In general, expression levels between the cell lines only differed slightly, with NF54*attB*$^{\text{hGrx1-roGFP2}}$ showing the highest expression level. As such increased protein concentrations did not appear to be responsible for the improved *in cellulo* performance of the sensor.

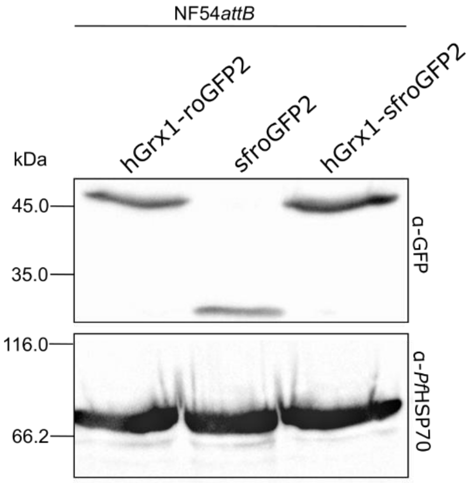

Figure 27. Expression levels of hGrx1-roGFP2, sfroGFP2, and hGrx1-sfroGFP2 in NF54*attB P. falciparum* parasites. Anti-GFP AB was used to detect the different biosensor variants. Anti-PfHSP70 AB was used as a loading control. The background was subtracted using the rolling ball algorithm. The contrast was enhanced by 0.01%. Band intensities were adjusted to the loading control and compared between parasite lines using Fiji [Schindelin et al. 2012; Heimsch et al. 2022].

4.1.4 Structural elucidation of sfroGFP2 variants and hGrx1-sfroGFP2

The *in vitro* examinations carried out within this work showed a different result than *in cellulo* examinations. The functional characterization did not point to the reason for the improved FI of sfroGFP2 *in cellulo* either. To examine the influence of structural stability on the biosensors' properties, structural examinations were therefore carried out.

4.1.4.1 Crystallization of sfroGFP2^{R30S}

For the crystallization of sfroGFP2^{R30S}, the recombinantly produced protein was purified and subsequently concentrated to 30 mg/ml. Different crystallization screens (see **2.9**) were used, to find conditions that enabled the crystallization of sfroGFP2^{R30S}. An ideal crystallization condition was identified using 10% polyethylene glycol (PEG) 6,000, 30% ethanol, and 100 mM sodium acetate. After one day, crystals appeared at RT (**Figure 28**).

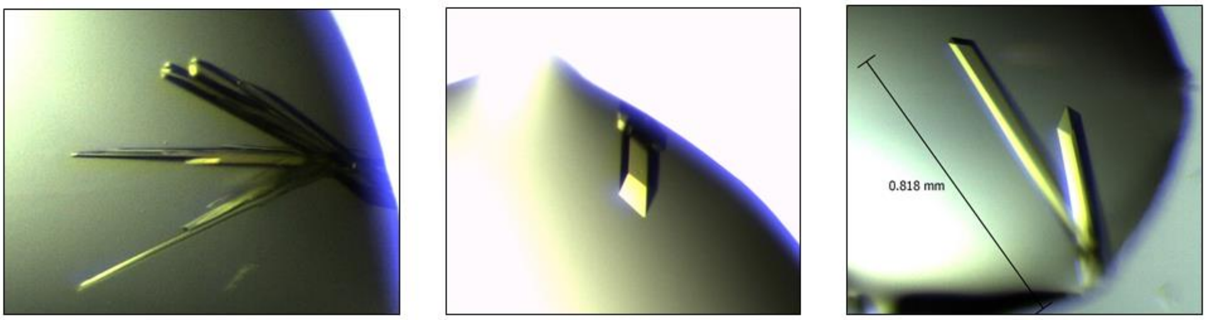

Figure 28. Crystals of native sfroGFP2^{R30S}. Crystals of native sfroGFP2^{R30S} grown in the sitting drop approach. 30 mg/ml sfroGFP2^{R30S}, 10% PEG 6,000, 30% ethanol, 100 mM sodium acetate. Due to the natural coloration, the protein crystals could be easily distinguished from salt crystals. The best crystal diffracted to a resolution of 1.35 Å.

The x-ray crystal structure was solved with a resolution of 1.35 Å. The solution of the structure was achieved via molecular replacement. The sfroGFP2^{R30S} monomer shows the typical GFP fold consisting of an eleven-stranded β-barrel with an inner α-helix. The latter contains the covalently bound chromophore, a 4-(p-hydroxybenzylidene)-imidazolidin-5-one.

4.1.4.2 Crystallization of sfroGFP2^{N39Y}

Numerous crystallization screens listed in **2.9** were used to find conditions that enabled the crystallization of sfroGFP2^{N39Y}. The protein was recombinantly produced, purified, and subsequently concentrated to 30 mg/ml. Ideal crystallization conditions could be identified using the in-house crystallization screen PEG2 (**2.9**). Crystals grew using 30% PEG 4,000. Crystals appeared after five days at RT (**Figure 29**).

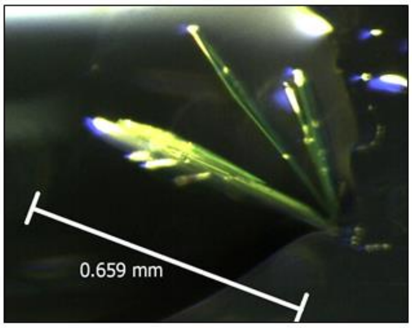

Figure 29. Crystals of native sfroGFP2^{N39Y}. Crystals of native sfroGFP2^{N39Y} grown in the sitting drop approach, 30 mg/ml sfroGFP2^{N39Y}, 30% PEG 4,000. Due to the natural coloration, the protein crystals could be easily distinguished from salt crystals. The best crystal diffracted to a resolution of 2.0 Å.

Further optimization of these crystallization conditions was not necessary, as the crystals diffracted to a resolution of 2.0 Å. The structure was solved via molecular replacement. The typical GFP fold consisting of the β-barrel and the inner α-helix was seen here as well.

4.1.4.3 Crystallization of sfroGFP2^{R223F}

After expression and purification of sfroGFP2^{R223F}, the protein was concentrated to 30 mg/ml. Various crystallization screens (**2.9**) were used to find conditions that enable the crystallization of sfroGFP2^{R223F}. Some conditions led to the generation of crystals (**Figure 30**). However, the best crystals generated in this work diffracted only to a resolution of 8.0 Å, which was not good enough to solve the three-dimensional structure. The initial conditions were optimized by varying the precipitant and protein concentrations (15 mg/ml to 45 mg/ml) in 24-well plates using both the hanging drop and sitting drop approaches. Even these efforts did not generate crystals with a sufficiently good quality. Taken together, it has so far not been possible to solve the three-dimensional structure of sfroGFP2^{R223F}.

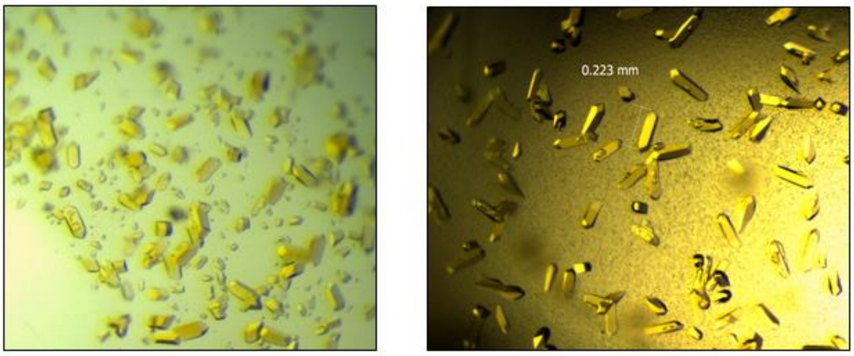

Figure 30. Crystals of native sfroGFP2^{R223F}. Crystals of native sfroGFP2^{R223F} grown in the handing drop approach only diffracted to a resolution of 8.0 Å.

4.1.4.4 Crystallization of hGrx1-sfroGFP2

The proximity-based redox-biosensor hGrx1-sfroGFP2 should be crystallized in order to solve its three-dimensional structure. For this purpose, the recombinantly produced protein was purified and concentrated. Different crystallization screens (2.9) were used to identify conditions that enabled the protein to crystallize. Various protein concentrations (15 mg/ml to 60 mg/ml) were tested. However, none of the tested conditions led to the crystallization of the protein of interest. The flexible structure of the sensor, which consists of hGrx1 and sfroGFP2 connected by a linker, was presumably too unstable to allow crystallization of the protein. To increase the stability of the fusion sensor, the resolving cysteine of hGrx1 (C26), and the redox-active cysteines of sfroGFP2 (C147 and C204) were mutated to serine, one at a time. The proteins hGrx1-sfroGF2$^{C26S\text{-}C147S}$ and hGrx1-sfroGF2$^{C26S\text{-}C204S}$ were both used for further crystallization approaches. Prior to this, the proteins were glutathionylated to increase intramolecular stability through association with glutathione. Again, the different crystallization screens were used to find suitable conditions for crystallization.

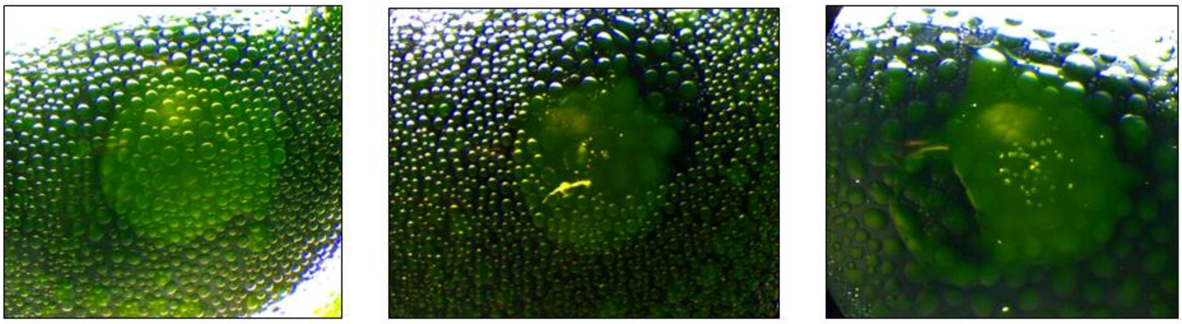

Figure 31. Crystallization approaches of native hGrx1-sfroGFP2. Crystallization approaches of native hGrx1-sfroGFP2 via the hanging drop method in a 24-well plate. Phase separation could be achieved, but no protein crystals occurred.

However, this did not lead to the formation of a protein crystal. Phase separation was observed in some crystallization approaches (**Figure 31**). However, even further variation of these initial conditions did not lead to the crystallization of the protein of interest. In summary, it has so far not been possible to crystallize hGrx1-sfroGFP2.

4.1.4.5 Structural comparison of sfroGFP2 and mutants

The structures were studied to identify potential differences between sfroGFP2 and other commonly used redox-biosensors that could provide an explanation for the improved spectral properties of this variant *in cellulo* since it was hypothesized that the improved FI of sfroGFP2 could be due to improved structural stability of the protein, which resulted from certain superfolding mutations.

Based on the x-ray crystal structure of sfroGFP2 [Schuh 2021; Heimsch et al. 2022] the two superfolding mutations S30R and Y39N [Pédelacq et al. 2006] were identified to be of particular interest as they lead to novel interactions between adjacent β-strands. In this structure, residues R30 and N39 formed hydrogen bonds to D19 and D36, respectively (**Figure 32**). In comparison, these interactions do not occur in roGFP2 (PDB 1JC1 and 1JC0). The F223R mutation in sfroGFP2, which was introduced in accordance with roTurbo [Dooley et al. 2012] probably does not interact with other amino acids, as R223 points towards the solvent phase (**Figure 32**). An effect on the x-ray structure in sfroGFP2^{R223F} was therefore not expected.

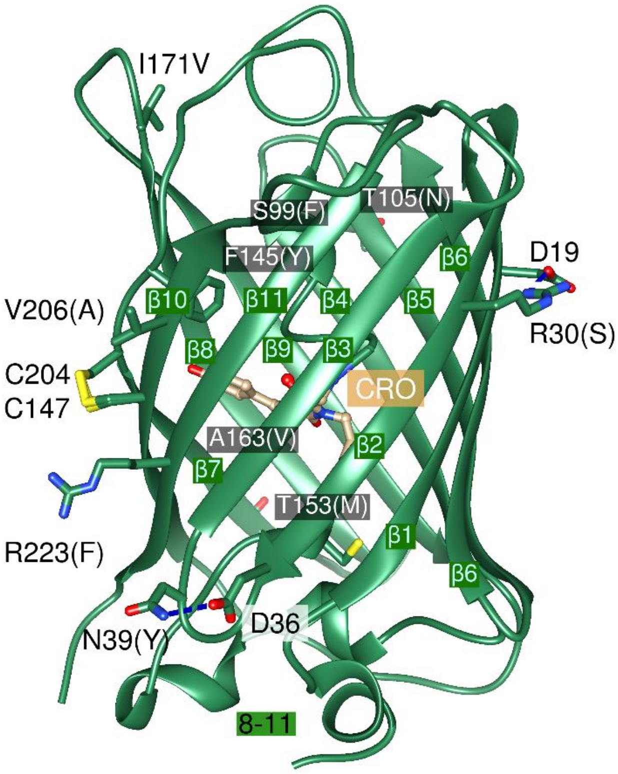

Figure 32. Structure of sfroGFP2. The model of sfroGFP2 was solved via molecular replacement. The protein crystal diffracted to a resolution of 1.1 Å. The two cysteines C147 and C204 formed a disulfide bridge (represented in yellow). All sf mutations and the redox-related cysteine mutations are labeled. The letters in brackets indicates the amino acids in the original roGFP2. The N- and C-termini are labeled with capital letters. The chromophore is shown in orange, CRO = chromophore. [Schuh 2021; Heimsch et al. 2022].

Comparing the sfroGFP2 structure and the structures of sfroGFP2^{R30S} and sfroGFP2^{N39Y} revealed differences at the N-terminus and in the location of a surface loop (8-11) (**Figure 33**). Since this region is involved in monomer–monomer interactions it is probably not relevant for the stability of the sfroGFP2 structure.

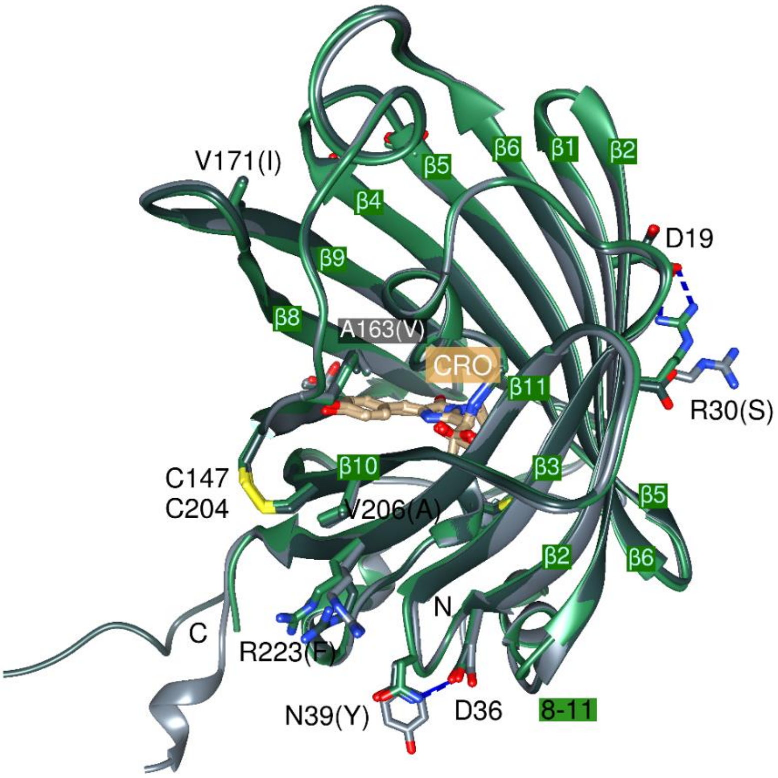

Figure 33. Comparison between the structural models of sfroGFP2 (green), sfroGFP2^{R30S} (dark grey), and sfroGFP2^{N39Y} (grey). All structures were solved by molecular replacement. All sf mutations and the redox-related cysteine mutations are labeled. The letter in brackets indicates the amino acids in the original roGFP2 protein. The N- and C-termini are labeled with capital letters. The chromophore is shown in orange, CRO = chromophore. Furthermore, the individual β-strands are labeled. The main structural differences between the three variants occur at the N-terminus and in the loop region 8-11, labeled in green [Heimsch et al. 2022].

In the sfroGFP2 structure, the amino acid R30 is located centrally on the β2-strand interacting with D19 from the neighboring strand (β1). Here, a bond between E17 (β1) and R122 (β6) connected strand β6 to β1. Moreover, strands β5 and β6 are connected with a salt bridge formed from R122 to E115 (β5). Furthermore, E111 (β5) and K113 (β5) from the same strand are connected with a bond. As a result, the strands β1, β2, β5, and β6 are connected via a network of ionic interactions, resulting in an ion pair network in the vicinity of R30 (**Figure 34**). Additionally, in the sfroGFP2 structure, the amino acid N39 interacts with D36 through a hydrogen bond (**Figure 33**).

In the sfroGFP2^{R30S} structure, the much smaller side chain of the S30 in comparison to R30 is no longer able to interact with residues D19 (β1) or E32 (β2), instead, S30 is hydrogen-bonded to E17 (β1). Here, compared to the sfroGFP2 structure, the E17 side chain adopts a completely different conformation. As a result, R122 (β6) is no longer able to connect strands β1 and β6 (**Figure 34**).

The sfroGFP2^{N39Y} structures contain four monomers in the asymmetric unit. Here, the side chain of R30 (β2) adopts different conformations in the subunits, thereby interacting with E32 (β2) or E17 (β1). In two of the four sfroGFP2^{N39Y} monomers, R122 (β6) also interacts with E17 (β1) and not just with E115 (β5), as seen in sfroGFP2 (**Figure 34**). The amino acid Y39 in sfroGFP2^{N39Y} no longer interacts with D36 (β2), as it points into the solvent (**Figure 33**).

Additional differences in the structure occurred in the chromophore region. In both sfroGFP2^{R30S} and sfroGFP2^{N39Y} structures, the chromophore was shifted slightly within the barrel by about 0.2 Å and 0.3 Å, respectively compared to the sfroGFP2 structure. However, this shift was not significant as the coordinate errors are almost as large.

As described above, larger structural differences between the three variants (sfroGFP2, sfroGFP2^{R30S}, and sfroGFP2^{N39Y}) appear in the network of ionic interactions. Here, the most complex ion network is formed in sfroGFP2, which can indeed potentially improve the structural stability of this redox-biosensor.

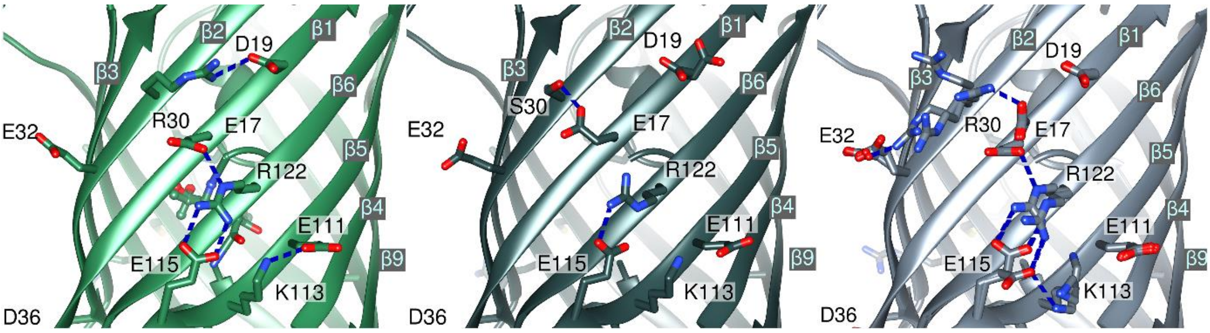

Figure 34. Close-up comparison of the structural models of sfroGFP2 (green), sfroGFP2^{R30S} (dark grey), and sfroGFP2^{N39Y} (grey). Comparison of the surrounding of R30 in sfroGFP2 and sfroGFP2^{N39Y} or S30 in the structure of sfroGFP2^{R30S}. Differences in the network of ionic interactions are visible. Individual β-strands are labeled. CRO = chromophore [Heimsch et al. 2022].

4.2 mScarlet-I-SoNar and mScarlet-I-iNap2 as biosensors for NADH:NAD$^+$ and NADPH

4.2.1 *In vitro* characterization of recombinant mScarlet-I-SoNar and mScarlet-I-iNap2

In preliminary work, certain functional *in vitro* characterizations of recombinant mScarlet-I-SoNar and mScarlet-I-iNap2 had already been carried out. Spectral properties, pH response at pH values ranging from pH 5.0 to pH 9.0, and specificity analysis with lower nucleotide concentrations are therefore published elsewhere [Krickeberg 2020].

4.2.1.1 pH response of recombinant mScarlet-I-SoNar and mScarlet-I-iNap2

Previously performed experiments showed an improved pH response of recombinant SoNar and iNap2 when fused to mScarlet-I [Krickeberg 2020]. Nevertheless, pH-dependent changes in ratio between pH 7.0 to pH 9.0 were visible. To study the pH response of the two sensors in this specific range in more detail, pH responses were monitored in small steps between pH 6.5 and pH 9.0. As shown in **Figure 35A** the fluorescence ratio of mSc.-I-SoNar, calculated with the actual sensor internal wavelengths ($R = \frac{420\text{ nm}}{485\text{ nm}}$), decreased drastically with rising pH values. This was the case when the sensor was equilibrated with either NAD$^+$ or NADH. In comparison, using the mScarlet-I wavelength instead of the pH-dependent 485 nm wavelength to calculate the ratio ($R = \frac{420\ nm}{569\ nm}$), it was much more stable and less susceptible to changes in pH (**Figure 35B**).

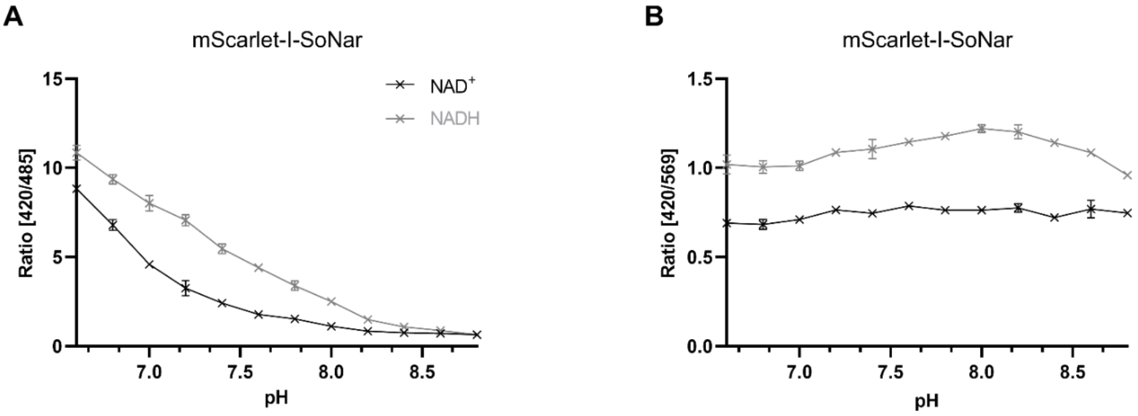

Figure 35. pH response of recombinant mScarlet-I-SoNar. (**A**) Sensor internal excitation wavelengths were used to detect emission at 510 nm. The ratio was calculated as $R = \frac{420\ nm}{485\ nm}$. (**B**) The pH-dependent 485 nm excitation wavelength was replaced with the excitation wavelength of mScarlet-I at 569 nm. The ratio was therefore calculated as $R = \frac{420\ nm}{569\ nm}$. Here, a more stable pH response is visible. Means ± SD are shown.

This effect could also be seen for mSc.-I-iNap2. The ratio drastically decreased with rising pH when calculated with the internal sensor wavelengths ($R = \frac{420\ nm}{485\ nm}$) (**Figure 36A**). In comparison, the ratio was more stable when calculating the ratio as follows: $R = \frac{420\ nm}{569\ nm}$. However, the ratio of mSc.-I-iNap2 equilibrated with NADPH was not completely unaffected by changes in pH (**Figure 36B**). Though, the ratio was quite stable between pH 7.5 and pH 8.0. Above a pH of 8.0, the ratio decreased.

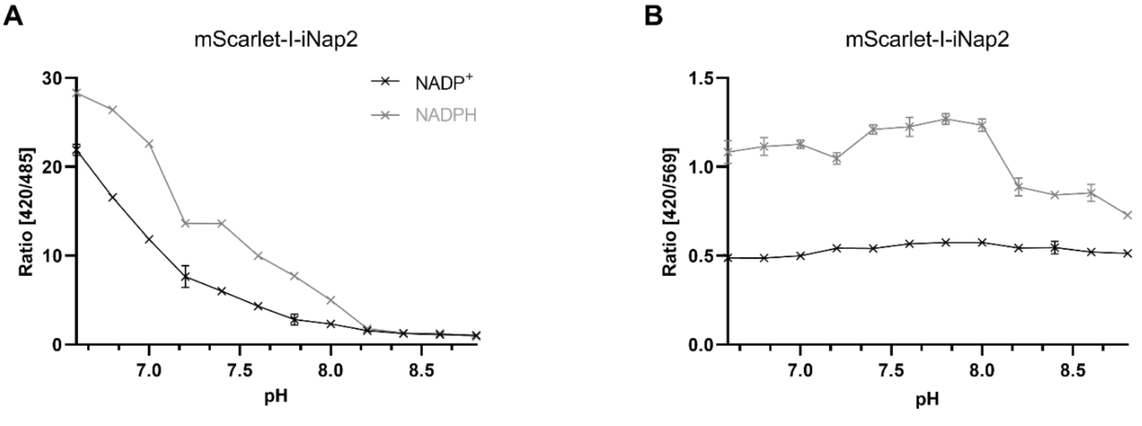

Figure 36. pH response of recombinant mScarlet-I-iNap2. (**A**) Sensor internal excitation wavelengths were used to detect emission at 510 nm. The ratio was calculated as $R = \frac{420\ nm}{485\ nm}$. (**B**) The pH-dependent 485 nm excitation wavelength was replaced with the excitation wavelength of mScarlet-I at 569 nm. The ratio was therefore calculated as $R = \frac{420\ nm}{569\ nm}$. Even though the ratio was much more stable, a decrease in ratio for recombinant mSc.-I-iNap2 equilibrated with NADPH was visible above a pH of 8.0. Means ± SD are shown.

4.2.1.2 Specificity of recombinant mScarlet-I-SoNar and mScarlet-I-iNap2

Previous measurements within this working group had been carried out to study the specificity of the two biosensors [Krickeberg 2020]. For this purpose, the ratio was measured after incubation with different nucleotides. For mSc.-I-iNap2 the maximal NADPH concentration tested within those measurements was 50 µM; as saturation was not visible here, additional measurements with higher NADPH concentrations were performed as part of this work. For comparison, specificity measurements of mSc.-I-SoNar, which were published before [Krickeberg 2020], are shown here as well. The ratio of mSc.-I-SoNar increased with rising NADH concentrations. A slight decrease in ratio was visible with rising NAD$^+$ concentrations. None of the other nucleotides tested led to a strong change in ratio (**Figure 37A**).

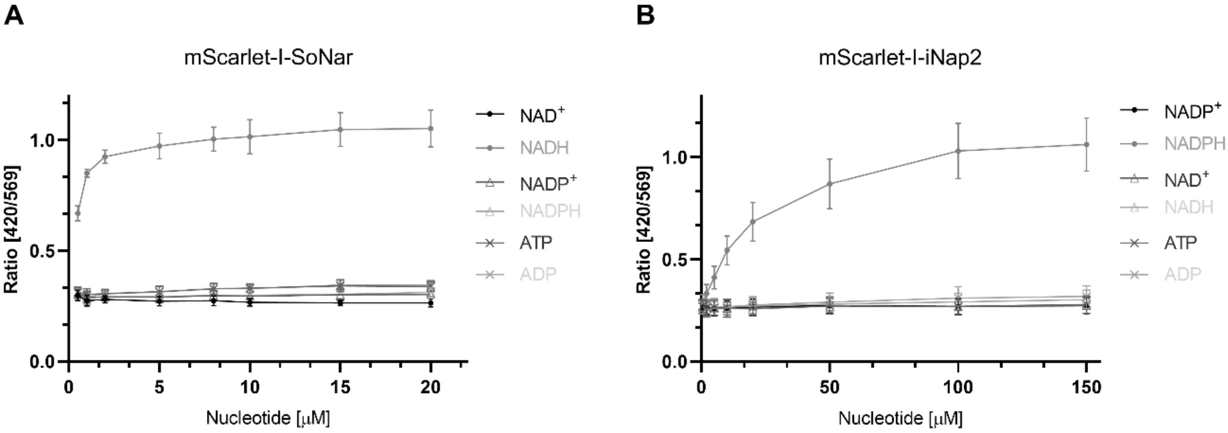

Figure 37. Specificity of recombinant mScarlet-I-SoNar and mScarlet-I-iNap2. (**A**) Recombinant mSc.-I-SoNar was equilibrated with different nucleotides at various concentrations. NAD$^+$ and NADH changed the fluorescence ratio of mSc.-I-SoNar [Krickeberg 2020]. (**B**) Recombinant mSc.-I-iNap2 was equilibrated with different nucleotides at various concentrations. A change in ratio was only visible when the sensor was equilibrated with NADPH. Means ± SD are shown.

In comparison, a change in ratio of mSc.-I-iNap2 was only seen, when equilibrated with NADPH. None of the other nucleotides tested changed the ratio to any extent (**Figure 37B**). Therefore, mSc.-I-iNap2 was found to be strictly dependent on NADPH. As shown in **Figure 37B**, a change in ratio of recombinant mSc.-I-iNap2 was visible up to a concentration of 150 µM.

4.2.1.3 Dynamic change in ratio of recombinant mScarlet-I-SoNar and mScarlet-I-iNap2

The dynamic change in the ratio of recombinant mSc.-I-SoNar and mSc.-I-iNap2 after adding NAD(P)H and NAD(P)$^+$ was examined. The ratio was measured basally before adding NAD(P)H. The ratio was measured over time and subsequently NAD(P)$^+$ was added. Again, the ratio was measured over time. At baseline, the ratio of mSc.-I-SoNar was stable. The ratio increased after adding NADH (0.2 µM). Adding NAD$^+$ (2 mM) led to a decrease in ratio (**Figure 38A**). This effect was even more pronounced when a higher NAD(H) concentration was used. The ratio of mSc.-I-SoNar increased to a higher extent when adding 1 µM NADH. This increase was reversible and diminishable after adding NAD$^+$ (10 mM) (**Figure 38B**). The ratio of mSc.-I-iNap2 increased after adding NADPH (20 µM). Subsequently, adding 2 mM NADP$^+$ did not change the ratio to any extent (**Figure 38C**). Using higher NADP$^+$ concentrations (10 mM) led to a decrease in ratio (**Figure 38D**). However, the low ratio that was seen at the beginning of the measurement without any additions could not be reached again.

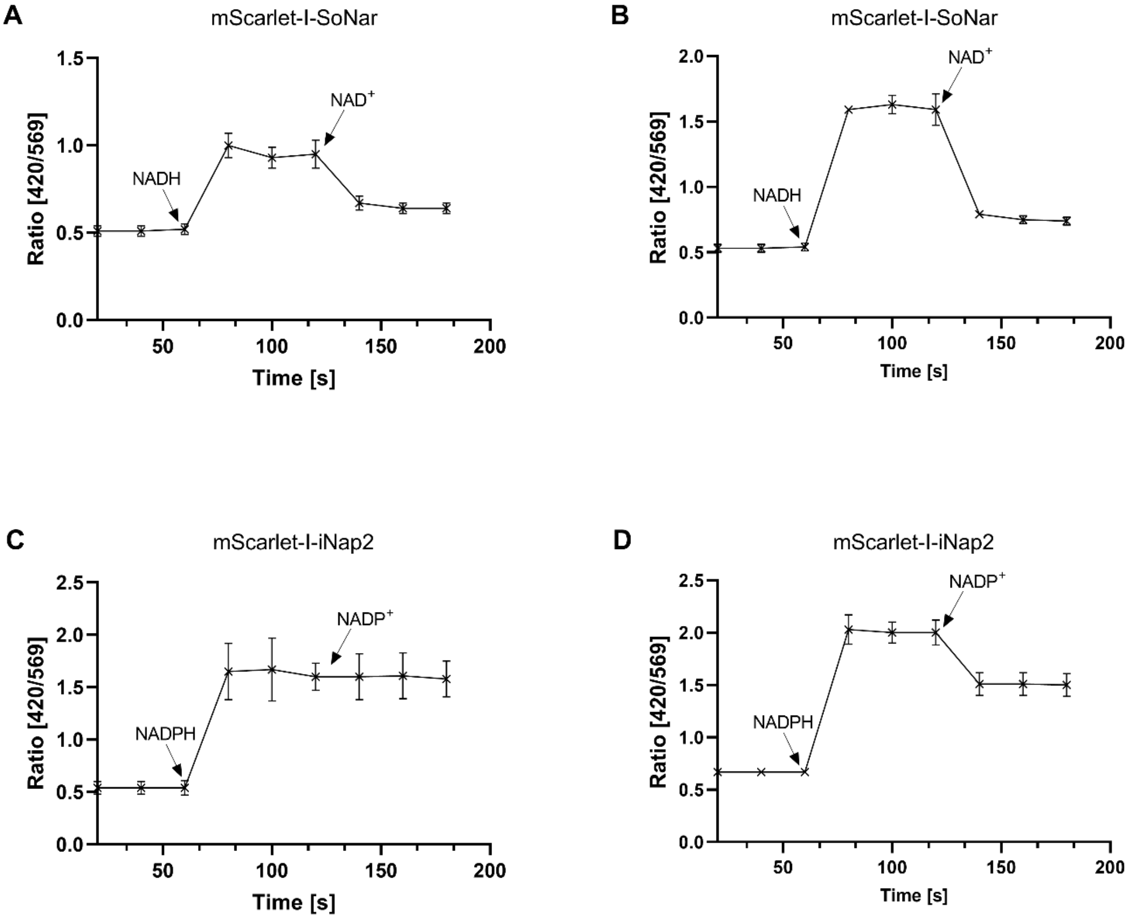

Figure 38. Dynamic change in the ratio of recombinant mScarlet-I-SoNar and mScarlet-I-iNap2. (**A**) The ratio of recombinant mSc.-I-SoNar basal, after adding 0.2 µM NADH, and 2 mM NAD$^+$ is shown. (**B**) The fluorescence ratio of recombinant mSc.-I-SoNar basal, after addition of 1 µM NADH, and 10 mM NAD$^+$ is shown. (**C**) Ratio of recombinant mSc.-I-iNap2 basal, after adding 20 µM NADPH, and 2 mM NADP$^+$ is shown. (**D**) The fluorescence ratio of recombinant mSc.-I-iNap2 basal, after adding 20 µM NADPH, and 10 mM NADP$^+$ is shown. Means ± SD are shown.

4.2.1.4 Direct interaction of recombinant mScarlet-I-SoNar and mScarlet-I-iNap2 with compounds and antimalarial drugs

To differentiate between pharmacological effects of antimalarial drugs on the parasites' NADPH level or NADH:NAD$^+$ ratio and direct interactions of drugs with the two biosensor variants, *in vitro* interaction studies with recombinant mSc.-I-SoNar and mSc.-I-iNap2 and certain antimalarial drugs and compounds were performed prior to *in cellulo* measurements. Besides equilibrating recombinant mSc.-I-SoNar with different antimalarials and compounds, the protein was also treated with NAD$^+$ and NADH. Recombinant biosensor, equilibrated in buffer was used as a control. The ratio ($R = \frac{420\ nm}{569\ nm}$) was measured after incubation times of 5 min, 4 h, and 24 h at 37 °C. After 5 min of incubation, treatment with NADH and very high concentrations of MB, PD, and DOXY increased the fluorescence ratio of mSc.-I-SoNar (**Figure 39A**). After 4 h incubation, additionally, high H_2O_2 concentrations influenced the ratio (**Figure 39B**). This was also the case for an incubation time of 24 h (**Figure 39C**). Here, treatment with NADH did not significantly increase the sensor ratio anymore. For subsequent *in cellulo* experiments, antimalarials and compounds were used only in concentrations that showed no direct influence on the ratio.

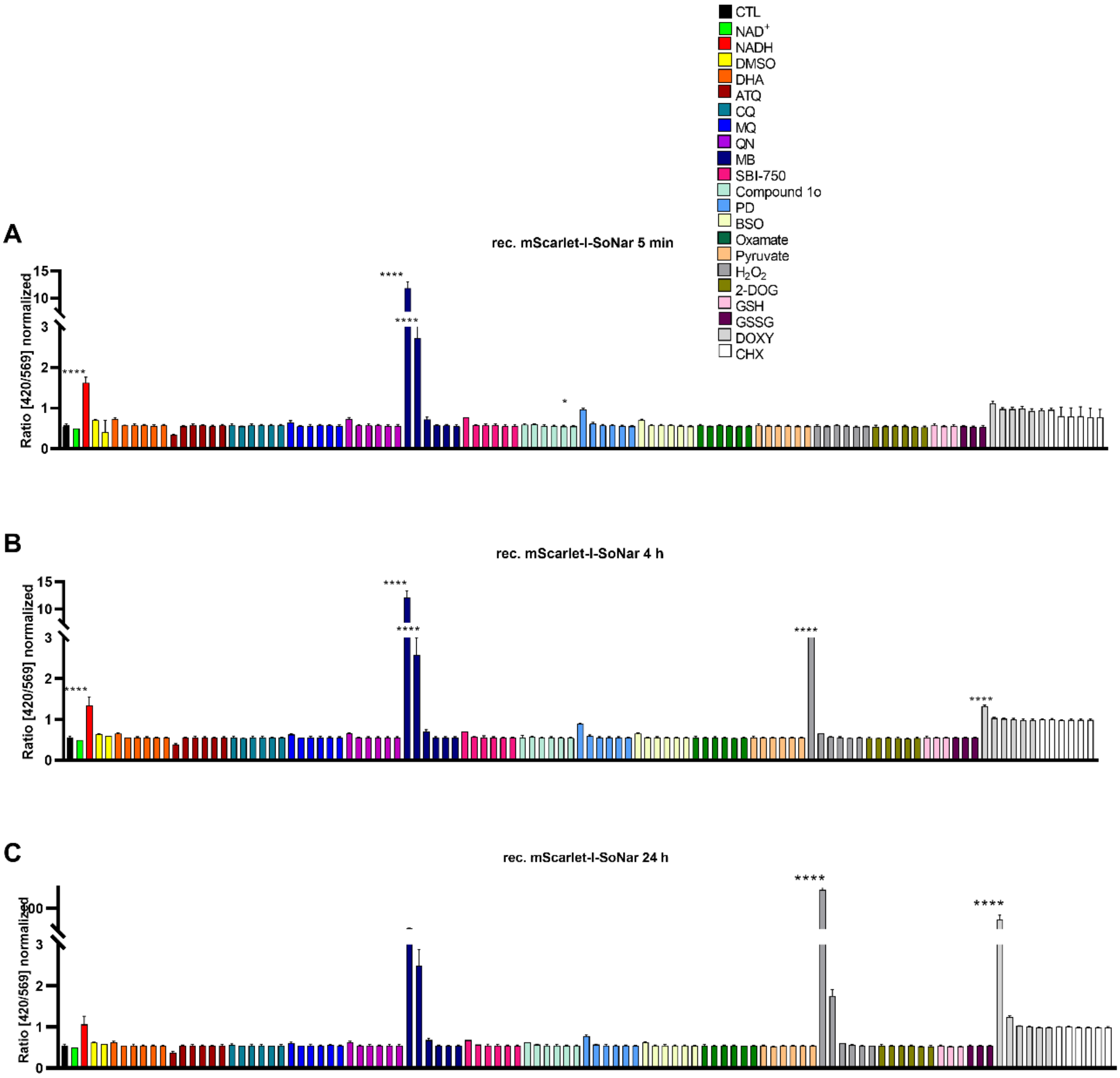

Figure 39. Direct interaction of antimalarial drugs and compounds with recombinant mScarlet-I-SoNar. The fluorescence ratio was measured after 5 min incubation of recombinant mSc.-I-SoNar with different antimalarial agents and compounds (**A**), after 4 h incubation (**B**), and after 24 h incubation (**C**). The measured concentrations are shown in decreasing order of magnitude (1 mM, 100 µM, 10 µM, 1 µM, 100 nM, and 10 nM). Oxamate, pyruvate, and 2-DOG were tested in the following concentrations: 10 mM, 1 mM, 100 µM, 10 µM, 1 µM, 100 nM. Means ± SD are shown for three independent experiments. A one-way ANOVA test with 95% confidence intervals with the Dunnett's multiple comparison test was applied for statistical analysis of significance (*, $p < 0.05$; **, $p < 0.01$; ***, $p < 0.001$; ****, $p < 0.0001$). CTL = control, DHA = dihydroartemisinin. ATQ = atovaquone, CQ = chloroquine, MQ = mefloquine, QN = quinine, MB = methylenblue, PD = plasmodione, BSO = buthionine sulphoximine, 2-DOG = 2-dioxygluocose, GSH = reduced glutathione, GSSG = oxidized glutathione, DOXY = doxycycline, CHX = cycloheximinde.

The effects of antimalarial drugs and compounds on the ratio of mSc.-I-iNap2 were comparable. Here, the recombinant sensor was additionally treated with $NADP^+$ and NADPH. A recombinant biosensor equilibrated in buffer was used as a control. The ratio ($R = \frac{420\text{ nm}}{569\text{ nm}}$) was measured after incubation times of 5 min, 4 h, and 24 h at 37 °C. Short-term incubation (5 min) with NADPH and very high concentrations of MB, PD, and DOXY increased the biosensors ratio (**Figure 40A**). High ATQ concentrations (1 mM) decreased the ratio. After an incubation time of 4 h, additionally, high H_2O_2 concentrations increased the ratio (**Figure 40B**). This was also the case for long-term incubations (24 h) (**Figure 40C**). Moreover, 24 h incubation with NADPH did no longer significantly change the ratio. Lower and therefore, more physiologically relevant antimalarial and compound concentrations did not significantly change the biosensor’s ratio compared to the control.

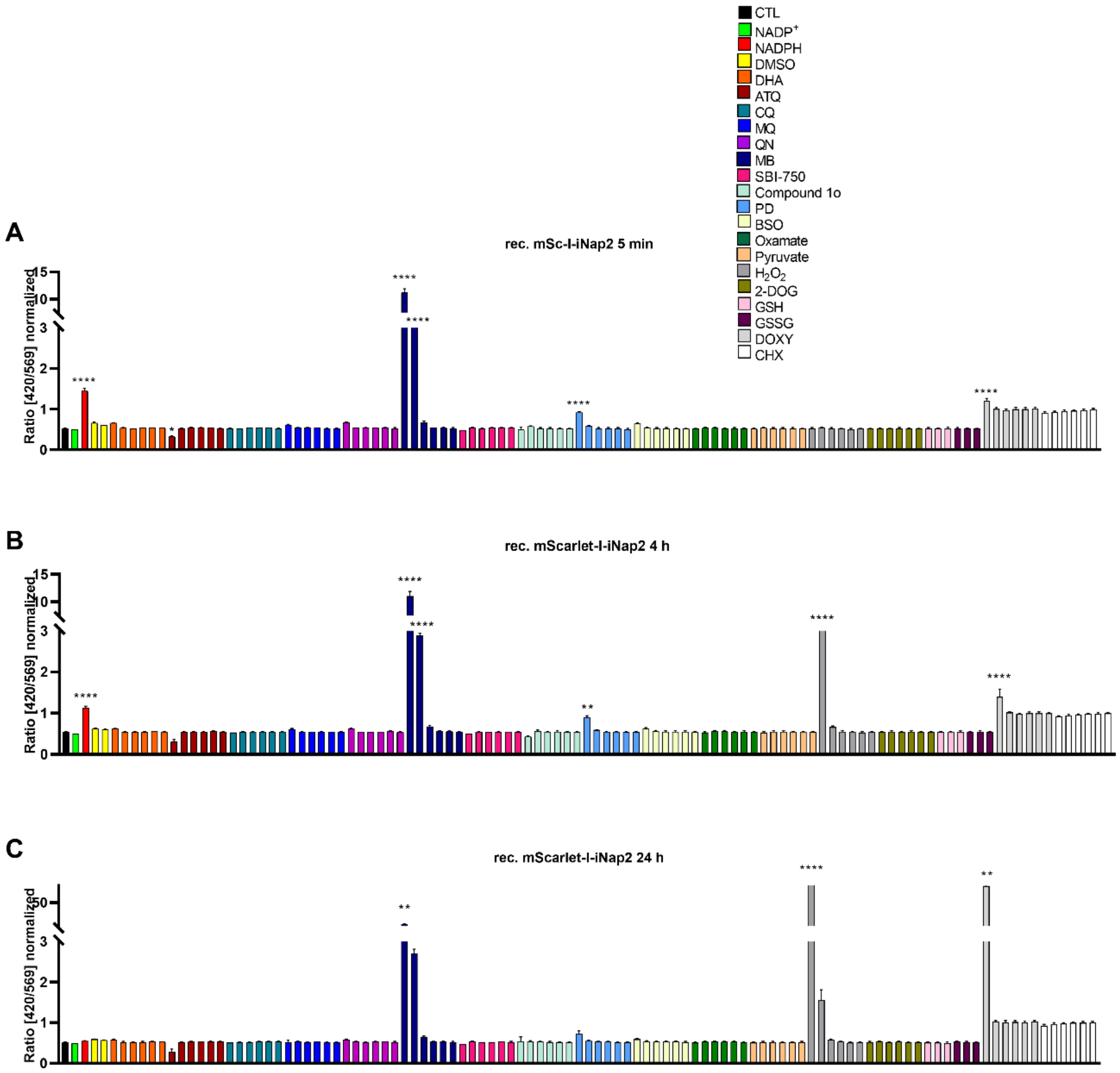

Figure 40. Direct interaction of antimalarial drugs and compounds with recombinant mScarlet-I-iNap2. The fluorescence ratio was measured after 5 min incubation of recombinant mSc.-I-iNap2 with different antimalarial agents and compounds (**A**), after both 4 h incubation (**B**), and 24 h incubation (**C**). The measured concentrations are shown in decreasing order of magnitude (1 mM, 100 µM, 10 µM, 1 µM, 100 nM, and 10 nM). Oxamate, pyruvate, and 2-DOG were tested in the following concentrations: 10 mM, 1 mM, 100 µM, 10 µM, 1 µM, 100 nM. DMSO was tested in a concentration of 10% and 5%. Means ± SD are shown for three independent experiments. A one-way ANOVA test with 95% confidence intervals with the Dunnett's multiple comparison test was applied for statistical analysis of significance (*, $p < 0.05$; **, $p < 0.01$; ***, $p < 0.001$; ****, $p < 0.0001$). CTL = control, DHA = dihydroartemisinin. ATQ = atovaquone, CQ = chloroquine, MQ = mefloquine, QN = quinine, MB = methylenblue, PD = plasmodione, BSO = buthionine sulphoximine, 2-DOG = 2-dioxyglucose, GSH = reduced glutathione, GSSG = oxidized glutathione, DOXY = doxycycline, CHX = cycloheximinde.

4.2.2 *In cellulo* characterization of NADPH and NADH:NAD$^+$ biosensors

4.2.2.1 *In cellulo* expression of hGrx1-sfroGFP2, mScarlet-I-SoNar, and mScarlet-I-iNap2 in NF54*attB Plasmodium falciparum* parasites

The parasite line NF54*attB*$^{\text{hGrx1-sfroGFP2}}$ was generated in cooperation with Dr. Katharina Schuh. Therefore, cloning, transfection, and generation of clonal parasite lines were described within her doctoral thesis [Schuh 2021]. For the transfection of NF54*attB* parasites with mScarlet-I-SoNar or mScarlet-I-iNap2, both plasmids pDC2-CAM-[mSc.-I-SoNar]-*attP* and pDC2-CAM-[mSc.-I-iNap2]-*attP* were used to stably integrate the biosensors into the parasites' genome via homologous recombination. After successful transfection, the fluorescence of the parasites' bulk culture was monitored using epifluorescence microscopy. Clonal parasite lines were generated using limited dilution (**3.6.9**). Blood PCR was performed to verify stable integration of the various biosensors, using a forward primer for the non-essential cg6-5' locus and a reverse primer for the BSD locus of the NF54*attB* parasite line (**2.7.1.2**). A 1.6 kb PCR product confirmed stable integration of the biosensors (**Figure 41**). Additionally, the expression of the various biosensors at the protein level was verified using Western blot analysis (**Figure 42**). An anti-GFP AB was used to detect the various biosensors. A band of the expected size was visible for each sensor-positive sample. Anti-PfAldolase AB was used as a loading control. Representative images from epifluorescence microscopy of NF54*attB*$^{\text{hGrx1-sfroGFP2}}$, NF54*attB*$^{\text{mSc.-I-SoNar}}$, and NF54*attB*$^{\text{mSc.-I-iNap2}}$ clones are shown in **Figure 43**.

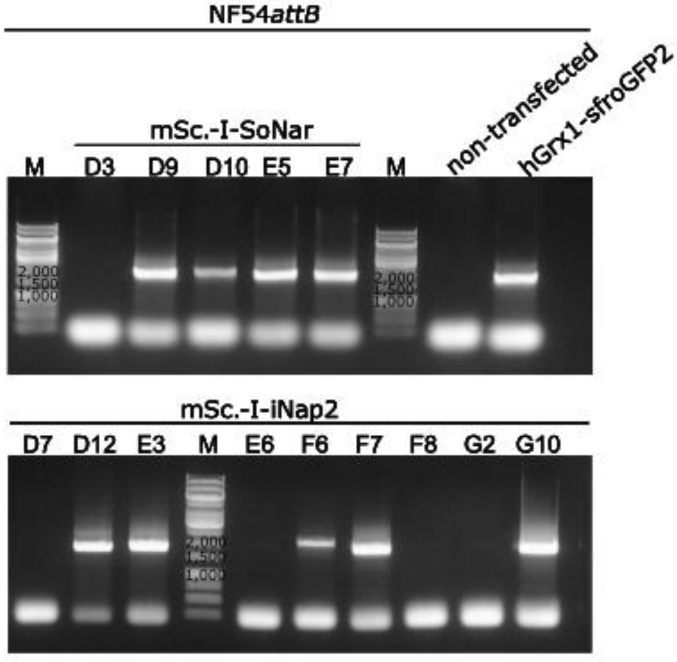

Figure 41. Verification of stable integration of mScarlet-I-SoNar and mScarelt-I-iNap2 in NF54*attB* via PCR. Successful integration was verified via integration PCR. A band of the expected size of 1.6 kb is visible. M = marker, sizes indicated in bp. The numbers above the agarose gel indicate samples from different clonal parasite lines. Non-transfected NF54*attB* parasites were used as a negative control. A sample of NF54*attB*$^{\text{hGrx1-sfroGFP2}}$ parasites was used as a positive control.

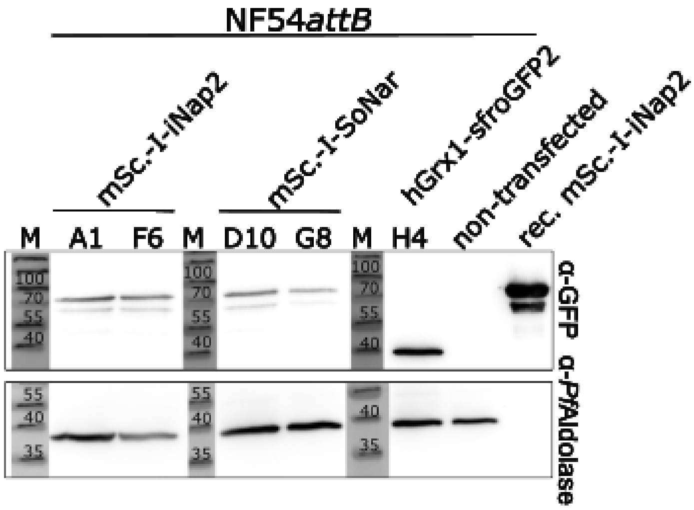

Figure 42. Western blot analysis of NF54*attB*$^{\text{mScarlet-I-SoNar}}$ and NF54*attB*$^{\text{mSc.-I-iNap2}}$. Anti-GFP AB was used to identify the different biosensors. Non-transfected NF54*attB* parasites were used as a negative control. Recombinant mSc.-I-iNap2 was used as a positive control. Anti-PfAldolase AB was used as a loading control. M = marker, size indicated in kDa. The numbers above the gel indicate samples from different clonal parasite lines. Molecular weight of mSc.-I-iNap2 and mSc.-I-SoNar = 70 kDa, hGrx1-sfroGFP2 = 48 kDa, PfAldolase = 40 kDa.

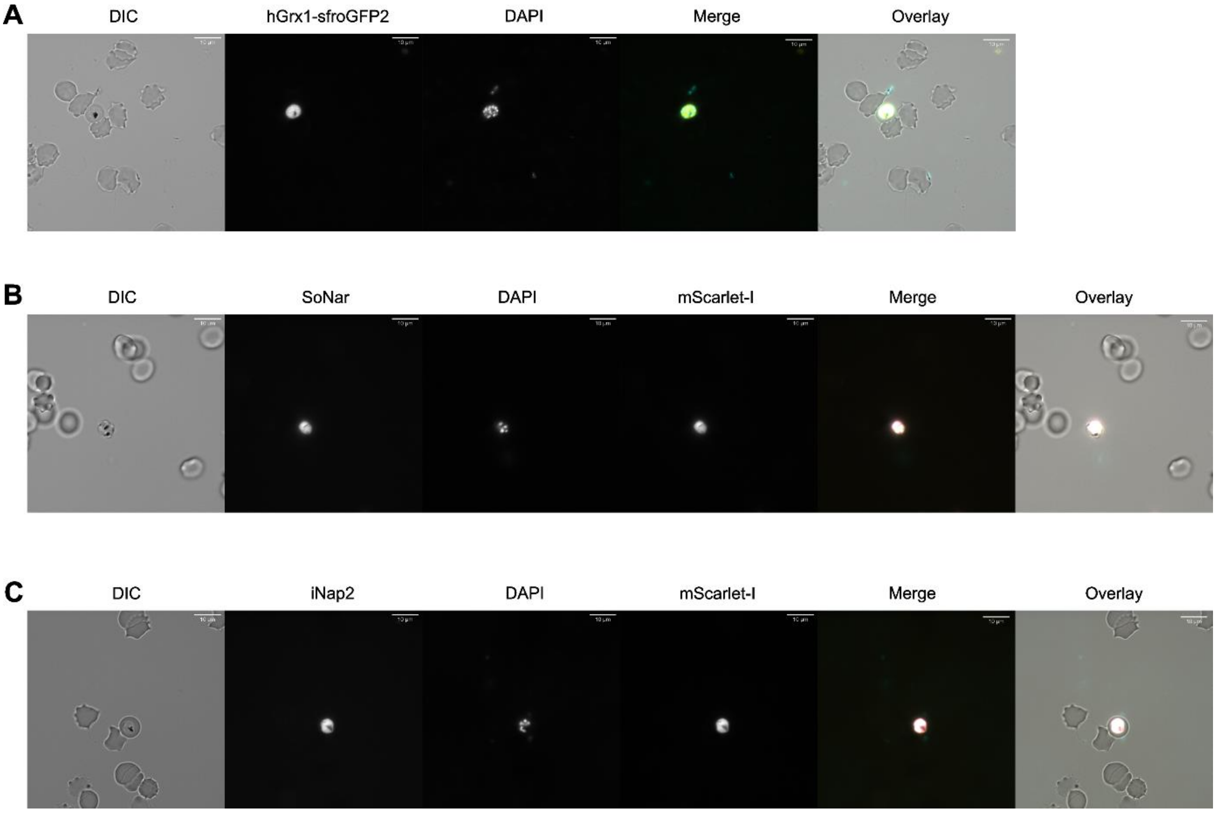

Figure 43. Microscopy image of NF54*attB*$^{\text{hGrx1-sfroGFP2}}$, NF54*attB*$^{\text{mSc.-I-SoNar}}$, and NF54*attB*$^{\text{mSc.-I-iNap2}}$. (**A**) The NF54*attB*$^{\text{hGrx1-sfroGFP2}}$ clone H4 was used to verify microscopically the expression of the biosensor. The hGxr1-sfroGFP2 signal was visible using the GFP filter. The nucleus was stained using DAPI. Merge and overlay images confirmed cytosolic localization of the biosensor. (**B**) The NF54*attB*$^{\text{mSc.-I-SoNar}}$ clone G8 was used to verify microscopically the expression of the biosensor. The SoNar signal was visible using the GFP filter. The nucleus was stained using DAPI. The mScarlet-I fluorescence could be detected using the mCherry filter. Merge and overlay images confirmed cytosolic localization of the biosensor. (**C**) The NF54*attB*$^{\text{mSc.-I-iNap2}}$ clone F6 was used to verify microscopically the expression of the biosensor. The iNap2 signal was visible using the GFP filter. The nucleus was stained using DAPI. mScarlet-I fluorescence could be detected using the mCherry filter. Merge and overlay images confirmed cytosolic localization of the biosensor. DIC = differential interference contrast. The fluorescence signal is visualized in grey. For merge and overlay, the colors were set to yellow, cyan, and magenta.

4.2.2.2 *In cellulo* spectral scans of NF54*attB*$^{\text{mScarlet-I-SoNar}}$ and NF45*attB*$^{\text{mScarlet-I-iNap2}}$

Spectral excitation scan as well as spectral emission scan after excitation at 420 nm, with NF54*attB* parasites expressing mSc.-I-SoNar or mSc.-I-iNap2 equilibrated in Ringer's solution or 1x PBS, were recorded. Hereby, changes in spectral properties under glucose deprivation were demonstrated. Due to the low FI of both biosensors and the high intrinsic FI of the parasites, the excitation peaks were not very pronounced. Nevertheless, the expected spectrum was recognizable (**Figure 44**). The excitation peak at 420 nm for NF54*attB*$^{\text{mSc.-I-SoNar}}$ was not as pronounced as the excitation peak at 485 nm (**Figure 44A**). Throughout the whole spectrum, the FI was higher for parasites resuspended in Ringer's solution than for parasites resuspended in 1x PBS and thereby under glucose deprivation. An emission spectral scan after excitation at 420 nm showed a single emission peak at 510 nm, confirming the excitation peak at 420 nm (**Figure 44B**). Here, parasites resuspended in Ringer's solution showed a higher FI than parasites resuspended in 1x PBS. Again, glucose deprivation led to a decrease in FI of the biosensor.

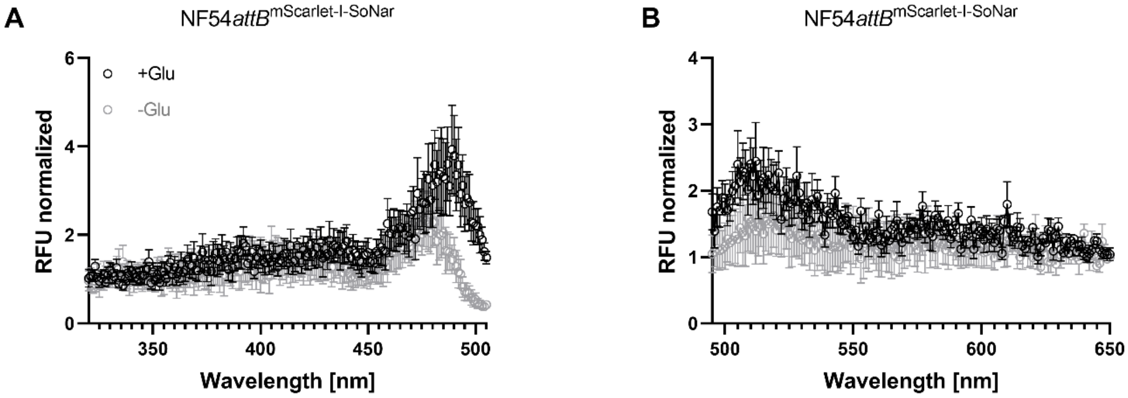

Figure 44. Spectral excitation and emission scans after excitation at 420 nm of NF54*attB*$^{\text{mSc.-I-SoNar}}$. (**A**) Spectral excitation scan of enriched NF54*attB*$^{\text{mSc.-I-SoNar}}$ parasites equilibrated in Ringer's solution (black) or 1x PBS (grey). (**B**) Spectral emission scan after excitation at 420 nm of enriched NF54*attB*$^{\text{mSc.-I-SoNar}}$ parasites equilibrated in Ringer's solution (black) or 1x PBS (grey). 2.0x 10^6 trophozoite-stage parasites per measurement were used. Means ± SD are shown. RFU = relative fluorescence units.

Spectral excitation scan and spectral emission scan after excitation at 420 nm were recorded with enriched NF54*attB*$^{\text{mSc.-I-iNap2}}$ parasites equilibrated in Ringer's solution and 1x PBS. Spectral scans were comparable to the spectral scans recorded using NF54*attB*$^{\text{mSc.-I-SoNar}}$ parasites. Two excitation maxima at 420 nm and around 490 nm were visible (**Figure 45A**). The latter was more pronounced here as well. Parasites resuspended in Ringer's solution showed a higher FI throughout the whole spectrum than parasites resuspended in 1x PBS. Emission spectral scan after excitation at 420 nm showed a single emission peak at 510 nm, with an increased FI when parasites were equilibrated in Ringer's solution (**Figure 45B**). Here as well, glucose deprivation of the parasites decreased the FI of the biosensor.

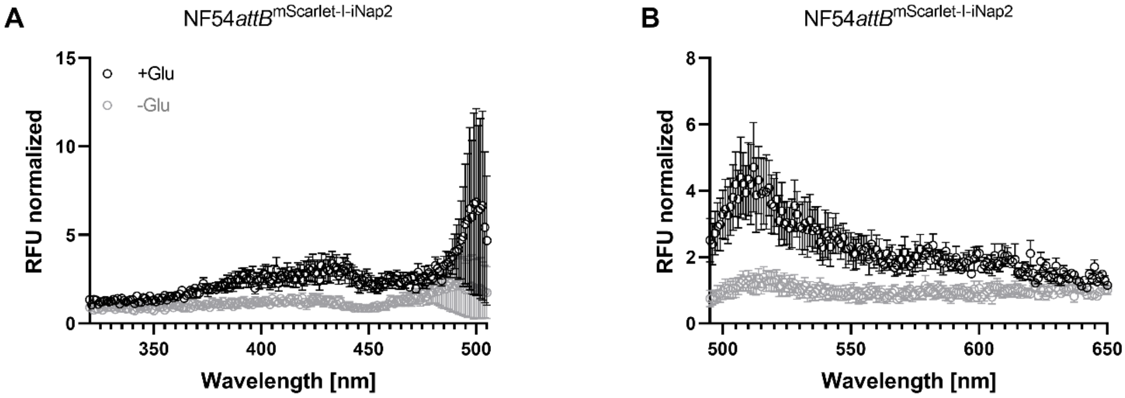

Figure 45. Spectral excitation and emission scan after excitation at 420 nm of NF54*attB*$^{\mathbf{mSc.\text{-}I\text{-}iNap2}}$. (**A**) Spectral excitation scan of enriched NF54*attB*$^{mSc.\text{-}I\text{-}iNap2}$ parasites equilibrated in Ringer's solution (black) or 1x PBS (grey). (**B**) Spectral emission scan after excitation at 420 nm of enriched NF54*attB*$^{mSc.\text{-}I\text{-}SoNar}$ parasites equilibrated in Ringer's solution (black) or 1x PBS (grey). 2.0x 10^6 trophozoite-stage parasites per measurement were used. Means ± SD are shown. RFU = relative fluorescence units.

4.2.2.3 *In cellulo* dynamic change in ratio of NF54*attB*$^{\mathbf{mScarlet.\text{-}I\text{-}SoNar}}$ and NF45*attB*$^{\mathbf{mScarlet\text{-}I\text{-}iNap2}}$

In addition to the spectral scans the dynamic change in ratio of NF54*attB*$^{mSc.\text{-}I\text{-}SoNar}$ and NF45*attB*$^{mSc.\text{-}I\text{-}iNap2}$ was recorded basally and after adding oxamate or DIA, respectively. The ratio of enriched trophozoite-stage NF54*attB*$^{mSc.\text{-}I\text{-}SoNar}$ parasites was monitored basally for 96 sec. Subsequently, oxamate, a competitive inhibitor of the lactate dehydrogenase, was added. This inhibited the conversion of pyruvate to lactate. After adding oxamate, the ratio increased immediately by 1.35-fold, indicating an increase in the NADH:NAD$^+$ ratio. The ratio was further monitored for 30 min, during which time the ratio remained unchanged (**Figure 46**).

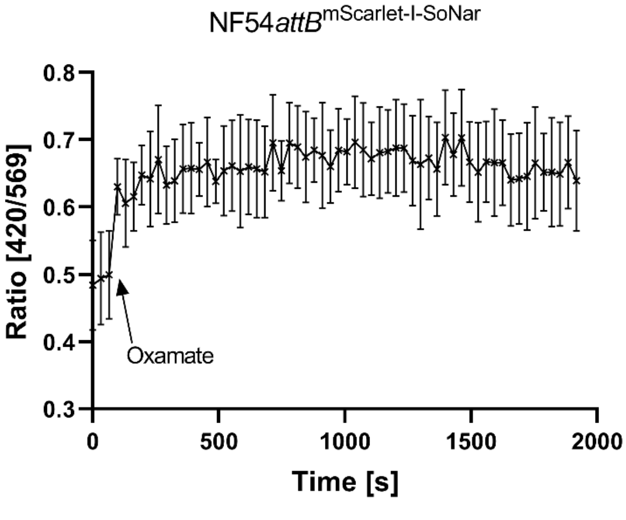

Figure 46. *In cellulo* dynamic change in the ratio of NF54*attB*$^{\mathbf{mSc.\text{-}I\text{-}SoNar}}$. The fluorescence ratio of NF54*attB*$^{mSc.\text{-}I\text{-}SoNar}$ was detected for 96 sec. Thereafter, the parasites were treated with 8 mM oxamate. Subsequently, the ratio was measured over 30 min. Means ± SD are shown.

Moreover, the ratio of enriched trophozoite-stage NF54*attB*$^{\text{mSc.-I-iNap2}}$ parasites was monitored basally for 96 sec. Subsequently, the change of ratio after adding DIA was monitored. The ratio decreased immediately by 0.7-fold, indicating a decrease in NADPH level, and remained at the same level until the end of the measurement (**Figure 47**).

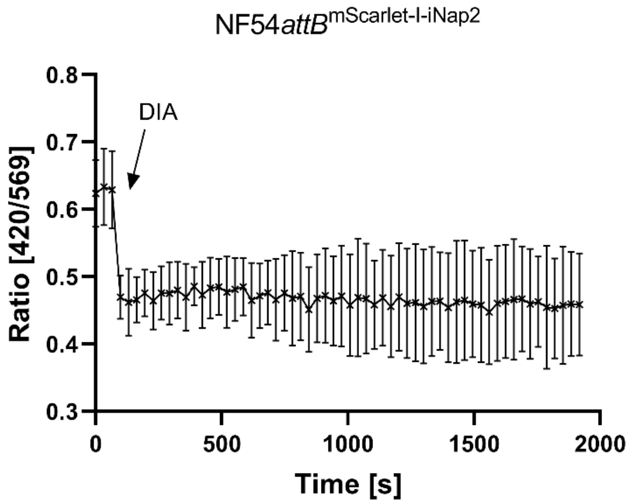

Figure 47. *In cellulo* dynamic change in ratio of NF54*attB*$^{\text{mSc.-I-iNap2}}$. The fluorescence ratio of NF54*attB*$^{\text{mSc.-I-iNap2}}$ was detected for 96 sec, then the parasites were treated with 160 µM DIA. Subsequently, the ratio was measured over 30 min. Means ± SD are shown.

4.3 sfpHluorin as an improved pH biosensor

The pH biosensor sfpHluorin [Reifenrath and Boles 2018] was used in this work to monitor changes in the pH of the parasites' cytosol upon drug treatment. This was necessary since the ratio of both biosensors mSc.-I-SoNar and mSc.-I-iNap2 were not completely independent of changes in pH. If the cytosolic pH of the parasites remained constant, this pH dependence was not problematic. However, if the cytosolic pH changed due to treatment with antimalarial drugs or compounds, this could have affected the ratio of the biosensors. A direct influence of the substances on the NADPH level and the NADH:NAD$^+$ ratio would therefore, no longer be clearly detectable. Moreover, the enhanced FI of sfpHluorin over pHluorin [Reifenrath and Boles 2018] is a big advantage for its usage in *Plasmodium*, since it comes along with an improved utilization in these small organisms. The establishment of this biosensor in *Plasmodium* was therefore of great interest. Prior to *in cellulo* use of the pH biosensor, it should be characterized *in vitro*. Eric Springer carried out stable integration of sfpHluorin into NF54*attB* parasites and *in cellulo* characterization in our lab, which are therefore not reported within this work.

4.3.1 Heterologous overexpression and purification of sfpHluorin

Recombinant sfpHluorin was produced using *E. coli* M15 cells and the pQE30 expression vector. Using the 6xHis-tag of the protein, Ni-NTA affinity chromatography could be performed to purify the recombinant protein. Imidazole concentrations of 25 mM and above were used to collect the protein of interest. High amounts of up to 50 mg of pure protein per half liter of *E. coli* culture could be obtained. A representative gel of sfpHluorin after purification using affinity chromatography is shown in **Figure 48**.

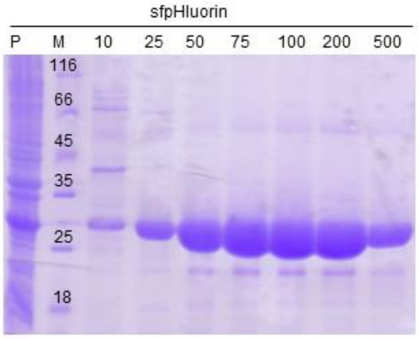

Figure 48. SDS-gel of a purification of recombinant sfpHluorin. A 12% SDS-gel after Coomassie staining is shown. M = marker, size indicated in kDa, P = pellet; the numbers above the gel indicate imidazole concentrations in mM. Molecular weight of sfpHluorin = 27 kDa.

4.3.2 *In vitro* characterization of recombinant sfpHluorin

4.3.2.1 pH response of recombinant sfpHluorin

Fluorescent excitation and emission scans were recorded with recombinant sfpHluorin equilibrated in buffers with pH values ranging from pH 5.0 to pH 9.0. As shown in **Figure 49A** two pH-dependent excitation peaks at around 390 nm and 470 nm were visible. At lower pH values, FI at 470 nm increased, whereas FI at 390 nm was higher with more alkaline pH values. Spectral emission scans after excitation at 390 nm (**Figure 49B)** and 470 nm (**Figure 49C**) resulted in a single pH dependent emission peak at 510 nm. When excited at 390 nm, the FI at 510 was highest for alkaline pH values. Excitation at 470 nm showed the highest emission FI at 510 nm for acidic pH values. Calculating the ratio ($R = \frac{390\text{ nm}}{470\text{ nm}}$) showed a strong pH-dependent change (**Figure 50**). This indicated the stable use of sfpHluorin as a pH biosensor for monitoring pH changes in a range between pH 5.5 to pH 8.5.

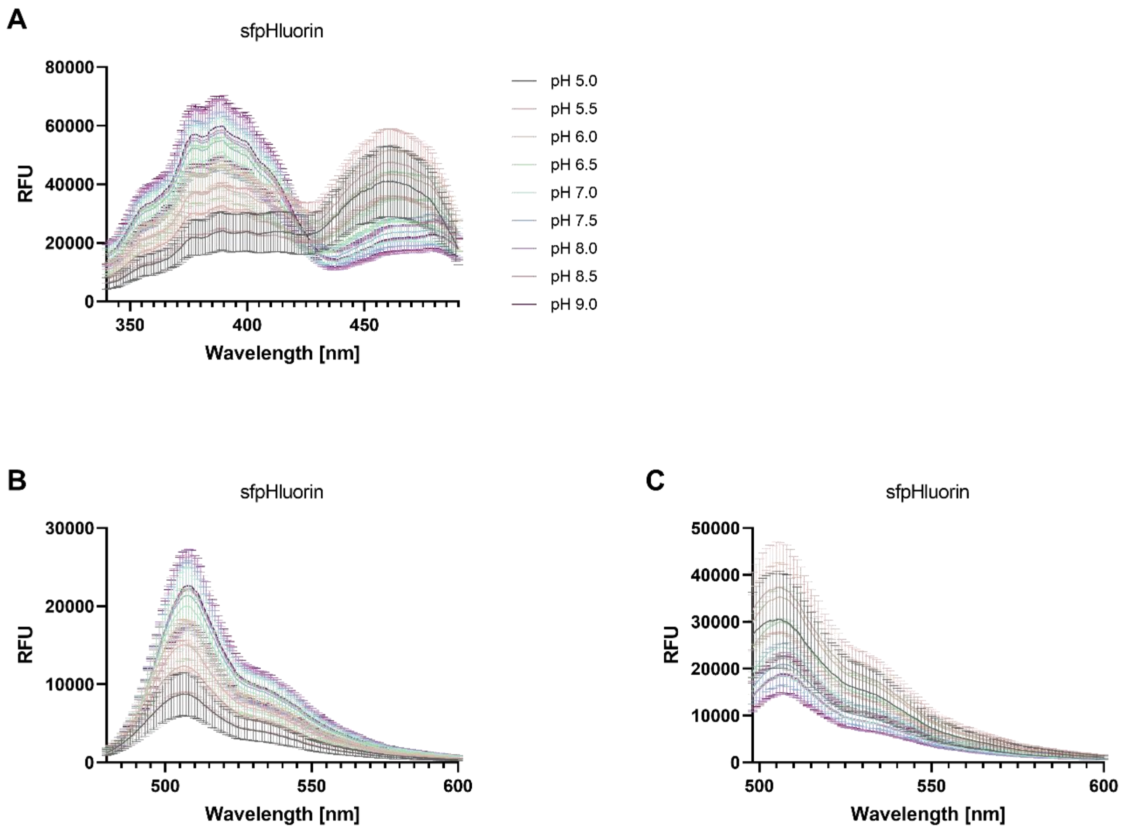

Figure 49. pH-dependent spectral scans of recombinant sfpHluorin. (**A**) pH-dependent excitation scan of recombinant sfpHluorin using buffers with pH-values between 5.0 and 9.0. (**B**) pH-dependent emission scan after excitation at 390 nm of recombinant sfpHluorin equilibrated in buffers with pH-values between 5.0 and 9.0. (**C**) pH-dependent emission scan after excitation at 470 nm of recombinant sfpHluorin equilibrated in buffers with pH-values between 5.0 and 9.0. Means ± SD are shown. RFU = relative fluorescence units.

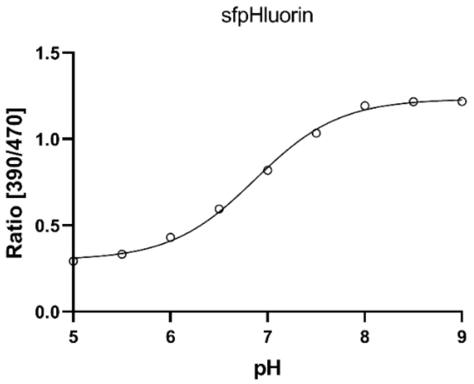

Figure 50. pH-dependent change in ratio of recombinant sfpHluorin. Recombinant sfpHluorin was equilibrated in buffers with pH values ranging from 5.0 to 9.0. The fluorescence ratio was calculated ($R = \frac{390\ \text{nm}}{470\ \text{nm}}$) and plotted against pH. A sigmoidal dose-response curve was plotted using GraphPadPrism 8. Means ± SD are shown.

4.3.2.2 Direct interaction of recombinant sfpHluorin with compounds and antimalarial drugs

To differentiate between pharmacological effects of antimalarial drugs on the parasites' cytosolic pH value and direct interactions of drugs with sfpHluorin, the *in vitro* interaction with recombinant sfpHluorin and certain antimalarial drugs and compounds was studied. Therefore, recombinant sfpHluorin was equilibrated with different concentrations of various antimalarials and compounds. Moreover, sfpHluorin was equilibrated in buffer with pH 5.0 and 9.0. sfpHluorin equilibrated in buffer with pH 7.5 was used as a control. The ratio ($R = \frac{390\ \text{nm}}{470\ \text{nm}}$) was measured after 5 min, 4 h, and 24 h incubation at 37 °C.

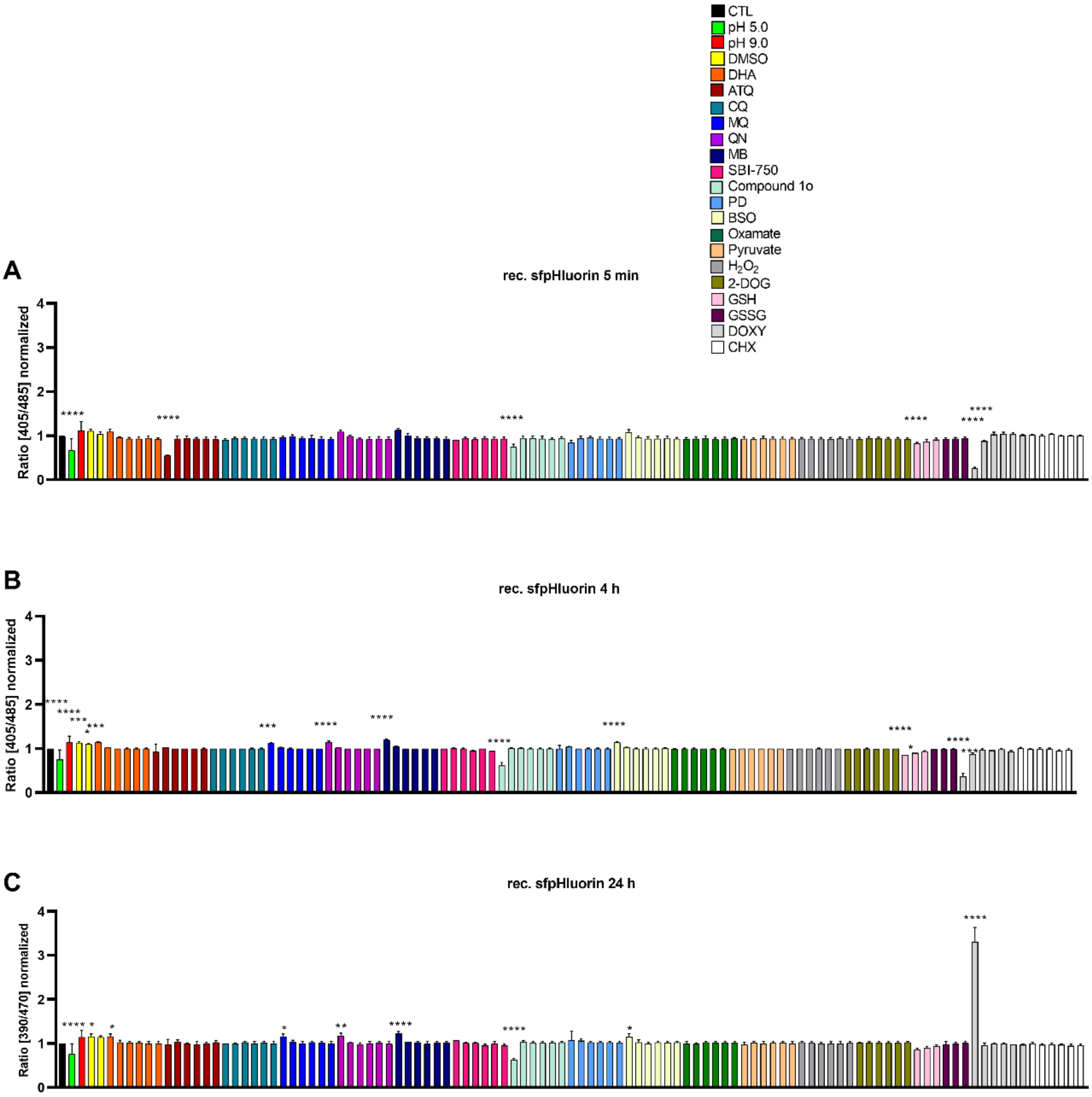

Figure 51. Direct interaction of antimalarial agents and compounds with recombinant sfpHluorin. The fluorescence ratio was measured after 5 min incubation of recombinant sfpHluorin with different antimalarial agents and compounds (**A**), and both 4 h incubation (**B**), and 24 h incubation (**C**). The measured concentrations are shown in decreasing order of magnitude (1 mM, 100 µM, 10 µM, 1 µM, 100 nM, and 10 nM). Oxamate, pyruvate, and 2-DOG were tested in the following concentrations: 10 mM, 1 mM, 100 µM, 10 µM, 1 µM, 100 nM. DMSO was tested in a concentration of 10% and 5%. Means ± SD are shown for three independent experiments. A one-way ANOVA test with 95% confidence intervals with the Dunnett's multiple comparison test was applied for statistical analysis of significance (*, $p < 0.05$; **, $p < 0.01$; ***, $p < 0.001$; ****, $p < 0.0001$). CTL = control, DHA = dihydroartemisinin. ATQ = atovaquone, CQ = chloroquine, MQ = mefloquine, QN = quinine, MB = methylenblue, PD = plasmodione, BSO = buthionine sulphoximine, 2-DOG = 2-dioxyglucose, GSH = reduced glutathione, GSSG = oxidized glutathione, DOXY = doxycycline, CHX = cycloheximinde.

After 5 min incubation, very high concentrations of ATQ, compound 1o, GSH, and DOXY influenced the biosensor's ratio (**Figure 51A**). After 4 h incubation high concentrations of MQ, QN, MB, and BSO also significantly increased the ratio (**Figure 51B**). This was also the case for long-term (24 h) incubations (**Figure 51C**). For subsequent *in cellulo* experiments, antimalarials and compounds were used only in concentrations that showed no direct influence on the ratio.

4.4 Establishment of redox measurements using flow cytometry

In previous work of our lab, biosensor-based measurements were carried out using confocal laser scanning microscopy (CLSM) or plate reader detection [Kasozi et al. 2013; Mohring et al. 2016; Rahbari et al. 2017b; Schuh et al. 2018]. Both measuring principles have their advantages and disadvantages, like complex sample preparation, long measuring and analysis time. In this work, all of those limitations were overcome by establishing a biosensor-based measurement using flow cytometry. For this purpose, measurements with NF54*attB* parasites stably expressing the redox-biosensor hGrx1-sfroGFP2 were performed in parallel using plate reader detection and flow cytometry. Subsequently, the results received were compared. Beforehand, the redox-biosensor signal was determined using flow cytometry and the settings were adjusted in such a way that the sensor's positive signal could be separated from the parasites' intrinsic fluorescence signal. For this purpose, NF54*attB* parasites with and without sensor (hGrx1-sfroGFP2) were used. First, the fluorescence range of the intrinsic parasite signal was defined for both channels (KO525 $\lambda_{Exc.}$ 405 nm, $\lambda_{Em.}$ 525/40 nm and FITC $\lambda_{Exc.}$ 485 nm, $\lambda_{Em.}$ 525/40 nm) (**Figure 52A,B**). Here, a signal was visible after excitation with both wavelengths. Then, the area representing the redox-biosensor signal for both channels was defined using NF54*attB*$^{hGrx1\text{-}sfroGFP2}$ parasites (**Figure 52C,D**). For those measurements, another signal with higher fluorescence values than the parasites' intrinsic fluorescence signal was visible for both channels. Both signals–the intrinsic fluorescence one and the specific redox-biosensor one–were clearly distinguishable.

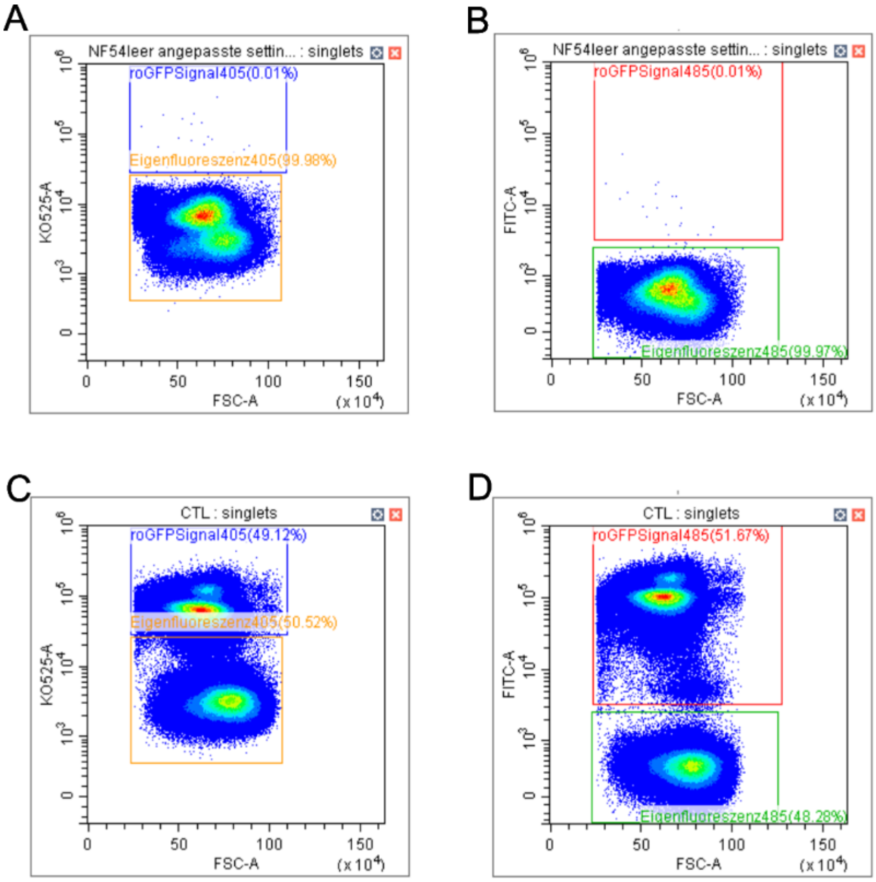

Figure 52. Flow cytometry settings. Scatter plot of the KO252 channel ($\lambda_{Exc.}$ 405, $\lambda_{Em.}$ 525/40 nm) (**A**) and FITC channel ($\lambda_{Exc.}$ 488, $\lambda_{Em.}$ 525/40 nm) (**B**) of NF54*attB* parasites. Intrinsic fluorescence is visible in both channels. Scatter plot of the KO252 channel ($\lambda_{Exc.}$ 405, $\lambda_{Em.}$ 525/40 nm) (**C**) and FITC channel ($\lambda_{Exc.}$ 488, $\lambda_{Em.}$ 525/40 nm) (**D**) for NF54*attB*$^{hGrx1\text{-}sfroGFP2}$ parasites. Fluorescence of redox-biosensors is detectable separately from the intrinsic parasite signal.

The corresponding histogram of NF54*attB*$^{hGrx1\text{-}sfroGFP2}$ parasites showed a peak, reflecting the sensor signal for both channels (**Figure 53A,B**). The peak representing the intrinsic fluorescence signal of the parasites is not displayed here. Oxidizing the parasites using 1 mM DIA slightly shifted the peak. In the KO525 channel ($\lambda_{Exc.}$ 405, $\lambda_{Em.}$ 525/40 nm), the peak slightly shifted to the right, representing a higher FI (**Figure 53C**), whereas the FI decreased slightly in the FITC channel ($\lambda_{Exc.}$ 488, $\lambda_{Em.}$ 525/40 nm) compared to untreated parasites (**Figure 53D**). Reduction of the parasites with 10 mM DTT changed the peak in an opposite way. The FI after excitation at 405 nm decreased (**Figure 53E**) and increased after excitation at 488 nm (**Figure 53F**) compared to untreated parasites. The normalized ratio calculated was $R_{CTL} = 0.64$, $R_{DIA} = 2.0$, and $R_{DTT} = 0.5$. The fold change in ratio was 3.1 for fully oxidized parasites compared to control parasites. Full reduction of the parasites decreased the ratio by 0.8-fold.

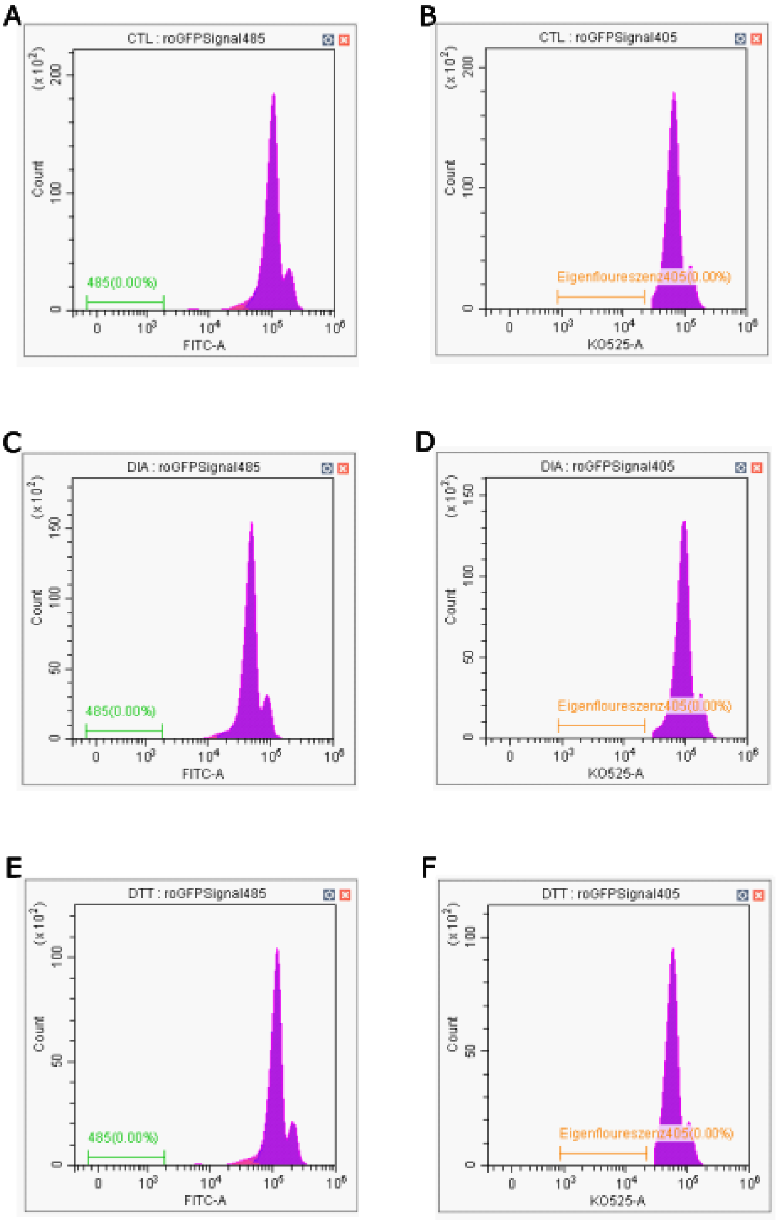

Figure 53. Histograms of flow cytometry measurements. Biosensor signal of untreated NF54*attB*$^{\text{hGrx1-sfroGFP2}}$ parasites in the KO252 channel ($\lambda_{\text{Exc.}}$ 405, $\lambda_{\text{Em.}}$ 585/42 nm) (**A**) and FITC channel ($\lambda_{\text{Exc.}}$ 488, $\lambda_{\text{Em.}}$ 585/42 nm) (**B**). NF54*attB*$^{\text{hGrx1-sfroGFP2}}$ parasites were fully oxidized using 1 mM DIA. The biosensor signal in the KO252 channel ($\lambda_{\text{Exc.}}$ 405, $\lambda_{\text{Em.}}$ 585/42 nm) increased (**C**), while the signal decreased in the FITC channel ($\lambda_{\text{Exc.}}$ 488, $\lambda_{\text{Em.}}$ 585/42 nm) (**D**). Full reduction of NF54*attB*$^{\text{hGrx1-sfroGFP2}}$ parasites using DTT led to a slight decrease in the signal of the KO252 channel ($\lambda_{\text{Exc.}}$ 405, $\lambda_{\text{Em.}}$ 585/42 nm) (**E**) whereas the signal in FITC channel ($\lambda_{\text{Exc.}}$ 488, $\lambda_{\text{Em.}}$ 585/42 nm) increased (**F**).

All other cell lines used in this work (NF54*attB*$^{\text{mSc.-I-SoNar}}$, NF54*attB*$^{\text{mSc.-I-iNap2}}$, and NF54*attB*$^{\text{sfpHluorin}}$) showed a clear sensor signal in the corresponding channels as well, which was distinguishable from the intrinsic fluorescence of the parasites. To detect the mScarlet-I signal of NF54*attB*$^{\text{mSc.-I-SoNar}}$ and NF54*attB*$^{\text{mSc.-I-iNap2}}$, the PE channel was used ($\lambda_{\text{Exc.}}$ 488, $\lambda_{\text{Em.}}$ 585/42 nm). The histograms of NF54*attB*$^{\text{mSc.-I-iNap2}}$ parasites are shown as an example in **Figure 54**. The different channels (FITC, KO525, PE, and ECD) are shown. In each case, the intrinsic fluorescence signal, represented in green, is clearly distinguishable from the sensor-positive signal of mSc.-I-iNap2, represented in purple.

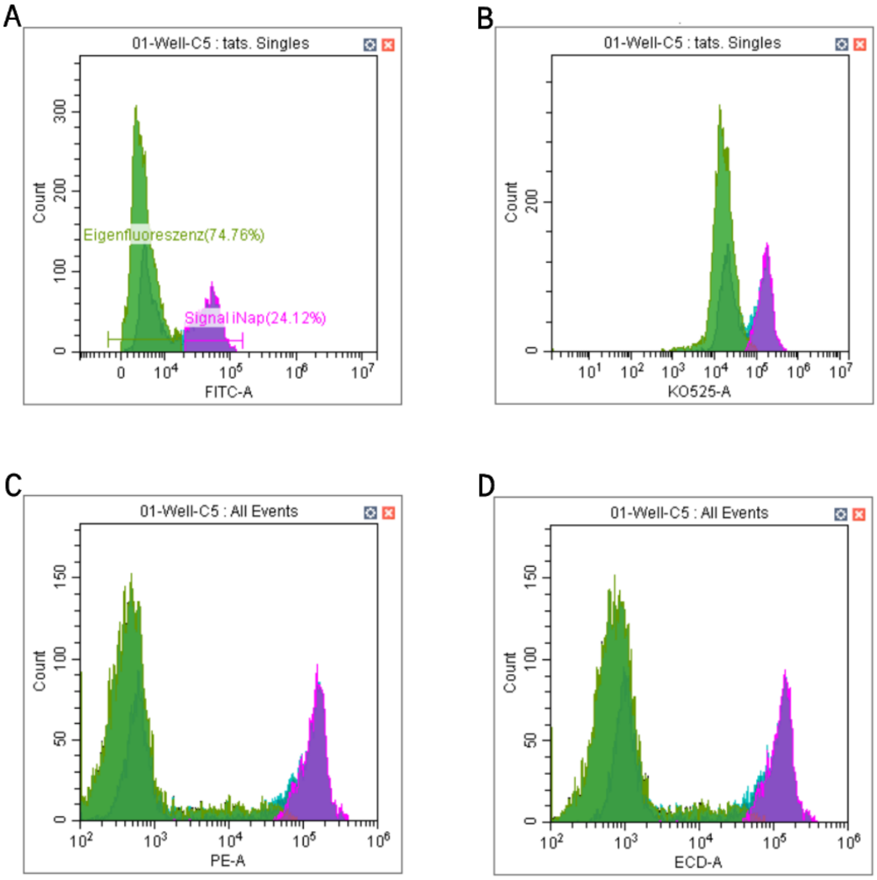

Figure 54. Histogram of NF54*attB*$^{mScarlet\text{-}I\text{-}iNap2}$ signal. Signal of NF54*attB*$^{mSc.\text{-}I\text{-}iNap2}$ parasites in FITC channel ($\lambda_{Exc.}$ 488, $\lambda_{Em.}$ 585/42 nm) (**A**), KO525 channel ($\lambda_{Exc.}$ 405, $\lambda_{Em.}$ 585/42 nm) (**B**), PE channel ($\lambda_{Exc.}$ 488, $\lambda_{Em.}$ 585/42 nm) (**C**), and ECD channel ($\lambda_{Exc.}$ 488, $\lambda_{Em.}$ 610/20 nm) (**D**). The parasites' intrinsic fluorescence signal is represented in green and the sensor fluorescence signal is represented in purple, respectively.

Following these basic flow cytometry settings, comparative redox measurements were performed using plate reader detection and flow cytometry. Therefore, NF54*attB*$^{hGrx1\text{-}sfroGFP2}$ trophozoite-stage parasites were magnetically enriched. Two different clonal parasite lines were used, namely NF54*attB*$^{hGrx1\text{-}sfroGFP2}$ A12 and H4, and their results were compared. The parasites were treated with 1 mM GSSG and 100 µM PD for 5 min and with 800 µM DHA for 1 h. These agents and concentrations were chosen as they were tested in previous studies [Kasozi et al. 2013; Bielitza et al. 2015; Mohring et al. 2016], and therefore the results could be compared even better. Moreover, fully oxidized (1 mM DIA) and fully reduced (10 mM DTT) parasites were measured to compare the increase or decrease in ratio. The incubation time was 5 min. Untreated parasites were used as a control. After incubation, the respective FI was measured using plate reader detection and flow cytometry. Subsequently, the ratio and OxD were calculated.

Within the measurements using the clonal parasite line NF54*attB*$^{hGrx1\text{-}sfroGFP2}$ A12 none of the tested substances (GSSG, PD, and DHA) led to a significant change in ratio when measured using plate reader detection. Treatment with DIA increased the ratio significantly (**Figure 55A**). Furthermore, the OxD values increased after treatment with all substances (**Table 7**). The flow cytometry measurements showed a comparable result for this clonal parasite line. A significant change in ratio was detected here for parasites treated with DIA and DTT (**Figure 55B**). OxD values were in a comparable range, except for GSSG and DHA treatment, which showed a lower OxD value for the flow cytometry measurement (**Table 7**).

The clonal parasite line NF54*attB*$^{hGrx1-sfroGFP2}$ H4 showed slight differences between both measurements. The increase in ratio after treatment with DIA was significant in both cases (**Figure 55C,D**). Treatment with PD and DHA significantly increased the redox ratio when measured using a plate reader (**Figure 55C**). In contrast, the measurement carried out using flow cytometry showed a significant effect for PD only. Here, GSSG did not increase the ratio significantly (**Figure 55D**). OxD values were in a comparable range except for DHA treatment. The OxD value of NF54*attB*$^{hGrx1-sfroGFP2}$ H4 after DHA treatment was higher when measured using a plate reader. However, this value showed a high standard deviation (**Table 7**).

OxD values between the two clonal parasite lines were comparable with a few exceptions. The OxD value of NF54*attB*$^{hGrx1-sfroGFP2}$ A12 after GSSG treatment measured using plate reader detection was higher compared to all other values. However, the standard deviation was very high here. Furthermore, treatment with DHA showed higher OxD values for both clonal parasite lines when measured using plate reader detection.

Taken together, the results between the two clonal parasite lines and both measuring principles varied only slightly. Subsequent measurements were carried out with the clonal parasite line NF54*attB*$^{hGrx1-sfroGFP2}$ H4 only using flow cytometry.

Table 7. Comparison of OxD values of NF54*attB*$^{hGrx1-sfroGFP2}$ cytosol after treatment with antimalarial agents and redox-active compounds using plate reader detection and flow cytometry.

	OxD [%]			
	Clone A12		Clone H4	
Substance	**Plate reader**	**Flow cytometry**	**Plate reader**	**Flow cytometry**
CTL	24.4 ± 10.3	38.5 ± 17.8	24.7 ± 10.4	19.7 ± 5.1
GSSG	48.9 ± 34.5	13.2 ± 4.6	13.0 ± 3.9	18.4 ± 11.1
PD	53.2 ± 24.4	49.9 ± 20.4	57.4 ± 16.0	50.5 ± 13.8
DHA	60.9 ± 5.3	39.6 ± 6.8	72.7 ± 13.8	30.1 ± 2.1

OxD = degree of oxidation, CTL = control, GSSG = oxidized glutathione, PD = plasmodione, DHA = dihydroartemisinin. Means ± SD are shown.

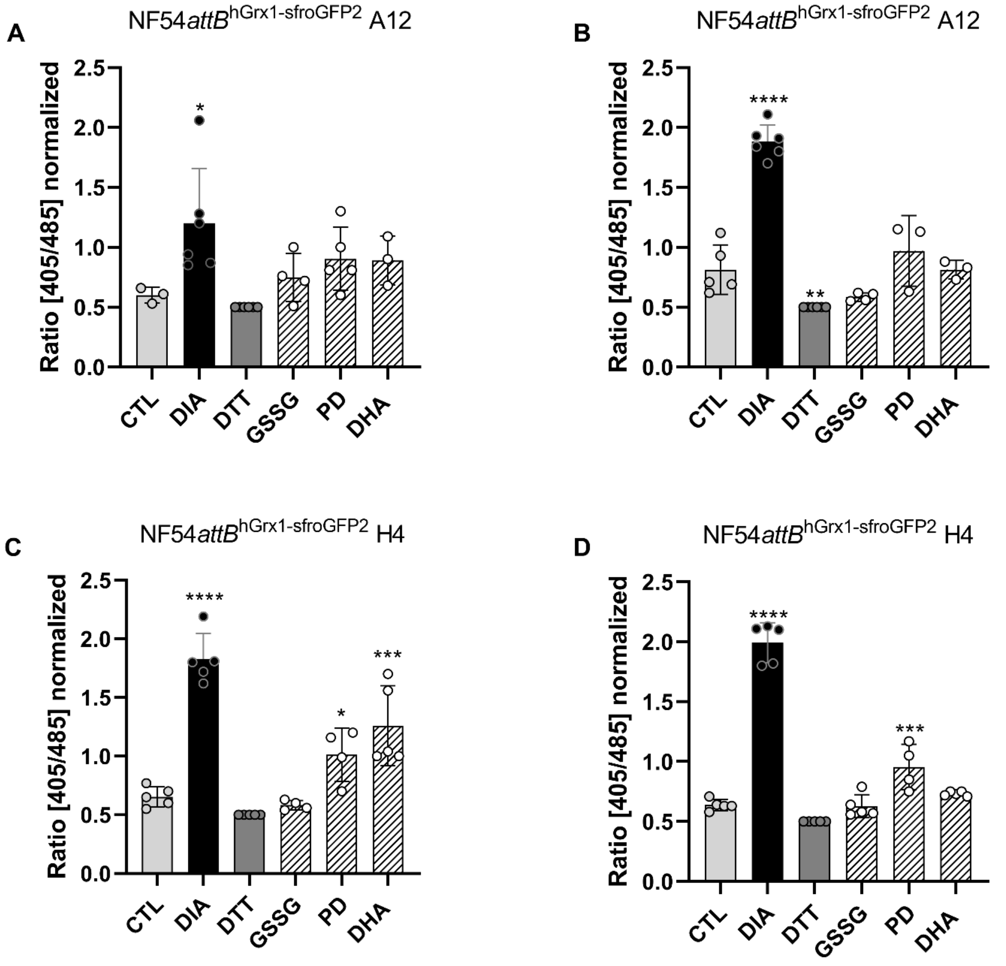

Figure 55. Comparison of redox measurements using plate reader detection and flow cytometry. Ratio of NF54*attB*$^{hGrx1\text{-}sfroGFP2}$ clone A12 after treatment with antimalarials or redox-active compounds using plate reader detection (**A**) or flow cytometry (**B**). Ratio of NF54*attB*$^{hGrx1\text{-}sfroGFP2}$ clone H4 after treatment with antimalarials or redox-active compounds using plate reader detection (**C**) or flow cytometry (**D**). Means ± SD are shown. The ratio of DTT-treated parasites was set to $R_{DTT} = 0.5$ and all other ratios were normalized accordingly. A one-way ANOVA test with 95% confidence intervals with the Dunnett's multiple comparison test was applied for statistical analysis of significance (*, $p < 0.05$; **, $p < 0.01$; ***, $p < 0.001$; ****, $p < 0.0001$). CTL = control, DIA = diamide, DTT = dithiothreitol, GSSG = oxidized glutathione, PD = plasmodione, DHA = dihydroartemisinin.

To establish a medium throughput assay, which allows the performance of biosensor-based measurements in a time-saving way and under physiological conditions, redox measurements were performed with whole cell culture without prior enrichment. This should help avoid time-consuming sample preparation. Furthermore, cells were fewer stressed and did not need to rest prior to further use. Sorbitol-synchronized trophozoite-stage parasites were used for this purpose as well. Again, the impact of GSSG, PD, and DHA on the redox ratio and the OxD, at the same concentrations and incubation times as used before, was determined using flow cytometry. None of the tested antimalarial agents and redox-active compounds significantly increased the redox ratio (**Figure 56A**). The OxD values for the measurements performed with 100,000 parasites were in a comparable range with measurements carried out using enriched parasites (**Table 8**). The same measurement was repeated with a lower cell number–1,000 events instead of 100,000 events–to shorten the measurement time and make it possible to perform a medium throughput assay. Here, none of the tested substances significantly increased the redox ratio (**Figure 56B**). OxD values were in general higher than the measurements with a larger sample size (**Table 8**). However, in this series of measurements, untreated control parasites also showed a higher OxD.

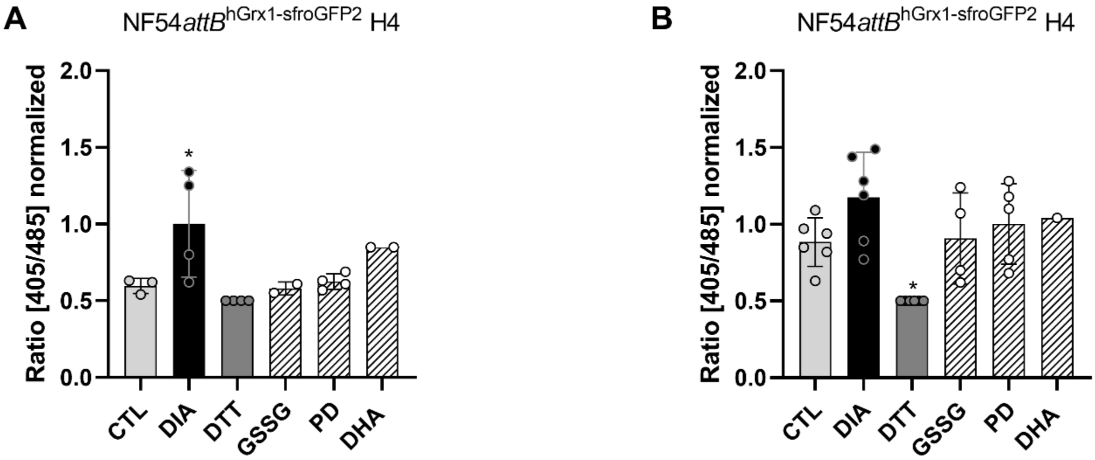

Figure 56. Comparison of cell number using flow cytometry. The redox ratio of NF54*attB*$^{\text{hGrx1-sfroGFP2}}$ clone H4 after treatment with antimalarial agents or redox-active compounds. Different cell numbers were used, and effects were compared. (**A**) The ratio was calculated based on the median FI of 100,000 cells per measurement. (**B**) The ratio calculated on basis of the median FI of 1,000 cells per measurement. Means ± SD are shown. The ratio of DTT-treated parasites was set to $R_{DTT} = 0.5$ and all other ratios were normalized accordingly. A one-way ANOVA test with 95% confidence intervals with the Dunnett's multiple comparison test was applied for statistical analysis of significance (*, $p < 0.05$; **, $p < 0.01$; ***, $p < 0.001$; ****, $p < 0.0001$). CTL = control, DIA = diamide, DTT = dithiothreitol, GSSG = oxidized glutathione, PD = plasmodione, DHA = dihydroartemisinin.

Table 8. Comparison of OxD values of NF54*attB*$^{\text{hGrx1-sfroGFP2}}$ cytosol after treatment with antimalarial agents and redox-active compounds.

	OxD [%]	
Substance	**100,000 parasites**	**1,000 parasites**
CTL	20.4 ± 4.9	66.3 ± 14.2
GSSG	15.3 ± 5.0	70.5 ± 11.0
PD	38.6 ± 11.8	80.5 ± 5.8
DHA	57.0 ± 2.0	56.4

OxD = degree of oxidation, CTL = control, DIA = diamide, DTT = dithiothreitol, GSSG = oxidized glutathione, PD = plasmodione, DHA = dihydroartemisinin. Means ± SD are shown.

Moreover, glutathione-dependent redox potential could be determined in *P. falciparum* for the first time using whole cell culture. The calculated cytosolic glutathione-dependent redox potential was - 303.13 mV.

4.5 Pharmacological effects of antimalarial agents on the cytosolic GSSG:GSH, NADPH, NADH:NAD$^+$, and pH of drug-sensitive NF54*attB* parasites

The previously established flow cytometry-based, 96-well plate assay was used to monitor the effect of different antimalarials and new compounds on the cytosolic GSSG:GSH, NADPH, NADH:NAD$^+$, and pH of drug-sensitive NF54*attB* parasites. Therefore, NF54*attB*^{sfpHluorin}, NF54*attB*$^{hGrx1\text{-}sfroGFP2}$, NF54*attB*$^{mSc.\text{-}I\text{-}iNap2}$, and NF54*attB*$^{mSc.\text{-}I\text{-}SoNar}$ parasites in whole cell culture were treated with different antimalarials and compounds with concentrations of 10x EC_{50} and 100x EC_{50}, respectively. The EC_{50} values used are listed in **Table 9**. The median FI of 1,000 sensor-positive parasites per measurement was used to calculate the biosensors fluorescence ratio after an incubation time of 5 min, 1 h, 3 h, 6 h, and 24 h. Additionally, the OxD was calculated using the hGrx1-sfroGFP2 fluorescence ratio. In the series of measurements carried out within this work, the effects of known antimalarial drugs, such as DHA, ATQ, and CQ, as well as compound 1o and PD–agents mediating antimalarial effect–on the cytosolic pH, GSSG:GSH, NADPH, and NADH:NAD+ were investigated. Moreover, the effects of the antibiotic DOXY were studied. Furthermore, the newly described compound SBI-750 [Berneburg et al. 2022], showing antimalarial effectivity in the nanomolar range was investigated in detail.

Table 9. EC_{50} values of antimalarial agents.

Antimalarial agent	EC_{50} value	Antimalarial agent	EC_{50} value
DHA	5.0 nM[1,2]	Compound 1o	5.6 nM[2]
ATQ	0.5 nM[2]	PD	50.0 nM[3]
CQ	6.9 nM[2]	SBI-750	83.8 nM[4]

[1][Nardella et al. 2020]; [2][Rahbari 2017a]; [3][Cichocki et al. 2021]; [4][Haeussler 2018].

In this work, treatment with 10x EC_{50} and 100x EC_{50} ATQ had no significant effect on the fluorescence ratio of the cytosolic biosensors at any of the concentrations and time points tested. The redox ratio of the fully oxidized biosensor (1 mM DIA), which was used as a control, significantly increased the ratio (**Figure 57A**). The fluorescence ratio of sfpHluorin was not affected at any of the time points or concentrations tested (**Figure 57B**). Although slight differences in the fluorescence ratio were seen for the ratio of mSc.-I-iNap2 for example after an incubation time of 3 h with 10x EC_{50} ATQ or 24 h incubation with 10x EC_{50} and 100x EC_{50} ATQ, none of those effects were significant. **Figure 57** shows an example of the redox ratio after ATQ treatment in comparison to control, fully oxidized, and fully reduced parasites (**Figure 57A**) and the fluorescence ratio of all other investigated biosensors after 3 h and 24 h of incubation with 10x EC_{50} and 100x EC_{50} ATQ (**Figure 57B**). OxD values after ATQ treatment were comparable to mock-treated control parasites and sometimes slightly lower. Throughout this series of measurements, the values remained at the same level (**Table 10**).

The changes in fluorescence ratios after 3 h and 24 h incubation times with CQ are shown as an example in **Figure 57**. The treatment with CQ showed the strongest effects after long-term incubation of 24 h (**Figure 57**). After this incubation period, the redox ratio of hGrx1-sfroGFP2 (**Figure 57C**) and the fluorescence ratios of mSc.-I-iNap2 and mSc.-I-SoNar (**Figure 57D**) increased, indicating an increase in GSSG:GSH, and changes in the NADPH levels, and NADH:NAD$^+$ ratios. However, only some of those effects were marginally significant, and measuring data showed high standard deviations. Ratios of DIA- and DTT-treated parasites were increased and decreased compared to mock-treated parasites, as expected. The cytosolic pH did not change at any of the time points or concentrations tested (**Figure 57D**). OxD values after CQ treatment increased slightly over time. However, most of the values were comparable with the OxD value of mock-treated control parasites. Only 24 h incubation with 100x EC_{50} CQ increased the OxD to 71.9% ± 16.6% (**Table 10**). Treatment with DHA, the active metabolite of all artemisinin-based drugs, significantly increased the cytosolic redox ratio (**Figure 57E**) and the fluorescence ratio of mSc.-I-SoNar (**Figure 57F**) after 24 h using a concentration of 100x EC_{50}. This effect was also seen with an increase in OxD (OxD_{DHA24h} = 75.0% ± 0.8%) compared to mock-treated parasites (OxD_{CTL24h} = 32.1% ± 6.6%) (**Table 10**). 24 h incubation with DHA at a concentration of 10x EC_{50} also increased the ratio of mSc.-I-SoNar. However, this increase was not significant (**Figure 57F**). An influence on the mSc.-I-iNap2 ratio or the sfpHluorin ratio could not be seen at any time point or concentration tested within this series of measurements. In addition to the change in fluorescence ratios after 24 h incubation with DHA, the effect of DHA treatment after 3 h incubation is shown in **Figure 57E and F** as an example.

Table 10. OxD values of NF54*attB*$^{hGrx1\text{-}sfroGFP2}$ cytosol after treatment with ATQ, CQ, and DHA.

10x EC_{50}			**100x EC_{50}**		
Substance	**Incubation time**	**OxD [%]**	**Substance**	**Incubation time**	**OxD [%]**
CTL (DMSO)	5 min	31.5 ± 9.7			
CTL (H_2O)	5 min	31.9 ± 7.3			
ATQ	5 min	34.4 ± 7.9	ATQ	5 min	29.8 ± 0.3
CQ	5 min	31.3 ± 7.7	CQ	5 min	28.9 ± 7.5
DHA	5 min	30.4 ± 10.1	DHA	5 min	29.4 ± 0.3
CTL (DMSO)	1 h	43.1 ± 13.7			
CTL (H_2O)	1 h	38.0 ± 5.5			
ATQ	1 h	32.8 ± 13.2	ATQ	1 h	31.0 ± 0.3
CQ	1 h	34.9 ± 10.6	CQ	1 h	44.0 ± 6.6
DHA	1 h	29.0 ± 8.5	DHA	1 h	45.2 ± 0.5
CTL (DMSO)	3 h	30.2 ± 11.1			
CTL (H_2O)	3 h	26.3 ± 3.9			
ATQ	3 h	19.7 ± 6.2	ATQ	3 h	22.7 ± 0.2
CQ	3 h	39.6 ± 16.8	CQ	3 h	46.8 ± 1.4
DHA	3 h	20.3 ± 9.5	DHA	3 h	29.7 ± 0.3
CTL (DMSO)	6 h	24.9 ± 10.1			
CTL (H_2O)	6 h	24.8 ± 6.9			
ATQ	6 h	23.6 ± 6.2	ATQ	6 h	21.2 ± 0.2
CQ	6 h	38.3 ± 12.2	CQ	6 h	47.5 ± 4.5
DHA	6 h	25.6 ± 3.3	DHA	6 h	29.7 ± 0.3
CTL (DMSO)	24 h	23.1 ± 5.3			
CTL (H_2O)	24 h	32.1 ± 6.6			
ATQ	24 h	17.2 ± 9.3	ATQ	24 h	13.5 ± 0.1
CQ	24 h	51.9 ± 37.3	CQ	24 h	71.9 ± 16.6
DHA	24 h	44.4 ± 10.5	DHA	24 h	75.0 ± 0.8

OxD = degree of oxidation; CTL = control, mock-treated parasites with DMSO or H_2O_{dd}, final concentration 1%; ATQ = atovaquone; CQ = chloroquine; DHA = dihydroartemisinin. Means ± SD are shown.

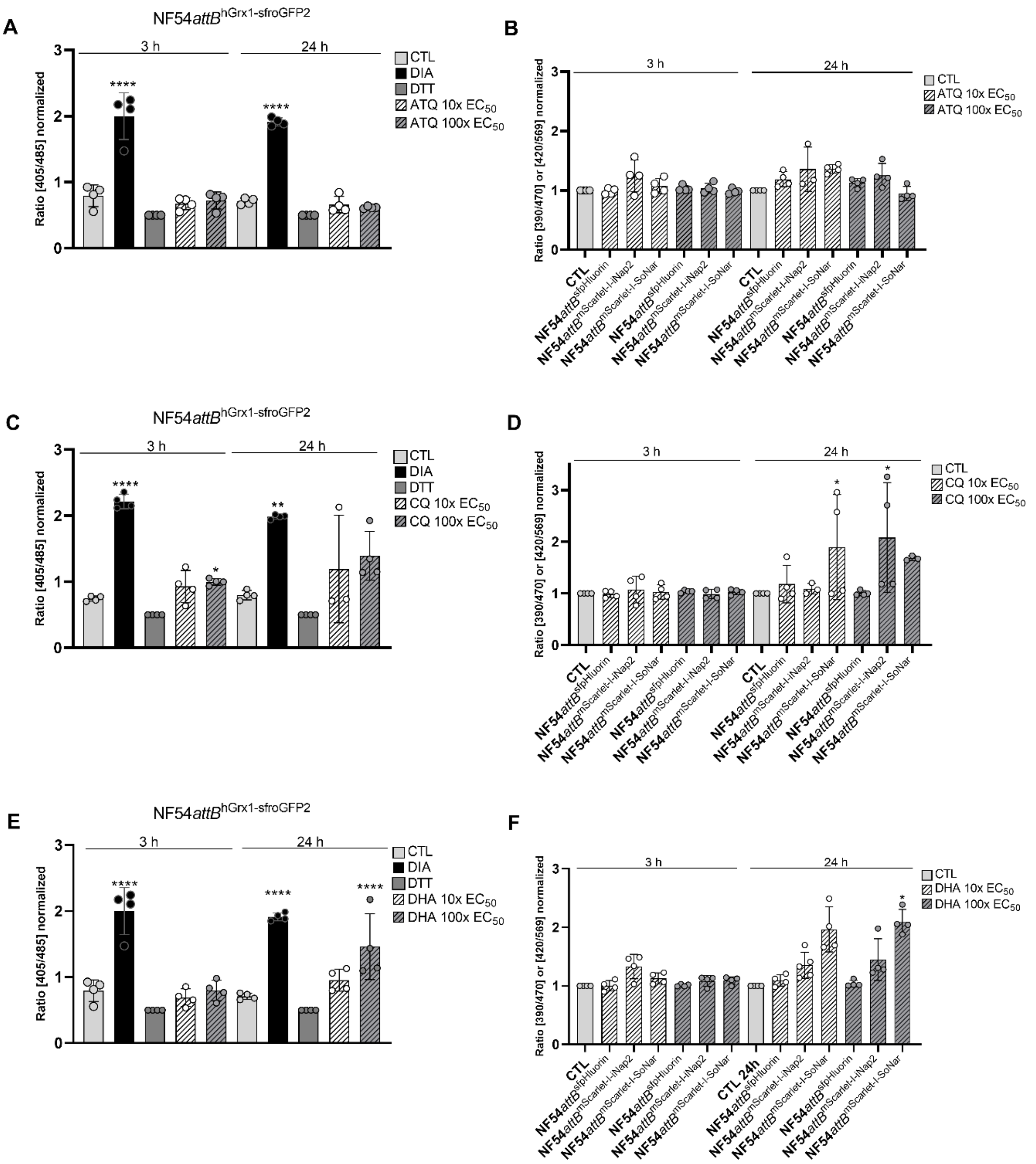

Figure 57. Effects of selected antimalarial agents on the cytosolic GSSG:GSH, NADPH, NADH:NAD$^+$, and pH of drug-sensitive NF54*attB P. falciparum* parasites. (**A**) The effect of ATQ on the redox ratio of NF54*attB*$^{\text{hGrx1-sfroGFP2}}$ trophozoite-stage parasites is shown. Mock-treated (1% DMSO) parasites were used as a control. Fully oxidized (1 mM DIA) and fully reduced (10 mM DTT) parasites were used to compare the redox ratio. (**B**) Change in the fluorescence ratio of sfpHluorin, mSc.-I-iNap2, and mSc.-I-SoNar after treatment with ATQ is shown. Mock-treated (1% DMSO) parasites were used as a control. (**C**) The redox ratio of NF54*attB*$^{\text{hGrx1-sfroGFP2}}$ trophozoite-stage parasites after treatment with CQ is shown. Mock-treated (1% H_2O_{dd}) parasites were used as a control. Fully oxidized (1 mM DIA) and fully reduced (10 mM DTT) parasites were used to compare the redox ratio. (**D**) The fluorescence ratio of NF54*attB*$^{\text{sfpHluorin}}$, NF54*attB*$^{\text{mSc.-I-iNap2}}$, and NF54*attB*$^{\text{mSc.-I-SoNar}}$ after CQ treatment is shown. Mock-treated (1% H_2O_{dd}) parasites were used as a control. (**E**) The effect of DHA on the redox ratio is shown. Mock-treated (1% DMSO) parasites were used as control. Fully oxidized (1 mM DIA) and fully reduced (10 mM DTT) parasites were used to compare the redox ratio. (**F**) Change in the fluorescence ratio of NF54*attB*$^{\text{sfpHluorin}}$, NF54*attB*$^{\text{mSc.-I-iNap2}}$, and NF54*attB*$^{\text{mSc.-I-SoNar}}$ after DHA treatment is shown. Mock-treated (1% DMSO) trophozoite-stage parasites were used as a control. Ratios were normalized; therefore, the redox ratio of fully reduced parasites was set to $R_{DTT} = 0.5$. For all the other biosensors, the ratio of control parasites was set to $R_{CTL} = 1$. Means ± SD are shown. Each data point represents the ratio calculated on basis of the median FI of 1,000 parasites. A one-way ANOVA test with 95% confidence intervals with the Dunnett's multiple comparison test was applied for statistical analysis of significance (*, $p < 0.05$; **, $p < 0.01$; ***, $p < 0.001$; ****, $p < 0.0001$). CTL = control, DIA = diamide, DTT = dithiothreitol, ATQ = atovaquone, CQ = chloroquine, DHA = dihydroartemisinin.

The impact of compound 1o, an antiplasmodial arylmethylamino steroid, on the cytosolic GSSG:GSH, NADPH, NADH:NAD$^+$, and pH was tested. After an incubation time of 6 h, 100x EC$_{50}$ of compound 1o significantly increased the redox ratio (**Figure 58A**). The OxD increased to 46.5% ± 0.5% in comparison to mock-treated control parasites that had an OxD value of 24.9% ± 0.3% (**Table 11**). None of the other conditions tested significantly affected the redox ratio. Long-term incubations (24 h) with 10x EC$_{50}$ of compound 1o significantly increased the fluorescence ratio of mSc.-I-iNap2 (**Figure 58B**). However, none of the other conditions tested affected the ratio. Additionally, the fluorescence ratio of mSc.-I-SoNar increased after 24 h incubation with 10x EC$_{50}$ of compound 1o. However, this effect was not significant. The fluorescence ratio of sfpHluorin was not affected to any extent within this series of measurements. As an example, the changes in fluorescence ratios after an incubation time of 6 h and 24 h with 10x EC$_{50}$ and 100x EC$_{50}$ of compound 1o are shown in **Figure 58**.

Treatment with PD, an antimalarial redox-active 3-benzyl-menadione, significantly increased the redox ratio after an incubation time of 6 h for both concentrations tested (**Figure 58C**). This oxidizing effect could also be seen with an increase in OxD to 54.1% ± 15.1% for 10x EC$_{50}$ and 51.0% ± 0.5% for 100x EC$_{50}$ PD, which was doubled in comparison to the OxD of mock-treated control parasites (OxD$_{CTL6h}$ = 24.9% ± 10.1%) (**Table 11**). 24 h incubation with 100x EC$_{50}$ of PD significantly affected the redox ratio (**Figure 58C**). The increase in OxD values was comparable to the OxD after 6 h incubation with PD (**Table 11**). Moreover, the fluorescence ratio of mSc.-I-iNap2 and mSc.-I-SoNar increased significantly after 24 h incubation with PD (**Figure 58D**). The cytosolic pH was not affected due to the measurements (**Figure 58D**). As an example, changes in fluorescence ratios after 6 h and 24 h incubation with PD are shown in **Figure 58**.

Table 11. OxD values of NF54*attB*$^{hGrx1\text{-}sfroGFP2}$ cytosol after treatment with compound 1o and PD.

10x EC_{50}			100x EC_{50}		
Substance	**Incubation time**	**OxD [%]**	**Substance**	**Incubation time**	**OxD [%]**
CTL (DMSO)	5 min	31.5 ± 9.7			
Compound 1o	5 min	36.2 ± 7.5	Compound 1o	5 min	35.5 ± 0.4
PD	5 min	41.8 ± 4.7	PD	5 min	36.1 ± 0.4
CTL (DMSO)	1 h	43.1 ± 13.7			
Compound 1o	1 h	42.6 ± 12.2	Compound 1o	1 h	45.3 ± 0.5
PD	1 h	44.2 ± 12.5	PD	1 h	45.3 ± 0.5
CTL (DMSO)	3 h	30.2 ± 11.1			
Compound 1o	3 h	44.5 ± 5.3	Compound 1o	3 h	48.6 ± 0.5
PD	3 h	50.6 ± 11.5	PD	3 h	52.6 ± 0.5
CTL (DMSO)	6 h	24.9 ± 10.1			
Compound 1o	6 h	37.8 ± 9.7	Compound 1o	6 h	46.5 ± 0.5
PD	6 h	54.1 ± 15.1	PD	6 h	51.0 ± 0.5
CTL (DMSO)	24 h	23.1 ± 5.3			
Compound 1o	24 h	43.9 ± 19.8	Compound 1o	24 h	24.3 ± 0.2
PD	24 h	39.7 ± 5.2	PD	24 h	58.4 ± 0.6

OxD = degree of oxidation; CTL = control, mock-treated parasites with DMSO, final concentration 1%; PD = plasmodione. Means ± SD are shown.

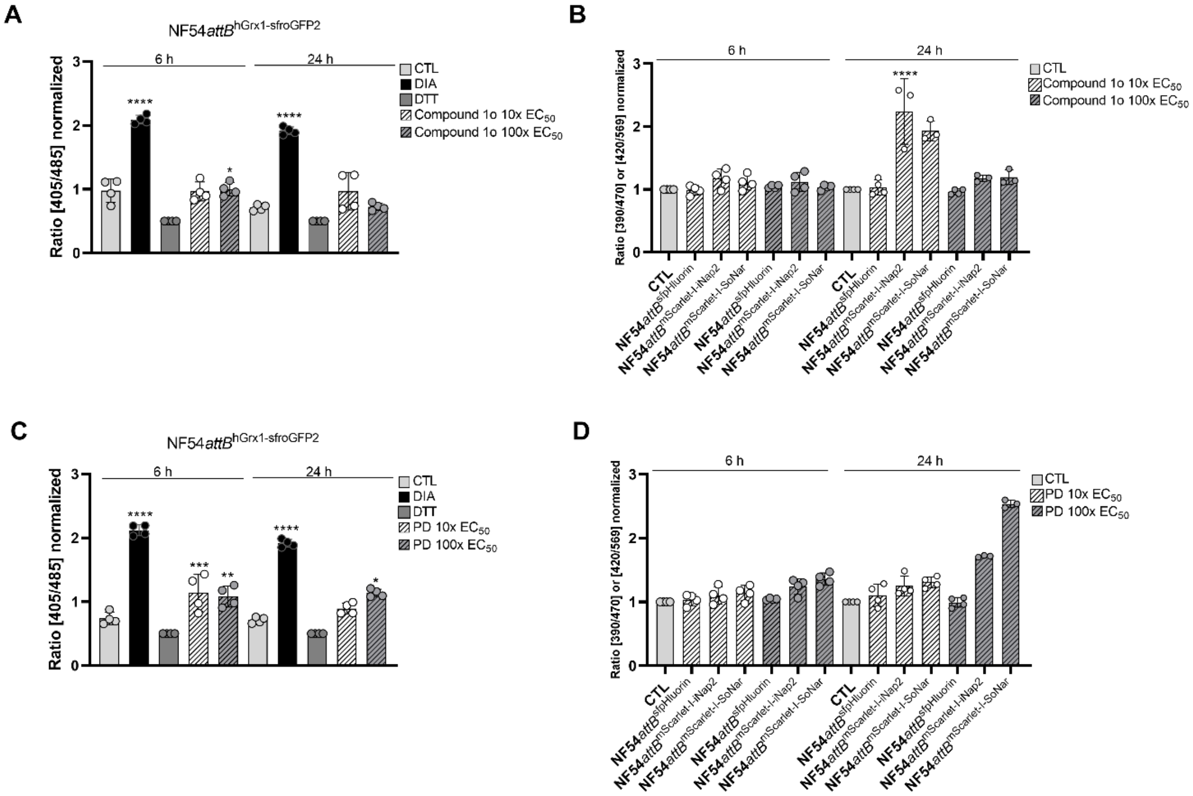

Figure 58. Effects of compound 1o and PD on the cytosolic GSSG:GSH, NADPH, NADH:NAD$^+$, and pH of drug-sensitive NF54*attB P. falciparum* parasites. (**A**) The effect of compound 1o on the redox ratio of NF54*attB*$^{hGrx1\text{-}sfroGFP2}$ trophozoite-stage parasites is shown. Mock-treated (1% DMSO) parasites were used as a control. Fully oxidized (1 mM DIA) and fully reduced (10 mM DTT) parasites were used to compare the redox ratio. (**B**) Change in the fluorescence ratio of sfpHluorin, mSc.-I-iNap2, and mSc.-I-SoNar after treatment with compound 1o is shown. Mock-treated (1% DMSO) parasites were used as a control. (**C**) The redox ratio of NF54*attB*$^{hGrx1\text{-}sfroGFP2}$ trophozoite-stage parasites after treatment with PD is shown. Mock-treated (1% DMSO) parasites were used as control. Fully oxidized (1 mM DIA) and fully reduced (10 mM DTT) parasites were used to compare the redox ratio. (**D**) Fluorescence ratio of NF54*attB*^{sfpHluorin}, NF54*attB*$^{mSc.\text{-}I\text{-}iNap2}$, and NF54*attB*$^{mSc.\text{-}I\text{-}SoNar}$ after PD treatment is shown. Mock-treated (1% DMSO) parasites were used as a control. Ratios were normalized; therefore, the redox ratio of fully reduced parasites was set to $R_{DTT} = 0.5$. For all other biosensors, the ratio of control parasites was set to $R_{CTL} = 1$. Means ± SD are shown. Each data point represents the ratio, calculated based on the median FI of 1,000 parasites. A one-way ANOVA test with 95% confidence intervals with the Dunnett's multiple comparison test was applied for statistical analysis of significance (*, $p < 0.05$; **, $p < 0.01$; ***, $p < 0.001$; ****, $p < 0.0001$). CTL = control, DIA = diamide, DTT = dithiothreitol, PD = plasmodione.

The concentration of the antibiotic DOXY, which mediates antimalarial effect that was tested in this series of measurements was 5 µM. Right after a short incubation period, strong effects on the fluorescence ratios of all biosensors tested were determined (**Figure 59**). In particular, the significant increase in the fluorescence ratio of sfpHluorin had to be considered (**Figure 59A**). After an incubation time of 1 h, the ratio increased significantly, suggesting an increase in the cytosolic pH. This increase peaked after an incubation time of 3 h. The redox ratio significantly increased after an incubation time of 1 h (**Figure 59B**), which was also reflected in the OxD values (**Table 12**). The strongest oxidation with an OxD value of 76.8% ± 4.9% was seen after an incubation time of 3 h (OxD_{CTL3h} = 26.3% ± 3.9%); afterward, the OxD values dropped again. Furthermore, the fluorescence ratios of mSc.-I-iNap2 (**Figure 59C**) and mSc.-I-SoNar (**Figure 59D**) were massively affected. Significant increases were seen after only 5 min of incubation. However, since DOXY seemed already to change the pH in the cytosol after an incubation time of 1 h, the interpretation of the mSc.-I-iNap2 and mSc.-I-SoNar data had to be taken carefully. Even though significant increases in fluorescence ratios were seen at almost all measured time points, the strongest effect seemed to be after an incubation period of 3 h for all investigated biosensors. After 24 h incubation, the ratio of most biosensors decreased and, except for the fluorescence ratio of mSc.-I-SoNar, was no longer significantly changed.

Table 12. OxD values of NF54*attB*$^{\text{hGrx1-sfroGFP2}}$ cytosol after treatment with DOXY.

Substance	**Incubation time**	**OxD [%]**
CTL (H_2O)	5 min	31.9 ± 7.3
DOXY (5 µM)	5 min	37.3 ± 5.3
CTL (H_2O)	1 h	38.0 ± 5.5
DOXY (5 µM)	1 h	69.9 ± 2.7
CTL (H_2O)	3 h	26.3 ± 3.9
DOXY (5 µM)	3 h	76.8 ± 5.0
CTL (H_2O)	6 h	24.8 ± 6.9
DOXY (5 µM)	6 h	63.9 ± 8.1
CTL (H_2O)	24 h	32.1 ± 6.6
DOXY (5 µM)	24 h	44.0 ± 17.6

OxD = degree of oxidation; CTL = control, mock-treated parasites with H_2O_{dd}, final concentration 1%; DOXY = doxycycline. Means ± SD are shown.

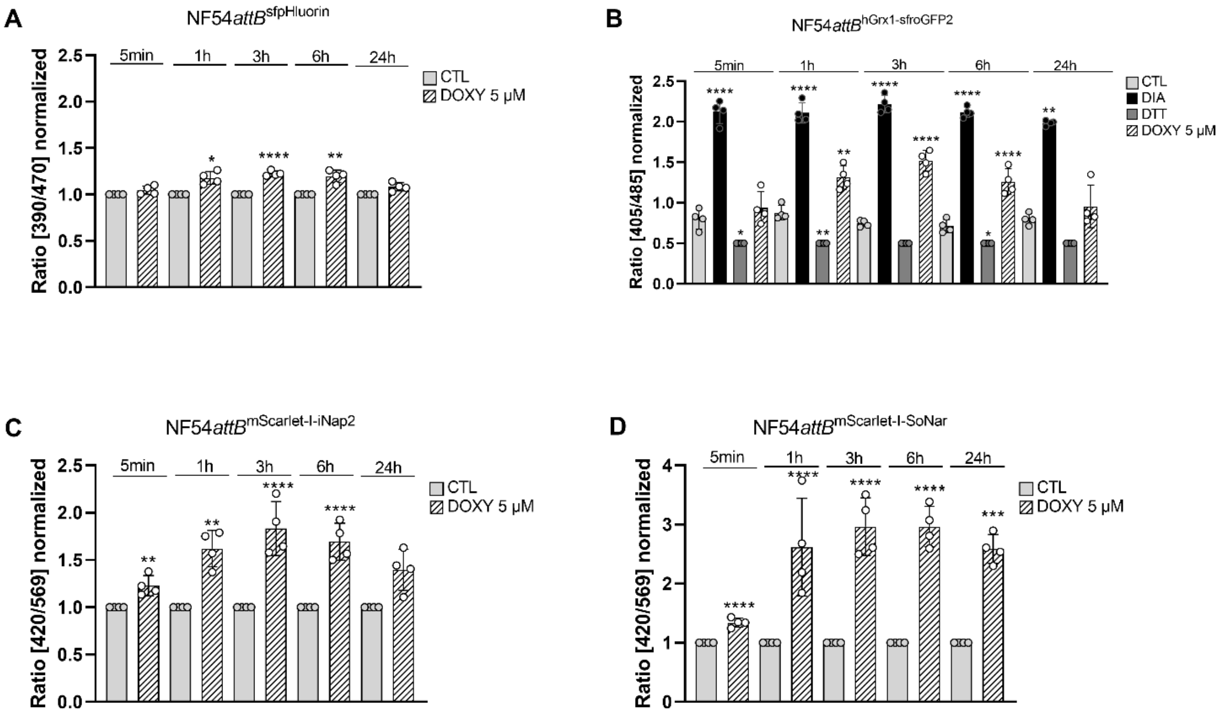

Figure 59. Effect of DOXY on the cytosolic GSSG:GSH, NADPH, NADH:NAD$^+$, and pH of drug-sensitive NF54*attB P. falciparum* parasites. The effect of 5 µM DOXY was investigated after an incubation time of 5 min up to 24 h. Mock-treated parasites (1% DMSO) were used as a control. (**A**) The fluorescence ratios of NF54*attB*$^{\text{sfpHluorin}}$ trophozoite-stage parasites after DOXY treatment are shown. (**B**) Changes in the redox ratios after treatment with DOXY are shown. Fully oxidized (1 mM DIA) and fully reduced (10 mM DTT) NF54*attB*$^{\text{hGrx1-sfroGFP2}}$ trophozoite-stage parasites were used to compare the redox ratio. (**C**) Changes in the fluorescence ratios of NF54*attB*$^{\text{mSc.-I-iNap2}}$ after DOXY treatment are shown. (**D**) The fluorescence ratio of NF54*attB*$^{\text{mSc.-I-SoNar}}$ trophozoite-stage parasites after treatment with DOXY are shown. The ratios were normalized; therefore, the redox ratio of fully reduced parasites was set to $R_{DTT} = 0.5$ and the control ratio of all other biosensors was set to $R_{CTL} = 1$. Means ± SD are shown. Each data point represents the ratio, calculated based on the median FI of 1,000 parasites. A one-way ANOVA test with 95% confidence intervals with the Dunnett's multiple comparison test was applied for statistical analysis of significance (*, $p < 0.05$; **, $p < 0.01$; ***, $p < 0.001$; ****, $p < 0.0001$). CTL = control, DIA = diamide, DTT = dithiothreitol, DOXY = doxycycline.

Treatment with the newly described antimalarial compound SBI-750 (compound N-(((2R,4S)-1-cyclobutyl-4-hydroxypyrrolidin-2-yl)methyl)-6-fluoro-4-methyl-11-oxo-10,11dihydrodibenzo[b,f]1,4-thiazepine-8-carboxamide (SBI-0797750)) had no effect on the fluorescence ratio of sfpHluorin (**Figure 60A**). The effects on the redox ratio, however, were very strong. Treatment with SBI-750 significantly increased the redox ratio, which can be seen after only 5 min of incubation with a concentration of 100x EC_{50} (**Figure 60B**). Here, the OxD increased to 73.1% ± 0.7% and thereby more than doubled compared to mock-treated control parasites ($OxD_{CTL5min}$ 31.5% ± 9.7%) (**Table 13**). During the measurement, the OxD increased in a time-dependent manner. After 24 h, 100x EC_{50} of SBI-750 oxidized the parasites' cytosol drastically (OxD_{SBI24h} = 106.1% ± 1.1%). Significant oxidative effects were also seen for lower SBI-750 concentrations (10x EC_{50}), starting–with a slight time delay–after an incubation time of 1 h. At this concentration, incubation for 24 h strongly affected the parasites' cytosol as well. The fluorescence ratio of mSc.-I-Nap2 decreased slightly for incubation times between 5 min and 6 h (**Figure 60C**). However, within this series of measurements, none of those effects were significant. After 24 h incubation with an SBI-750 concentration of 10x EC_{50}, the ratio of mSc.-I-iNap2 increased significantly, indicating an increase in NADPH level after this long incubation period. Furthermore, the NADH:NAD$^+$ ratio increased significantly after an incubation time of 24 h with an SBI-750 concentration of 10xEC$_{50}$ (**Figure 60D**). Shorter incubation times showed no significant effect.

Table 13. OxD values of NF54*attB*$^{\text{hGrx1-sfroGFP2}}$ cytosol after treatment with SBI-750.

10x EC$_{50}$			**100x EC$_{50}$**		
Substance	**Incubation time**	**OxD [%]**	**Substance**	**Incubation time**	**OxD [%]**
CTL (DMSO)	5 min	31.5 ± 9.7			
SBI-750	5 min	56.8 ± 2.7	SBI-750	5 min	73.1 ± 0.7
CTL (DMSO)	1 h	43.1 ± 13.7			
SBI-750	1 h	93.3 ± 7.6	SBI-750	1 h	90.4 ± 0.9
CTL (DMSO)	3 h	30.2 ± 11.1			
SBI-750	3 h	93.5 ± 2.0	SBI-750	3 h	95.2 ± 1.0
CTL (DMSO)	6 h	24.9 ± 10.1			
SBI-750	6 h	92.0 ± 3.5	SBI-750	6 h	99.1 ± 1.0
CTL (DMSO)	24 h	23.1 ± 5.3			
SBI-750	24 h	104.3 ± 9.8	SBI-750	24 h	106.1 ± 1.1

OxD = degree of oxidation; CTL = control, mock-treated parasites with DMSO final concentration 1%. Means ± SD are shown.

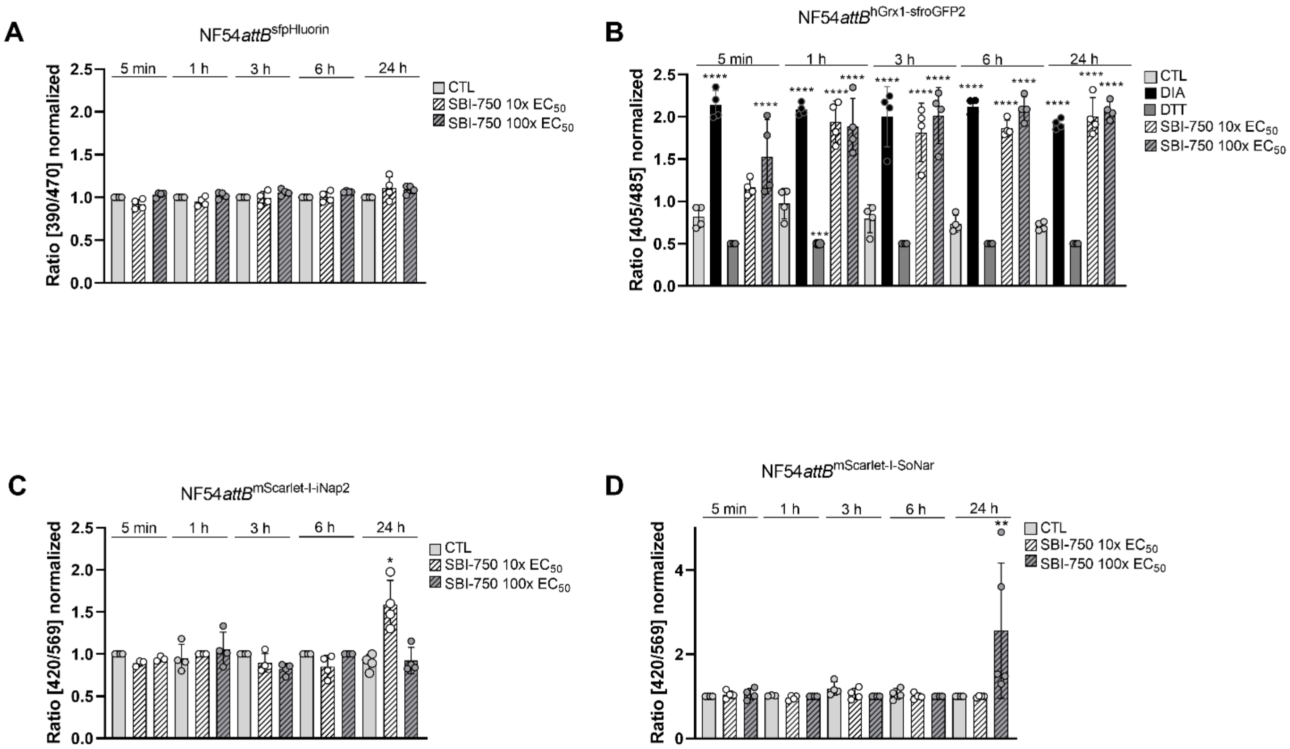

Figure 60. Effect of SBI-750 on the cytosolic GSSG:GSH, NADPH, NADH:NAD$^+$, and pH of drug-sensitive NF54*attB P. falciparum* parasites. The effect of 10x and 100x EC$_{50}$ of SBI-750 was investigated after an incubation time of 5 min up to 24 h. Mock-treated parasites (1% DMSO) were used as a control. (**A**) The fluorescence ratios of NF54*attB*^{sfpHluorin} trophozoite-stage parasites after treatment with SBI-750 are shown. (**B**) Changes in the redox ratios after treatment with SBI-750 are shown. Fully oxidized (1 mM DIA) and fully reduced (10 mM DTT) NF54*attB*$^{hGrx1\text{-}sfroGFP2}$ trophozoite-stage parasites were used to compare the redox ratio. (**C**) Changes in the fluorescence ratios of NF54*attB*$^{mSc.\text{-}I\text{-}iNap2}$ after SBI-750 treatment are shown. (**D**) The fluorescence ratios of NF54*attB*$^{mSc.\text{-}I\text{-}SoNar}$ trophozoite-stage parasites after treatment with SBI-750 are shown. The ratios were normalized; therefore, the redox ratio of fully reduced parasites was set to $R_{DTT} = 0.5$, and the control ratio of all other biosensors was set to $R_{CTL} = 1$. Means ± SD are shown. Each data point represents the ratio, calculated based on the median FI of 1,000 parasites. A one-way ANOVA test with 95% confidence intervals with the Dunnett's multiple comparison test was applied for statistical analysis of significance (*, $p < 0.05$; **, $p < 0.01$; ***, $p < 0.001$; ****, $p < 0.0001$). CTL = control, DIA = diamide, DTT = dithiothreitol.

4.6 Short-term incubation studies of SBI-750 on GSSG:GSH, NADPH, NADH:NAD$^+$, and pH of drug-sensitive NF54*attB* parasites

To study the oxidizing effect of SBI-750 in more detail, short-term incubation experiments up to an incubation time of 1 h were carried out with various SBI-750 concentrations (1x EC$_{50}$, 3x EC$_{50}$, 5x EC$_{50}$, 7x EC$_{50}$, 10x EC$_{50}$). After an incubation time of just 5 min, both concentrations 7x EC$_{50}$ and 10x EC$_{50}$ of SBI-750 increased the redox ratio significantly (**Figure 61B**). This significant increase in redox ratio was seen for all tested SBI-750 concentrations after an incubation time of 10 min. The redox ratio increased further; however, a longer incubation period of 1 h did not show a stronger effect on the redox ratio than an incubation time of 30 min. This time and concentration-dependent increase in oxidation could also be seen by means of the OxD (**Table 14**). Moreover, NADPH levels changed after short-term incubations. Initial effects were seen after an incubation period of 5 min (**Figure 61C**). The fluorescence ratio of mSc.-I-iNap2 decreased significantly after treatment with 7x EC_{50} and 10x EC_{50} of SBI-750. However, this effect was not yet as strong as the changes in the redox ratio. As the incubation time increased, the fluorescence ratios of mSc.-I-iNap2 decreased further, indicating a significant decrease in NADPH levels. The reduction in ratio after incubation times of 30 min and 1 h was comparable. No significant changes in the fluorescence ratios of mSc.-I-SoNar were seen for the conditions tested in this series of measurements (**Figure 61D**). Cytosolic pH values were stable for all tested conditions since no change in the fluorescence ratio of sfpHluorin could be determined (**Figure 61A**).

Table 14. OxD values of NF54*attB*$^{hGrx1\text{-}sfroGFP2}$ cytosol after short-term treatment with SBI-750.

	Incubation time			
SBI-750 concentration	**5 min**	**10 min**	**30 min**	**1 h**
	OxD [%]			
CTL (DMSO)	26.1 ± 7.4	51.2 ± 12.4	15.8 ± 8.1	37.1 ± 6.3
1x EC_{50}	34.2 ± 10.5	71.8 ± 10.3	66.0 ± 9.6	84.1 ± 7.3
3x EC_{50}	36.4 ± 12.2	82.2 ± 6.2	91.9 ± 3.7	99.9 ± 7.9
5x EC_{50}	43.9 ± 11.9	93.0 ± 6.1	96.1 ± 2.9	103.4 ± 0.4
7x EC_{50}	54.4 ± 4.1	94.3 ± 2.5	98.9 ± 1.1	103.7 ± 1.4
10x EC_{50}	61.9 ± 10.8	98.4 ± 2.2	100.5 ± 2.3	103.5 ± 1.6

CTL = control parasites, mock-treated with 1% DMSO. Means ± SD are shown.

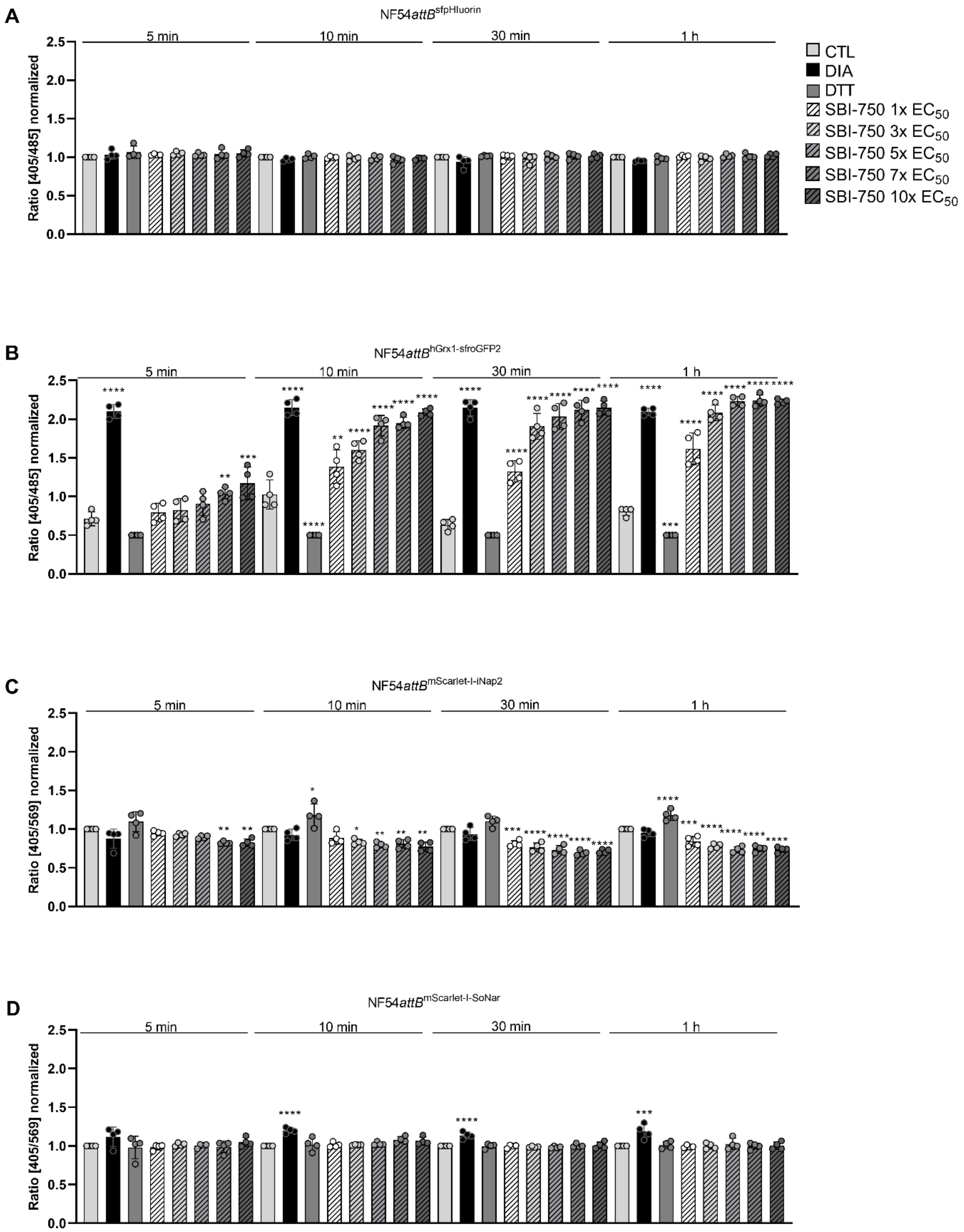

Figure 61. Effect of SBI-750 after short-term incubation on the cytosolic GSSG:GSH, NADPH, NADH:NAD$^+$, and pH of drug-sensitive NF54*attB P. falciparum* parasites. The effect of various SBI-750 concentrations (1x EC_{50}, 3x EC_{50}, 5x EC_{50}, 7x EC_{50}, and 10x EC_{50}) was investigated after an incubation time of 5 min up to 1 h. Mock-treated parasites (1% DMSO) were used as a control. (**A**) The fluorescence ratios of NF54*attB*^{sfpHluorin} after SBI-750 treatment are shown. (**B**) Changes in the redox ratios after treatment with SBI-750 are shown. Fully oxidized (1 mM DIA) and fully reduced (10 mM DTT) parasites were used to compare the redox ratio. (**C**). Changes in the fluorescence ratios of NF54*attB*$^{mSc.\text{-}I\text{-}iNap2}$ after treatment with SBI-750 are shown. (**D**) Ratios of NF54*attB*$^{mSc.\text{-}I\text{-}SoNar}$ trophozoite-stage parasites after treatment with SBI-750 are shown. Means ± SD are shown. Each data point represents the ratio, calculated on basis of the median FI of 1,000 parasites. The ratios were normalized; therefore, the redox ratio of fully reduced parasites was set to $R_{DTT} = 0.5$ and the control ratio of all other biosensors was set to $R_{CTL} = 1$. A one-way ANOVA test with 95% confidence intervals with the Dunnett's multiple comparison test was applied for statistical analysis of significance (*, $p < 0.05$; **, $p < 0.01$; ***, $p < 0.001$; ****, $p < 0.0001$). CTL = control, DIA = diamide, DTT = dithiothreitol.

In these short-term measurements, strong effects on redox metabolism could be seen. The fluorescence ratio of mSc.-I-SoNar did not change. To investigate the potential effects on energy metabolism, additional experiments with additional H_2O_2 treatment were performed. H_2O_2 was used as a naturally occurring stimulus, simulating additional 'oxidative stress'. For this purpose, the experiments were performed with NF54*attB*$^{\text{mSc.-I-SoNar}}$ trophozoite-stage parasites only. After an incubation time of 10 min with 10x EC_{50} of SBI-750, the cells were additionally stressed with 20 µM to 1,000 µM H_2O_2 for an additional 10 min. The fluorescence ratio did not change after this treatment (**Figure 62A**). Cells were further stressed twice with the same H_2O_2 concentrations. As seen in **Figure 62B**, the ratio of mSc.-I-SoNar decreased slightly for all conditions tested. However, none of these effects were significant.

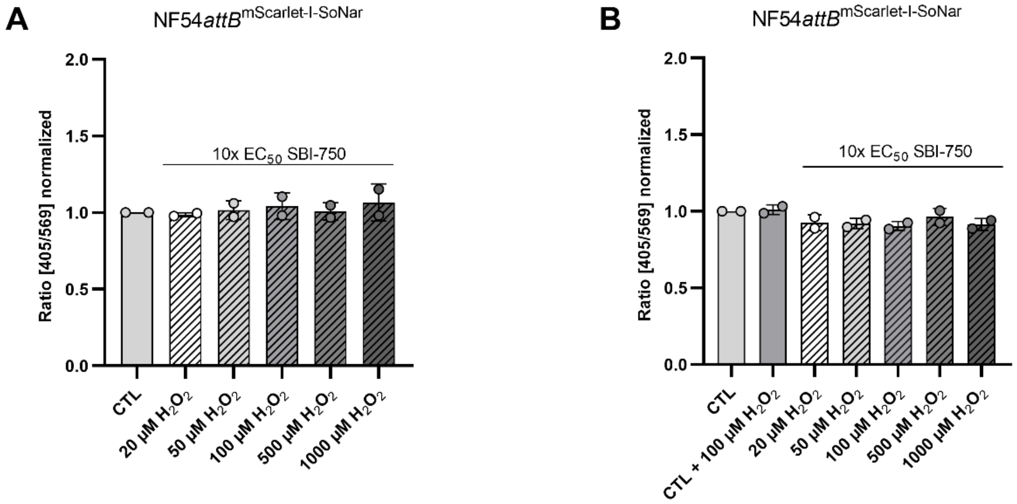

Figure 62. Effect of SBI-750 with additional H_2O_2 treatment on the cytosolic NADH:NAD$^+$ ratio of drug-sensitive NF54*attB P. falciparum* parasites. (**A**) Trophozoite-stage NF54*attB*$^{\text{mSc.-I-SoNar}}$ parasites were treated with 10x EC_{50} of SBI-750 for 10 min. Thereafter, cells were additionally treated with 20-1,000 µM H_2O_2 for 10 min. (**B**) Trophozoite-stage NF54*attB*$^{\text{mSc.-I-SoNar}}$ parasites were treated with 10x EC_{50} SBI-750 for 10 min. Thereafter, cells were additionally treated with 20-1,000 µM H_2O_2 for 10 min. This H_2O_2 pressure was performed three times in total. Mock-treated parasites (1% DMSO or 1% DMSO and 100 µM H_2O_2) were used as a control. The ratio was normalized to $R_{CTL} = 1$. Means ± SD of two biological and technical replications are shown. Each data point represents the ratio, calculated based on the median FI of 1,000 parasites. A one-way ANOVA test with 95% confidence intervals with the Dunnett's multiple comparison test was applied for statistical analysis of significance (*, $p < 0.05$; **, $p < 0.01$; ***, $p < 0.001$; ****, $p < 0.0001$). CTL = control.

5. DISCUSSION

5.1 The molecular basis of the improved fluorescence intensity of sfroGFP2

sfroGFP2 represents a redox-biosensor that contains all roGFP2 substitutions [Hanson et al. 2004], the full set of sf mutations (S30R, Y39N, N105T, Y145F, I171V, and A206V) [Pédelacq et al. 2006], and in addition the F223R mutation from roTurbo [Dooley et al. 2012]. Compared to (hGrx1-) roGFP2, sfroGFP2–when expressed in *P. falciparum* parasites–shows enhanced FI [Schuh et al. 2018; Heimsch et al. 2022]. This improved property greatly facilitates the performance of redox measurements in these small unicellular parasites. The improved FI enables accurate plotting of the region of interest (ROI), which is mandatory for CLSM-based measurements and particularly difficult for measurements in subcellular compartments. Furthermore, due to the improved FI, a lower laser power level can be used during the measurement, thereby reducing photobleaching–an irreversible reduction of the fluorophore [Bloedel Hearing Research Center; Waters 2013]. The improved FI also brings advantages for measurements using plate reader detection. The sensor signal can be distinguished from the background noise much better. Furthermore, a lower gain can be used. The fluorescence gain represents an amplification factor that allows for better data resolution. On the one hand a high gain enables the distinction between low signals and blanks, but on the other hand, it can easily result in overflow in case a brighter signal is present. As a result, an incorrect gain setting can lead to unusable data [BMG labtech]. Through the fusion of sfroGFP2 with hGrx1, a sensor was generated that not only brings considerable advantages for the redox measurements itself but can also efficiently display changes in the glutathione redox homeostasis. In previous studies, it was shown that non-fused sfroGFP2 equilibrates with GSH and GSSG in a time-dependent manner. However, oxidation of the sensor by GSSG was more pronounced in the presence of Grx, and even more efficient when Grx was directly linked to sfroGFP2 (hGrx1-sfroGFP2) [Schuh et al. 2018]. Therefore, for further studies, the hGrx1-sfroGFP2 fusion sensor was used, which can also be used in potentially Grx-free subcellular compartments to monitor changes in the glutathione redox homeostasis.

In this work, it was demonstrated that *P. falciparum* parasites stably expressing sfroGFP2 or hGrx1-sfroGFP2 showed an improved FI compared to parasites stably expressing hGrx1-roGFP2, which is in agreement with previously published results [Schuh et al. 2018]. As part of this work, the molecular basis, which is subjected to this improved characteristic should be identified. For this purpose, sfroGFP2 was characterized *in vitro* and *in cellulo* in comparison with other redox-biosensor variants.

Due to the ratiometric readout of the sensor, the absolute protein quantity is irrelevant for its functionality [Rahbari et al. 2017b]. However, since this might influence the FI, Western blot analysis was used to examine the expression levels of the different sensors, expressed in the cytosol of *P. falciparum* parasites. As a result, enhanced expression levels of (hGrx1)-sfroGFP2 over hGrx1-roGFP2 were excluded as a cause for the improved FI. Further *in vitro* investigations were therefore carried out.

During the development of sfroGFP2, the FI of the redox-biosensor should be improved, admittedly, other sensor properties should not be affected. To verify this, the pH responsiveness and the midpoint potential were determined. All redox-biosensor variants investigated within this work were pH-insensitive at physiologically meaningful pH values between pH 6.0 and 8.0. The calculated midpoint potentials of all investigated sensors were similar to roGFP2-based biosensors. Taken together, the investigated sensors are suitable for measuring oxidizing effects within the cytosol and most of the subcellular compartments of *Plasmodium* parasites. Surprisingly, *in vitro* (hGrx1)-roGFP2 showed a better FI over (hGrx1)-sfroGFP2. However, this contradictory behavior is in accordance with findings from previous work [Schuh et al. 2018; Schuh 2021]. The spectral behavior of the various redox-biosensor variants was investigated in more detail. Spectral scans were recorded at different temperatures, mimicking temperature conditions needed for *in cellulo* examinations. Thereby a more stable FI for sfroGFP2-based biosensors at higher temperatures (37 °C) was observed since the reduction in FI at higher temperature was almost negligible compared to the decrease in FI of roGFP2. The FI was in general higher for both hGrx1-fusion sensors (hGrx1-roGFP2 and hGrx1-sfroGFP2). Here, a potentially stabilizing effect of hGrx1 leading to an improvement in FI of the actual sensor was conceivable. For Trx that featured the Grx fold, a stabilizing effect that has a positive impact on other proteins has been described [LaVallie et al. 2000]. Based on this property, Trx is used as a fusion protein in expression and purification. Thus, protein aggregation can be avoided and the folding behavior of the protein of interest can be improved [LaVallie et al. 2000]. Another difference that may be responsible for the opposing *in vitro* and *in cellulo* results are potential protein-protein interactions occurring within the parasites. Recording spectral scans with recombinant biosensors equilibrated in parasite cell extract should mimic the environmental conditions present in the parasite. Also here, an improved FI of sfroGFP2 compared to roGFP2 was not monitored, ruling out protein-protein interactions as the only cause of improved spectral properties. However, findings from *in vivo* or *in cellulo* measurements cannot always be explained by usage of *in vitro* examinations, since the environment in an intact cell differs strongly from cell extract or buffer. The concentrations of different molecules as well as their interactions with membranes or each other cannot fully be remodeled *in vitro*. Thus, molecular crowding occurring within intact cells can lead to huge differences between measurements carried out *in vivo* or *in vitro* [Minton 2006; Rivas and Minton 2016]. Besides the surrounding milieu, furthermore, different cells used for expression can influence protein properties [Deller et al. 2016], which may partly explain differences between recombinant protein expressed using *E. coli* bacteria and redox-biosensors expressed by *Plasmodium* parasites. Taken together, the functional examinations could not explain the improved fluorescence properties of sfroGFP2 over roGFP2. However, regarding the fluorescence of fluorescent proteins, especially the structural stability of the fluorophore is important, since it maintains the conjugated π-electron system and the dipole moment, where both components are important for fluorescence [Lakowicz 2016]. To study this in more detail, structural examinations were performed. The structures of roGFP2 and sfroGFP2 differ, based on the sf substitutions contained in the latter, which results in a different conformation of residues between the two variants (**Figure 63**).

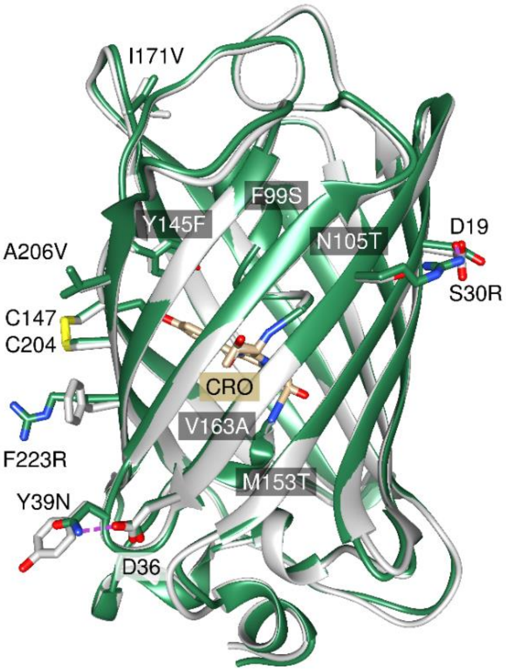

Figure 63. Comparison between the structural models of sfroGFP2 (green) and roGFP2 (light grey). The structure of roGFP2 (light grey) in overlay with the structure of sfroGFP2 (green) is shown. The amino acids modified in sfroGFP2 are labeled. The redox-related cysteines (C147 and C204) form a disulfide bridge, which is shown in yellow. The chromophore is shown in orange, CRO = chromophore. Adapted from [Schuh 2021].

Already Pédelacq and colleagues suggested that the both sf mutations S30R and Y39N have the highest impact on the folding stability of the protein, therefore, these specific mutations were reversed in sfroGFP2 [Pédelacq et al. 2006]. Comparing the crystal structures of sfroGFP2, sfroGFP2^{R30S}, and sfroGFP2^{N39Y} demonstrated the presence of a complex ion network in the surrounding of residue 30 in sfroGFP2 and sfroGFP2^{N39Y} (containing R30) that is disrupted in the crystal structure of sfroGFP2^{R30S} and accordingly not present in roGFP2, as this sensor does not contain the sf mutation S30R (**Figure 64**). This ion network between adjacent strands probably increased the stability of sfroGFP2.

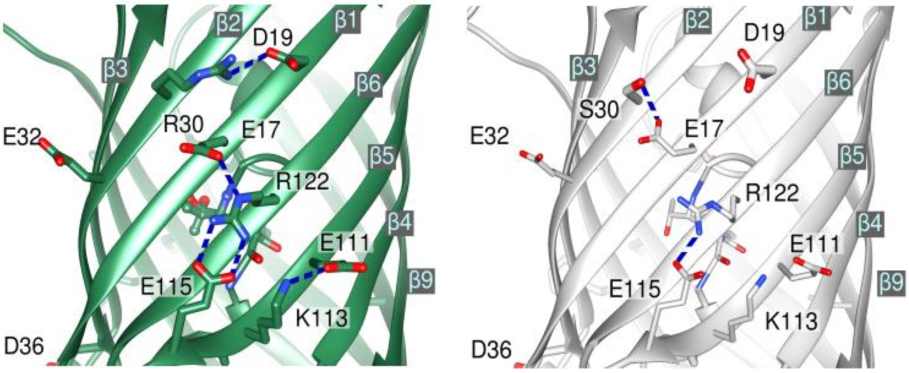

Figure 64. Close-up comparison of the structural models sfroGFP2 (green) and roGFP2 (light grey). Comparison of the surrounding of R30 in sfroGFP2 and S30 in the structure of roGFP2 (1jc1). Differences in the network of ionic interactions are visible.

This hypothesis was confirmed using rigidity analysis, which was performed in cooperation with Prof. Gohlke and Dr. Gertzen (Heinrich Heine University Düsseldorf), showing that the sf mutation S30R is important for the stability of sfroGFP2 (**Figure 65A**). Using this analysis demonstrated a higher structural stability for roGFP2 and sfroGFP2 over GFP. Furthermore, it was shown that in sfroGFP2 the sf substitutions stabilized the β-barrel structure and had an effect on the barrel center such that the fluorophore remained structurally stable until the end of the implemented constraint dilution simulation (**Figure 65B**) [Heimsch et al. 2022].

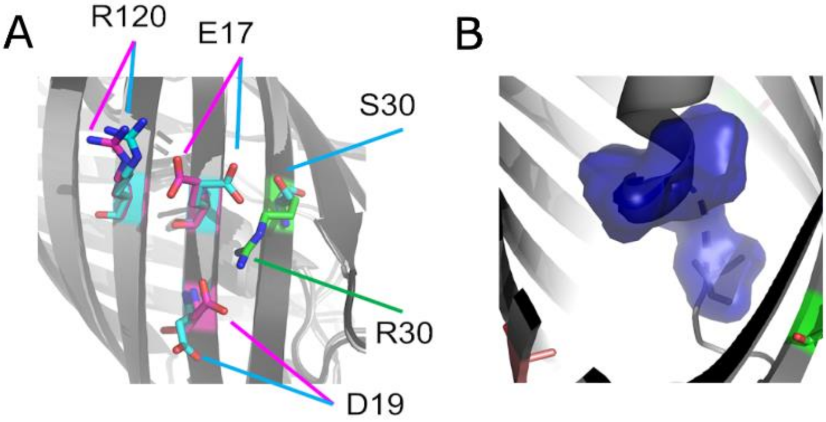

Figure 65. Close-ups of roGFP2 and sfroGFP2 during constraint dilution simulations. (**A**) sfroGFP2 (dark grey) and roGFP2 (medium grey) are superimposed. The presence of the sf mutations (green, R30 in sfroGFP2 and S30 in roGFP2) leads to a different network of the surrounding residues in sfroGFP2 (magenta) than in roGFP2 (light blue). (**B**) The fluorophore is the last rigid structure in sfroGFP2. Adapted from [Heimsch et al. 2022].

Taken together, sfroGFP2 reveals higher structural stability, which was identified as the molecular basis for the improved fluorescence intensity of this biosensor. These findings are of great interest for future sensor developments and the usage of biosensors in small unicellular organisms or subcellular compartments.

5.2 mScarlet-I-SoNar, mScarlet-I-iNap2, and sfpHluorin as dynamic biosensors for NADH:NAD$^+$, NADPH, and pH

Both biosensors SoNar and iNap2 were fused to mScarlet-I to overcome the pH dependency of the biosensors. Therewith, the pH response became much more stable, especially at physiologically relevant pH values between pH 7.0 and pH 8.0. The biosensor mSc.-I-iNap2 was strictly specific towards NADPH and displayed changes up to a concentration of 150 µM. Thus, this sensor was ideally suited to monitor changes in NADPH levels in *Plasmodium*, since NADPH concentrations of less than 100 µM are described for these parasites [Jortzik and Becker 2012]. However, by monitoring the fluorescence ratio of the biosensor after the addition of NADPH and NADP$^+$, it could be demonstrated, that NADP$^+$ was able to decrease the fluorescence ratio when added in high amounts (10 mM). Therewith, the increase in ratio upon NADPH addition was abolished. However, when defining the specificity of a biosensor, the situation present in the cell must always be taken into account. In mammalian cells, NADPH is much more abundant under homeostatic conditions compared to NADP$^+$. NADP$^+$:NADPH ratios of 1:20 to 1:100 are described for mammalian cells [Wamelink et al. 2008; Zhao et al. 2018]. In *Plasmodium* the antioxidative capacity of the parasites is highly dependent on NADPH, since the glutathione- and the thioredoxin-redox systems consume NADPH. As a result, the concentration of NADPH (< 100 µM) is higher than the concentration of NADP$^+$ [Jortzik and Becker 2012]. Therefore, the high NADP$^+$ concentrations that could affect the fluorescence ratio of the sensor *in vitro* are in a dimension, which does not occur physiologically in *Plasmodium*. The addition of 2 mM NADP$^+$, a concentration that is still many times higher than the NADP$^+$ concentration present in the cell, did no longer influence the fluorescence ratio. From a physiological point of view, therefore, mSc.-I-iNap2 is exclusively an NADPH sensor and not a ratio sensor (**Figure 66A**). This finding is in agreement with other publications [Tao et al. 2017].

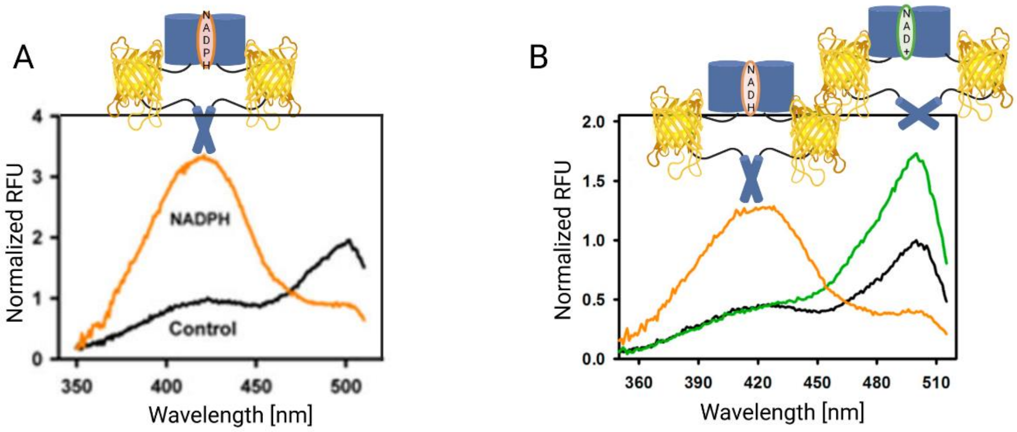

Figure 66. Excitation spectra of SoNar and iNap1. (**A**) Excitation spectra of iNap1 after the addition of 100 µM NADPH (orange). Spectra is normalized to the peak intensity in the control condition (black). Emission was measured at 530 nm, adapted from [Tao et al. 2017]. (**B**) Excitation spectra of SoNar after addition of 20 mM NAD$^+$ (green) or 20 mM NADH (orange). Spectra is normalized to the peak intensity in the control condition (black). Emission was measured at 530 nm, adapted from [Zhao et al. 2015]. RFU = relative fluorescence units. Created with BioRender.com.

The fluorescence ratio of mSc.-I-SoNar was sensitive to NADH and NAD^+ *in vitro* (**Figure 66B**). This sensor represents therefore a ratio sensor, which was already described by Zhao et al. 2015. Dependent on the cell or tissue to be investigated different NAD^+:NADH ratios are described. In the cytosol of different cells, ratios of 60:1 to 1,000:1 exist, however, some publications also report lower ratios of 0.1-10 [Lin and Guarente 2003; Zhao et al. 2018]. NAD^+ and NADH concentrations of the cytosol of HEK293T cells, for example, could be examined using different biosensors; here concentrations of ~106 µM for NAD^+ and ~0.12 µM for NADH were determined [Zhao et al. 2018]. Exact concentrations are not reported for *P. falciparum* so far, however, in infected human erythrocytes, the NAD^+ content of the RBC increases by 10-fold [Zerez et al. 1990] suggesting an upregulation of glycolytic pathways, which can also be confirmed by the increased consumption of glucose in contrast to uninfected RBC [Sherman 1979]. Since the parasitic energy production during the intraerythrocytic development is exclusively dependent on glycolysis [MacRae et al. 2013; O'Hara et al. 2014; Oyelade et al. 2016], one can assume, that NAD(H) is present in the parasite predominantly in its oxidized form. Thus, it seems reasonable that mSc.-I-SoNar can display the parasitic NADH:NAD^+ ratio.

Furthermore, the biosensors did not only react towards direct NAD(P)H treatment *in vitro* but also upon changes in physiological conditions within *in cellulo* examinations. For example, treating parasites, stably expressing mSc.-I-SoNar, with the pyruvate analogue oxamate that directly inhibits the conversion of pyruvate to lactate by the lactate dehydrogenase [Ye et al. 2016], increased the fluorescence ratio of mSc.-I-SoNar immediately. Due to the inhibition of lactate dehydrogenase, pyruvate is no longer converted to lactate, which would be accompanied by consumption of NADH. Since this pathway was inhibited, conversion of pyruvate and consumption of NADH was impeded. As a result, the NADH:NAD^+ ratio increased.

Moreover, the availability of glucose and the associated change in the metabolic state of the cell is accompanied with a change in the fluorescence ratio of mSc.-I-SoNar and mSc.-I-iNap2. It could be demonstrated in this work that glucose deprivation resulted in decreased FI of both sensors, which was associated with a reduction in the respective fluorescence ratio. The lack of glucose deprived glycolysis and PPP of educt (**Figure 67**), reduced the NADH:NAD^+ ratio and NADPH levels and thus, led to a reduced FI of the sensors.

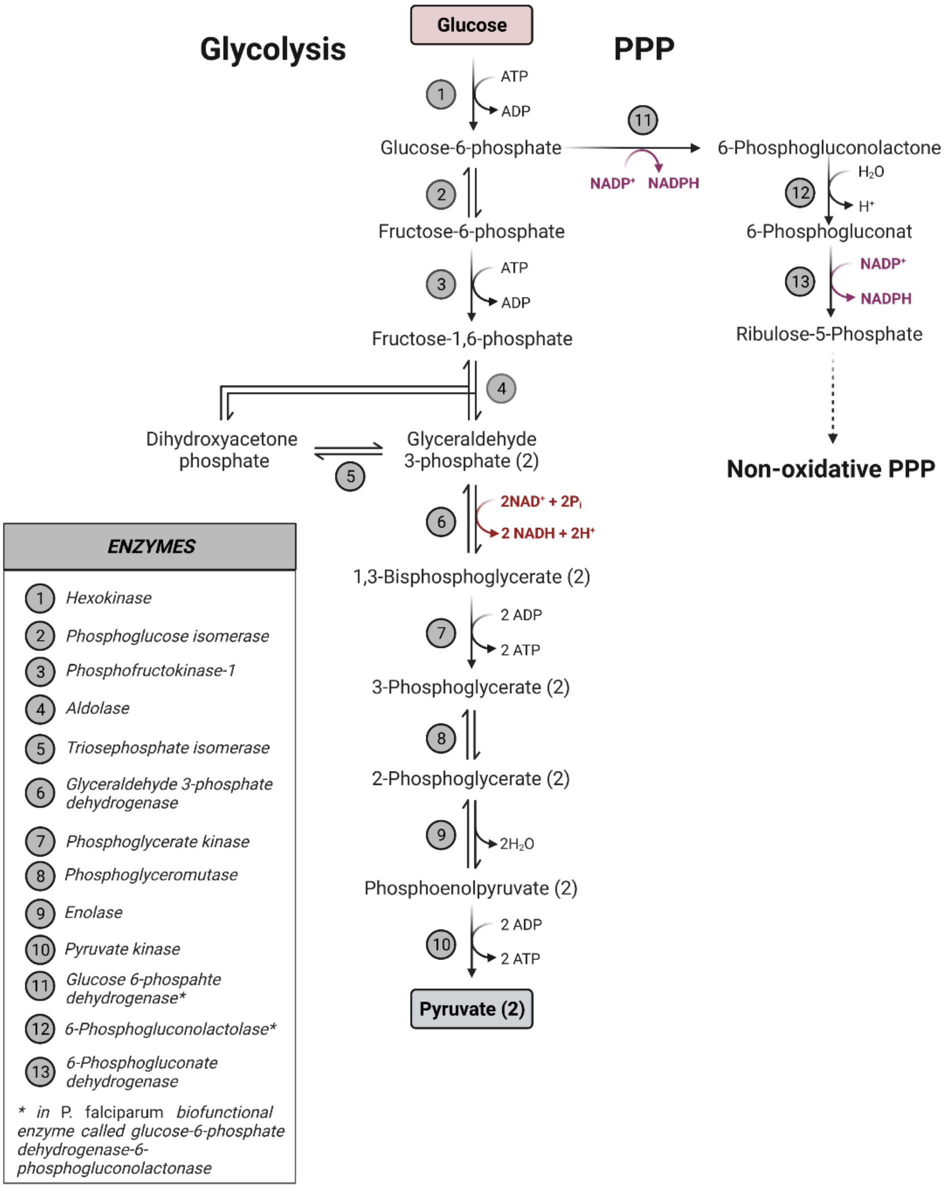

Figure 67. Connection between glycolysis and PPP. In the first step of the glycolysis, glucose is phosphorylated, leading to the generation of glucose-6-phosphate, which represents a connection between glycolysis and PPP. During glycolysis, NADH is generated. PPP provides NADPH. Both pathways cannot take place without glucose. Created with BioRender.com.

In addition to the usage of mSc.-I-SoNar and mSc.-I-iNap2, the improved pH biosensor sfpHluorin [Reifenrath and Boles 2018] was utilized in the present work. This sensor was used to monitor the pH in the parasites' cytosol to exclude extreme pH changes due to the treatment with antimalarials or compounds, which could, if very strong, still affect the ratio of mSc.-I.-SoNar and mSc.-I-iNap2. *In vitro* examinations demonstrated pH-dependent spectral properties of this biosensor. The FI of the excitation peak at 390 nm increased for alkaline pH values, whereas the excitation peak near 470 nm was highest for more acidic pH values. This is in accordance with other publications [Reifenrath and Boles 2018]. The resulting pH-dependent change in the fluorescence ratio was also consistent with the results of other publications [Reifenrath and Boles 2018]. These results confirmed the usage of sfpHluorin for monitoring changes in pH, ranging between pH 5.5 and pH 8.5.

5.3 Optimizing the detection of the glutathione redox potential in *Plasmodium falciparum*

Life-cell biosensor-based investigations of *Plasmodium* parasites were carried out up to now using CLSM or plate reader detection [Kasozi et al. 2013; Mohring et al. 2016, 2016; Rahbari et al. 2017b; Schuh et al. 2018]. CLSM enables the monitoring of a single cell and provides information on cell morphology and the parasite-stage. However, the amount of parasites investigated is small, with normally up to 15 trophozoite-stage parasites per measurement. Furthermore, the sample preparation process is time-consuming, since this measurement method requires the enrichment of trophozoite-staged parasites, using magnetic cell separation. This magnetical enrichment is not just time-consuming but also represents an additional stress factor for the parasites. Moreover, magnetic enrichment of parasites is possible only at specific parasite-stages, since this methodology requires the presence of haemozoin, the paramagnetic malaria pigment produced from heme due to hemoglobin digestion. This insoluble crystalline dimer of FPPIX is only detectable at developmental stages beyond the ring form [Rebelo et al. 2012; Delahunt et al. 2014]. Based on this, it has so far been impossible to study ring-stage parasites using genetically encoded biosensors. Moreover, the measurement itself and the following data analysis is time-consuming as the ROI has to be drawn around every single parasite to obtain the specific FI that is needed to calculate the ratio. In comparison, using plate reader detection allows the measurement of a whole cell population, leading to more robust data. For these measurements, normally up to 2.0x 10^6 parasites per well are used [Schuh 2021]. Additionally, the measurement process and the data analysis are quickly performed since there is no need to draw an ROI. The plate reader software displays the FI of emission after excitation at both wavelengths right away. Nonetheless, the sample preparation process requires the enrichment of trophozoite-stage parasites as well and is therefore as time-consuming and limiting regarding the investigated parasite-stages as the sample preparation process for CLSM measurements. Furthermore, information about a single cell is lost since only cell populations can be measured using plate reader detection. Another point to consider is the correction of the fluorescence signal by the intrinsic fluorescence of the cell or even the fluorescence signal of a used compound. While correction is very simple when using flow cytometry, this can be problematic, when measurements are performed using plate reader detection. Here, the intrinsic fluorescence of the measured cell population cannot be detected. Instead, the intrinsic fluorescence of another non-transfected population must be used for the correction. Even if trophozoite-stages are always used, the age of the parasites may vary (20 hpi to 40 hpi). Moreover, if the fluorescence signal of the transfected cell population is very low, the correction may result in negative fluorescence values, making it impossible to calculate a fluorescence ratio. All these difficulties do not play a role when using flow cytometry. Furthermore, the establishment of a flow cytometry-based measuring-method paves the way for studying effects on different parasite-stages in a fast way and under normal cell culture conditions. The aim of this work was to develop a medium-throughput assay that allows the measurement of non-enriched parasites in a 96-well plate system. The stepwise comparison of both measuring methods–plate reader detection versus flow cytometry–performed within this work demonstrated marginal differences between both methods that can be explained by an increased standard deviation of some samples, a different OxD of the control sample, certain differences between the clonal parasite lines, and the different principles of the two measurement methods. Usage of plate reader detection enables the measurement of a whole cell population. With regard to biosensor measurements, the fluorescence signal from this whole population is used to calculate the ratio. In contrast, using flow cytometry a rapid multi-parametric analysis of single cells in solution is possible. Based on this measurement method, each cell is analyzed for visible light scatter (FSC and SSC) and one or multiple fluorescence parameters. Thereby, the FSC indicates the relative size of the cell and the SSC the internal complexity or granularity of the cell. Due to the fluidic system, the sample is focused on the laser intercept point, where it can be analyzed. The optical system, consisting of lasers and collection optics, generates visible and fluorescent light signals. Here, a series of dichroic filters direct the fluorescent light to specific detectors and bandpass filters, determining the specific wavelengths, so that each individual fluorochrome can be detected and measured [McKinnon 2018]. The first flow cytometry-based examinations using NF54*attB*$^{\text{hGrx1-sfroGFP2}}$ parasites showed a clear sensor signal, which was easily distinguishable from the intrinsic fluorescence of the parasites. Treating the parasites with DIA led to an oxidation of the sensor, which resulted in an increase in ratio by 3.1-fold. Reduction of the sensor by treating the parasite with DTT decreased the ratio by 0.8-fold. These changes in ratio were in a range that is known from former plate reader or CLSM measurements [Kasozi et al. 2013; Mohring et al. 2016]. The associated histogram showed for each peak, a slight “shoulder” next to the main peak, representing a small cell population that however, seemed to have a stronger fluorescence signal compared to the parasite population that was reflected by the main peak. This, most likely, reflected the fluorescence of multiple infected erythrocytes. Since no sorter was available to separate these individual populations from each other and subsequently examine them microscopically, this remains only a conjecture. To detect the mScarlet-I signal from both biosensors mSc.-I-SoNar and mSc.-I-iNap2, the PE ($\lambda_{\text{Exc.}}$ 488 nm, $\lambda_{\text{Em.}}$ 585/42 nm) channel was used. Usage of the ECD channel ($\lambda_{\text{Exc.}}$ 488 nm, $\lambda_{\text{Em.}}$ 610/20 nm) for the measurements would have also been possible. However, the separation between the parasites’ intrinsic signal and the sensor signal and therewith the signal to noise ratio was not as good, as a result, the PE channel was used ultimately.

In these first comparative studies, the influence of GSSG, DHA, and PD on the glutathione-dependent redox potential was investigated. Although the used concentrations were quite high, they were chosen, since the influence of these substances in said concentrations had already been studied in previous work [Kasozi et al. 2013; Bielitza et al. 2015; Mohring et al. 2016]. All substances increased the redox ratio, whereas the effect of GSSG in the measurements performed in this work did not show such a strong effect as in the measurements performed by Kasozi and colleagues. However, it must be taken into account that all previously performed measurements were performed with transient transfected 3D7 *P. falciparum* parasites and the measurement was performed using CLSM. Therefore, the investigated cell number was smaller–up to 15 parasites per measurement for CLSM versus several hundred thousand cells, used for flow cytometry and plate reader detections. Comparative measurements were then performed with enriched and non-enriched parasites using flow cytometry. Furthermore, different cell numbers per measurement were tested. Individual differences between the measurements were identified here as well. Again, an increased standard deviation, as well as already basally more oxidized parasites, seem to be causal for the measurement differences. Comparing the measurements with non-enriched cells showed higher OxD values after drug treatment for the measurement with 1,000 cells compared to the measurement with 100,000 cells. However, the parasites used for the measurement with 1,000 cells seemed to be generally more oxidized, since the OxD value of the control group was already high. Comparing the change in OxD values between the receptive control group and the treated groups revealed changes in OxD that were in a comparable range, even if the OxD values of the treated parasites were, in general, higher for measurements with 1,000 cells. It was hypothesized that this effect was not due to the smaller sample size used, but rather a random effect of these parasites. Subsequent experiments using 1,000 cells per measurement showed an OxD value for the control group that was in the same range as the OxD values of the control group examined in previously performed measurements with enriched parasites or 100,000 non-enriched cells. The performance of a flow cytometry measurement using 1,000 iRBCs per measurement was identified as a reliable method and applied for further studies. In addition, using flow cytometry, the glutathione-dependent redox potential of the cytosol of NF54*attB* parasites in whole cell culture could be determined for the first time. The calculated E_{GSH} value was -303 mV, which is comparable to previous measurements with magnetically enriched cells. In previous studies, the parasite lines NF54*attB*$^{hGrx1\text{-}roGFP2}$ and NF54*attB*^{sfroGFP2} were used to determine the parasites' cytosolic glutathione-dependent redox potential via CLSM. The E_{GSH} values here were -304 mV and - 303 mV, respectively [Schuh et al. 2018]. The E_{GSH} of 3D7 *P. falciparum* parasites was in comparison more negative, with a value of -309 mV [Mohring et al. 2017].

Taken together, it could be demonstrated that the usage of flow cytometry shows comparable results to previous measurement methods and has considerable advantages over CLSM and plate reader detection.

5.4 Pharmacological effects of antimalarial agents on the cytosolic GSSG:GSH, NADPH, NADH:NAD$^+$, and pH of drug-sensitive *Plasmodium falciparum* NF54*attB* parasites

Pharmacological effects of different antimalarial agents on the cytosolic GSSG:GSH, NADPH, and NADH:NAD$^+$ were investigated. In addition, the cytosolic pH was monitored. Prior to the *in cellulo* measurements, a direct interaction of the antimalarial agents and the used biosensors was excluded using *in vitro* examinations. The ratio of recombinant hGrx1-sfroGFP2 was affected when incubated with 1 mM DIA, 10 mM DTT, or 10% DMSO. These results were as expected since DIA directly oxidizes the cysteines C147 and C204, which leads to the formation of a disulfide bridge. This direct chemical interaction with the sensor is used as a control. The same applies to the incubation with DTT, which reduced the ratio. High DMSO concentrations (10%) did not only affect the sensor but could also have negative effects on the parasites. For *in cellulo* experiments, therefore, a final DMSO concentration of maximal 1% was used. Certain antimalarials affected the ratio of the sensor when used in very high concentrations. However, this was already seen previously for certain substances [Schuh et al. 2018]. These antimalarials were therefore not used at all within *in cellulo* experiments or in such low concentrations that a direct influence on the sensor could be excluded. Surprisingly, within these *in vitro* examinations different concentrations of GSH increased the ratio, however, a reduction in the ratio would have been expected here. This phenomenon was explained by the used glutathione, which was presumable not exclusively present in its reduced form. To investigate the effects of GSH on the sensor in more detail, the usage of a backup system consisting of GR and NADPH, which keeps glutathione in its reduced form, would be useful. In previous studies, however, the reaction of different redox-sensors (including hGrx1-sfroGFP2) after incubation with GSH and GSSG, using a backup system, has already been carried out [Schuh et al. 2018]. Here, it was shown that the redox ratio decreased under conditions that keep GSH in its reduced form. Furthermore, it was also shown that the ratio of mSc.-I-SoNar and mSc-I-iNap2 was affected by certain antimalarials in high concentrations. These substances were also either not used or used in concentrations that showed no direct influence on the sensors. After long-term incubations, the NAD(P)H controls used showed hardly any effect on the ratio. These effects could be explained by the oxidation of the substances over time and were thus, as expected.

5.4.1 Effects of commonly used antimalarials

Live-cell imaging of the stably expressed biosensors after short-, mid-, and long-term antimalarial drug incubations confirmed, that the mode of action of ATQ, CQ, and DHA may not be linked to a disruption of the cytosolic redox-metabolism. Besides confirming previous results [Kasozi et al. 2013; Schuh et al. 2018], it was shown for the first time, that ATQ did not influence the cytosolic NADH:NAD$^+$ ratio, or the cytosolic pH. Schuh et al. tested the effect of ATQ on the redox ratio of NF54*attB*$^{\text{hGrx1-roGFP2}}$ and NF54*attB*$^{\text{sfroGFP2}}$ after an incubation time of 4 h and 24 h. Within those experiments, none of the tested concentrations showed a significant impact on the cytosolic redox ratio [Schuh et al. 2018]. In contrast to the cytosolic effects, 4 h ATQ incubation increased the OxD in the mitochondria of NF54*attB* parasites [Gnädig et al. 2020]. Based on the working principle of ATQ it is not surprising that the OxD of this specific subcellular compartment is affected but not the parasites' cytosol. The inhibition of the mitochondrial electron transport chain by ATQ leads to a rapid failure of the membrane potential within the mitochondria [Schlitzer 2008]. However, since

ATP synthesis via oxidative phosphorylation is believed to be non-essential in the asexual-stages of *Plasmodium*, the major lethal effects of ATQ seem to be attributed to the inhibition of ubiquinone redox regeneration, which is required for pyrimidine biosynthesis [Verdaguer et al. 2021]. During pyrimidine biosynthesis, uridine-5-monophosphate is formed, which is converted to cytidine-5-triphosphate under ATP consumption (**Figure 68**) [Heinrich et al. 2014]. At this point, the ATP levels of ATQ treated parasites should be higher compared to untreated parasites, which could be monitored in pursuing investigations using ATP sensors, like ATeam (Adenosine 5'-Triphosphate indicator based on Epsilon subunit for Analytical Measurements) [Imamura et al. 2009; Kotera et al. 2010]. In a later step, pyrimidine ribonucleotides are reduced to deoxyribonucleotides by ribonucleotide reductase. This reaction is NADPH-dependent, as the reduced dicysteine center of ribonucleotide reductase is regenerated by Grx. The oxidized Grx produced in this reaction is reduced by glutathione. Subsequently, GSSG is reduced by GR, which is accompanied by NADPH consumption (**Figure 68**) [Heinrich et al. 2014]. Inhibition of pyridine biosynthesis downstream could thus, lead much more to a decrease in cytosolic GSSG:GSH ratios–where the cytosol of *Plasmodium* is already reducing–and potentially a slight increase in NADPH levels.

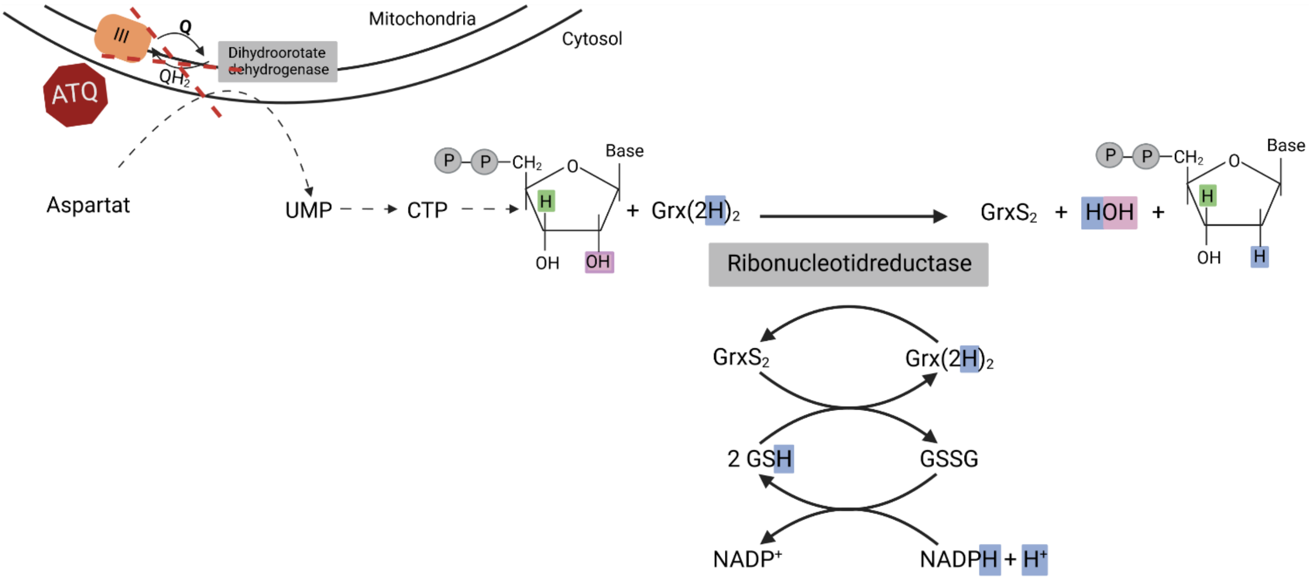

Figure 68. Pyrimidine biosynthesis, mechanism of ribonucleotide reductase, and effect of ATQ. Inhibition of complex III of the mitochondrial electron transport chain. As a result, ubiquinone is no longer regenerated, which is required for pyrimidine biosynthesis. ATQ = atovaquone, III = complex 3 of the mitochondrial electron transport chain; Q = ubiquinone; QH_2 = ubihydroquinone; UMP = uridine-5'-monophosphate; CTP = cytidine-5'-triphosphate. Adapted from [Heinrich et al. 2014], created with BioRender.com.

The results generated in this work provide preliminary evidence that this could indeed be the case in *Plasmodium*. After mid- and long-term incubations, a slight increase in the fluorescence ratio of mSc.-I-iNap2, which was most evident after 24h, was seen (**Figure 69**). Although this effect did not reach significance an increase in NADPH level is indicated.

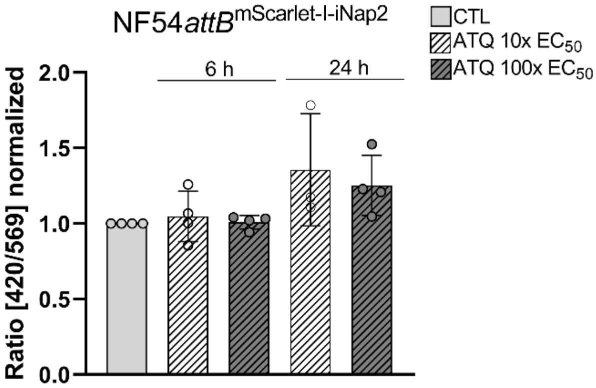

Figure 69. Effect of ATQ after mid- and long-term incubation on the cytosolic NADPH of drug-sensitive NF54*attB* *P. falciparum* parasites. The fluorescence ratio of NF54*attB*$^{\text{mSc.-I-iNap2}}$ after incubation with 10x and 100x EC_{50} ATQ for 6 h and 24 h is shown. Mock-treated parasites (1% DMSO) were used as a control. Means ± SD are shown. Each data point represents the ratio, calculated on basis of the median FI of 1,000 parasites. The ratios were normalized; therefore, the control ratio was set to $R_{CTL} = 1$. A one-way ANOVA test with 95% confidence intervals with the Dunnett's multiple comparison test was applied for statistical analysis of significance. CTL = control, ATQ = atovaquone.

Furthermore, the OxD values for all measurements showed slightly lower values than the mock-treated control group (**Table 10**). However, this is difficult to measure with the currently available redox-biosensors used in *Plasmodium*, since the redox-sensors are already basally reduced due to their midpoint potential (~ -280 mV) and the negative redox potential of the parasitic cytosol (~ - 300 mV). Therefore, only oxidizing effects can be reliably measured, but not reducing effects. For this purpose, redox-sensors would be needed that have a more negative midpoint potential than those currently used in *Plasmodium*. Redox-biosensors with different midpoint potentials were already generated, like roGFP2-iL, showing a less negative midpoint potential (~ -240 mV). This sensor was generated to measure oxidizing effects in organelles such as the ER, which is less reducing than the cytosol [Aller et al. 2013]. Currently, a new redox-biosensor, based on red fluorescent protein–roCherry–was generated, showing a midpoint potential of -311 mV [Shokhina et al. 2019], with which it could be possible to monitor reducing effects in the cytosol (**Figure 70**).

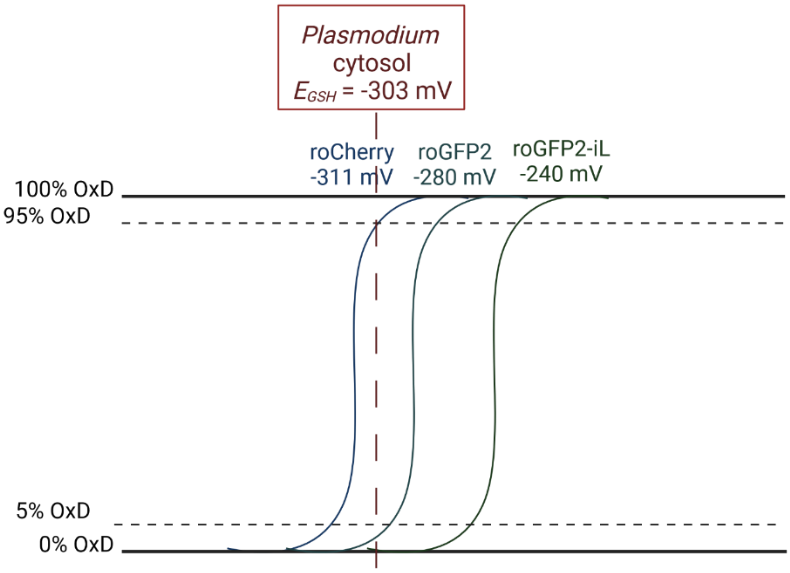

Figure 70. Midpoint potential of roGFP2, roGFP2-iL, and roCherry. Comparison between the midpoint potentials of roGFP2, roGFP2-iL, and roCherry. The degree of sensor oxidation in the cytosol of *P. falciparum*, which has an E_{GSH} of about -303 mV is visualized. OxD = degree of oxidation; E_{GSH} = glutathione redox potential. Adapted from [Meyer and Dick 2010], created with BioRender.com.

In the series of measurements carried out within this work, CQ just showed an effect after long-term incubation of 24 h. The CQ concentrations tested here were 10x and 100x EC_{50}, respectively. In previous measurements of the group, using transiently transfected $3D7^{hGrx1\text{-}roGFP2}$ parasites, 4 h incubation with 50x EC_{50} CQ significantly increased the redox ratio. The sample size of the CLSM based measurement was significantly smaller compared to the flow cytometry-based measurement carried out in this work. This could explain the differences seen in the results. Furthermore, 4 h incubation with 3.2 µM and 6.4 µM CQ (corresponding to 500x EC_{50} and 1,000x EC_{50}) increased the redox ratio of $3D7^{hGrx1\text{-}roGFP2}$ parasites significantly [Mohring et al. 2016]. This suggests that higher CQ concentrations may affect the glutathione-dependent redox potential, leading to measurable effects in the cytosol. However, when using those high concentrations, the morphology of the parasites should be checked if they were still intact or whether the effects seen would be more indicative for the death of the parasites. As shown by Kasozi and colleagues, short-term incubations (5 min) did not affect the parasites' redox ratio [Kasozi et al. 2013]. An effect on the fluorescence ratios of mSc.-I-iNap2 and mSc.-I-SoNar were only seen after an incubation time of 24 h. Here, one could assume that the resulting oxidizing effects after 24 h incubation triggers other metabolic pathways to ensure the maintenance of a reducing environment, like upregulation of the PPP to produce NADPH, which is required for the antioxidative capacity of the parasite. However, inspecting the parasites based on Giemsa smears after long-term incubations for 24 h suggested that the parasite population was impaired. This effect seemed to be stronger for the parasites treated with 100x EC_{50}. Based on this finding, an interpretation of the data after long-term incubations should be made cautiously. Also, this antimalarial agent seems to cause redox-related effects rather in specific subcellular compartments than in the cytosol. As shown by Gnädig and colleagues, CQ significantly increases the redox ratio after 4 h (5 µM) and 24 h (50 nM) incubation (corresponding to ~ 700x and 7x EC_{50}) in the mitochondria [Gnädig et al. 2020]. These investigations were carried out with 3D7$^{hGrx1\text{-}roGFP2}$ parasites using CLSM.

Incubations with DHA showed a significant effect on the cytosolic redox ratio as well as the NADH:NAD$^+$ ratio only after long-term incubations (24 h) with very high concentrations (100x EC_{50}). Again, due to the strong drug pressure with such a high concentration, an interpretation should be made cautiously. In previous studies of the working group, a significant increase of the cytosolic redox ratio was measured for 4 h incubation with 50x EC_{50} artemisinin and 24 h incubation with 4x EC_{50} artemisinin, respectively [Mohring et al. 2016]. These studies were performed with magnetically enriched trophozoite-stages measured using CLSM. For the measurements carried out in the present work, a larger sample number was used. Thus, differences in the results could be explained by differences in the measurement conditions.

Taken together, the commonly used antimalarials, tested within this work (ATQ, CQ, DHA), showed only a slight change in the cytosolic redox homeostasis, if at all. The detected effects usually occurred only after long incubation periods. However, with an E_{GSH} value of -303 mV the cytosol of NF54*attB* parasites is highly reducing. Small changes in GSSG concentrations could hence cause large changes in the cytosolic glutathione-dependent redox potential. To maintain the reducing state, transporter-mediated removal of GSSG seems to be a common mechanism to regulate the cytosolic glutathione homeostasis in eukaryotes [Hirrlinger et al. 2001; Morgan et al. 2013]. Furthermore, in *Plasmodium* parasites, GSSG is also exported to the host cell to maintain the reducing state of the cytosol [Atamna and Ginsburg 1997]. This could explain why effects are only seen when high drug concentrations or long drug exposure times are used. It is conceivable that GSSG produced by short-term treatment with low drug concentrations may have been exported to subcellular compartments or the host cell so that no cytosolic changes in the redox ratio or related NADPH levels and NADH:NAD$^+$ ratios are detectable. To effectively study such effects, the simultaneous use of several biosensors, which are based on different fluorescent proteins would be beneficial. These biosensors could be expressed in different subcellular compartments of the parasites. Since the usage of different fluorescent proteins enables the usage of specific excitation and emission wavelengths, a change in fluorescence ratio could be attributed to the corresponding biosensor and therewith the appropriate compartment. In other cells, like HeLa, multiple sensors have already been used simultaneously. In a study of Zhao's working group multiple-parametric imaging for example of NADPH, NADH, thiol redox state, and H_2O_2 in single HeLa cells was performed. In this study, the different biosensors were targeted to specific subcellular compartments or expressed in the cytosol. Since each sensor could be exited with a different specific wavelength, the emission signals were distinguished and different effects in the different compartments were studied [Zou et al. 2018]. However, regarding *Plasmodium* parasites the genetic transformation is limited by the number of selectable markers available – like hDHFR, fungal BSD, and bacterial neomycin phosphotransferase. Thus, WR99210, blasticidin, and G418 can be used for selection [Ganesan et al. 2011]. Furthermore, puromycin-N-acetyltransferase, mediating resistance to puromycin [Koning-Ward et al. 2001], dihydrofolate reductase-thymidylate synthase mediating resistance to the antimalarial drug pyrimethamine, or yeast dihydroorotate dehydrogenase (yDHODH) mediating resistance to all mitochondrial electron transport chain inhibitors can be used as selection markers [Ganesan et al. 2011]. However, due to the working principle of the latter, this selection marker should not be used if the effects of specific antimalarial agents, like ATQ are to be studied. Moreover, simultaneously stable integration of multiple biosensors into the genome of *Plasmodium* parasites is difficult and usage of transiently transfected parasites comes with limitations, like stress conferred by the selection agent, development of resistance against the selection agent, and loss of plasmid and associated fluorescence after several weeks [Schuh et al. 2018]. Those limitations could potentially be overcome by the usage of the CRISPR/Cas9 system that could be used to generate a parasite line stably expressing multiple biosensors, enabling the monitoring of changes in the redox homeostasis within the whole cell.

5.4.2 Effects of the antimalarial agents compound 1o and PD

The effects of the antimalarial agents compound 1o and PD were tested. Both agents are not approved as antimalarials, however, they show antimalarial efficacy. Compound 1o is a fast-acting and highly active agent against *P. falciparum* blood-stages with an EC_{50} of 1-5 nM [Krieg et al. 2017]. Furthermore, oral administration reduced parasitemia in *P. berghei*-infected mice. In addition, this compound is able to block parasite transmission from mice to mosquitoes efficiently [Krieg et al. 2017]. The MoA of compound 1o is so far not completely understood. However, a chelate-based quinone methide mechanism that involved metal or heme bioactivation is indicated. Initial studies using a cytosolic glutathione redox-sensor showed a dose-dependent change of the intracellular redox ratio after long-term treatment with compound 1o, indicating oxidation and alterations in the intracellular redox potential [Krieg et al. 2017; Rahbari 2017a]. However, in this study, the increase in fluorescence ratio was not significant for any of the tested concentrations (4-20x EC_{50}). The increase after mid-term incubations (4 h) with 50x and 100x EC_{50} was comparable and not significant for both treatments [Krieg et al. 2017]. These findings were confirmed by Schuh and colleagues, demonstrating that incubation with 100x EC_{50} compound 1o for 4 h did not show any effect on the cytosolic redox homeostasis. In said study, the redox ratio increased after 24 h incubation with 10x EC_{50}, however, this effect was not significant [Schuh et al. 2018]. In addition, it was shown that this compound can increase H_2O_2 levels in the cytosol and mitochondrion, with a significant effect on the latter after long-term incubations [Rahbari 2017a; Rahbari et al. 2017c]. Within the scope of this work, it could be tested for the first time whether compound 1o affect the cytosolic NADPH, NADH:NAD$^+$, or pH. However, the tested conditions hardly affected the cytosolic GSSG:GSH, NADPH, NADH:NAD$^+$, and pH. In the series of measurements carried out within this work, only mid-term incubations (6 h) with very high concentrations (100x EC_{50}) affected the redox ratio. Shorter incubation times did not significantly affect the redox ratio which is in line with previously performed studies [Krieg et al. 2017]. The fluorescence ratio of mSc.-I-SoNar and mSc.-I-iNap2 was affected only after 24 h incubations. At a time when the parasites were so severely affected by the treatment with such high concentrations that an interpretation of these data is not meaningful. Besides targeting the pathogens directly, it could be shown that compound 1o can modulate human immune cells and therewith might boost antiparasitic defense and facilitate the clearance of pathogens. In the said study it was demonstrated, that compound 1o increased glycolysis in M1 macrophages [Blum et al. 2021]. However, NADH:NAD$^+$ modulating effects within the cytosol of the parasites could not be seen in this work. Since a putative impact of compound 1o on the mitochondrial metabolism, leading to increasing H_2O_2 levels was seen in previous studies [Rahbari et al. 2017c; Rahbari 2017a] a disturbance of the redox homeostasis in subcellular compartments rather than the cytosol is conceivable. Furthermore, recent data suggest that PfPK2 may be a potential target of compound 1o [Rahlfs, personal communication, 15th November, 2021]. This enzyme, localized in the apicoplast, is essential for the survival of the parasites and the maintenance of the organelle. PfPK2 has already been classified as a potential target for the development of new antimalarials, as it is one of the rate-limiting enzymes of the vital glycolytic pathways [Chan et al. 2007; Swift et al. 2020]. Further organelle-specific studies are of great importance to support the preliminary data. The use of ATP sensors, like ATeam [Imamura et al. 2009; Kotera et al. 2010], in combination with the use of the NADH:NAD$^+$ sensor mSc.-I-SoNar, not just in the parasites' cytosol but also targeted to specific subcellular compartments, could make a major contribution to the understanding of the MoA of compound 1o.

PD is a rapid-acting 3-benzyl-menadione against asexual *Plasmodium* blood-stages and early gametocytes. It mediates its effect by acting as a redox cycler, thereby disturbing the redox homeostasis of the iRBC. Among other activities, PD mimics the natural protection of G6PD deficiency and induces its effects specifically to parasitized RBC, whereas uninfected G6PD-sufficient or -deficient RBC are not harmed. However, in this work, it was shown that unlike treatment with SBI-750, PD had no significant effects on the cytosolic NADPH level, suggesting a different underlying mechanism. Furthermore, PD acts on other targets, like GR-catalyzed redox cycling or inhibition of hematin formation. Inhibition of the parasites' mitochondrial electron transport chain was not observed although PD is structurally related to ATQ [Ehrhardt et al. 2013; Bielitza et al. 2015, 2015; Ehrhardt et al. 2016]. Within the series of measurements carried out in this work an oxidizing effect of the parasites' cytosol was observed by an increased redox ratio. The oxidizing effect was seen most strongly for mid- and long-term incubations, which is in accordance with other publications [Bielitza et al. 2015]. Furthermore, a concentration-dependent increase in the redox potential of the apicoplast was demonstrated in a previous study. This effect was explained based on the benzylic oxidation of PD, which is closely related to the formation of a benzylic semiquinone radical. This reaction can be catalyzed by the *P. falciparum* apicoplast ferredoxin-NADP$^+$ reductase, leading to an increase in the redox ratio of this compartment [Cichocki et al. 2021]. To confirm this finding it would be of big interest to study changes in the NADPH levels in the apicoplast upon PD treatment. However, until now only cytosolic NADPH levels in *Plasmodium* can be monitored using the biosensor mSc.-I-iNap2, established in this work.

5.4.3 Effects of the antibiotic DOXY

In addition to commonly used antimalarials, the effects of the antibiotic DOXY were investigated. Since this treatment increased the fluorescence ratio of sfpHluorin significantly, it must be assumed that the cytosolic pH value had increased. As a result, no interpretation of the mSc.-I-SoNar and mSc.-I-iNap2 data can be made, since it cannot be excluded that changes in the fluorescence ratio of both biosensors were due to pH changes and not exclusively to changes in NADPH levels or NADH:NAD$^+$ ratio.

It is known that DOXY mediates its effect by blocking protein translation in the apicoplast. This leads to a delayed death drug response after the second 48 h asexual growth cycle in a concentration-depended manner [Dahl et al. 2006; Wilson et al. 2015; Okada et al. 2020]. Due to the treatment, the apicoplast inherited by the progeny of treated parasites are abnormal [Dahl and Rosenthal 2007]. Meaning that the parasite can survive with no or damaged apicoplast, while it remains in the iRBC. However, the parasite is unable to develop further and establish a successful new infection. The reason therefore might be the involvement of exported products, generated within the anabolic pathways of the apicoplast [Ralph et al. 2004]. As described by Okada and colleagues, at concentrations above 5 µM, DOXY kills the parasite with first-cycle activity and mediates off-target effects outside the apicoplast [Okada et al. 2020]. Indeed, in this work, off-target effects in the cytosol were seen at a DOXY concentration of 5 µM, even after short-term incubation. DOXY massively affected the cytosolic redox homeostasis, demonstrated by a significant increase in redox ratio already after short incubation times. In addition, the fluorescence ratio of mSc.-I-SoNar and mSc.-I-iNap2 increased significantly due to the treatment. However, since the pH changed upon treatment it cannot be clearly stated whether the NADPH levels and the NADH:NAD$^+$ ratio have actually changed. Since the fluorescence ratio for mSc.-I-SoNar seems to be more stable to pH fluctuations in the range around pH 8.0 than the ratio of mSc.-I-iNap2, one could hypothesize that treatment with DOXY indeed increased the cytosolic NADH:NAD$^+$ ratios. This might indicate an increase in ATP production via glycolysis, which could be verified by means of ATP sensors [Imamura et al. 2009; Kotera et al. 2010].

5.4.4 SBI-750 disrupts the redox homeostasis in the cytosol of *Plasmodium falciparum*

The unique set of genetically encoded sensors, established in this work, was used to study the MoA of the potent and fully selective PfGluPho inhibitor SBI-750 in more detail. This compound mimics the effect of the genetic disease G6PD deficiency [Berneburg et al. 2022]. In this human enzymopathy [Luzzatto et al. 2020] G6PD, which is normally found in the cytoplasm of all cells [Richardson and O'Malley 2021] is deficient. This housekeeping enzyme plays a crucial role in preventing cellular damage from ROS, which is especially important in RBC since these cells are particularly vulnerable to ROS due to their role in oxygen transport [Richardson and O'Malley 2021]. Oxygen binds reversibly to the 4 heme residues within hemoglobin. Due to spontaneous conformational fluctuations in the heme pocket, water or a small anion can enter the pocket, thus an electron transfer between the iron and the oxygen occurs, resulting in methemoglobin and superoxide radical production. The provision of NADPH is critical to counteract this auto-oxidant process, making G6PD the key to facing oxidative challenges in RBC [Luzzatto et al. 2020]. Moreover, mature RBCs have no protein synthesis, resulting in a decreased G6PD activity as they age [Luzzatto et al. 2020]. During times with increased ROS production, the deficiency can result in acute hemolytic anemia that can for example be induced by certain antimalarial agents [Richardson and O'Malley 2021]. In sum, in RBCs G6PD deficiency leads to a reduction of the NADPH:NADP$^+$ ratio and disturbs the redox equilibration. However, in malaria infection, these mechanisms enhance the phagocytosis of the parasitized RBC [Allen et al. 2015]. In contrast to RBC, in *Plasmodium* parasites the oxidative branch of the PPP is not the only supplier of NADPH. Moreover, glutamate dehydrogenase and isocitrate dehydrogenase are suggested to be sources of NADPH [Preuss et al. 2012]. Thus, in principle, the inhibition of the PPP and therewith a diminished provision of NADPH could be compensated by these two systems. However, glutamate dehydrogenase is dispensable for the asexual intraerythrocytic development [Storm et al. 2011] and the contribution of the isocitrate dehydrogenase is still unclear [Allen et al. 2015]. Furthermore, since double crossover disruption revealed that PfGluPho–the unique bifunctional enzyme consisting of G6PD and 6PGL–is essential for the growth of blood-stages, the importance of the PfGluPho within the plasmodial PPP as supplier for NADPH was demonstrated [Allen et al. 2015]. Through the use of a high-throughput assay and the screening of various compound libraries against the G6PD activity of PfGluPho, two selective inhibitors against PfG6PD and parasite blood-stages were identified, namely ML276 and ML304 [Maloney et al. 2010; Haeussler et al. 2019]. SBI-750–a further development from ML304–shows nanomolar activity against recombinant PfGluPho, PvG6PD, and *P. falciparum* blood-stage parasites. In previous studies, it was demonstrated that SBI-750 disturbs the cytosolic glutathione-dependent redox potential after 4 h incubation, as well as the cytosolic and mitochondrial H_2O_2 homeostasis of *P. falciparum* trophozoite-stage parasites, already at low nanomolar concentrations [Berneburg et al. 2022]. These findings were confirmed within this work. Furthermore, it was shown, that the massive increase of the redox ratio occurred much earlier. The results generated in this work demonstrated that SBI-750 perturbed the redox homeostasis already after short incubation times with low nanomolar concentrations. Already after 10 min the treatment with 1x EC_{50} significantly increased the redox ratio. An increase in OxD with a value of 71.8% ± 10.3% was detected. Furthermore, it could be shown for the first time that a time-delayed reduction in NADPH levels occurred (**Figure 71**). After an incubation period of 30 min, NADPH levels decreased significantly at all concentrations tested. At this incubation time, the highest tested SBI-750 concentration within this series of measurements (10x EC_{50}) led to a massive oxidation of the parasites' cytosol ($OxD_{SBI30min}$ = 100.5% ± 2.3%). These findings demonstrate that resulting from the inhibition of the plasmodial PPP, the parasites' antioxidative systems lack NADPH. It can be concluded that the generation of free radicals and ROS by physiological processes occurring within the parasite [Becker et al. 2004], can no longer be compensated by the antioxidative capacity, leading to a disturbed redox homeostasis. These processes already occur after a very short treatment time, which is evident from the massive increase in cytosolic GSSG:GSH ratio that was seen already after short incubation times.

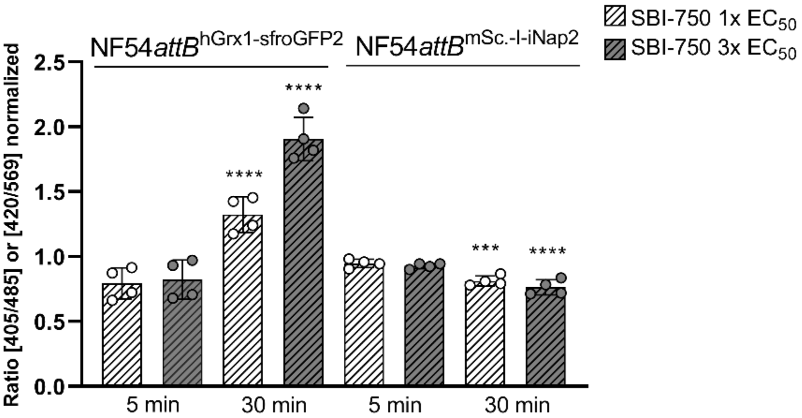

Figure 71. Effect of SBI-750 after short-term incubation on the cytosolic GSSG:GSH and NADPH of drug-sensitive NF54*attB P. falciparum* parasites. The fluorescence ratio of NF54*attB*$^{hGrx1-sfroGFP2}$ and NF54*attB*$^{mSc.-l-iNap2}$ after incubation with 1x and 3x EC_{50} SBI-750 for 5 min and 30 min is shown. Mock-treated parasites (1% DMSO) were used as a control. Means ± SD are shown. Each data point represents the ratio, calculated on basis of the median FI of 1,000 parasites. A one-way ANOVA test with 95% confidence intervals with the Dunnett's multiple comparison test was applied for statistical analysis of significance (*, $p < 0.05$; **, $p < 0.01$; ***, $p < 0.001$; ****, $p < 0.0001$).

Besides producing NADPH, the PPP is furthermore important for the production of pentose sugars, resulting from the non-oxidative branch, which are needed for the synthesis of nucleic acids (**Figure 72**). As a result, inhibition of PfGluPho and thus PPP could lead to decreased production of ribose-5-phosphate. Within the non-oxidative branch of the PPP, transketolase (TKT) represents the key enzyme [Joshi et al. 2008]. This homodimeric enzyme [Boateng et al. 2020] plays a vital role in the survival and replication of the malaria parasite and was identified as a novel drug target [Joshi et al. 2008]. TKT links the PPP to glycolysis, moreover, in *Plasmodium*, PfTKT is also used in the reverse PPP mechanism using fructose-6-phosphate and glyceraldehyde-3-phosphate to generate more ribose-5-phosphate (**Figure 72**) [Boateng et al. 2020]. Thus, a reduced ribose-5-phosphate production due to PPP inhibition via SBI-750 could potentially be compensated by the link between glycolysis and PPP via PfTKT.

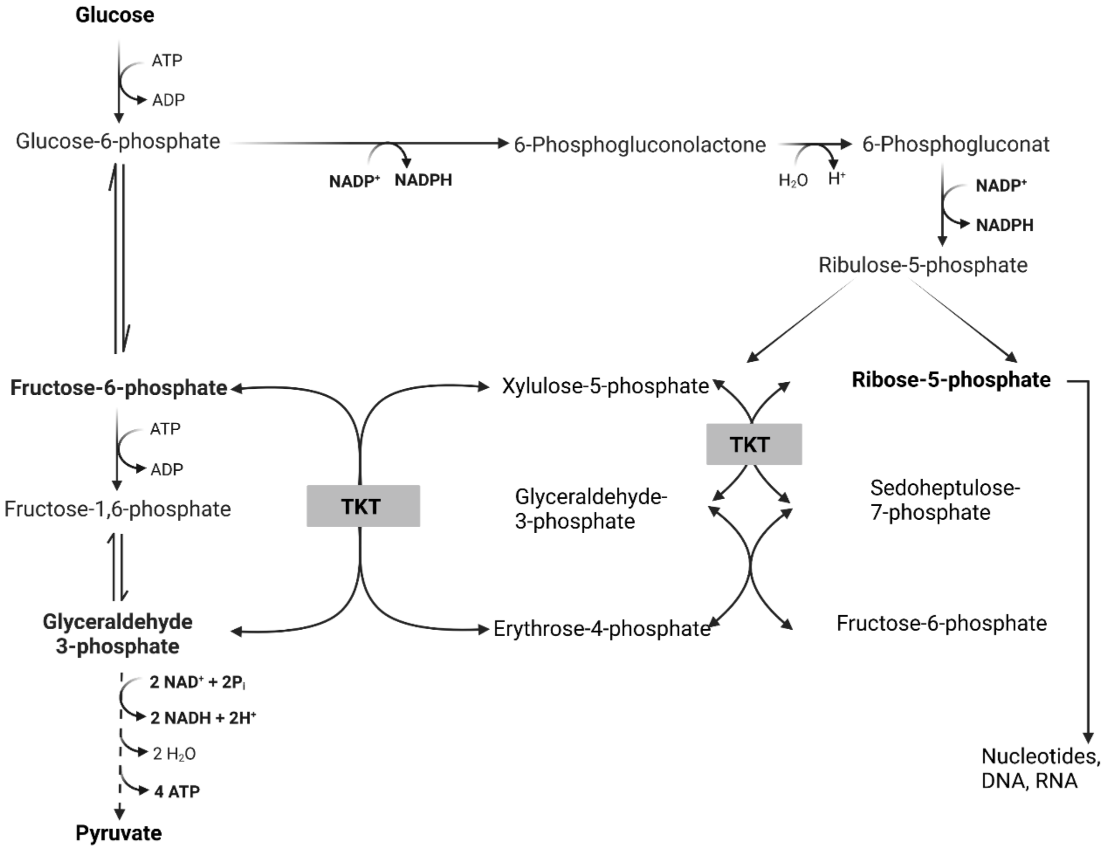

Figure 72. Connection between PPP and glycolysis via TKT. The PPP produces NADPH and ribose-5-phosphate for redox regulation and biosynthesis. Via TKT, the non-oxidative branch of the PPP is connected to glycolysis. TKT = transketolase. Adapted from [Ge et al. 2020], created with BioRender.com

However, this raises the question to what extent glyceraldehyde-3-phosphate is withdrawn from energy production and used for the generation of ribose-5-phosphate. If fructose-6-phosphate and glyceraldehyde-3-phosphate were further used for energy production, this would be associated with an increase in NADH:NAD$^+$ ratios or an unchanged ratio. However, if these substrates were fed via PfTKT to the non-oxidative branch of the PPP and used for the generation of ribose-5-phosphate, this would rather decrease the NADH:NAD$^+$ ratios. In this work, it was demonstrated, using the newly established biosensor mSc.-I-SoNar that upon SBI-750 treatment, the NADH:NAD$^+$ ratio was still maintained for quite a long time. No significant effect was seen, except for the 24 h incubation with 100x EC_{50} SBI-750. However, as previously described, interpretation of these long-term incubation data should be made with caution. Therefore, a disruption of the NADH:NAD$^+$ ratio due to the treatment with SBI-750 seemed unlikely, which gives first evidence that fructose-6-phosphate and glyceraldehyde-3-phosphate were continued to be used for energy production. This seems reasonable since the asexual-stages of *Plasmodium* are primarily dependent on glycolysis for energy production [MacRae et al. 2013; O'Hara et al. 2014; Oyelade et al. 2016]. Even additional ‘oxidative stress’, simulated in this work by the addition of H_2O_2, did not significantly alter the NADH:NAD$^+$ ratios. Therefore, SBI-750 did not seem to affect the parasites’ cytosolic energy production. However, to study the effects of SBI-750 towards the energy-producing pathways in more detail, the usage of ATeam sensors [Imamura et al. 2009] to monitor changes in ATP levels would be beneficial. Furthermore, the simultaneous use of sensors in different compartments [Zou et al. 2018] as described above would provide information about individual effects and their interplay in the complex redox network of the entire cell.

In conclusion, the establishment of a flow cytometry-based assay and the usage of a unique set of genetically encoded biosensors–some of which were used for the first time in *Plasmodium*–allowed studying the MoA of agents with antimalarial activity in more detail. Therewith, preliminary data was confirmed and further supplemented. Moreover, the knowledge gained in this study about the molecular basis underlying the improved sensor properties of sfroGFP2 can be used for the development of future sensors. Several obstacles associated with the examination of small unicellular parasites were overcome in this study. The knowledge gained here can be transferred from *Plasmodium* as a model organism not only to other unicellular parasites but can also be beneficial for the examinations of larger cells and especially their subcellular compartments.

6. REFERENCES

ALLEN, S.M., LIM, E.E., JORTZIK, E., PREUSS, J., CHUA, H.H., MACRAE, J.I., RAHLFS, S., HAEUSSLER, K., DOWNTON, M.T., MCCONVILLE, M.J., BECKER, K., AND RALPH, S.A. 2015. Plasmodium falciparum glucose-6-phosphate dehydrogenase 6-phosphogluconolactonase is a potential drug target. *FEBS J 282*, 19, 3808–3823.

ALLER, I., ROUHIER, N., AND MEYER, A.J. 2013. Development of roGFP2-derived redox probes for measurement of the glutathione redox potential in the cytosol of severely glutathione-deficient rml1 seedlings. *Front Plant Sci 4*, 506.

ALY, A.S.I., VAUGHAN, A.M., AND KAPPE, S.H.I. 2009. Malaria parasite development in the mosquito and infection of the mammalian host. *Annu Rev Microbiol 63*, 195–221.

ARIEY, F., WITKOWSKI, B., AMARATUNGA, C., BEGHAIN, J., LANGLOIS, A.-C., KHIM, N., KIM, S., DURU, V., BOUCHIER, C., MA, L., LIM, P., LEANG, R., DUONG, S., SRENG, S., SUON, S., CHUOR, C.M., BOUT, D.M., MÉNARD, S., ROGERS, W.O., GENTON, B., FANDEUR, T., MIOTTO, O., RINGWALD, P., LE BRAS, J., BERRY, A., BARALE, J.-C., FAIRHURST, R.M., BENOIT-VICAL, F., MERCEREAU-PUIJALON, O., AND MÉNARD, D. 2014. A molecular marker of artemisinin-resistant Plasmodium falciparum malaria. *Nature 505*, 7481, 50–55.

ARISUE, N., AND HASHIMOTO, T. 2015. Phylogeny and evolution of apicoplasts and apicomplexan parasites. *Parasitol Int 64*, 3, 254–259.

ASHLEY, E.A., AND PHYO, A.P. 2018. Drugs in Development for Malaria. *Drugs 78*, 9, 861–879.

ATAMNA, H., AND GINSBURG, H. 1997. The malaria parasite supplies glutathione to its host cell--investigation of glutathione transport and metabolism in human erythrocytes infected with Plasmodium falciparum. *Eur J Biochem 250*, 3, 670–679.

BANNISTER, L.H., HOPKINS, J.M., FOWLER, R.E., KRISHNA, S., AND MITCHELL, G.H. 2000. A Brief Illustrated Guide to the Ultrastructure of Plasmodium falciparum Asexual Blood Stages. *Parasitology Today 16*, 10, 427–433.

BATHKE, J. 2014. *Strukturelle und kinetische Charakterisierung der Nicotinsäuremononukleotid-Adenylyltransferase des Malariaparasiten Plasmodium falciparum*. Dissertation. URL: http://geb.uni-giessen.de/geb/volltexte/2015/11627/pdf/BathkeJochen_2015_06_03.pdf.

BECKER, K., RAHLFS, S., NICKEL, C., AND SCHIRMER, R.H. 2003. Glutathione--functions and metabolism in the malarial parasite Plasmodium falciparum. *Biol Chem 384*, 4, 551–566.

BECKER, K., TILLEY, L., VENNERSTROM, J.L., ROBERTS, D., ROGERSON, S., AND GINSBURG, H. 2004. Oxidative stress in malaria parasite-infected erythrocytes: host-parasite interactions. *Int J Parasitol 34*, 2, 163–189.

BENČINA, M. 2013. Illumination of the spatial order of intracellular pH by genetically encoded pH-sensitive sensors. *Sensors (Basel) 13*, 12, 16736–16758.

BENVENUTI, M., AND MANGANI, S. 2007. Crystallization of soluble proteins in vapor diffusion for x-ray crystallography. *Nat Protoc 2*, 7, 1633–1651.

BERNEBURG, I., PEDDIBHOTLA, S., HEIMSCH, K.C., PREUSS, J., MALONEY, P., GOSALIA, P., HAEUSSLER, K., RAHBARI, M., SKOROKHOD, O., VALENTE, E., ULLIERS, D., SIMULA, L.F., BUCHHOLZ, K., HEDRICK, M.P., HERSHBERGER, P., CHUNG, T.D.Y., JACKSON, SCHWARZER, E., RAHLFS, S., BODE, L., BECKER, K., AND PINKERTON, AB. 2022. An optimized dihydrodibenzothiazepine lead compound (SBI-0797750) as a potent and selective inhibitor of Plasmodium falciparum and vivax glucose 6-phosphate dehydrogenase 6-phosphogluconolactonase. *Antimicrob Agents Chemother* e0210921.

BIELITZA, M., BELORGEY, D., EHRHARDT, K., JOHANN, L., LANFRANCHI, D.A., GALLO, V., SCHWARZER, E., MOHRING, F., JORTZIK, E., WILLIAMS, D.L., BECKER, K., ARESE, P., ELHABIRI, M., AND DAVIOUD-CHARVET, E. 2015. Antimalarial NADPH-Consuming Redox-Cyclers As Superior Glucose-6-Phosphate Dehydrogenase Deficiency Copycats. *Antioxid Redox Signal 22*, 15, 1337–1351.

BLOEDEL HEARING RESEARCH CENTER. *Olympus Fluoview-1000 User's Guide*. https://depts.washington.edu/digmicro/fv-1000_pdf/FV-1000%20User%20Guide.pdf. Accessed 9 December 2021.

BLUM, L., ULSHÖFER, T., HENKE, M., KRIEG, R., BERNEBURG, I., GEISSLINGER, G., BECKER, K., PARNHAM, M.J., AND SCHIFFMANN, S. 2021. The immunomodulatory potential of the arylmethylaminosteroid sc1o. *J Mol Med (Berl) 99*, 2, 261–272.

BMG LABTECH. *How to optimise fluorescence gain*. https://www.bmglabtech.com/de/what-is-the-gain-and-why-do-bmg-labtech-microplate-readers-have-an-adjustable-gain-for-fluorescent-intensity-and-luminescent-assays/. Accessed 9 December 2021.

BOATENG, R.A., TASTAN BISHOP, Ö., AND MUSYOKA, T.M. 2020. Characterisation of plasmodial transketolases and identification of potential inhibitors: an in silico study. *Malar J 19*, 1, 442.

BOHME, C.C., ARSCOTT, L.D., BECKER, K., SCHIRMER, R.H., AND WILLIAMS, C.H. 2000. Kinetic characterization of glutathione reductase from the malarial parasite Plasmodium falciparum. Comparison with the human enzyme. *J Biol Chem 275*, 48, 37317–37323.

BRADFORD, M.M. 1976. A rapid and sensitive method for the quantitation of microgram quantities of protein utilizing the principle of protein-dye binding. *Analytical Biochemistry 72*, 1-2, 248–254.

CARSON, S., MILLER, H.B., AND WITHEROW, D.S., Eds. 2012. *Molecular biology techniques. A classroom laboratory manual*. Academic Press, Amsterdam.

CDC. 2018. *About Malaria - Biology*. https://www.cdc.gov/malaria/about/biology/index.html. Accessed 20 March 2020.

CDC. 2020a. *About Malaria - Disease*. https://www.cdc.gov/malaria/about/. Accessed 12 March 2020.

CDC. 2020b. *Malaria*. https://www.cdc.gov/parasites/malaria/index.html. Accessed 4 March 2020.

CHALFIE, M., TU, Y., EUSKIRCHEN, G., WARD, W.W., AND PRASHER, D.C. 1994. Green fluorescent protein as a marker for gene expression. *Science 263*, 5148, 802–805.

CHAN, M., TAN, D.S.H., AND SIM, T.S. 2007. Plasmodium falciparum pyruvate kinase as a novel target for antimalarial drug-screening. *Travel Med Infect Dis 5*, 2, 125–131.

CHAYEN, N.E., AND SARIDAKIS, E. 2008. Protein crystallization: from purified protein to diffraction-quality crystal. *Nat Methods 5*, 2, 147–153.

CICHOCKI, B.A., DONZEL, M., HEIMSCH, K.C., LESANAVIČIUS, M., FENG, L., MONTAGUT, E.J., BECKER, K., ALIVERTI, A., ELHABIRI, M., ČĖNAS, N., AND DAVIOUD-CHARVET, E. 2021. Plasmodium falciparum Ferredoxin-NADP+ Reductase-Catalyzed Redox Cycling of Plasmodione Generates Both Predicted Key Drug Metabolites: Implication for Antimalarial Drug Development. *ACS Infect Dis 7*, 7, 1996–2012.

CLARK, I.A., AND COWDEN, W.B. 2003. The pathophysiology of falciparum malaria. *Pharmacology & Therapeutics 99*, 2, 221–260.

CORMACK, B.P., VALDIVIA, R.H., AND FALKOW, S. 1996. FACS-optimized mutants of the green fluorescent protein (GFP). *Gene 173*, 1, 33–38.

COWMAN, A.F., HEALER, J., MARAPANA, D., AND MARSH, K. 2016. Malaria: Biology and Disease. *Cell 167*, 3, 610–624.

CRAMERI, A., WHITEHORN, E.A., TATE, E., AND STEMMER, W.P. 1996. Improved green fluorescent protein by molecular evolution using DNA shuffling. *Nat Biotechnol 14*, 3, 315–319.

CUBITT, A.B., HEIM, R., ADAMS, S.R., BOYD, A.E., GROSS, L.A., AND TSIEN, R.Y. 1995. Understanding, improving and using green fluorescent proteins. *Trends in Biochemical Sciences 20*, 11, 448–455.

DAHL, E.L., AND ROSENTHAL, P.J. 2007. Multiple antibiotics exert delayed effects against the Plasmodium falciparum apicoplast. *Antimicrob Agents Chemother 51*, 10, 3485–3490.

DAHL, E.L., SHOCK, J.L., SHENAI, B.R., GUT, J., DERISI, J.L., AND ROSENTHAL, P.J. 2006. Tetracyclines specifically target the apicoplast of the malaria parasite Plasmodium falciparum. *Antimicrob Agents Chemother 50*, 9, 3124–3131.

DATOO, M.S., NATAMA, M.H., SOMÉ, A., TRAORÉ, O., ROUAMBA, T., BELLAMY, D., YAMEOGO, P., VALIA, D., TEGNERI, M., OUEDRAOGO, F., SOMA, R., SAWADOGO, S., SORGHO, F., DERRA, K., ROUAMBA, E., ORINDI, B., RAMOS LOPEZ, F., FLAXMAN, A., CAPPUCCINI, F., KAILATH, R., ELIAS, S., MUKHOPADHYAY, E., NOE, A., CAIRNS, M., LAWRIE, A., ROBERTS, R., VALÉA, I., SORGHO, H., WILLIAMS, N., GLENN, G., FRIES, L., REIMER, J., EWER, K.J., SHALIGRAM, U., HILL, A.V.S., AND TINTO, H. 2021. Efficacy of a low-dose candidate malaria vaccine, R21 in adjuvant Matrix-M, with seasonal administration to children in Burkina Faso: a randomised controlled trial. *The Lancet 397*, 10287, 1809–1818.

DELAHUNT, C., HORNING, M.P., WILSON, B.K., PROCTOR, J.L., AND HEGG, M.C. 2014. Limitations of haemozoin-based diagnosis of Plasmodium falciparum using dark-field microscopy. *Malar J 13*, 147.

DELLER, M.C., KONG, L., AND RUPP, B. 2016. Protein stability: a crystallographer's perspective. *Acta Crystallogr F Struct Biol Commun 72*, Pt 2, 72–95.

DEPONTE, M., BECKER, K., AND RAHLFS, S. 2005. Plasmodium falciparum glutaredoxin-like proteins. *Biol Chem 386*, 1, 33–40.

DOOLEY, C.T., DORE, T.M., HANSON, G.T., JACKSON, W.C., REMINGTON, S.J., AND TSIEN, R.Y. 2004. Imaging dynamic redox changes in mammalian cells with green fluorescent protein indicators. *J Biol Chem 279*, 21, 22284–22293.

DOOLEY, C.T., LI, L., MISLER, J.A., AND THOMPSON, J.H. 2012. Toxicity of 6-hydroxydopamine: live cell imaging of cytoplasmic redox flux. *Cell Biol Toxicol 28*, 2, 89–101.

EHRHARDT, K., DAVIOUD-CHARVET, E., KE, H., VAIDYA, A.B., LANZER, M., AND DEPONTE, M. 2013. The antimalarial activities of methylene blue and the 1,4-naphthoquinone 3-4-(trifluoromethyl)benzyl-menadione are not due to inhibition of the mitochondrial electron transport chain. *Antimicrob Agents Chemother 57*, 5, 2114–2120.

EHRHARDT, K., DEREGNAUCOURT, C., GOETZ, A.-A., TZANOVA, T., GALLO, V., ARESE, P., PRADINES, B., ADJALLEY, S.H., BAGREL, D., BLANDIN, S., LANZER, M., AND DAVIOUD-CHARVET, E. 2016. The Redox Cycler Plasmodione Is a Fast-Acting Antimalarial Lead Compound with Pronounced Activity against Sexual and Early Asexual Blood-Stage Parasites. *Antimicrob Agents Chemother 60*, 9, 5146–5158.

GANESAN, S.M., MORRISEY, J.M., KE, H., PAINTER, H.J., LAROIYA, K., PHILLIPS, M.A., RATHOD, P.K., MATHER, M.W., AND VAIDYA, A.B. 2011. Yeast dihydroorotate dehydrogenase as a new selectable marker for Plasmodium falciparum transfection. *Mol Biochem Parasitol 177*, 1, 29–34.

GARCÍA-BASTEIRO, A.L., BASSAT, Q., AND ALONSO, P.L. 2012. Approaching the target: the path towards an effective malaria vaccine. *Mediterr J Hematol Infect Dis 4*, 1, e2012015.

GE, T., YANG, J., ZHOU, S., WANG, Y., LI, Y., AND TONG, X. 2020. The Role of the Pentose Phosphate Pathway in Diabetes and Cancer. *Front Endocrinol (Lausanne) 11*, 365.

GHEZZI, P. 2005. Regulation of protein function by glutathionylation. *Free Radic Res 39*, 6, 573–580.

GNÄDIG, N.F., STOKES, B.H., EDWARDS, R.L., KALANTAROV, G.F., HEIMSCH, K.C., KUDERJAVY, M., CRANE, A., LEE, M.C.S., STRAIMER, J., BECKER, K., TRAKHT, I.N., ODOM JOHN, A.R., MOK, S., AND FIDOCK, D.A. 2020. Insights into the intracellular localization, protein associations and artemisinin resistance properties of Plasmodium falciparum K13. *PLoS Pathog 16*, 4, e1008482.

GOLDBERG, D.E. 2005. Hemoglobin degradation. *Curr Top Microbiol Immunol 295*, 275–291.

GREGSON, A., AND PLOWE, C.V. 2005. Mechanisms of resistance of malaria parasites to antifolates. *Pharmacol Rev 57*, 1, 117–145.

GRETES, M.C., POOLE, L.B., AND KARPLUS, P.A. 2012. Peroxiredoxins in parasites. *Antioxid Redox Signal 17*, 4, 608–633.

GUTSCHER, M., PAULEAU, A.-L., MARTY, L., BRACH, T., WABNITZ, G.H., SAMSTAG, Y., MEYER, A.J., AND DICK, T.P. 2008. Real-time imaging of the intracellular glutathione redox potential. *Nat Methods 5*, 6, 553–559.

HAEUSSLER, K. 2018. *Characterization and inhibition of NADPH-producing enzymes from the pentose phosphate pathway of Plasmodium parasites*. Dissertation. URL: http://geb.uni-giessen.de/geb/volltexte/2019/13949/pdf/HaeusslerKristina_2018_12_18.pdf.

HAEUSSLER, K., BERNEBURG, I., JORTZIK, E., HAHN, J., RAHBARI, M., SCHULZ, N., PREUSS, J., ZAPOL'SKII, V.A., BODE, L., PINKERTON, A.B., KAUFMANN, D.E., RAHLFS, S., AND BECKER, K. 2019. Glucose 6-phosphate dehydrogenase 6-phosphogluconolactonase: characterization of the Plasmodium vivax enzyme and inhibitor studies. *Malar J 18*, 1, 22.

HANSON, G.T., AGGELER, R., OGLESBEE, D., CANNON, M., CAPALDI, R.A., TSIEN, R.Y., AND REMINGTON, S.J. 2004. Investigating mitochondrial redox potential with redox-sensitive green fluorescent protein indicators. *J Biol Chem 279*, 13, 13044–13053.

HEIM, R., CUBITT, A.B., AND TSIEN, R.Y. 1995. Improved green fluorescence. *Nature 373*, 6516, 663–664.

HEIMSCH, K.C., GERTZEN, C., SCHUH, A.K., NIETZEL, T., RAHLFS, S., PRZYBORSKI, J.M., GOHLKE, H., SCHWARZLÄNDER, M., BECKER, K., AND FRITZ-WOLF, K. 2022. Structure and function of redox-sensitive superfolder green fluorescent protein variant. *Antioxid Redox Signal*, online ahead of print.

HEINRICH, P.C., MÜLLER, M., AND GRAEVE, L., Eds. 2014. *Löffler/Petrides Biochemie und Pathobiochemie*. Springer Berlin Heidelberg, Berlin, Heidelberg.

HILLER, N., FRITZ-WOLF, K., DEPONTE, M., WENDE, W., ZIMMERMANN, H., AND BECKER, K. 2006. Plasmodium falciparum glutathione S-transferase--structural and mechanistic studies on ligand binding and enzyme inhibition. *Protein Sci 15*, 2, 281–289.

HIRRLINGER, J., KÖNIG, J., KEPPLER, D., LINDENAU, J., SCHULZ, J.B., AND DRINGEN, R. 2001. The multidrug resistance protein MRP1 mediates the release of glutathione disulfide from rat astrocytes during oxidative stress. *J Neurochem 76*, 2, 627–636.

HUNG, Y.P., ALBECK, J.G., TANTAMA, M., AND YELLEN, G. 2011. Imaging cytosolic NADH-NAD(+) redox state with a genetically encoded fluorescent biosensor. *Cell Metab 14*, 4, 545–554.

IMAMURA, H., NHAT, K.P.H., TOGAWA, H., SAITO, K., IINO, R., KATO-YAMADA, Y., NAGAI, T., AND NOJI, H. 2009. Visualization of ATP levels inside single living cells with fluorescence resonance energy transfer-based genetically encoded indicators. *Proc Natl Acad Sci U S A 106*, 37, 15651–15656.

JAEGER, T., AND FLOHÉ, L. 2006. The thiol-based redox networks of pathogens: unexploited targets in the search for new drugs. *Biofactors 27*, 1-4, 109–120.

JAKOB, U., AND REICHMANN, D., Eds. 2013. *Oxidative Stress and Redox Regulation*. SpringerLink Bücher. Springer, Dordrecht.

JOICE, R., NILSSON, S.K., MONTGOMERY, J., DANKWA, S., EGAN, E., MORAHAN, B., SEYDEL, K.B., BERTUCCINI, L., ALANO, P., WILLIAMSON, K.C., DURAISINGH, M.T., TAYLOR, T.E., MILNER, D.A., AND MARTI, M. 2014. Plasmodium falciparum transmission stages accumulate in the human bone marrow. *Sci Transl Med 6*, 244, 244re5.

JORTZIK, E., AND BECKER, K. 2012. Thioredoxin and glutathione systems in Plasmodium falciparum. *Int J Med Microbiol 302*, 4-5, 187–194.

JORTZIK, E., MAILU, B.M., PREUSS, J., FISCHER, M., BODE, L., RAHLFS, S., AND BECKER, K. 2011. Glucose-6-phosphate dehydrogenase-6-phosphogluconolactonase: a unique bifunctional enzyme from Plasmodium falciparum. *Biochem J 436*, 3, 641–650.

JORTZIK, E., WANG, L., AND BECKER, K. 2012. Thiol-based posttranslational modifications in parasites. *Antioxid Redox Signal 17*, 4, 657–673.

JOSHI, S., SINGH, A.R., KUMAR, A., MISRA, P.C., SIDDIQI, M.I., AND SAXENA, J.K. 2008. Molecular cloning and characterization of Plasmodium falciparum transketolase. *Mol Biochem Parasitol 160*, 1, 32–41.

KAHANA, J.A., AND SILVER, P.A. 2001. Use of the A. victoria green fluorescent protein to study protein dynamics in vivo. *Curr Protoc Mol Biol Chapter 9*, Unit9.7C.

KANZOK, S.M., RAHLFS, S., BECKER, K., AND SCHIRMER, R.H. 2002. Thioredoxin, Thioredoxin Reductase, and Thioredoxin Peroxidase of Malaria Parasite Plasmodium falciparum *347*, 370–381.

KANZOK, S.M., SCHIRMER, R.H., TURBACHOVA, I., IOZEF, R., AND BECKER, K. 2000. The thioredoxin system of the malaria parasite Plasmodium falciparum. Glutathione reduction revisited. *J Biol Chem 275*, 51, 40180–40186.

KARIUKI, S.N., AND WILLIAMS, T.N. 2020. Human genetics and malaria resistance. *Hum Genet 139*, 6-7, 801–811.

KASOZI, D., MOHRING, F., RAHLFS, S., MEYER, A.J., AND BECKER, K. 2013. Real-time imaging of the intracellular glutathione redox potential in the malaria parasite Plasmodium falciparum. *PLoS Pathog 9*, 12, e1003782.

KATS, L.M., COOKE, B.M., COPPEL, R.L., AND BLACK, C.G. 2008. Protein trafficking to apical organelles of malaria parasites - building an invasion machine. *Traffic 9*, 2, 176–186.

KAVISHE, R.A., KOENDERINK, J.B., AND ALIFRANGIS, M. 2017. Oxidative stress in malaria and artemisinin combination therapy: Pros and Cons. *FEBS J 284*, 16, 2579–2591.

KEHR, S., STURM, N., RAHLFS, S., PRZYBORSKI, J.M., AND BECKER, K. 2010. Compartmentation of redox metabolism in malaria parasites. *PLoS Pathog 6*, 12, e1001242.

KENNIS, J.T.M., LARSEN, D.S., VAN STOKKUM, I.H.M., VENGRIS, M., VAN THOR, J.J., AND VAN GRONDELLE, R. 2004. Uncovering the hidden ground state of green fluorescent protein. *Proc Natl Acad Sci U S A 101*, 52, 17988–17993.

KNOBLOCH, J., Ed. 2003. *Malaria. Grundlagen und klinische Praxis*. UNI-MED science. UNI-MED-Verl., Bremen, London, Boston.

KONING-WARD, T.F. de, WATERS, A.P., AND CRABB, B.S. 2001. Puromycin-N-acetyltransferase as a selectable marker for use in Plasmodium falciparum. *Mol Biochem Parasitol 117*, 2, 155–160.

KOSTYUK, A.I., PANOVA, A.S., KOKOVA, A.D., KOTOVA, D.A., MALTSEV, D.I., PODGORNY, O.V., BELOUSOV, V.V., AND BILAN, D.S. 2020. In Vivo Imaging with Genetically Encoded Redox Biosensors. *Int J Mol Sci 21*, 21.

KOTERA, I., IWASAKI, T., IMAMURA, H., NOJI, H., AND NAGAI, T. 2010. Reversible dimerization of Aequorea victoria fluorescent proteins increases the dynamic range of FRET-based indicators. *ACS Chem Biol 5*, 2, 215–222.

KOZLOV, M. 2021. Resistance to front-line malaria drugs confirmed in Africa. *Nature 597*, 7878, 604.

KRAUTH-SIEGEL, R.L., MÜLLER, J.G., LOTTSPEICH, F., AND SCHIRMER, R.H. 1996. Glutathione reductase and glutamate dehydrogenase of Plasmodium falciparum, the causative agent of tropical malaria. *Eur J Biochem 235*, 1-2, 345–350.

KRICKEBERG, D. 2020. *Establishment of genetically encoded biosensors to measure NAD+/NADH and NADPH in the malaria parasite Plasmodium falciparum*. Master thesis. Unpublished.

KRIEG, R., JORTZIK, E., GOETZ, A.-A., BLANDIN, S., WITTLIN, S., ELHABIRI, M., RAHBARI, M., NURYYEVA, S., VOIGT, K., DAHSE, H.-M., BRAKHAGE, A., BECKMANN, S., QUACK, T., GREVELDING, C.G., PINKERTON, A.B., SCHÖNECKER, B., BURROWS, J., DAVIOUD-CHARVET, E., RAHLFS, S., AND BECKER, K. 2017. Arylmethylamino steroids as antiparasitic agents. *Nat Commun 8*, 14478.

LAEMMLI, U.K. 1970. Cleavage of structural proteins during the assembly of the head of bacteriophage T4. *Nature 227*, 5259, 680–685.

LAKOWICZ, J.R., Ed. 2016. *Principles of fluorescence spectroscopy*. Springer, New York.

LAVALLIE, E.R., LU, Z., DIBLASIO-SMITH, E.A., COLLINS-RACIE, L.A., AND MCCOY, J.M. 2000. Thioredoxin as a fusion partner for production of soluble recombinant proteins in Escherichia coli *2000*, 322–340.

LIM, L., AND MCFADDEN, G.I. 2010. The evolution, metabolism and functions of the apicoplast. *Philos Trans R Soc Lond B, Biol Sci 365*, 1541, 749–763.

LIN, S.-J., AND GUARENTE, L. 2003. Nicotinamide adenine dinucleotide, a metabolic regulator of transcription, longevity and disease. *Current Opinion in Cell Biology 15*, 2, 241–246.

LUCIUS, R., LOOS-FRANK, B., AND LANE, R.P., Eds. 2018. *Biologie von Parasiten*. Springer Spektrum, Berlin, Heidelberg.

LÜERSEN, K., WALTER, R.D., AND MÜLLER, S. 2000. Plasmodium falciparum-infected red blood cells depend on a functional glutathione de novo synthesis attributable to an enhanced loss of glutathione. *Biochem J 346 Pt 2*, Pt 2, 545–552.

LUKYANOV, K.A., AND BELOUSOV, V.V. 2014. Genetically encoded fluorescent redox sensors. *Biochim Biophys Acta 1840*, 2, 745–756.

LUZZATTO, L., ALLY, M., AND NOTARO, R. 2020. Glucose-6-phosphate dehydrogenase deficiency. *Blood 136*, 11, 1225–1240.

MACRAE, J.I., DIXON, M.W., DEARNLEY, M.K., CHUA, H.H., CHAMBERS, J.M., KENNY, S., BOTTOVA, I., TILLEY, L., AND MCCONVILLE, M.J. 2013. Mitochondrial metabolism of sexual and asexual blood stages of the malaria parasite Plasmodium falciparum. *BMC Biol 11*, 67.

MAHON, M.J. 2011. pHluorin2: an enhanced, ratiometric, pH-sensitive green florescent protein. *Adv Biosci Biotechnol 2*, 3, 132–137.

MALONEY, P., HEDRICK, M., PEDDIBHOTLA, S., HERSHBERGER, P., MILEWSKI, M., GOSALIA, P., LI, L., PREUSS, J., SUGARMAN, E., HOOD, B., SUYAMA, E., NGUYEN, K., VASILE, S., SERGIENKO, E., SALANAWIL, S., STONICH, D., SU, Y., DAHL, R., MANGRAVITA-NOVO, A., VICCHIARELLI, M., MCANALLY, D., SMITH, L.H., ROTH, G., DIWAN, J., CHUNG, T.D.Y., PINKERTON, A.B., BODE, L., AND BECKER, K. 2010. Probe Reports from the NIH Molecular Libraries Program. A Selective Inhibitor of Plasmodium falciparum Glucose-6-Phosphate Dehydrogenase (PfG6PDH).

MARKS, M., GUPTA-WRIGHT, A., DOHERTY, J.F., SINGER, M., AND WALKER, D. 2014. Managing malaria in the intensive care unit. *Br J Anaesth 113*, 6, 910–921.

MARTINDALE, J.L., AND HOLBROOK, N.J., Eds. 2002. *Cellular response to oxidative stress: signaling for suicide and survival* 192.

MATTHEWS, H., DUFFY, C.W., AND MERRICK, C.J. 2018. Checks and balances? DNA replication and the cell cycle in Plasmodium. *Parasit Vectors 11*, 1, 216.

MAWSON, A.R. 2013. The pathogenesis of malaria: a new perspective. *Pathog Glob Health 107*, 3, 122–129.

MCKINNON, K.M. 2018. Flow Cytometry: An Overview. *Curr Protoc Immunol 120*, 5.1.1-5.1.11.

MCPHERSON, A., AND GAVIRA, J.A. 2014. Introduction to protein crystallization. *Acta Crystallogr F Struct Biol Commun 70*, Pt 1, 2–20.

MEIERJOHANN, S., WALTER, R.D., AND MÜLLER, S. 2002. Glutathione synthetase from Plasmodium falciparum. *Biochem J 363*, Pt 3, 833–838.

METZGER, W.G., SULYOK, Z., THEURER, A., AND KÖHLER, C. 2020. Entwicklung von Impfstoffen gegen Malaria – aktueller Stand. *Bundesgesundheitsblatt Gesundheitsforschung Gesundheitsschutz 63*, 1, 45–55.

MEYER, A.J., AND DICK, T.P. 2010. Fluorescent protein-based redox probes. *Antioxid Redox Signal 13*, 5, 621–650.

MIESENBÖCK, G., ANGELIS, D.A. de, and ROTHMAN, J.E. 1998. Visualizing secretion and synaptic transmission with pH-sensitive green fluorescent proteins. *Nature 394*, 6689, 192–195.

MILNER, D.A. 2018. Malaria Pathogenesis. *Cold Spring Harb Perspect Med 8*, 1.

MINTON, A.P. 2006. How can biochemical reactions within cells differ from those in test tubes? *J Cell Sci 119*, Pt 14, 2863–2869.

MOHRING, F., JORTZIK, E., AND BECKER, K. 2016. Comparison of methods probing the intracellular redox milieu in Plasmodium falciparum. *Mol Biochem Parasitol 206*, 1-2, 75–83.

MOHRING, F., RAHBARI, M., ZECHMANN, B., RAHLFS, S., PRZYBORSKI, J.M., MEYER, A.J., AND BECKER, K. 2017. Determination of glutathione redox potential and pH value in subcellular compartments of malaria parasites. *Free Radic Biol Med 104*, 104–117.

MOLINA-CRUZ, A., DEJONG, R.J., ORTEGA, C., HAILE, A., ABBAN, E., RODRIGUES, J., JARAMILLO-GUTIERREZ, G., AND BARILLAS-MURY, C. 2012. Some strains of Plasmodium falciparum, a human malaria parasite, evade the complement-like system of Anopheles gambiae mosquitoes. *Proc Natl Acad Sci U S A 109*, 28, E1957-62.

MORGAN, B., EZERIŅA, D., AMOAKO, T.N.E., RIEMER, J., SEEDORF, M., AND DICK, T.P. 2013. Multiple glutathione disulfide removal pathways mediate cytosolic redox homeostasis. *Nat Chem Biol 9*, 2, 119–125.

MORISE, H., SHIMOMURA, O., JOHNSON, F.H., AND WINANT, J. 1974. Intermolecular energy transfer in the bioluminescent system of Aequorea. *Biochemistry 13*, 12, 2656–2662.

MÜLLER, S. 2015. Role and Regulation of Glutathione Metabolism in Plasmodium falciparum. *Molecules 20*, 6, 10511–10534.

NARDELLA, F., HALBY, L., HAMMAM, E., ERDMANN, D., CADET-DANIEL, V., PERONET, R., MÉNARD, D., WITKOWSKI, B., MECHERI, S., SCHERF, A., AND ARIMONDO, P.B. 2020. DNA Methylation Bisubstrate Inhibitors Are Fast-Acting Drugs Active against Artemisinin-Resistant Plasmodium falciparum Parasites. *ACS Cent Sci 6*, 1, 16–21.

NKRUMAH, L.J., MUHLE, R.A., MOURA, P.A., GHOSH, P., HATFULL, G.F., JACOBS, W.R., AND FIDOCK, D.A. 2006. Efficient site-specific integration in Plasmodium falciparum chromosomes mediated by mycobacteriophage Bxb1 integrase. *Nat Methods 3*, 8, 615–621.

NOTHING BUT NETS. 2021. *Why nets?* https://nothingbutnets.net/the-solution/. Accessed 19 October 2021.

O'HARA, J.K., KERWIN, L.J., COBBOLD, S.A., TAI, J., BEDELL, T.A., REIDER, P.J., AND LLINÁS, M. 2014. Targeting NAD+ metabolism in the human malaria parasite Plasmodium falciparum. *PLoS ONE 9*, 4, e94061.

OKADA, M., GUO, P., NALDER, S.-A., AND SIGALA, P.A. 2020. Doxycycline has distinct apicoplast-specific mechanisms of antimalarial activity. *Elife 9*.

ORMÖ, M., CUBITT, A.B., KALLIO, K., GROSS, L.A., TSIEN, R.Y., AND REMINGTON, S.J. 1996. Crystal structure of the Aequorea victoria green fluorescent protein. *Science 273*, 5280, 1392–1395.

OYELADE, J., ISEWON, I., ROTIMI, S., AND OKUNOREN, I. 2016. Modeling of the Glycolysis Pathway in Plasmodium falciparum using Petri Nets. *Bioinform Biol Insights 10*, 49–57.

PALM, G.J., ZDANOV, A., GAITANARIS, G.A., STAUBER, R., PAVLAKIS, G.N., AND WLODAWER, A. 1997. The structural basis for spectral variations in green fluorescent protein. *Nat Struct Biol 4*, 5, 361–365.

PALMER, A.E., QIN, Y., PARK, J.G., AND MCCOMBS, J.E. 2011. Design and application of genetically encoded biosensors. *Trends Biotechnol 29*, 3, 144–152.

PAUL, F., ROATH, S., MELVILLE, D., WARHURST, D.C., AND OSISANYA, J.O.S. 1981. Separation of malaria-infected erythrocytes from whole blood: use of a selective high-gradient magnetic separation technique. *The Lancet 318*, 8237, 70–71.

PÉDELACQ, J.-D., CABANTOUS, S., TRAN, T., TERWILLIGER, T.C., AND WALDO, G.S. 2006. Engineering and characterization of a superfolder green fluorescent protein. *Nat Biotechnol 24*, 1, 79–88.

PERCÁRIO, S., MOREIRA, D.R., GOMES, B.A.Q., FERREIRA, M.E.S., GONÇALVES, A.C.M., LAURINDO, P.S.O.C., VILHENA, T.C., DOLABELA, M.F., AND GREEN, M.D. 2012. Oxidative stress in malaria. *Int J Mol Sci 13*, 12, 16346–16372.

PHILLIPS-HOWARD, P.A., NAHLEN, B.L., KOLCZAK, M.S., HIGHTOWER, A.W., TER KUILE, F.O., ALAII, J.A., GIMNIG, J.E., ARUDO, J., VULULE, J.M., ODHACHA, A., KACHUR, S.P., SCHOUTE, E., ROSEN, D.H., SEXTON, J.D., OLOO, A.J., AND HAWLEY, W.A. 2003. Efficacy of permethrin-treated bed nets in the prevention of mortality in young children in an area of high perennial malaria transmission in western Kenya. *Am J Trop Med Hyg 68*, 4 Suppl, 23–29.

PRASHER, D.C., ECKENRODE, V.K., WARD, W.W., PRENDERGAST, F.G., AND CORMIER, M.J. 1992. Primary structure of the Aequorea victoria green-fluorescent protein. *Gene 111*, 2, 229–233.

PREUSS, J., JORTZIK, E., AND BECKER, K. 2012. Glucose-6-phosphate metabolism in Plasmodium falciparum. *IUBMB Life 64*, 7, 603–611.

RAHBARI, M. 2017a. *Establishment of genetically encoded H2O2 probes and dynamic measurements of H2O2 levels in the malaria parasite Plasmodium falciparum*. Dissertation. URL: http://geb.uni-giessen.de/geb/volltexte/2018/13427/pdf/RahbariMahsa_2017_12_07.pdf.

RAHBARI, M., DIEDERICH, K., BECKER, K., KRAUTH-SIEGEL, R.L., AND JORTZIK, E. 2015. Detection of thiol-based redox switch processes in parasites - facts and future. *Biol Chem 396*, 5, 445–463.

RAHBARI, M., RAHLFS, S., JORTZIK, E., BOGESKI, I., AND BECKER, K. 2017b. H2O2 dynamics in the malaria parasite Plasmodium falciparum. *PLoS ONE 12*, 4, e0174837.

RAHBARI, M., RAHLFS, S., PRZYBORSKI, J.M., SCHUH, A.K., HUNT, N.H., FIDOCK, D.A., GRAU, G.E., AND BECKER, K. 2017c. Hydrogen peroxide dynamics in subcellular compartments of malaria parasites using genetically encoded redox probes. *Sci Rep 7*, 1, 10449.

RAHLFS, S., personal communication, 15th November, 2021.

RAHLFS, S., AND BECKER, K. 2001. Thioredoxin peroxidases of the malarial parasite Plasmodium falciparum. *Eur J Biochem 268*, 5, 1404–1409.

RAHLFS, S., NICKEL, C., DEPONTE, M., SCHIRMER, R.H., AND BECKER, K. 2003. Plasmodium falciparum thioredoxins and glutaredoxins as central players in redox metabolism. *Redox Rep 8*, 5, 246–250.

RAHLFS, S., SCHIRMER, R.H., AND BECKER, K. 2002. The thioredoxin system of Plasmodium falciparum and other parasites. *Cell Mol Life Sci 59*, 6, 1024–1041.

RALPH, S.A., VAN DOOREN, G.G., WALLER, R.F., CRAWFORD, M.J., FRAUNHOLZ, M.J., FOTH, B.J., TONKIN, C.J., ROOS, D.S., AND MCFADDEN, G.I. 2004. Tropical infectious diseases: metabolic maps and functions of the Plasmodium falciparum apicoplast. *Nat Rev Microbiol 2*, 3, 203–216.

REBELO, M., SHAPIRO, H.M., AMARAL, T., MELO-CRISTINO, J., AND HÄNSCHEID, T. 2012. Haemozoin detection in infected erythrocytes for Plasmodium falciparum malaria diagnosis-prospects and limitations. *Acta Trop 123*, 1, 58–61.

REDDIE, K.G., AND CARROLL, K.S. 2008. Expanding the functional diversity of proteins through cysteine oxidation. *Curr Opin Chem Biol 12*, 6, 746–754.

REIFENRATH, M., AND BOLES, E. 2018. A superfolder variant of pH-sensitive pHluorin for in vivo pH measurements in the endoplasmic reticulum. *Sci Rep 8*, 1, 11985.

REMINGTON, S.J. 2011. Green fluorescent protein: a perspective. *Protein Sci 20*, 9, 1509–1519.

RICHARDSON, S.R., AND O'MALLEY, G.F. 2021. StatPearls. Glucose 6 Phosphate Dehydrogenase Deficiency.

RIVAS, G., AND MINTON, A.P. 2016. Macromolecular Crowding In Vitro, In Vivo, and In Between. *Trends in Biochemical Sciences 41*, 11, 970–981.

ROSSATI, A., BARGIACCHI, O., KROUMOVA, V., ZARAMELLA, M., CAPUTO, A., AND GARAVELLI, P.L. 2016. Climate, environment and transmission of malaria. *Infez Med 24*, 2, 93–104.

ROTH, E.F., JR, CALVIN, M.C., MAX-AUDIT, I., ROSA, J., AND ROSA, R. 1988. The enzymes of the glycolytic pathway in erythrocytes infected with Plasmodium falciparum malaria parasites. *Blood 72*, 6, 1922–1925.

RTS, S.C.T.P. 2014. Efficacy and safety of the RTS,S/AS01 malaria vaccine during 18 months after vaccination: a phase 3 randomized, controlled trial in children and young infants at 11 African sites. *PLoS Med 11*, 7, e1001685.

SARMA, G.N., SAVVIDES, S.N., BECKER, K., SCHIRMER, M., SCHIRMER, R.H., AND KARPLUS, P.A. 2003. Glutathione Reductase of the Malarial Parasite Plasmodium falciparum: Crystal Structure and Inhibitor Development. *Journal of Molecular Biology 328*, 4, 893–907.

SATO, S. 2021. Plasmodium-a brief introduction to the parasites causing human malaria and their basic biology. *J Physiol Anthropol 40*, 1, 1.

SCHINDELIN, J., ARGANDA-CARRERAS, I., FRISE, E., KAYNIG, V., LONGAIR, M., PIETZSCH, T., PREIBISCH, S., RUEDEN, C., SAALFELD, S., SCHMID, B., TINEVEZ, J.-Y., WHITE, D.J., HARTENSTEIN, V., ELICEIRI, K., TOMANCAK, P., AND CARDONA, A. 2012. Fiji: an open-source platform for biological-image analysis. *Nat Methods 9*, 7, 676–682.

SCHLITZER, M. 2008. Antimalarial drugs - what is in use and what is in the pipeline. *Arch Pharm (Weinheim) 341*, 3, 149–163.

SCHUH, A.K. 2021. *Homöodynamik von Redoxpotential und Glutathionstoffwechsel des Malariaerregers Plasmodium falciparum*. Dissertation. URL: https://jlupub.ub.uni-giessen.de/bitstream/handle/jlupub/329/SchuhAnnaKatharina-2021-07-19.pdf?sequence=3&isAllowed=y.

SCHUH, A.K., RAHBARI, M., HEIMSCH, K.C., MOHRING, F., GABRYSZEWSKI, S.J., WEDER, S., BUCHHOLZ, K., RAHLFS, S., FIDOCK, D.A., AND BECKER, K. 2018. Stable Integration and Comparison of hGrx1-roGFP2 and sfroGFP2 Redox Probes in the Malaria Parasite Plasmodium falciparum. *ACS Infect Dis 4*, 11, 1601–1612.

SCHWARZLÄNDER, M., DICK, T.P., MEYER, A.J., AND MORGAN, B. 2016. Dissecting Redox Biology Using Fluorescent Protein Sensors. *Antioxid Redox Signal 24*, 13, 680–712.

SEEBER, F., AND STEINFELDER, S. 2016. Recent advances in understanding apicomplexan parasites. *F1000Res 5*.

SHERMAN, I.W. 1979. Biochemistry of Plasmodium (malarial parasites). *Microbiol Rev 43*, 4, 453–495.

SHIMOMURA, O. 1979. Structure of the chromophore of Aequorea green fluorescent protein. *FEBS Letters 104*, 2, 220–222.

SHIMOMURA, O., JOHNSON, F.H., AND SAIGA, Y. 1962. Extraction, purification and properties of aequorin, a bioluminescent protein from the luminous hydromedusan, Aequorea. *J Cell Comp Physiol 59*, 223–239.

SHOKHINA, A.G., KOSTYUK, A.I., ERMAKOVA, Y.G., PANOVA, A.S., STAROVEROV, D.B., EGOROV, E.S., BARANOV, M.S., VAN BELLE, G.J., KATSCHINSKI, D.M., BELOUSOV, V.V., AND BILAN, D.S. 2019. Red fluorescent redox-sensitive biosensor Grx1-roCherry. *Redox Biol 21*, 101071.

SIES, H. 1997. Oxidative stress: oxidants and antioxidants. *Exp Physiol 82*, 2, 291–295.

SIES, H., BERNDT, C., AND JONES, D.P. 2017. Oxidative Stress. *Annu Rev Biochem 86*, 715–748.

SKWARCZYNSKI, M., CHANDRUDU, S., RIGAU-PLANELLA, B., ISLAM, M.T., CHEONG, Y.S., LIU, G., WANG, X., TOTH, I., AND HUSSEIN, W.M. 2020. Progress in the Development of Subunit Vaccines against Malaria. *Vaccines (Basel) 8*, 3.

SOUSA SILVA, M., FERREIRA, A.E.N., GOMES, R., TOMÁS, A.M., PONCES FREIRE, A., AND CORDEIRO, C. 2012. The glyoxalase pathway in protozoan parasites. *Int J Med Microbiol 302*, 4-5, 225–229.

STINCONE, A., PRIGIONE, A., CRAMER, T., WAMELINK, M.M.C., CAMPBELL, K., CHEUNG, E., OLIN-SANDOVAL, V., GRÜNING, N.-M., KRÜGER, A., TAUQEER ALAM, M., KELLER, M.A., BREITENBACH, M., BRINDLE, K.M., RABINOWITZ, J.D., AND RALSER, M. 2015. The return of metabolism: biochemistry and physiology of the pentose phosphate pathway. *Biol Rev Camb Philos Soc 90*, 3, 927–963.

STORM, J., PERNER, J., APARICIO, I., PATZEWITZ, E.-M., OLSZEWSKI, K., LLINAS, M., ENGEL, P.C., AND MÜLLER, S. 2011. Plasmodium falciparum glutamate dehydrogenase a is dispensable and not a drug target during erythrocytic development. *Malar J 10*, 193.

SWIFT, R.P., RAJARAM, K., KEUTCHA, C., LIU, H.B., KWAN, B., DZIEDZIC, A., JEDLICKA, A.E., AND PRIGGE, S.T. 2020. The NTP generating activity of pyruvate kinase II is critical for apicoplast maintenance in Plasmodium falciparum. *Elife 9*.

TAO, R., ZHAO, Y., CHU, H., WANG, A., ZHU, J., CHEN, X., ZOU, Y., SHI, M., LIU, R., SU, N., DU, J., ZHOU, H.-M., ZHU, L., QIAN, X., LIU, H., LOSCALZO, J., AND YANG, Y. 2017. Genetically encoded fluorescent sensors reveal dynamic regulation of NADPH metabolism. *Nat Methods 14*, 7, 720–728.

TIWARI, S., SHARMA, N., SHARMA, G.P., AND MISHRA, N. 2021. Redox interactome in malaria parasite Plasmodium falciparum. *Parasitol Res 120*, 2, 423–434.

TRAMPUZ, A., JEREB, M., MUZLOVIC, I., AND PRABHU, R.M. 2003. Clinical review: Severe malaria. *Crit Care 7*, 4, 315–323.

TSE, E.G., KORSIK, M., AND TODD, M.H. 2019. The past, present and future of anti-malarial medicines. *Malar J 18*, 1, 93.

TSIEN, R.Y. 1998. The green fluorescent protein. *Annu Rev Biochem 67*, 509–544.

UNIPROT. *Proteomes - Plasmodium falciparum (isolate 3D7)*. https://www.uniprot.org/proteomes/UP000001450. Accessed 19 October 2021.

VERDAGUER, I.B., CRISPIM, M., ZAFRA, C.A., SUSSMANN, R.A.C., BURITICÁ, N.L., MELO, H.R., AZEVEDO, M.F., ALMEIDA, F.G., KIMURA, E.A., AND KATZIN, A.M. 2021. Exploring Ubiquinone Biosynthesis Inhibition as a Strategy for Improving Atovaquone Efficacy in Malaria. *Antimicrob Agents Chemother 65*, 4.

WACHTER, R.M. 2007. Chromogenic cross-link formation in green fluorescent protein. *Acc Chem Res 40*, 2, 120–127.

WALDO, G.S., STANDISH, B.M., BERENDZEN, J., AND TERWILLIGER, T.C. 1999. Rapid protein-folding assay using green fluorescent protein. *Nat Biotechnol 17*, 7, 691–695.

WAMELINK, M.M.C., STRUYS, E.A., AND JAKOBS, C. 2008. The biochemistry, metabolism and inherited defects of the pentose phosphate pathway: a review. *J Inherit Metab Dis 31*, 6, 703–717.

WATERS, J.C., Ed. 2013. *Live-cell fluorescence imaging* 114.

WHITE, N.J., PUKRITTAYAKAMEE, S., HIEN, T.T., FAIZ, M.A., MOKUOLU, O.A., AND DONDORP, A.M. 2014. Malaria. *The Lancet 383*, 9918, 723–735.

WHO. 2019a. *Malaria. Every 2 minutes, a child dies of malaria.* https://www.who.int/news-room/facts-in-pictures/detail/malaria. Accessed 19 October 2021.

WHO. 2019b. *World malaria report*. https://www.who.int/publications-detail/world-malaria-report-2019. Accessed 26 March 2020.

WHO. 2021a. *Q&A on RTS,S malaria vaccine*. https://www.who.int/news-room/q-a-detail/q-a-on-rts-s-malaria-vaccine. Accessed 19 October 2021.

WHO. 2021b. *World malaria report 2020*. https://www.who.int/publications/i/item/9789240015791. Accessed 9 August 2021.

WILSON, D.W., GOODMAN, C.D., SLEEBS, B.E., WEISS, G.E., JONG, N.W. de, ANGRISANO, F., LANGER, C., BAUM, J., CRABB, B.S., GILSON, P.R., MCFADDEN, G.I., AND BEESON, J.G. 2015. Macrolides rapidly inhibit red blood cell invasion by the human malaria parasite, Plasmodium falciparum. *BMC Biol 13*, 52.

YANG, J., CARROLL, K.S., AND LIEBLER, D.C. 2016. The Expanding Landscape of the Thiol Redox Proteome. *Mol Cell Proteomics 15*, 1, 1–11.

YE, W., ZHENG, Y., ZHANG, S., YAN, L., CHENG, H., AND WU, M. 2016. Oxamate Improves Glycemic Control and Insulin Sensitivity via Inhibition of Tissue Lactate Production in db/db Mice. *PLoS ONE 11*, 3, e0150303.

ZEREZ, C.R., ROTH, E.F., JR, SCHULMAN, S., AND TANAKA, K.R. 1990. Increased nicotinamide adenine dinucleotide content and synthesis in Plasmodium falciparum-infected human erythrocytes. *Blood 75*, 8, 1705–1710.

ZHAO, Y., HU, Q., CHENG, F., SU, N., WANG, A., ZOU, Y., HU, H., CHEN, X., ZHOU, H.-M., HUANG, X., YANG, K., ZHU, Q., WANG, X., YI, J., ZHU, L., QIAN, X., CHEN, L., TANG, Y., LOSCALZO, J., AND YANG, Y. 2015. SoNar, a Highly Responsive NAD+/NADH Sensor, Allows High-Throughput Metabolic Screening of Anti-tumor Agents. *Cell Metab 21*, 5, 777–789.

ZHAO, Y., JIN, J., HU, Q., ZHOU, H.-M., YI, J., YU, Z., XU, L., WANG, X., YANG, Y., AND LOSCALZO, J. 2011. Genetically encoded fluorescent sensors for intracellular NADH detection. *Cell Metab 14*, 4, 555–566.

ZHAO, Y., WANG, A., ZOU, Y., SU, N., LOSCALZO, J., AND YANG, Y. 2016. In vivo monitoring of cellular energy metabolism using SoNar, a highly responsive sensor for NAD(+)/NADH redox state. *Nat Protoc 11*, 8, 1345–1359.

ZHAO, Y., ZHANG, Z., ZOU, Y., AND YANG, Y. 2018. Visualization of Nicotine Adenine Dinucleotide Redox Homeostasis with Genetically Encoded Fluorescent Sensors. *Antioxid Redox Signal 28*, 3, 213–229.

ZOU, Y., WANG, A., SHI, M., CHEN, X., LIU, R., LI, T., ZHANG, C., ZHANG, Z., ZHU, L., JU, Z., LOSCALZO, J., YANG, Y., AND ZHAO, Y. 2018. Analysis of redox landscapes and dynamics in living cells and in vivo using genetically encoded fluorescent sensors. *Nat Protoc 13*, 10, 2362–2386.

7. APPENDIX

hGrx1-sfroGFP2

Sequence length: 1,137 bp

```
   1- ATGGCTCAAGAGTTTGTGAACTGCAAAATCCAGCCTGGGAAGGTGGTTGTGTTCATCAAG- 60
   1-M   A   Q   E   F   V   N   C   K   I   Q   P   G   K   V   V   V   F   I   K   -  20
  61-CCCACCTGCCCGTACTGCAGGAGGGCCCAAGAGATCCTCAGTCAATTGCCCATCAAACAA- 120
  21-P   T   C   P   Y   C   R   R   A   Q   E   I   L   S   Q   L   P   I   K   Q   -  40
 121-GGGCTTCTGGAATTTGTCGATATCACAGCCACCAACCACACTAACGAGATTCAAGATTAT- 180
  41-G   L   L   E   F   V   D   I   T   A   T   N   H   T   N   E   I   Q   D   Y   -  60
 181-TTGCAACAGCTCACGGGAGCAAGAACGGTGCCTAGAGTCTTTATTGGTAAAGATTGTATA- 240
  61-L   Q   Q   L   T   G   A   R   T   V   P   R   V   F   I   G   K   D   C   I   -  80
 241-GGCGGATGCAGTGATCTAGTCTCTTTGCAACAGAGTGGGGAACTGCTGACGCGGCTAAAG- 300
  81-G   G   C   S   D   L   V   S   L   Q   Q   S   G   E   L   L   T   R   L   K   - 100
 301-CAGATTGGAGCTCTGCAGACTAGTGGTGGTTCAGGTGGTGGTGGTTCAGGTGGTGGTGGT- 360
 101-Q   I   G   A   L   Q   T   S   G   G   S   G   G   G   G   S   G   G   G   G   - 120
 361-TCAGGTGGAGGAGGATCAGGAGGAGGAGGATCAGGAGGAGGAGGATCAGGAGGAGAATTC- 420
 121-S   G   G   G   G   S   G   G   G   G   S   G   G   G   G   S   G   G   E   F   - 140
 421-GTTAGTAAAGGAGAAGAACTTTTCACTGGAGTTGTCCCAATTCTTGTTGAATTAGATGGT- 480
 141-V   S   K   G   E   E   L   F   T   G   V   V   P   I   L   V   E   L   D   G   - 160
 481-GATGTTAATGGGCACAAATTTTCTGTCAGAGGAGAGGGTGAAGGTGATGCAACAAATGGA- 540
 161-D   V   N   G   H   K   F   S   V   R   G   E   G   E   G   D   A   T   N   G   - 180
 541-AAACTTACCCTTAAATTTATTAGTACTACTGGAAAACTACCTGTTCCATGGCCAACACTT- 600
 181-K   L   T   L   K   F   I   S   T   T   G   K   L   P   V   P   W   P   T   L   - 200
 601-GTCACTACTCTTACTTATGGTGTCCAATGCTTTAGTAGATACCCAGATCATATGAAAAGA- 660
 201-V   T   T   L   T   Y   G   V   Q   C   F   S   R   Y   P   D   H   M   K   R   - 220
 661-CATGACTTTTTCAAGAGTGCCATGCCCGAAGGTTATGTACAGGAAAGAACTATAAGTTTC- 720
 221-H   D   F   F   K   S   A   M   P   E   G   Y   V   Q   E   R   T   I   S   F   - 240
 721-AAAGATGACGGGACATACAAGACACGTGCTGAAGTCAAGTTTGAAGGTGATACCCTTGTT- 780
 241-K   D   D   G   T   Y   K   T   R   A   E   V   K   F   E   G   D   T   L   V   - 260
 781-AATAGAATCGAGTTAAAAGGTATTGATTTTAAAGAAGATGGAAACATTCTTGGACACAAA- 840
 261-N   R   I   E   L   K   G   I   D   F   K   E   D   G   N   I   L   G   H   K   - 280
 841-TTGGAATACAACTTTAACTGTCACAATGTATACATCACTGCAGACAAACAAAAGAATGGA- 900
 281-L   E   Y   N   F   N   C   H   N   V   Y   I   T   A   D   K   Q   K   N   G   - 300
 901-ATCAAAGCAAACTTCAAAATTAGACACAACGTAGAAGATGGAAGCGTTCAACTAGCAGAC- 960
 301-I   K   A   N   F   K   I   R   H   N   V   E   D   G   S   V   Q   L   A   D   - 320
 961-CATTATCAACAAAATACTCCAATTGGCGATGGCCCTGTCCTTTTACCAGACAACCATTAC-1020
 321-H   Y   Q   Q   N   T   P   I   G   D   G   P   V   L   L   P   D   N   H   Y   - 340
1021-CTGTCCACATGTTCTGTACTTTCGAAAGATCCCAACGAAAAGAGAGACCACATGGTCCTT-1080
 341-L   S   T   C   S   V   L   S   K   D   P   N   E   K   R   D   H   M   V   L   - 360
1081-CTTGAGAGAGTAACAGCTGCTGGGATTACACATGGCATGGATGAACTATACAAATAA   -1137
 361-L   E   R   V   T   A   A   G   I   T   H   G   M   D   E   L   Y   K   *       - 380
```

mScarlet-I-SoNar

Sequence length: 1,914 bp

```
   1-GTGAGCAAGGGCGAGGCAGTGATCAAGGAGTTCATGCGGTTCAAGGTGCACATGGAGGGC -  60
   1-V   S   K   G   E   A   V   I   K   E   F   M   R   F   K   V   H   M   E   G    -  20
  61-TCCATGAACGGCCACGAGTTCGAGATCGAGGGCGAGGGCGAGGGCCGCCCCTACGAGGGC - 120
  21-S   M   N   G   H   E   F   E   I   E   G   E   G   E   G   R   P   Y   E   G    -  40
 121-ACCCAGACCGCCAAGCTGAAGGTGACCAAGGGTGGCCCCCTGCCCTTCTCCTGGGACATC - 180
  41-T   Q   T   A   K   L   K   V   T   K   G   G   P   L   P   F   S   W   D   I    -  60
```

```
 181-CTGTCCCCTCAGTTCATGTACGGCTCCAGGGCCTTCATCAAGCACCCCGCCGACATCCCC - 240
  61-L  S  P  Q  F  M  Y  G  S  R  A  F  I  K  H  P  A  D  I  P   -  80
 241-GACTACTATAAGCAGTCCTTCCCCGAGGGCTTCAAGTGGGAGCGCGTGATGAACTTCGAG - 300
  81-D  Y  Y  K  Q  S  F  P  E  G  F  K  W  E  R  V  M  N  F  E   - 100
 301-GACGGCGGCGCCGTGACCGTGACCCAGGACACCTCCCTGGAGGACGGCACCCTGATCTAC - 360
 101-D  G  G  A  V  T  V  T  Q  D  T  S  L  E  D  G  T  L  I  Y   - 120
 361-AAGGTGAAGCTCCGCGGCACCAACTTCCCTCCTGACGGCCCCGTAATGCAGAAGAAGACA - 420
 121-K  V  K  L  R  G  T  N  F  P  P  D  G  P  V  M  Q  K  K  T   - 140
 421-ATGGGCTGGGAAGCGTCCACCGAGCGGTTGTACCCCGAGGACGGCGTGCTGAAGGGCGAC - 480
 141-M  G  W  E  A  S  T  E  R  L  Y  P  E  D  G  V  L  K  G  D   - 160
 481-ATTAAGATGGCCCTGCGCCTGAAGGACGGCGGCCGCTACCTGGCGGACTTCAAGACCACC - 540
 161-I  K  M  A  L  R  L  K  D  G  G  R  Y  L  A  D  F  K  T  T   - 180
 541-TACAAGGCCAAGAAGCCCGTGCAGATGCCCGGCGCCTACAACGTCGACCGCAAGTTGGAC - 600
 181-Y  K  A  K  K  P  V  Q  M  P  G  A  Y  N  V  D  R  K  L  D   - 200
 601-ATCACCTCCCACAACGAGGACTACACCGTGGTGGAACAGTACGAACGCTCCGAGGGCCGC - 660
 201-I  T  S  H  N  E  D  Y  T  V  V  E  Q  Y  E  R  S  E  G  R   - 220
 661-CACTCCACCGGCGGCATGGACGAGCTGTACAAGACTAGTGGTGGTTCAGGTGGTGGTGGT - 720
 221-H  S  T  G  G  M  D  E  L  Y  K  T  S  G  G  S  G  G  G  G   - 240
 721-TCAGGTGGTGGTGGTTCAGGTGGAGGAGGATCAGGAGGAAACAGAAAGTGGGGTTTGTGT - 780
 241-S  G  G  G  G  S  G  G  G  G  S  G  G  N  R  K  W  G  L  C   - 260
 781-ATCGTCGGTATGGGTAGATTAGGTTCCGCCTTAGCAGACTATCCTGGTTTTGGTGAAAGT - 840
 261-I  V  G  M  G  R  L  G  S  A  L  A  D  Y  P  G  F  G  E  S   - 280
 841-TTTGAATTGAGAGGTTTCTTTGATGTTGATCCAGAAAAAGTTGGTAGACCAGTTAGAGGT - 900
 281-F  E  L  R  G  F  F  D  V  D  P  E  K  V  G  R  P  V  R  G   - 300
 901-GGTGTTATTGAACATGTTGATTTGTTGCCACAAAGAGTTCCAGGTAGAATTGAAATTGCT - 960
 301-G  V  I  E  H  V  D  L  L  P  Q  R  V  P  G  R  I  E  I  A   - 320
 961-TTGTTAACTGTTCCAAGAGAAGCTGCACAAAAAGCTGCAGATTTGTTAGTTGCTGCAGGT -1020
 321-L  L  T  V  P  R  E  A  A  Q  K  A  A  D  L  L  V  A  A  G   - 340
1021-ATTAAAGGTATTTTGAACTTCGCACCAGTTGTTTTAGAAGTTCCAAAGGAAGTTGCTGTT -1080
 341-I  K  G  I  L  N  F  A  P  V  V  L  E  V  P  K  E  V  A  V   - 360
1081-GAAAACGTTGATTTCTCAGCAGGTTACAACTCTGATAACGTTTACATCATGGCTGATAAG -1140
 361-E  N  V  D  F  S  A  G  Y  N  S  D  N  V  Y  I  M  A  D  K   - 380
1141-CAAAAGAATGGTATTAAAGCAAACTTCAAGATCAGACATAATGTTGAAGATGGTTCAGTT -1200
 381-Q  K  N  G  I  K  A  N  F  K  I  R  H  N  V  E  D  G  S  V   - 400
1201-CAATTGGCTGATCATTACCAACAAAACACACCAATTGGTGACGGTCCAGTTTTGTTGCCA -1260
 401-Q  L  A  D  H  Y  Q  Q  N  T  P  I  G  D  G  P  V  L  L  P   - 420
1261-GATAACCATTACTTGTCTTTTCAATCAGTTTTGTCTAAAGATCCAAACGAAAAGAGAGAT -1320
 421-D  N  H  Y  L  S  F  Q  S  V  L  S  K  D  P  N  E  K  R  D   - 440
1321-CATATGGTTTTGTTAGAATTCGTTACTGCTGCAGGTATCACATTGGGTATGGATGAATTA -1380
 441-H  M  V  L  L  E  F  V  T  A  A  G  I  T  L  G  M  D  E  L   - 460
1381-TACAACGTTGATGGTGGTTCAGGTGGTACTGGTTCTAAAGGTGAAGAATTGTTTACAGGT -1440
 461-Y  N  V  D  G  G  S  G  G  T  G  S  K  G  E  E  L  F  T  G   - 480
1441-GTTGTTCCAATTTTAGTTGAATTGGATGGTGACGTTAATGGTCATAAATTTTCTGTTTCA -1500
 481-V  V  P  I  L  V  E  L  D  G  D  V  N  G  H  K  F  S  V  S   - 500
1501-GGTGAAGGTGAAGGTGACGCTACTTACGGTAAATTGACATTGAAATTGATCTGTACTACT -1560
 501-G  E  G  E  G  D  A  T  Y  G  K  L  T  L  K  L  I  C  T  T   - 520
1561-GGTAAATTACCAGTTCCATGGCCAACTTTAGTTACTACATTGGGTTACGGTTTAAAGTGT -1620
 521-G  K  L  P  V  P  W  P  T  L  V  T  T  L  G  Y  G  L  K  C   - 540
1621-TTTGCTAGATACCCAGATCATATGAAGCAACATGATTTCTTTAAGTCTGCAATGCCAGAA -1680
 541-F  A  R  Y  P  D  H  M  K  Q  H  D  F  F  K  S  A  M  P  E   - 560
1681-GGTTACGTTCAAGAAAGAACAATTTTCTTTAAAGATGATGGTAACTACAAGACTAGAGCT -1740
 561-G  Y  V  Q  E  R  T  I  F  F  K  D  D  G  N  Y  K  T  R  A   - 580
1741-GAGGTTAAGTTCGAAGGTGACACATTGGTTAACAGAATCGAATTAAAGGGTATTGGTTTT -1800
 581-E  V  K  F  E  G  D  T  L  V  N  R  I  E  L  K  G  I  G  F   - 600
1801-AAAGAAGATGGTAACATCTTGGGTCATAAATTAGAATACAATGGTTTGGCAGGTTTGACA -1860
 601-K  E  D  G  N  I  L  G  H  K  L  E  Y  N  G  L  A  G  L  T   - 620
1861-AGATTATCCTTTGCTATATTGAATCCTAAGTGGAGAGAAGAAATGATGGGTTAA       -1914
 621-R  L  S  F  A  I  L  N  P  K  W  R  E  E  M  M  G  *         - 640
```

mScarlet-I-iNap2

Sequence length: 1,914 bp

```
   1-GTGAGCAAGGGCGAGGCAGTGATCAAGGAGTTCATGCGGTTCAAGGTGCACATGGAGGGC -  60
   1-V  S  K  G  E  A  V  I  K  E  F  M  R  F  K  V  H  M  E  G   -  20
  61-TCCATGAACGGCCACGAGTTCGAGATCGAGGGCGAGGGCGAGGGCCGCCCCTACGAGGGC - 120
  21-S  M  N  G  H  E  F  E  I  E  G  E  G  E  G  R  P  Y  E  G   -  40
 121-ACCCAGACCGCCAAGCTGAAGGTGACCAAGGGTGGCCCCCTGCCCTTCTCCTGGGACATC - 180
  41-T  Q  T  A  K  L  K  V  T  K  G  G  P  L  P  F  S  W  D  I   -  60
 181-CTGTCCCCTCAGTTCATGTACGGCTCCAGGGCCTTCATCAAGCACCCCGCCGACATCCCC - 240
  61-L  S  P  Q  F  M  Y  G  S  R  A  F  I  K  H  P  A  D  I  P   -  80
 241-GACTACTATAAGCAGTCCTTCCCCGAGGGCTTCAAGTGGGAGCGCGTGATGAACTTCGAG - 300
  81-D  Y  Y  K  Q  S  F  P  E  G  F  K  W  E  R  V  M  N  F  E   - 100
 301-GACGGCGGCGCCGTGACCGTGACCCAGGACACCTCCCTGGAGGACGGCACCCTGATCTAC - 360
 101-D  G  G  A  V  T  V  T  Q  D  T  S  L  E  D  G  T  L  I  Y   - 120
 361-AAGGTGAAGCTCCGCGGCACCAACTTCCCTCCTGACGGCCCCGTAATGCAGAAGAAGACA - 420
 121-K  V  K  L  R  G  T  N  F  P  P  D  G  P  V  M  Q  K  K  T   - 140
 421-ATGGGCTGGGAAGCGTCCACCGAGCGGTTGTACCCCGAGGACGGCGTGCTGAAGGGCGAC - 480
 141-M  G  W  E  A  S  T  E  R  L  Y  P  E  D  G  V  L  K  G  D   - 160
 481-ATTAAGATGGCCCTGCGCCTGAAGGACGGCGGCCGCTACCTGGCGGACTTCAAGACCACC - 540
 161-I  K  M  A  L  R  L  K  D  G  G  R  Y  L  A  D  F  K  T  T   - 180
 541-TACAAGGCCAAGAAGCCCGTGCAGATGCCCGGCGCCTACAACGTCGACCGCAAGTTGGAC - 600
 181-Y  K  A  K  K  P  V  Q  M  P  G  A  Y  N  V  D  R  K  L  D   - 200
 601-ATCACCTCCCACAACGAGGACTACACCGTGGTGGAACAGTACGAACGCTCCGAGGGCCGC - 660
 201-I  T  S  H  N  E  D  Y  T  V  V  E  Q  Y  E  R  S  E  G  R   - 220
 661-CACTCCACCGGCGGCATGGACGAGCTGTACAAGACTAGTGGTGGTTCAGGTGGTGGTGGT - 720
 221-H  S  T  G  G  M  D  E  L  Y  K  T  S  G  G  S  G  G  G  G   - 240
 721-TCAGGTGGTGGTGGTTCAGGTGGAGGAGGATCAGGAGGAAACAGAAAGTGGGGTTTGTGT - 780
 241-S  G  G  G  G  S  G  G  G  G  S  G  G  N  R  K  W  G  L  C   - 260
 781-ATCGTCGGTATGGGTAGATTAGGTTCCGCCTTAGCAGACTATCCTGGTTTTGGTGAAAGT - 840
 261-I  V  G  M  G  R  L  G  S  A  L  A  D  Y  P  G  F  G  E  S   - 280
 841-TTTGAATTGAGAGGTTTCTTTTCTAGGTCGGCTGAAAAAGTTGGTAGACCAGTTAGAGGT - 900
 281-F  E  L  R  G  F  F  S  R  S  A  E  K  V  G  R  P  V  R  G   - 300
 901-GGTGTTATTGAACATACAGATTTGTTGCCACAAAGAGTTCCAGGTAGAATTGAAATTGCT - 960
 301-G  V  I  E  H  T  D  L  L  P  Q  R  V  P  G  R  I  E  I  A   - 320
 961-TTGTTAACTGTTCCAAGAGAAGCTGCACAAAAAGCTGCAGATTTGTTAGTTGCTGCAGGT -1020
 321-L  L  T  V  P  R  E  A  A  Q  K  A  A  D  L  L  V  A  A  G   - 340
1021-ATTAAAGGTATTTTGAACTTCGCACCAGTTGTTTTAGAAGTTCCAAAGGAAGTTGCTGTT -1080
 341-I  K  G  I  L  N  F  A  P  V  V  L  E  V  P  K  E  V  A  V   - 360
1081-GAAAACGTTGATTTCTCAGCAGGTTACAACTCTGATAACGTTTACATCATGGCTGATAAG -1140
 361-E  N  V  D  F  S  A  G  Y  N  S  D  N  V  Y  I  M  A  D  K   - 380
1141-CAAAAGAATGGTATTAAAGCAAACTTCAAGATCAGACATAATGTTGAAGATGGTTCAGTT -1200
 381-Q  K  N  G  I  K  A  N  F  K  I  R  H  N  V  E  D  G  S  V   - 400
1201-CAATTGGCTGATCATTACCAACAAAACACACCAATTGGTGACGGTCCAGTTTTGTTGCCA -1260
 401-Q  L  A  D  H  Y  Q  Q  N  T  P  I  G  D  G  P  V  L  L  P   - 420
1261-GATAACCATTACTTGTCTTTTCAATCAGTTTTGTCTAAAGATCCAAACGAAAAGAGAGAT -1320
 421-D  N  H  Y  L  S  F  Q  S  V  L  S  K  D  P  N  E  K  R  D   - 440
1321-CATATGGTTTTGTTAGAATTCGTTACTGCTGCAGGTATCACATTGGGTATGGATGAATTA -1380
 441-H  M  V  L  L  E  F  V  T  A  A  G  I  T  L  G  M  D  E  L   - 460
1381-TACAACGTTGATGGTGGTTCAGGTGGTACTGGTTCTAAAGGTGAAGAATTGTTTACAGGT -1440
 461-Y  N  V  D  G  G  S  G  G  T  G  S  K  G  E  E  L  F  T  G   - 480
1441-GTTGTTCCAATTTTAGTTGAATTGGATGGTGACGTTAATGGTCATAAATTTTCTGTTTCA -1500
 481-V  V  P  I  L  V  E  L  D  G  D  V  N  G  H  K  F  S  V  S   - 500
1501-GGTGAAGGTGAAGGTGACGCTACTTACGGTAAATTGACATTGAAATTGATCTGTACTACT -1560
 501-G  E  G  E  G  D  A  T  Y  G  K  L  T  L  K  L  I  C  T  T   - 520
1561-GGTAAATTACCAGTTCCATGGCCAACTTTAGTTACTACATTGGGTTACGGTTTAAAGTGT -1620
 521-G  K  L  P  V  P  W  P  T  L  V  T  T  L  G  Y  G  L  K  C   - 540
```

```
1621-TTTGCTAGATACCCAGATCATATGAAGCAACATGATTTCTTTAAGTCTGCAATGCCAGAA -1680
 541-F  A  R  Y  P  D  H  M  K  Q  H  D  F  F  K  S  A  M  P  E   - 560
1681-GGTTACGTTCAAGAAAGAACAATTTTCTTTAAAGATGATGGTAACTACAAGACTAGAGCT -1740
 561-G  Y  V  Q  E  R  T  I  F  F  K  D  D  G  N  Y  K  T  R  A   - 580
1741-GAGGTTAAGTTCGAAGGTGACACATTGGTTAACAGAATCGAATTAAAGGGTATTGGTTTT -1800
 581-E  V  K  F  E  G  D  T  L  V  N  R  I  E  L  K  G  I  G  F   - 600
1801-AAAGAAGATGGTAACATCTTGGGTCATAAATTAGAATACAATGGTTTGGCAGGTTTGACA -1860
 601-K  E  D  G  N  I  L  G  H  K  L  E  Y  N  G  L  A  G  L  T   - 620
1861-AGATTATCCTTTGCTATATTGAATCCTAAGTGGAGAGAAGAAATGATGGGTTAA       -1914
 621-R  L  S  F  A  I  L  N  P  K  W  R  E  E  M  M  G  *         - 640
```

sfpHluorin

Sequence length: 716 bp

```
   1-ATGAGCAAAGGAGAAGAACTTTTCACTGGAGTTGTCCCAATTCTTGTTGAATTAGATGGT - 60
   1-M  S  K  G  E  E  L  F  T  G  V  V  P  I  L  V  E  L  D  G   - 20
  61-GATGTTAATGGGCACAAATTTTCTGTCCGTGGAGAGGGTGAAGGTGATGCTACAAACGGA - 120
  21-D  V  N  G  H  K  F  S  V  R  G  E  G  E  G  D  A  T  N  G   - 40
 121-AAACTCACCCTTAAATTTATTTGCACTACTGGAAAACTACCTGTTCCGTGGCCAACACTT - 180
  41-K  L  T  L  K  F  I  C  T  T  G  K  L  P  V  P  W  P  T  L   - 60
 181-GTCACTACTCTGTCTTATGGTGTTCAATGCTTTTCCCGTTATCCGGATCACATGAAACGG - 240
  61-V  T  T  L  S  Y  G  V  Q  C  F  S  R  Y  P  D  H  M  K  R   - 80
 241-CATGACTTTTTCAAGAGTGCCATGCCCGAAGGTTATGTACAGGAACGCACTATATCTTTC - 300
  81-H  D  F  F  K  S  A  M  P  E  G  Y  V  Q  E  R  T  I  S  F   - 100
 301-AAAGATGACGGGACCTACAAGACGCGTGCTGAAGTCAAGTTTGAAGGTGATACCCTTGTT - 360
 101-K  D  D  G  T  Y  K  T  R  A  E  V  K  F  E  G  D  T  L  V   - 120
 361-AATCGTATCGAGTTAAAGGGTATTGATTTTAAAGAAGATGGAAACATTCTTGGACACAAA - 420
 121-N  R  I  E  L  K  G  I  D  F  K  E  D  G  N  I  L  G  H  K   - 140
 421-CTCGAGTACAACTTTAACGAGCACTTGGTATACATCACGGCAGACAAACAAAAGAATGGA - 480
 141-L  E  Y  N  F  N  E  H  L  V  Y  I  T  A  D  K  Q  K  N  G   - 160
 481-ACCAAAGCTATCTTCCAAGTTCACCACAACGTTGAAGATGGTTCCGTTCAACTAGCAGAC - 540
 161-T  K  A  I  F  Q  V  H  H  N  V  E  D  G  S  V  Q  L  A  D   - 180
 541-CATTATCAACAAAATACTCCAATTGGCGATGGCCCTGTCCTTTTACCAGACAACCATTAC - 600
 181-H  Y  Q  Q  N  T  P  I  G  D  G  P  V  L  L  P  D  N  H  Y   - 200
 601-CTGCACACACAATCTGTCCTTTCGAAAGATCCCAACGAAAAGCGTGACCACATGGTCCTT - 660
 201-L  H  T  Q  S  V  L  S  K  D  P  N  E  K  R  D  H  M  V  L   - 220
 661-CTTGAGTTTGTAACTGCTGCTGGGATTACACATGGCATGGATGAGCTCTACAAATAT     - 716
 221-L  E  F  V  T  A  A  G  I  T  H  G  M  D  E  L  Y  K  *         - 240
```

8. ERKLÄRUNG

Ich erkläre: Ich habe die vorgelegte Dissertation selbständig und ohne unerlaubte fremde Hilfe und nur mit den Hilfen angefertigt, die ich in der Dissertation angegeben habe. Alle Textstellen, die wörtlich oder sinngemäß aus veröffentlichten Schriften entnommen sind, und alle Angaben, die auf mündlichen Auskünften beruhen, sind als solche kenntlich gemacht. Bei den von mir durchgeführten und in der Dissertation erwähnten Untersuchungen habe ich die Grundsätze guter wissenschaftlicher Praxis, wie sie in der „Satzung der Justus-Liebig-Universität Gießen zur Sicherung guter wissenschaftlicher Praxis“ niedergelegt sind, eingehalten.

Gießen, Januar 2022

Kim Heimsch